Heterogeneity of cellular compartments out of thermodynamic equilibrium

Von der Universität Bayreuth
zur Erlangung des Grades eines
Doktors der Naturwissenschaften (Dr. rer. nat.)
genehmigte Abhandlung

von

Claudia Maria Donth

aus Roth

1. Gutachter Prof. Dr. Matthias Weiss
2. Gutachter Prof. Dr. Axel Enders

Tag der Einreichung: 28.02.2020
Tag des Kolloquiums: 26.07.2021

Abstract
Cells are crowded by a multitude of structures of different sizes. So crowding can be expected to differ significantly depending on the locus within the cell as well as the lengthscale at which it is investigated. This thesis focuses on characterizing intracellular crowding states and crowding heterogeneities on several lengthscales. Living HeLa cells were analysed using fluorescence intensity imaging, ratiometric imaging, ratiometric FRET, FLIM, FLPM and FCS with the fluorescent sensors EGFP, Perceval HR and fCrH2. In addition, fCrH2 was proved to reflect only its surroundings' crowding state. Cytoplasmic crowding levels were found to exceed nucleoplasmic crowding levels, a difference that is retained to some degree after nuclear envelope breakdown. Crowding heterogeneity was found to be more pronounced in the cytoplasm than in the nucleoplasm on intermediate lengthscales, but not on lengthscales below several hundred nanometres. These results were found to be temporally invariant and independent of the existence of a cytoskeleton. Heterogeneity levels in mitotic compartments are very similar on all lengthscales investigated. Exposure to osmolar or oxidative stress as well as ATP depletion was found to influence crowding levels, but not their heterogeneities. A notable exception to this rule is osmolar stress, where intermediate crowding heterogeneity changes as well. The results of this thesis can be used in simulations on intracellular transport, e.g. in medical applications.

Zusammenfassung
Zellen sind dicht gepackte Systeme, die vielfältige Strukturen unterschiedlicher Größe enthalten. Es ist zu erwarten, dass die lokale Gedrängtheit sich stark unterscheidet, je nachdem, welcher Ort in der Zelle auf welcher Größenskala betrachtet wird. Ziel dieser Arbeit ist es, die intrazelluläre Gedrängtheit sowie deren Heterogenität auf mehreren Längenskalen zu charakterisieren. Lebende HeLa-Zellen wurden mittels fluoreszenzintensitätsbasierter und ratiometrischer Bildgebung, ratiometrischem FRET, FLIM, FLPM und FCS untersucht. Dabei wurden die Fluoreszenzsensoren EGFP, Perceval HR und fCrH2 verwendet. Bei letzterem wurde zunächst nachgewiesen, dass tatsächlich ausschließlich die Gedrängtheit der Umgebung wiedergegeben wird. Es wurde gezeigt, dass das Zytoplasma dichter gepackt ist als das Nukleoplasma. Dieser Unterschied wird teilweise auch nach dem Abbau der Kernmembran beibehalten. Die Heterogenität ist auf mittleren Längenskalen im Zytoplasma stärker ausgeprägt als im Nukleoplasma. Auf Längenskalen unter einigen hundert Nanometern verschwindet dieser Unterschied. Diese Ergebnisse sind zeitlich invariant und nicht an die Existenz des Zytoskeletts gebunden. In Mitosezellen ähneln sich die Heterogenitäten beider Kompartimente auf allen Längenskalen stark. Die Ausübung von osmolarem oder oxidativem Stress wie auch ATP-Entzug beeinflussen zwar die Gedrängtheit an sich, jedoch nicht deren Heterogenität. Lediglich unter osmolarem Stress ändert sich auch die Heterogenität der Kompartimente. Die Ergebnisse dieser Arbeit können beispielsweise in Simulationen von intrazellulären Transportprozessen verwendet werden und sind daher insbesondere für medizinische Anwendungen von Interesse.

Contents

Chapter 1

Introduction

When sifting through scientific literature published during the last few decades, one cannot fail to note one trait most of these studies have in common: they usually share the practice of focusing on averaged values of an ensemble of measurement data. In some cases critical reading even can raise the suspicion that the respective authors rather hope to distract the reader from inconveniently large standard deviations. If measurements are performed in fairly homogeneous samples, this approach is, of course, perfectly acceptable. However, if samples feature an intrinsic heterogeneity, invaluable information might get lost.

The aspect of intrinsic heterogeneity is especially important in biological applications, for example when investigating single cells or small cell populations. In the macroscopic world, fluctuations at this scale can often be neglected. This can be explained by the law of large numbers: the more often a measurement is repeated (i.e. the more cells are sampled), the closer to the expected value their average should be. However, strictly speaking, this theorem is only true for systems at equilibrium. Living organisms, on the other hand, are out of thermal equilibrium: in order to sustain life, energy has to be supplied and is consumed constantly. Yet in systems out of equilibrium, the law of large numbers does not always apply. Thus even macroscopic systems such as large organisms can exhibit large fluctuations[1].

On the single-cell level and below, i.e. within cells, random fluctuations can have a major impact on vital processes. Nevertheless, noise does not necessarily have to be detrimental: a lot of intracellular processes actually rely on randomness. A notable and well documented example of such processes is diffusional transport of molecules in cells[2] [3]. But there are many more examples of the importance of noise on the cellular level. In recent years fluc-

tuations in gene expression and their effect on organisms have been a subject of interest for many scientists[4] [5] [6]. Evolution itself is driven by stochastic gene mutations and "random" recombination of genetic material during sexual reproduction as well as chromosomal crossover or even parasexual gene transfer. Probably the most fundamental source of fluctuations on the intracellular levels is, however, intrinsic thermal noise in biochemical reactions[7]. After all, reactions generally depend on random collisions and transient binding of specific molecules. In view of the fact that many proteins exist only in low numbers within one cell - for example, in *Escherichia coli* about 75 % of all protein species are present in less than 250 copies[8] - a distinct spatial organization of intracellular contents should be expected to be advantageous for any cell. Yet membrane-enclosed compartments are a characteristic feature only in eukaryotic cells. Even though current estimates on the absolute number of prokaryote (and archaea) species on earth diverge by several orders of magnitude, experts agree that they far outnumber eukaryotes[9] [10] [11]. Even certain elements, such as nitrogen and phosphorus, are predominantly stored in prokaryotes[12]. In view of this obvious evolutionary success of prokaryotes, there has to be another, alternative or additional way of organizing intracellular contents.
Indeed it has been shown that *Caulobacter crescentus* can achieve a certain degree of compartmentalization based on chromosomal gene order[13]. Moreover, a brief glance at intracellular contents reveals that cells are tightly packed with a multitude of structures of vastly different sizes - ranging from sub-nanometres (e.g. dissolved ions) to several micrometres (e.g. organelles). In view of the fact that organelles are membrane-enclosed and usually occupy distinct spaces within cells, other, smaller structures can only occupy the remaining fraction of intracellular volume. So the diversity of molecular constituents of different sizes already results in some kind of structuring of the cell's inside. Consequently local molecule densities - or "crowding states" - can be expected to be highly heterogeneous throughout the cell. What is more, crowding states and heterogeneities might differ even within the same subcellular region depending on the lengthscales at which they are investigated. Keeping in mind the profound structural changes cells undergo in the course of one cell cycle, temporal variations in either observable are very likely to occur.

The fundamental aim of this thesis is to characterize intracellular crowding states as well as their heterogeneities on several lengthscales. This is achieved

by performing imaging-based as well as lifetime-based experiments in living HeLa cells transfected with various fluorescence markers.
Heterogeneity analysis is mainly based on the coefficient of variation, i.e. on a normalized standard deviation of observables. So, instead of limiting analyses to considering only averaged values (and possibly even hoping for small "errors"), the focus of this thesis lies explicitly in exploiting the spatial variation of an observable in order to deduce information about the cell's structure.
As monitoring cells throughout cell cycle progression is challenging, crowding states and crowding heterogeneities are analysed either in interphase cells or in metaphase cells. In addition, the influence of various treatments on interphase crowding states and crowding heterogeneities is investigated.
Since crowding has a profound impact on many intracellular processes, including protein formation, biochemical reactions and transport processes, the results found in this thesis can, for example, be used in simulations and evaluations of intracellular diffusion. Thus, especially bioinformatics and nanomedicine might benefit from insights gained in this thesis[14] [15] [16].

Part I

Fundamentals

Chapter 2

Theoretical Background

This chapter presents fundamentals of cell biology and biophysics relevant for this work. After a short description of the spatial organization of HeLa cells in interphase and metaphase, an overview of the basic principles of macromolecular crowding and hitherto existing evidence of its spatially heterogeneous nature will be given.

2.1 A Brief Overview of the Composition and Spatial Organization of HeLa Cells

According to cell theory, all living organisms consist of at least one cell. Cells are considered to be the basic building blocks of life, i.e. the most fundamental unit of structure, function and reproduction[17] [18]. Cells can be divided into two main categories, prokaryotes and eukaryotes, that make up the three domains of life on earth[19] [20]. The most prominent features separating eukaryotes from prokaryotes are size, the more complex organization of genetic information, the existence of a membrane-enclosed nucleus and membrane-enclosed organelles[21] [22].

There is an enormous diversity of organisms, even within one kingdom[21]. On a cellular level, however, organisms bear a striking similarity. Despite certain differences, they generally feature the same types of organelles and have comparable metabolisms[22]. Even some of the fundamental reaction pathways are widely conserved[23] [24] [25]. Therefore, results obtained by studying one type of cell can often be transferred to other cell types, a fact which is, in particular, important in medical applications.

In this work, all measurements were taken in interphase or metaphase cells of

the Göteborg strain of HeLa wildtype cells - a line of human cervical cancer cells widely used in scientific research [26] [27]. The subsequent introduction into intracellular organization focuses on the characteristics of these two cell cycle phases in this particular cell line. Still, many of the characteristics described below are widely conserved among species, and also the results of this thesis are likely to be transferable to other mammalian cells. For a more in-depth description of intracellular organization, see e.g. Alberts [22].

2.1.1 Composition and Spatial Organization of HeLa Cells in Interphase

A complete cycle of growth and division in HeLa cells takes approximately 22 h [28]. Around 95 % of this time the cell is in interphase [29], which is divided into three subphases: in S phase DNA is replicated, a process which takes about half the time of interphase. G1 and G2, two gap phases of varying lengths, are mainly used for cell growth and monitoring of the cell's internal and external environment [22] [30].
Interphase cells can be subdivided into two major compartments: nucleus and cytoplasm. Apart from a number of exceptions, mammalian cells have only one nucleus. It constitutes the biggest organelle in the cell. In the strain of HeLa cells used in this thesis it is most often ellipsoidal or kidney-shaped with semi-axis sizes of (23 ± 4) µm and (10 ± 3) µm, respectively. A schematic view of a typical HeLa cell in interphase is shown in Fig. 2.1. The perinuclear space is separated from the surrounding cytoplasm by a lipid bilayer membrane that is continuous with the rough endoplasmic reticulum. This allows the maintenance of a defined reaction space more or less independent of the processes in the cytoplasm, thus guaranteeing the accurate replication and transcription of the cellular genome. At the same time, nuclear pore complexes ensure regulated transport of molecules between nucleoplasm and cytoplasm [22].

The nucleoplasm consists mainly of DNA in the form of decondensed chromatin, RNA, nucleoli containing mainly genetic information of ribosomal RNA, as well as speckles, PML bodies and Cajal bodies. The liquid part of the nucleoplasm is referred to as nucleosol, containing dissolved molecules such as nucleotides and enzymes. The most prevalent types of proteins in the nucleus are DNA and RNA polymerases, histones and transcription factors [22]. The nucleus might also feature a dynamic network or a sponge-like structure of protein fibres reminiscent of the cytoskeleton [31]. Recently, however, the very

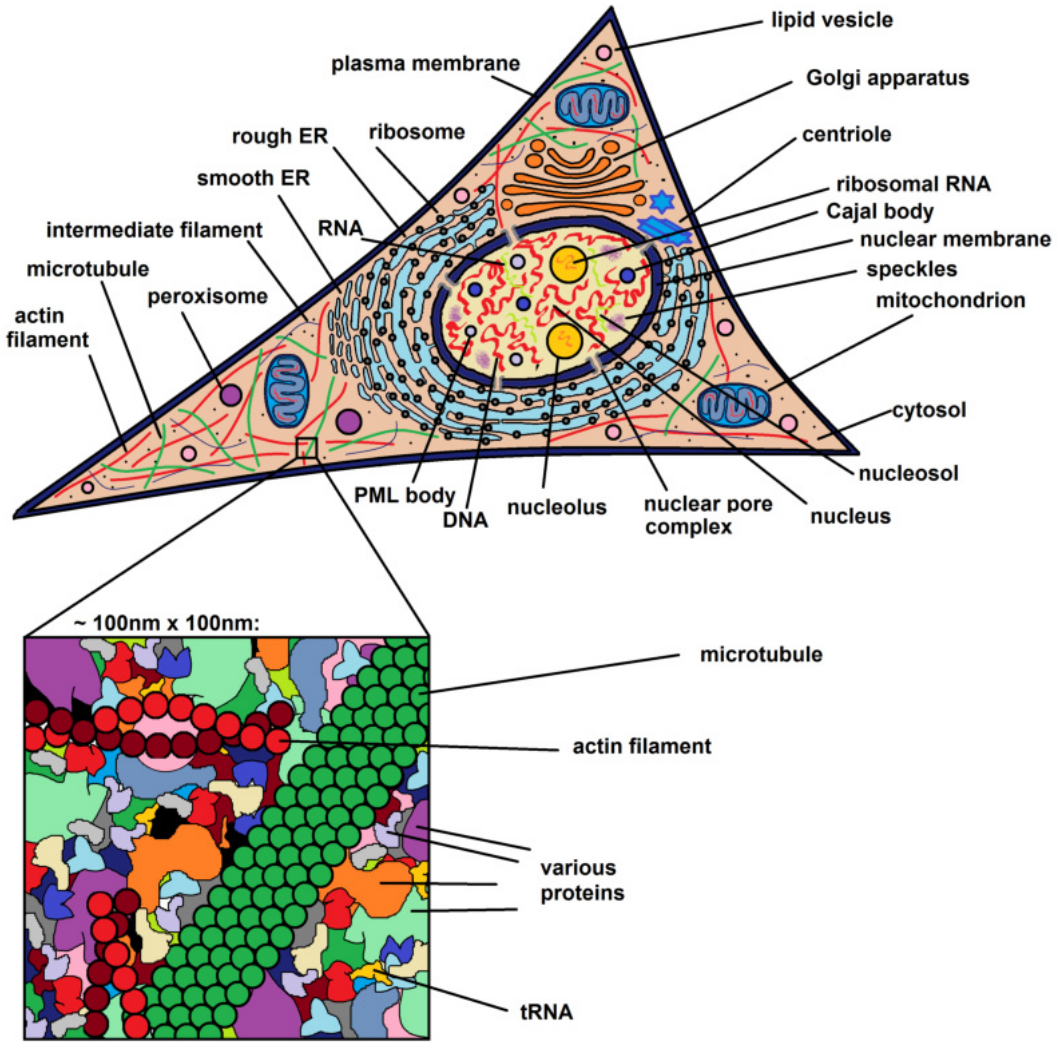

Figure 2.1: Schematic view of an interphase cell. Nucleoplasm and cytoplasm feature multiple structures of vastly different sizes and shapes. Some of them are enclosed by lipid membranes, some are not. The space between organelles and other large structures is occupied by structures such as proteins and dissolved (macro)molecules.

existence of this nuclear matrix has been called into question[32].

The cytoplasm, delimited by plasma membrane and nuclear membrane, consists of a liquid part, the cytosol, as well as a number of membrane-enclosed organelles of various sizes and non-soluble inclusions such as lipid droplets. On lengthscales of several micrometres, the architecture of the cytoplasm is dominated by large organelles like nucleus, mitochondria and Golgi apparatus. As shown in Fig. 2.1 the Golgi apparatus consists of several cisternae and is located close to the nucleus. The endoplasmic reticulum can be considered to be a large organelle spanning most of the cytoplasm. Due to its characteristic net-like structure, however, it should rather be counted to be a part of the 100 nm-lengthscale. Similarly, the cytoskeleton could be viewed as a part of

this lengthscale. It is a complex network featuring various protein filaments: microtubules, intermediate filaments as well as actin filaments[22].
Going below the 100 nm-scale (see zoomed in area in Fig. 2.1), cells feature structures such as non-soluble lipid droplets and small vesicles. The cytosol, i.e. the liquid part of the cytoplasm, constitutes about 70 % of the total cell volume. It is a complex concoction of small structures like protein filaments, dissolved molecules and water. Small proteins, carbohydrates and RNA molecules are typical examples of dissolved molecules. They range in size from 1 nm to 10 nm. On the subnanometer scale water and dissolved ions like Ca^{2+}, Na^{+}, Cl^{-} are abundant constituents of cells[22].
The compartmentalization achieved by this multi-scale nature of cellular architecture enables and facilitates the simultaneous implementation of highly diverse biochemical reactions in the cell. Various types of reactions require a certain type of environment. Confining them to several membrane-enclosed organelles, environmental conditions can be optimized for the respective reaction pathway without having to adjust the total cell interior to these conditions, a process that would cost a considerate amount of energy. Specific pH values differing from that of the cytoplasm, for example, can easily be maintained. Even reactions that include potentially harmful intermediate products and by-products, such as the generation of reactive oxygen species by the electron transport chain, can be performed without danger of harming the cell in total. This is due to the fact that the reaction is restricted to one specialized type of organelles, the mitochondria. But even without an encompassing membrane, subcompartments with locally varying biochemical conditions can be formed owing to the complex and dynamic network of cellular structures[22]. Of course, this compartmentalization can facilitate biochemical reactions by merely putting reactants in close proximity.
Another effect of intracellular multi-scale architecture is the fact that, although approximately 70 % of the cell's volume is water[22], physically the interior of cells does not behave like an ideal solution[33]. Cells rather show an effect referred to as macromolecular crowding. Macromolecular crowding has an impact on many intracellular processes, such as diffusional transport. It will be discussed in more detail in Sec. 2.2.
Although mammalian cells feature many distinct structures, nucleoplasm and cytoplasm are the only compartments accessible by combining the methods used in this work. While nucleoli could be clearly discriminated in imaging-based methods, cytoplasmic organelles could, at best, be seen as darker spots

in fluorescence images. However, no individual organelles could be identified in the cytoplasm. Therefore, analyses were restricted to areas in the recorded cells in which no conspicuous structure was visible to the naked eye. What is more, without labelling of additional intracellular structures the different subphases of interphase could not be differentiated. Considering the fact that interphase cells were recorded in unsynchronized cultures, it is assumed that all interphase subphases were recorded with probabilities according to their relative duration.

2.1.2 Major Changes upon Entry in Mitosis

The cellular genome being duplicated successfully, cells enter into mitosis to split into two daughter cells - provided the intra- and extracellular conditions are favourable. The five mitotic phases - prophase, prometaphase, metaphase, anaphase and telophase - are primarily defined by their movement of chromosomes as seen in the microscope[22]. Metaphase is the only mitotic phase considered in this work. So this passage focuses on the processes between entering into mitosis and forming a metaphase plate. A schematic view of a typical HeLa cell in metaphase and the conformational changes leading to this state is shown in Fig. 2.2. Examples of labelled structures in actual living cells in interphase and metaphase are displayed in Fig. 2.3.

During interphase (Fig. 2.2a) mammalian cells consist of two clearly distinguished types of protoplasm: nucleoplasm and cytoplasm. Upon entry into mitosis these compartments are not strictly separated any longer, since mammalian cells generally divide by open mitosis[34]. After the condensation of interphase DNA (Fig. 2.2a and Fig. 2.3a, b, and c) into sister chromatid shape and the onset of spindle assembly in prophase (Fig. 2.2b), prometaphase starts with the breakdown of the nuclear envelope (Fig. 2.2c). Chromosomes attach to spindle microtubules and, subsequently, are aligned at the equator of the fully formed metaphase spindle (Fig. 2.2d and 2.3d). Simultaneously, the flat, often triangular or trapezoid interphase HeLa cells detach from their growth surface and change to a spherical shape[22]. This procedure is accompanied by major changes in the shape and localization of several organelles: The endoplasmic reticulum changes from its mostly net-like interphase structure to a mostly sheet-like metaphase structure which is limited to the outside of the spindle region (Fig. 2.3b and 2.3e). At the same time the interphase

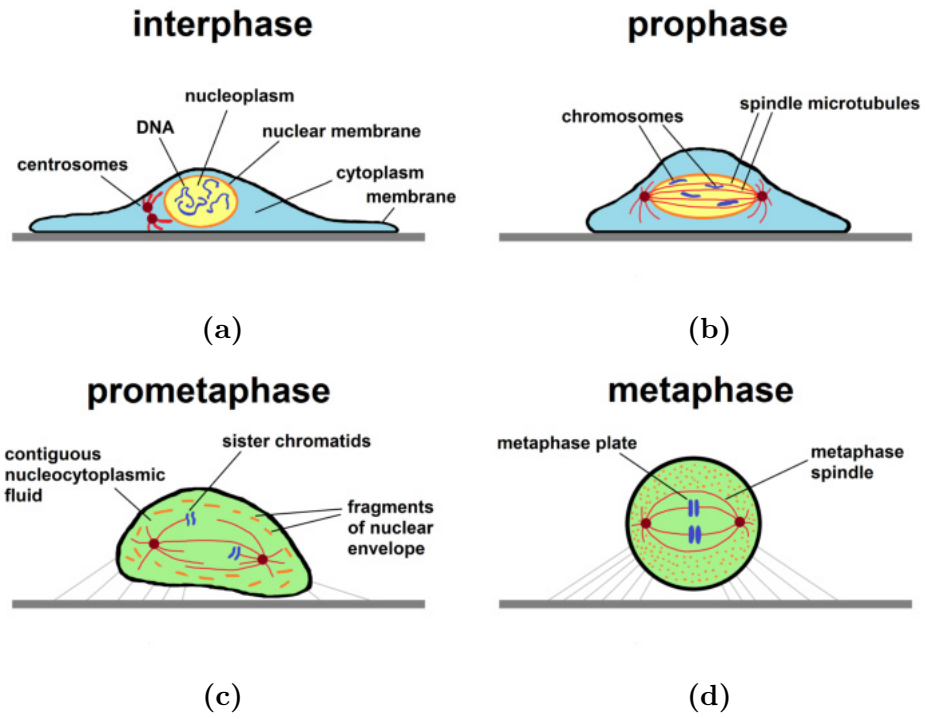

Figure 2.2: Schematic view of a cell's progression from interphase into metaphase. (a) In interphase the cell is attached to the surface. (b) Nuclear envelope breakdown in prophase is accompanied by the formation of a mitotic spindle. (c) In prometaphase the cell starts to detach from the surface. Simultaneously spindle microtubules attach to the chromosomes' kinetochores. (d) In metaphase the cell has assumed a globular shape, chromosomes are aligned in a metaphase plate.

Golgi apparatus disintegrates and its fragments, along with the former nuclear envelope's fragments, are evenly distributed throughout the whole cell (Fig. 2.3c and 2.3f). Even organelles that do not show any conspicuous structural changes, like e.g. mitochondria, display a characteristic spatial distribution during mitosis[35]. Due to this plainly disproportionate dispersal of big intracellular structures crowding states in the mitotic spindle region are likely to be different from those in its surroundings. In fact the exclusion of large structures from the spindle region has been shown to induce the accumulation of mitotic regulators in the spindle region[36]. As mitotic regulators are comparatively small, it is likely that the same effect holds true for other small molecules as well. Therefore it is legitimate to treat the metaphase spindle region and its surroundings as separate compartments analogous to nucleus and cytoplasm in interphase, although they lack a physical barrier such as the nuclear envelope.

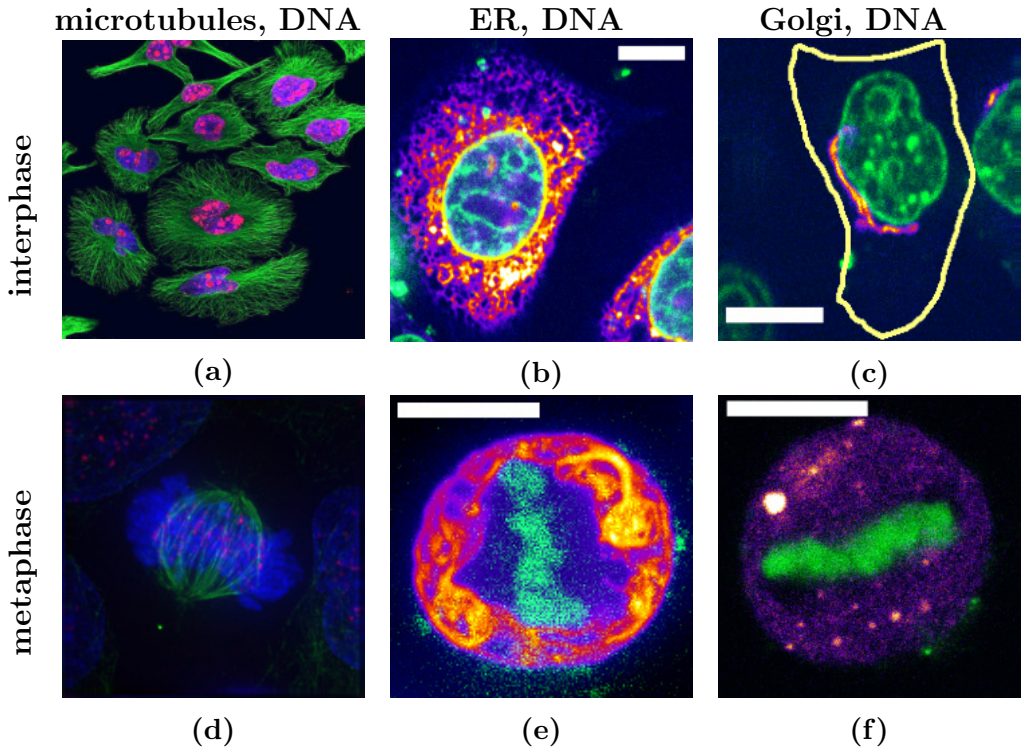

Figure 2.3: Intracellular components display marked differences between their interphase and metaphase structure and localizations. Top row: interphase cells, bottom row: metaphase cells. Fluorescently labelled structures: (a) + (d) Microtubules (green) and DNA (blue). In interphase: Ki-67 (violet), in metaphase: kinetochores (violet). (b) + (e) ER (fire) and DNA (green). (c) + (f) Golgi (fire) and DNA (green), interphase membrane traced in yellow for clarity. Scalebars 10 µm. Figure (a) taken from [37] (slightly changed), figure (d) taken from [38]. Scale in figures (a) and (d) not given by respective authors.

2.2 Macromolecular Crowding

2.2.1 Crowding and its Effects on Cellular Transport and Reaction Kinetics

About 70 % of the total cell volume is made of an elaborate mixture of dissolved molecules ranging in size from 1 nm to 100 nm [22]. Even cells as small as *Escherichia coli* contain several thousand different types of proteins [39]. About 1000 of these proteins are produced at levels high enough to be detected easily [40]. This miscellany of molecules is summarized by the terms "cytosol" or "nucleosol", respectively. Although their main ingredient is water, they cannot be viewed as ideal aqueous solutions [33] [41]. Protein filaments like actin and microtubules, which form the cytoskeleton, divide the cytosol into an intricate network of narrow pores [33] [42]. Moreover, while the cumulative concentration of all macromolecules can reach up to 300 mg ml^{-1} [43] or 20 % to 30 % of the

total cell volume[44] the concentrations of individual molecule types are usually small. Therefore, cellular fluids are referred to as "crowded" rather than "concentrated" [45].

Crowding has several major impacts on intracellular processes. First and foremost, the high overall concentration of macromolecules considerably reduces the volume of solvent available for molecules in the solution. Depending on the size of the investigated structure, it might be necessary to make the distinction between excluded volume and occupied volume[46] (see Fig. 2.4). As molecules are generally considered to be impenetrable, one increment of space can only be occupied by one molecule at a time. Therefore the term "occupied volume" (labelled black in Fig. 2.4) refers to the sum of all volume increments that have already been occupied by molecules. However, the volumes in between molecules that are not occupied might nevertheless be too small to provide enough space for another molecule. This is, of course, especially true for big molecules. As a result, the "excluded volume fraction", i.e. all volume unavailable to the centre of mass of a certain type of molecule (labelled red in Fig. 2.4), can substantially exceed the occupied volume fraction. Please do note that the excluded volume fraction can vary considerably for different types of molecules while the occupied volume fraction remains the same for all types of molecules in a sample (see Fig. 2.4a vs. Fig. 2.4b). For example, for two hard spherical particles of similar size the excluded volume is four times the occupied volume[47]. However, one must keep in mind that in biological specimen the particles, i.e. individual molecules or molecule complexes, are, by no means, of equal size but rather cover a wide range of sizes. For example, in the cytoplasm of human cervical cancer cells (HeLa), the protein content follows a Poisson distribution with an average molecular weight of 80 kDa[48]. It can be assumed that the excluded volume fraction of a tracer particle of 20 kDa in a cellular fluid would be even higher than that obtained in solutions of globular proteins of 20 kDa.
It must be noted that the excluded and occupied volume fractions virtually are the same for tracer molecules significantly smaller than the surrounding particles.

As a direct result of this excluded volume effect, the effective concentration of individual molecule species in the solvent is increased considerably. This leads to an increase in chemical activity by changing equilibrium constants and rates

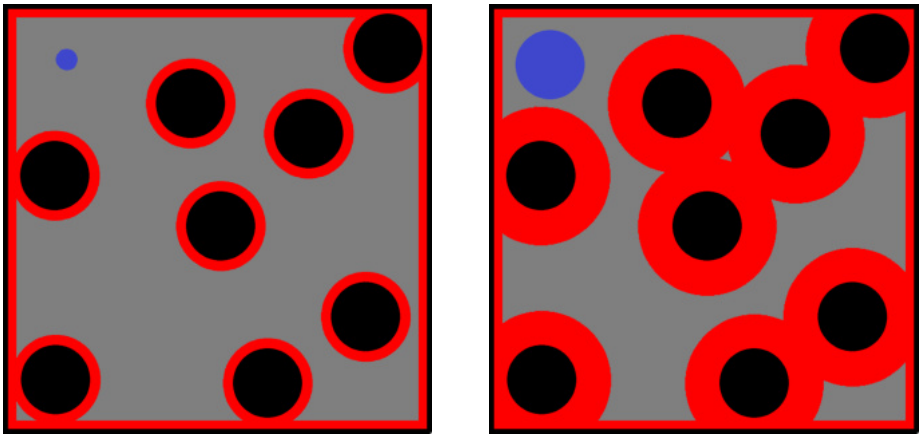

Figure 2.4: Occupied and excluded volume for tracer particles of different sizes. While the occupied volume (black) is identical for tracer particles (blue) of all sizes, much less volume is excluded (red) for (a) tracer particles significantly smaller than the surrounding particles than for (b) tracer particles of the same size as the surrounding particles. Please note that excluded volume is depicted with respect to the tracer particles' centre of mass.

of biochemical reactions[49]. Especially at high crowding levels dissociation constants may be altered by preferring the association of macromolecules to their dissociation[50]. This is due to the fact that a large number of monomers is very likely to occupy more volume than a single polymer. The conformation of macromolecules can be altered by mere crowding effects as well. Crowding, in particular, can significantly accelerate the folding of proteins to their final, often roughly globular shape[51]. This can easily be explained when keeping in mind that a globular particle occupies a considerably smaller volume than an unfolded protein chain. Therefore, by increasing the overall volume occupancy, reactions and folding processes are gradually shifted towards 'more compact' molecule shapes.

An additional important effect of macromolecular crowding on intracellular dynamics is its impact on diffusion. Compared to diffusion in pure water, a tracer particle's motion can be slowed down considerably in a crowded medium such as cellular protoplasms[33]. By means of TIRF and FRAP, for example, Swaminathan et al.[52] found the diffusion coefficient of BCECF, a small fluorescent molecule, in the vicinity of the ventral surface of epithelial cells to be ten-fold lower than in water. Subdiffusive behaviour is frequently reported for biological samples[2] [46] [48] [53]. The anomaly factor α of subdiffusive systems has even been considered to serve as a measure for the crowdedness of cells[48]. The impact of macromolecular crowding on a specific molecule depends mainly on the molecular weight and, to some lesser extent, on the molecule's shape[49].

Effects on molecule motion and reaction kinetics are more pronounced for big molecules than for small ones and affect elongated particles more than globular ones. As the size effect is highly non-linear[54], dynamic behaviour is manipulated much stronger in macromolecules than in smaller particles such as amino acids. Thus macromolecular crowding can be summarized as a phenomenon caused by large molecules, mainly affecting other large molecules. On the other hand, comparatively small particles are considerably affected by excluded volume effects as well as subdiffusion, particularly if they are involved in reactions featuring pronounced changes in their tertiary and/or quaternary structure[45].

Considering the enormous impact of macromolecular crowding on intracellular dynamics it is astonishing that life is possible at all. However, one must keep in mind that biomolecules actually evolved to function in exactly this kind of environment[46] [55] [56] [57]. It is with the help of macromolecular crowding effects that proteins are folded to and stabilized in exactly the shape that is required to guarantee efficient functioning. Subdiffusion has been shown to enhance signal propagation and protein complex formation as well as to increase the probability of finding reaction partners[58]. Considering the fact that crowding is a characteristic feature conserved in all cells as well as in the extracellular environment of multicellular organisms - albeit at varying levels - it might even be thought of as an essential prerequisite to life itself. Even the previously reported disparate crowding states in cytoplasm and nucleoplasm of the same cell[59] might not be a mere side effect from intracellular architecture but also a mandatory requirement for proper functioning of cellular metabolism and reproduction.
Therefore it is not surprising to find that biochemical reactions in test tubes can behave in a radically different way from the way they naturally do in cells[60]. Results obtained in in-vitro experiments in dilute solutions can differ from in-vivo values by several orders of magnitude. That is why they often fail to reflect physiological conditions. Consequently it is essential to study biochemical reactions, for example in medical research, in realistically crowded conditions. There are, however, some major difficulties that have to be taken into account. It might seem to be the obvious choice to analyse a reaction in its native environment, i.e. inside a living cell. But this raises some problems: as previously stated, individual concentrations of one molecule type inside a cell can be extremely low and might be hard or impossible to detect. Moreover, physiological cells harbour a plethora of different mol-

ecules - typical eukaryotic cells are thought to synthesize some 10^5 different proteins[22]. So reaction products of the investigated reaction might, in turn, participate as reagents in various new reaction pathways. For example, the eukaryotic protein calmodulin is supposed to interact with approximately 180 targets including transcription factors, ion channels, enzymes and structural proteins[33] [61]. Thus, even at sufficiently high concentrations, intermediate reaction products might be too short-lived to be detectable. While working with highly concentrated extracts of cells or cell lysates would eliminate the problem of too low concentrations, short molecule lifetimes or interference from other molecules could still be present. In vitro experiments in solutions with high concentrations of artificial crowding agents such as dextran, ficoll, polyethylene glycol and others have been performed by various groups[62] [63]. In this approach undesirable chemical side-effects of native cellular fluids are avoided, whereas the purely steric effects of macromolecular crowding are maintained. A recent study by Stiehl et al.[64] however pointed out that artificial crowding agents fail to reflect the inherent heterogeneity of living cells. Recent evidence of this intracellular heterogeneity is discussed in the next section.

2.2.2 Recent Evidence of the Heterogeneous Nature of Macromolecular Crowding

These days we are used to thinking of cells as crowded systems. In most studies, however, the effects of macromolecular crowding are tacitly assumed to be homogeneous throughout the cell. This assumption seems to be highly questionable given the multi-scale nature of intracellular architecture described above. The mere existence of membrane-bound organelles constitutes an intrinsic spatial inhomogeneity within the cytoplasm. Moreover, organelles are not randomly distributed within the cell: the Golgi apparatus is located close to the nuclear membrane, the endoplasmic reticulum is even contiguous with it. Mitochondria have been reported to be located preferentially near sites of high ATP consumption. Cells even spend a considerable amount of their energy supply on the maintenance of this organelle distribution[33]. In addition, the cytoplasm is permeated by cytoskeletal filaments. These filaments are by no means distributed isotropically throughout the cytoplasm. They rather feature distinct local inhomogeneities[65] [66] which vary spatially as well as temporally[33]. Indeed individual microtubules as well as actin filaments are dynamically unstable as they are growing and shrinking alternately[22].

It was already proposed in 1923 that it might be adequate to describe the cytoplasm not as a homogeneous solution but as a sol-gel[67]. This theory views the cytoplasm as a combination of distinct fluid and solid phases. Depending on the local level of interaction between intracellular constituents the cytoplasm is believed to behave either like an integrated network (gel) or a disordered colloidal solution (sol). A sol-gel description of the cytoplasm might even explain the anomalous diffusion characteristics of tracer particles in cellular protoplasm. More recent evidence suggests that at least half of the cytoplasmic protein content seems to be resident in the solid phase of cytoplasm, i.e. on or in close association with membranes[33]. At the same time the aqueous phase of cytoplasm is crowded with macromolecules. This theory is supported by numerous FRAP studies which reported on significant immobile fractions of cytoplasmic proteins[68] [69] [70] [71] [72] [73]. In fact many proteins, initially assumed to be more or less homogeneously distributed in the cytoplasm, now are known to be localized on membranes or on cytoskeletal filaments[33]. It stands to reason that their reaction partners will preferentially be in close proximity to these localized proteins, even if they are not attached to membranes or cytoskeletal filaments themselves. Indeed a colocalization of enzyme and substrate or regulatory protein and target already prior to interaction has been proposed for several proteins[33]. Colocalization phenomena might also explain how competing interactions can be discriminated within one cell when - as is the case for the protein calmodulin mentioned above - affinities for the majority of binding partners lie within one order of magnitude[33].
Montero-Llopis et al.[13] demonstrated convincingly that *Caulobacter crescentus* uses some form of compartmentalization by localized synthesis of proteins. Although this prokaryote lacks membrane-bound organelles, mRNA processes are spatially organized in a way that prevents ribosomes from diffusing freely. Thus translation and protein synthesis are localized spatially according to chromosomal gene order. Since each gene occupies only a specific locus on the chromosome[74], a functional compartmentalization of the cell interior is achieved solely by means of production of specific protein species within small subregions.
The various benefits of this membraneless compartmentalization for the cell are obvious. Thus it stands to reason that eukaryotic cells might employ a similar principle in addition to membrane-bound organelles. This would inevitably lead to a form of ordering in the aqueous phase of cytoplasm. Considering the

plethora of molecules inside cells with sizes ranging from few nanometres to several micrometres the occupied volume fraction is most likely to vary spatially and possibly also temporally. This, in turn, would have a significant impact on the characteristics of reaction kinetics and transport in the cell.

Indeed recent studies suggested a heterogeneity of crowding states in biological fluids: Lampo et al.[75] performed single particle tracking of mRNA molecules in *Escherichia coli* and *Saccharomyces cerevisiae*. In both organisms they found particle motion to be ergodic, subdiffusive and non-Gaussian at all timescales. They could attribute non-Gaussianity to a combination of a significant heterogeneity between particle trajectories and local spatiotemporal heterogeneities within individual trajectories. They argue that non-Gaussianity as well as the broad spectrum of diffusivities could be a general feature of macromolecularly crowded systems. They even compare crowded fluids to colloidal fluids near their glass transition, a system in which similar displacement distributions have been observed[76][77]. Indeed earlier bacterial cytoplasm[78] as well as human cells[79] were reported to possess glass-like properties. Remarkably, both cell types show very similar tracer behaviour, even though *Escherichia coli* is prokaryotic whereas *Saccharomyces cerevisiae* is eukaryotic. Unfortunately, as a side-effect of the small size of *Escherichia coli* and *Saccharomyces cerevisiae*, Lampo et al. could not pinpoint whether heterogeneity between trajectories is an inter- or intracellular phenomenon.
Witzel et al.[80] performed single particle tracking of chemically inert tracer particles in the cytoplasm of *Dictyostelium discoideum*. They observed tracer diffusion with a non-Gaussian distribution of increments within each trajectory. Most likely this distribution of increments is caused by the cytoplasm's spatio-temporal heterogeneity: their novel fit model, which is based on randomly distributed diffusivities to describe medium heterogeneities, was well suited to describe experimental data. Up to now it has not been possible to discern whether diffusion constants vary only spatially or also temporally. Witzel et al., however, could demonstrate that non-Gaussian diffusion is a feature of the cytoplasm which is independent of cytoskeleton components at least to some degree: by repeating their measurements while progressively removing cytoskeleton elements by drug-induced depolymerization they could show that heterogeneity is reduced, but does not vanish.
Struntz et al.[81] performed SPIM-FCS in *Caenorhabditis elegans* embryo membrane and cytoplasm to obtain diffusion maps of the peripheral membrane pro-

tein PLC1δ1 with high spatiotemporal resolution. They were able to observe spatially varying diffusion coefficients in membranes as well as in cytoplasm. Most likely this pixelwise variation can be attributed to a local heterogeneity of the environment surrounding the tracer.
In a recent study by Stiehl et al.[64] cellular protoplasm was shown to feature a distinct spatial heterogeneity of its volume occupancy on the meso- and nanoscale. This suggests a self-similar texture of cellular protoplasm, although no lengthscales bigger than that accessible by FCS experiments were considered. Interestingly, however, cellular protoplasm was shown to be significantly more heterogeneous than biomimetic fluids.
A study by Schweizer et al.[36] established that spatio-temporal variations in intracellular crowding levels are sufficient to induce a significant accumulation of mitotic regulators in the spindle region of metaphase cells. Furthermore, Pawar et al.[82] observed that diffusion in the mitotic spindle of HeLa cells in metaphase is anisotropic in the spindle region.
Massignan et al.[83] demonstrated by a set of simulations that Brownian motion in an inhomogeneous medium of spatially varying diffusion constants results in nonergodic subdiffusion. In particular, they could show that ergodicity-breaking does not require particle immobilization, as is often assumed, but can be introduced solely by disorder.
Wang et al.[84] observed Fickian yet non-Gaussian diffusion spanning broad timescales for liposomes diffusing in nematic solutions of F-actin filaments. This system features a broad distribution of diffusivities which are likely to be due to the environment's heterogeneity[85]. They propose that non-Gaussian diffusion in soft materials is likely to be more prevalent than expected. Nevertheless they argue that non-Gaussian diffusive systems are not always required to feature multiple diffusion coefficients.
Kühn et al.[86] propose a new approach to describe protein diffusion in cells, based on the construction of a realistic 3d-digital model of a cell. This model was generated using data gathered by confocal microscopy. In it the cell is segmented into a number of subcompartments, namely cytoplasm, nucleoplasm and nuclear envelope. In each of these subcompartments protein dynamics is modelled by numerical mesoscopic methods. Structures beyond the resolution limit of confocal microscopy are accounted for by assigning an effective, spatially varying porosity to the cell. This porosity is characterized by using the (inhomogeneous) equilibrium distribution of a chemically inert fluorescent protein. Heterogeneous fluorescence intensity is interpreted as being homoge-

neous in the liquid phase in which diffusion takes place. Diffusion in porous media, i.e. diffusion in the liquid phase alternating with diffusion in a medium with constrained motion, is modelled by spatially varying "effective" diffusion coefficients depending on spatially varying local porosities. Separate diffusion coefficients are assigned to the different subcompartments. These porous media were assumed to be immobile during the course of a FRAP measurement. Kühn's model was invented as a means to evaluate FRAP data. For previous FRAP analysis methods numerous assumptions have to be made. Until now, however, details of intracellular structure and their impact on tracer diffusion have been included only to some extent. Therefore FRAP data could not be compared directly to FCS data, as, usually, FRAP experiments underestimate diffusion coefficients[86]. The new analysis method was applied to FRAP data of freely diffusing EYFP in NLFK and HeLa cells. The results were compared to FCS data of the same system. Fluorescence intensity distributions measured immediately after the bleaching event were used as a starting point for simulations of post-bleach evolution of fluorescence in the entire cell. Fluorophore distributions were simulated for every time step during fluorescence recovery and fluorescence intensity was computed in the same focal plane in which the experiment was performed. They found excellent correlations between simulated and experimental fluorescence recovery. In fact simulated diffusion coefficients were significantly closer to correct diffusion coefficients than diffusion coefficients obtained by the more commonly applied Soumpasis analysis method[86].

By microinjecting fluorescent tracer particles of different sizes (average hydrodynamic radii of 3.5 nm and 24 nm) into fibroblasts, Luby-Phelps et al.[87] observed subcompartments in the cytoplasm in which large tracers could not be found. Later these subcompartments could be demonstrated to be very flat, containing many filament bundles within a meshwork of thin filaments mostly made up of actin and actin-binding proteins[66]. Although size-excluding and non-excluding compartments differed in ultrastructure and cell height, Luby-Phelps et al. could not detect any kind of membrane or other physical barrier. Due to the fine filament network within the excluding compartments they suggested a molecular sieving mechanism caused by a network of obstacles behind the size-dependent partitioning of tracer particles. Reduced cell height in size-excluding compartments could not entirely be ruled out as the reason for size-dependent partitioning. But sieving was later determined to be the more likely mechanism[88]. With mean pore sizes of 50 nm and partition coefficients

decaying with the cube of the tracer radius, also particles smaller than the nominal percolation cut-off are significantly excluded.

Despite the fact that these results clearly suggest crowding to be much more complex than discussed up to now, data on the multi-scale heterogeneity of cellular fluids still are rather scarce. Moreover, virtually all previous studies focused on analysing the heterogeneity of transport processes in cells. Investigating the impact of crowding on diffusion properties of tracer particles the majority of groups probed actual crowding heterogeneities only indirectly. However, diffusion is not only influenced by crowding but can also be affected by other processes such as biochemical interactions between tracer particle and native cellular components[53]. Moreover, Parry et al.[78] demonstrated that cellular metabolism fluidizes the bacterial cytoplasm. Witzel et al.[80] found microtubules to have a similar effect, while the actin cortex rather seems to confine larger particles. An influence of viscosity and membranes on diffusion characteristics is possible as well[89]. As macromolecular crowding is thought to have an impact on virtually all intracellular processes it is quite evident that some further studies are required.
This thesis aims at a more direct characterization of the heterogeneity of intracellular crowding states. By means of confocal fluorescence imaging, ratiometric FRET imaging and lifetime-based techniques, intracellular heterogeneities of macromolecular crowding levels are analysed on multiple lengthscales. In all of these measurements, nucleoplasm and cytoplasm of interphase as well as spindle and spindle periphery of metaphase cells are investigated separately. In addition to that it will be determined whether various stress treatments affect intracellular crowding levels or their heterogeneities.

Chapter 3

Microscopy

The following chapter introduces fluorescence microscopy as a means of investigating static and dynamic processes in living cells. A brief introduction to the principles of fluorescence is followed by a short description of the confocal microscopy setup. Then various advanced microscopy techniques used in this thesis will be presented.

The most basic forms of compound microscopes have been known for more than 400 years. They have been used to study biological specimen for approximately 350 years[90]. These microscopes usually feature an objective lens in close proximity to the sample as well as an ocular lens. Combining these two types of lenses enables the user to see a real image. Even these early bright field microscopes could already reach magnifications of up to 270 times[90]. In the 19th century, sample illumination by electric lamps was invented to improve image quality. In accordance with the Abbe diffraction limit resolution is limited not only by the utilized objective but also by the wavelength of illumination light. So turn-of-the-century scientists aspired to improve image quality by using wavelengths as low as possible. It was pure coincidence that Köhler witnessed fluorescent structures in a microscope for the first time when he operated with ultraviolet light in 1904[91]. The advent of fluorescence labelling techniques since the 1930s[92] and the invention of lasers as well as the implementation of dichroic filters in the 1960s[93] have helped to make fluorescence microscopy to be today's method of choice for live cell imaging.

3.1 Principles of Fluorescence

The term fluorescence refers to the absorption of energy from particles or radiation by a material, almost immediately followed by the re-emission of energy in the form of light. This process results from a series of discrete steps: if light of the appropriate wavelength hits a fluorescently active atom or molecule, this molecule can absorb a specific quantum of energy which results in the excitation of a valence electron from singlet ground state to a higher energy level called excited state. A singlet state denotes an electronic state in which all electron spins are paired. The excited state can either be a singlet state or a triplet state in which the excited electron is no longer paired with the ground state electron but has the same spin. As intersystem crossing to a triplet state requires an additional forbidden spin transition, it is much more likely that a singlet excited state will form upon absorption, a process that typically takes a few femtoseconds[94].
The minimum excitation energy ΔT required for the transition of an electron from ground state S_0 to the excited state S_1 is

$$\Delta T = T_{S_1} - T_{S_0}, \tag{3.1}$$

while the energy dT carried by the incoming photon can be determined via Planck's law[95] as

$$dT = h\nu = \frac{hc}{\lambda}. \tag{3.2}$$

In this expression, ν is the frequency of the incoming photon, λ its wavelength. h denotes the Planck constant, c the speed of light.
Since the excited state usually consists of several sublevels termed vibronic levels, it depends on the wavelength of excitation light as well as the fluorophore's characteristics which energy level the valence electron will obtain. A schematic visualization of energy levels and transitions between them is given in Fig. 3.1. If the valence electron ascends to any other level than the lowest vibronic sublevel of a given state, excitation is followed by immediate and fast relaxation to the lowest vibronic sublevel by means of intramolecular non-radiative transitions. The energy emitted in this process of relaxation is dissipated in collisions of the excited molecule and surrounding solvent molecules. Because of this relaxation in the picosecond range, the shape of the emission spectrum usually is independent of the excitation wavelength, a principle summarized in Kasha's rule[96].

From the lowest vibronic sublevel the excited electron ultimately relaxes back

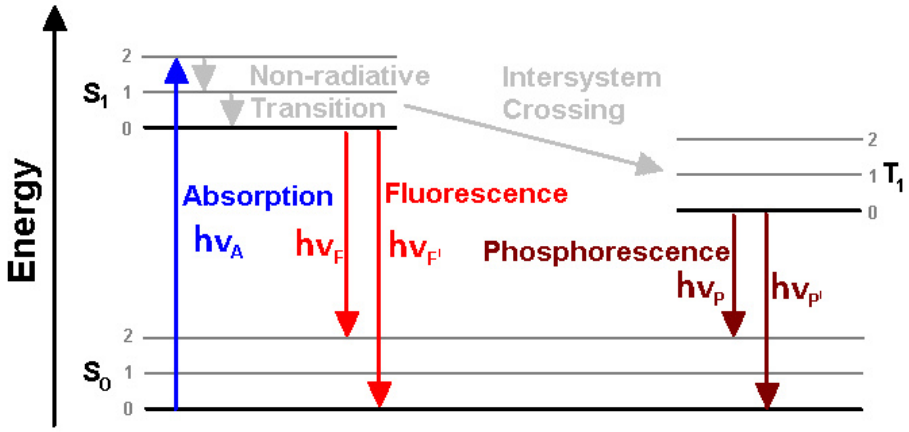

Figure 3.1: Schematic visualization of energy levels and transitions between them. Only processes relevant for this thesis are included. Variables: S_0 = singlet ground state, S_1 = singlet excited state, T_1 = triplet excited state, h =: Planck constant, ν = wavelength. Indices: A = absorption, F, F' = fluorescence, P, P' = phosphorescence.

to the ground state. Simultaneously a photon is emitted. The photons emitted during relaxation are collectively referred to as fluorescence light. In contrast to energy absorption, photon emittance is quite slow with average timescales of nano- to microseconds [97] [94].

Due to intramolecular vibronic energy loss, fluorescence light usually has less energy and consequently a higher wavelength than excitation light. The differences in wavelengths of emission and excitation spectra are referred to as Stokes shift, a material property of the utilized fluorophore used in fluorescence microscopy to separate the emitted fluorescence signal from excitation light [98].

3.2 Properties of Fluorophores Exploited in this Work

This section briefly sketches the properties of fluorophores that are directly exploited in this work. For a more detailed explanation as well as for other characteristic properties of fluorescent particles, see, for example, Lakowicz [94] or Ishikawa-Ankerhold et al. [99].

3.2.1 Photobleaching

Fluorescent molecules typically feature a system of several aromatic groups or, alternatively, a combination of neighbouring π-bonds [100]. As long as there is

no covalent modification of these groups that would irreversibly destroy the molecule, fluorophores can enter multiple cycles of excitation and emission. The process of molecules losing their ability to fluoresce is called photobleaching or fading and is mainly caused by chemical reactions between fluorescent molecules and their surrounding solvent molecules. Photodestructive and photochemical reactions occur particularly often if the fluorophore previously passed to the spin forbidden triplet state. Conversion from singlet to triplet as well as conversion from triplet back to singlet state involves a forbidden spin transition. Thus the molecule stays in the triplet state for a considerably longer period of time than it does in the excited singlet state. Additionally, molecules in the triplet state are highly reactive. In particular they tend to react with molecular oxygen. This process ultimately leads to the formation of reactive oxygen species (ROS). Those ROS are cytotoxic as they are able to oxidise biomolecules. In addition to that they can bleach further fluorophores in the cell[94] [99].

3.2.2 Fluorescence Lifetime

Having illuminated a fluorescently active sample with a δ-pulse of excitation light, a population of fluorophores will be in the excited state. As emission events are random, all excited fluorophores are equally likely to emit fluorescence photons in a given time period, resulting in a single exponential decay of excited state molecules. As fluorescence intensity $I(t)$ is proportional to the number of emitting fluorophores at each point of time, this can be written as

$$I(t) = I_0 \exp\left(-\frac{t}{\tau}\right). \tag{3.3}$$

The characteristic time τ for fluorescence intensity to be decreased to 1/e of its initial value I_0 is called fluorescence lifetime. Figuratively it can be considered to be the average time an electron stays in the excited state before relaxing back to the ground state. It is independent of the total fluorescence intensity. In the course of its fluorescence lifetime, while it is in the excited state, the fluorophore can change its conformation, interact with surrounding molecules or diffuse through the sample. This might actually change the duration of the excited state. So fluorescence lifetime can be used as a means of studying these processes independently of intensity levels. This will be explained in more detail in Sec. 3.7 and chapter 7[94] [99].

3.2.3 Förster Resonance Energy Transfer

Excited fluorophores can also release their additional energy non-radiatively by transferring it to another molecule via long-range dipole-dipole coupling, a process called Förster Resonance Energy Transfer or - although inappropriately - Fluorescence Resonance Energy Transfer (FRET, see Fig. 3.2). While the donor molecule has to be a fluorophore for FRET to occur, this is not necessarily required of the acceptor molecule.

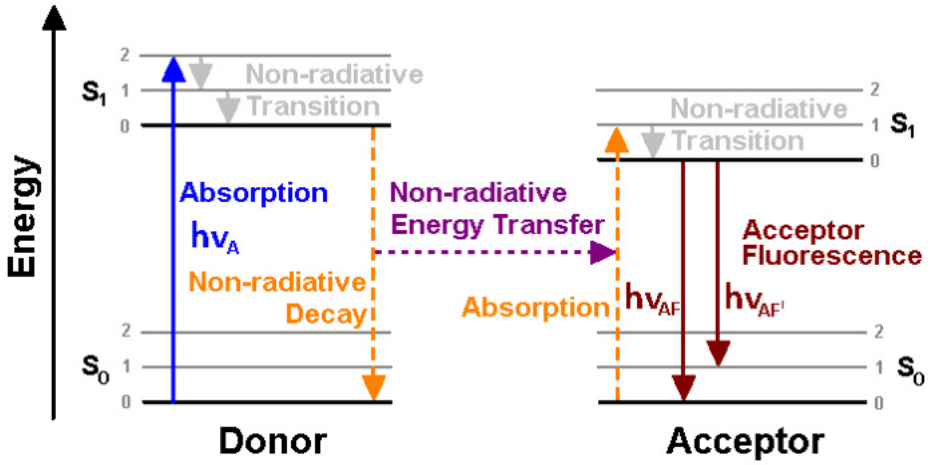

Figure 3.2: Schematic visualization of donor and acceptor energy levels. Only transitions relevant for FRET are included. Donor and acceptor ground states are not necessarily at the same energy level. Variables: S_0 = singlet ground state, S_1 = singlet excited state, $h =:$ Planck constant, ν = wavelength. Indices: A = absorption, AF, AF' = acceptor fluorescence.

FRET efficiency is a term that refers to the efficiency of energy transfer between donor and acceptor molecules. According to Förster's works on energy transfer it depends on a short physical distance between donor and acceptor, the relative orientation of their dipole moments as well as the spectral overlap of donor emission spectrum and acceptor absorption spectrum[101] [102]. Due to dipole-dipole coupling FRET efficiency is defined by

$$E_{FRET} = \frac{1}{1 + \left(\frac{r}{R_0}\right)^6} \tag{3.4}$$

with donor-to-acceptor separation distance r and the Förster radius R_0 being the characteristic distance where FRET efficiency for a specific FRET pair reaches 50%. As FRET efficiency scales inversely with the 6th power of the donor-to-acceptor distance, FRET reacts extremely sensitively to small

changes in proximity. In fact FRET can only occur if donor and acceptor molecules are not separated by more than approximately 10 nm. Thus FRET is an ideal method to analyse molecular distances and interactions beyond the resolution limits of classical light microscopy, although it reaches its limits when studying larger proteins or protein complexes[99].

Of course, donor-to-acceptor separation distances cannot be measured directly. There are, however, several methods to extract FRET efficiencies from measurement data. In lifetime-based measurement techniques, for example, FRET efficiencies can be calculated from donor lifetimes in the presence (τ_{DA}) and absence (τ_D) of the acceptor molecule[103]:

$$E_{FRET} = 1 - \frac{\tau_{DA}}{\tau_D}. \tag{3.5}$$

In sensitized emission FRET, the FRET efficiency can be determined from fluorescence intensities:

$$E_{FRET} = \frac{\zeta SE}{\zeta SE + D}. \tag{3.6}$$

In this expression, SE denotes fluorescence of acceptor molecules caused solely by energy transfer from donor molecules, D describes direct donor fluorescence. The prefactor ζ is determined by the ratio of donor and acceptor emission spectra and quantum yields[103].

Essentially there are three different principles for designing FRET-based biosensors. One way of analysing protein interaction is generating two separately labelled proteins, one of them carrying the donor, the other one the acceptor molecule. As soon as the two proteins interact, they are close enough for FRET to occur, resulting in a FRET signal that was not there before interaction. Another possibility is attaching both donor and acceptor molecules to the same biomolecule. This approach can be used for biomolecules that are anticipated to undergo proteolysis in the course of the experiment. Proteolysis would be visible in a loss of FRET signal upon separation of donor and acceptor beyond 10 nm. The third method is based on intramolecularly labelled biomolecules as well. If the link between donor and acceptor parts is designed in a way that it undergoes conformational changes upon stimulation by other molecules, e.g. reaction partners or solvent molecules, these interactions are reflected in changes in FRET signal[94] [99]. The FRET sensor used in this work, fCrH2, belongs to this third group of FRET constructs. Its conformation and thus FRET efficiency depicts the local crowding state of the sensor's surroundings[104] [105].

3.3 Fluorescence Microscopy

3.3.1 Fluorescence Microscopy in General

The first steps in fluorescence microscopy were taken at the beginning of the 20th century. Yet, these early setups did suffer from a number of serious problems: first and foremost the lack of intensive sources of excitation light and difficulties in proper separation of excitation and emission light. Today the most commonly used form of fluorescence microscopy is realized in the epi fluorescence microscope, developed in 1929 by Ellinger and Hirt [93]. In order to collect emission light towards the detector this kind of setup uses the same lens that was used for focusing excitation light on the sample. As the majority of the excitation light is transmitted through the sample, only a minor part of the excitation light is reflected back into the objective together with the emitted light. This process leads to a rather high signal-to-noise ratio. By inserting a dichroic mirror as beam splitter into the beam path between sample and detection unit, this excitation light is reflected back towards the light source [94] [99]. To minimize photobleaching during measurements, excitation bandpass filters are used in setups using high power fluorescence lamps as light sources to ensure that only light of the wavelengths required for excitation reaches the sample. In setups using lasers as excitation source, this is, of course, not necessary.

The Abbe limit defines the resolution limit for light microscopy [106]. This is the smallest possible distance d_{Abbe} at which two points can still be perceived to be separate. It is given by

$$d_{Abbe} = \frac{\lambda_{exc}}{2N.A.}. \tag{3.7}$$

For high resolution the experimenter should strive to use an objective lens with high numerical aperture $N.A$ to collect as much emitted fluorescence light as possible. Resolution can be enhanced by using an immersion fluid, such as oil or water, which abrogates reflections. Finally, resolution can be improved by choosing illumination wavelengths λ_{exc} as low as possible. This accounts for the discovery and invention of fluorescence microscopy. Of course, as wavelength scales inversely with energy, decreasing excitation wavelength can result in considerably high photo-damage

One of the main advantages of modern fluorescence microscopy is the ability to selectively label individual proteins with fluorescent dyes or proteins. Transmission light microscopy images the whole cell with all its components against a bright background. In modern fluorescence microscopy, however, only the structure of interest is monitored against a dark background. Thus a much higher signal-to-noise ratio can be achieved. The resolution of self-luminous structures, however, is described by slightly different principles. Due to diffraction a point light source in a sample is not recorded as a point, but as a bright central region, termed Airy disc. It is surrounded by a number of concentric rings - the Airy pattern. According to the Rayleigh criterion, two point light sources can be separated, when the first intensity minimum of the first source is localized in the centre maximum of the second source. This minimum distance is given by

$$d_{Airy} = \frac{0.61\lambda_{em}}{N.A.} = \frac{1.22\lambda_{em}}{2N.A.}. \tag{3.8}$$

Axial resolution is generally worse than lateral resolution and can be calculated by using the Fresnel-Huygens theory[107].
Note that in contrast to the Abbe limit here resolution is determined by emission wavelength λ_{em} and not by the wavelength of illumination light λ_{exc}.
For a sample emitting green light at 500 nm and a numerical aperture of 1.2, the lateral resolution limit would be 254 nm. Considering the fact that typical cells range from 1 µm to 100 µm, intracellular structures consequently being considerably smaller, this cannot be considered to be sufficient. Switching to lower emission wavelengths doesn't provide a solution to the problem as this would require even lower excitation wavelengths. In principle this can be done. But illumination with UV light tends to damage biomolecules and might perturb normal cell function and homoeostasis.
For measurements in cells it is recommendable to use a confocal laser scanning microscope instead of a wide field microscope, which was done in this work.

3.3.2 Confocal Laser Scanning Microscopy

Confocal laser scanning microscopy was invented by Minsky in 1957[93]. In contrast to wide field fluorescence microscopes, this type of microscope combines point-by-point illumination and simultaneous point-by-point detection for image acquisition instead of illuminating and recording the entire sample at once. Thus illumination in the focal plane and detection are restricted to

only one diffraction-limited point. This results in better resolution as well as in a significant decrease in signal from out-of-focus planes[99].

In the confocal setup, see Fig. 3.3, light from a laser is focused via a pinhole into the sample where it is used to excite fluorescent molecules. The emitted light from the sample passes the objective again, as well as a dichroic mirror, to get to the detector. A second pinhole is placed between the dichroic mirror and the detector. Both pinholes as well as the focus are optically conjugate planes - hence the name 'confocal'. That is why scattered light as well as out-of-focus signals from planes above or below the focal plane are eliminated by the second pinhole and do not reach the detector. In wide field microscopes these signals cause artefacts like distortion, glare or blurriness. By eliminating them the image's optical resolution is enhanced, especially in axial direction. In addition to that, improved axial resolution allows for optical sectioning. So acquisition of multiple images from several focal planes to reconstruct the 3D structure of an object is possible.

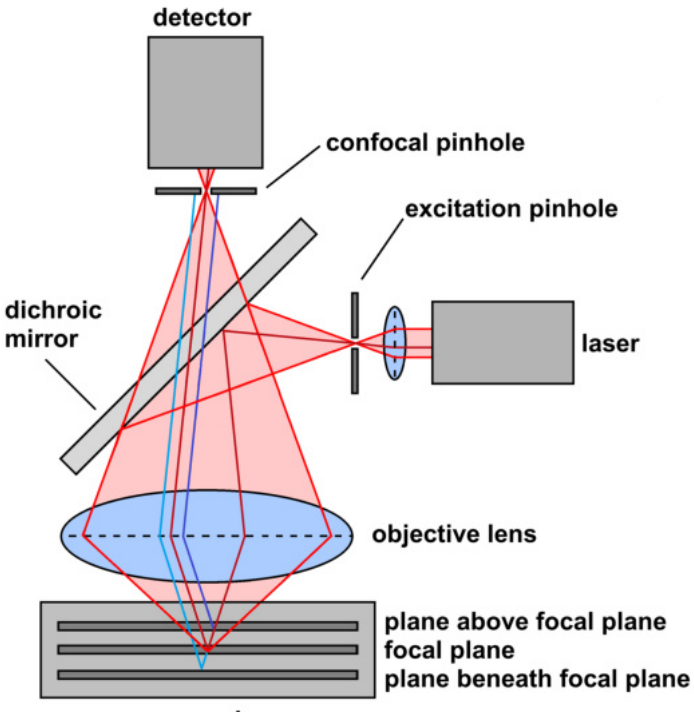

Figure 3.3: Schematic view of a confocal setup. Excitation light passes through a pinhole and is reflected by dichroic mirror to illuminate the sample. Emission light from the sample passes the dichroic mirror towards a detector. Due to the second pinhole only light from the focal plane (red) reaches the detector while light from out-of-focus planes (blue) is blocked. By this contrast and resolution are enhanced. However, if lasers are used as excitation light sources, the first pinhole is often omitted.

In lateral direction the resolution can be improved by a factor of $1/\sqrt{2}$, at least in theory. In reality, however, this factor can only be reached if the detection pinhole is nearly completely closed. In this case the signal intensity would decrease to virtually nothing. So the actual improvement in lateral resolution for common pinhole sizes is more likely to be in the range of 1/1.12 or even worse[107].

The cost of decreasing signal intensity for increasing resolution can be counterbalanced to some degree by long exposure times. This, however, would result in increased bleaching of the sample. Alternatively a sensitive detector, e.g. a photomultiplier tube (PMT) or an avalanche photo diode (APD), can be chosen. Both transform the incoming electromagnetic signal into a photoelectric current that can be recorded by a computer and can be used to reconstruct the actual image.

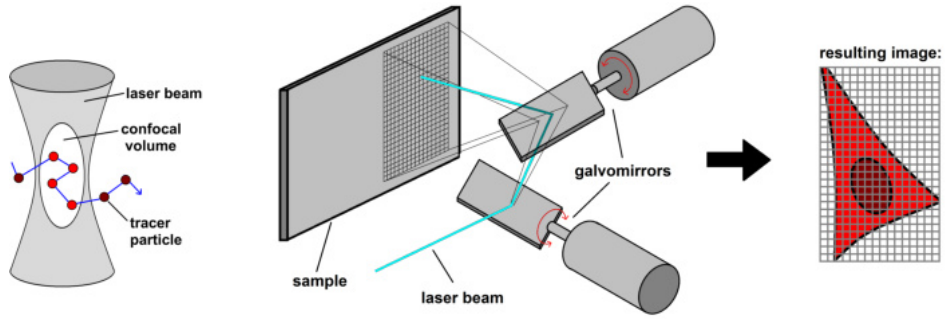

Figure 3.4: Principles of confocal laser scanning microscopy. (a) Fluorescent particles are only illuminated as long as they are within the confocal volume. (b) In order to obtain images the sample has to be scanned by the confocal volume. Fluorescence per volume position is translated into intensity per pixel.

Due to diffraction the illumination laser beam cannot be focused in a mathematical point, but rather constitutes a small, ellipsoid volume - the confocal volume (see Fig. 3.4a). During laser scanning this confocal volume is moved through the sample in x- and y- direction step by step (see Fig. 3.4b). At each step the fluorescence intensity coming from the volume's inside is recorded. As the confocal volume is open to the rest of the sample, particles can freely diffuse in and out of the volume, thus giving rise to fluctuations in fluorescence intensity for prolonged illumination of the same spot. This is exploited in techniques like FCS and FLPM, see Sec. 3.6 and Sec. 3.7.2, respectively[99] [107].

3.4 Ratiometric Förster Resonance Energy Transfer (Ratiometric FRET)

As was discussed in Sec. 3.3.2, confocal microscopy does improve resolution, but only to a small degree. Structures and processes beyond the resolution limit of confocal microscopy can be achieved in several ways. One method would be to switch to super-resolution microscopy techniques. Many of these techniques provide astonishing image qualities. Yet, they generally suffer from one central problem: their temporal resolution is insufficient for investigating dynamic processes in living cells. A different method to access processes beyond the confocal resolution limit is using FRET-based sensors. FRET efficiency is inversely proportional to the 6th power of donor-to-acceptor distance (see Eq. 3.4). In consequence, FRET efficiency is extremely sensitive with respect to small changes in donor-to-acceptor proximity. So FRET can be used to study molecular interactions at a lengthscale of approximately 5 nm.
The easiest way to measure FRET is sensitized emission FRET, i.e. exciting the donor and recording fluorescence in the acceptor channel. However, in general the overlap of donor and acceptor spectra results in spectral bleed-through, i.e. donor emission in the acceptor channel and direct excitation of the acceptor by donor excitation. Therefore sensitized emission FRET requires careful calibration. This is usually done by imaging a set of three samples, one of which contains only donor molecules, one of which contains only acceptor molecules; a third sample is the actual FRET sample. With these three images the FRET efficiency E_{FRET} can be calculated using Eq. 3.6.
In this thesis FRET experiments were done in living cells with an intramolecularly labelled FRET sensor. Thus this calibration could not be performed. Consequently the experimental procedure for FRET experiments applied in this thesis (see Fig. 3.5) is only loosely based on sensitized emission FRET: the sample is illuminated with a wavelength appropriate for direct donor excitation. Fluorescence emission is, however, recorded simultaneously in the donor and acceptor channels. Taking advantage of the fact that the molar ratio of donor and acceptor is always 1 in intramolecularly labelled FRET sensors, FRET can be measured by taking the pixelwise ratio of acceptor emission F to donor and acceptor emission $D + F$:

$$F_{FRET} = \frac{F}{D + F}. \tag{3.9}$$

This FRET ratio F_{FRET} should not be confused with the actual FRET efficiency E_{FRET} (Eq. 3.6). However, it has the same functional form and can serve as an estimate for FRET efficiency[103].

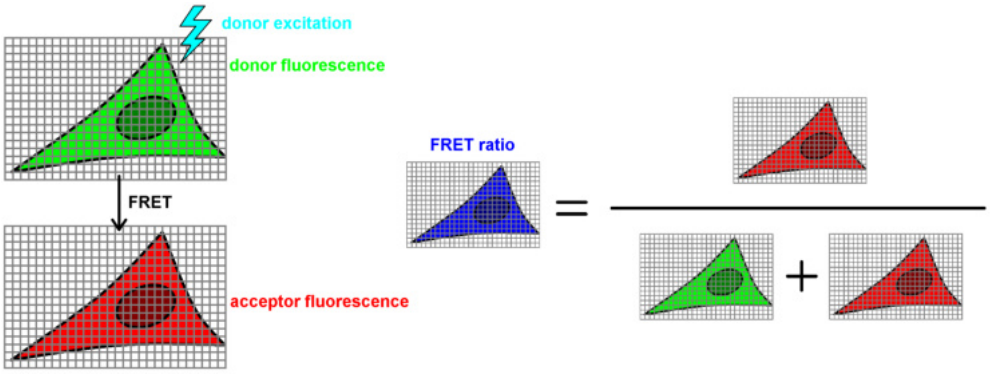

Figure 3.5: Principle of FRET measurements. Images are simultaneously acquired in both donor and acceptor channel during donor illumination. The pixel-wise FRET ratio is calculated from these two images.

3.5 Fluorescence Recovery after Photobleaching (FRAP) and Fluorescence Loss In Photobleaching (FLIP)

Depending on the fluorescence microscope technique used in the experiment, a fluorophore property can be classified either as a measurement artefact that is to be avoided or it can be targeted specifically as an observable to solve a particular scientific problem. Probably the most prominent example is photobleaching - usually a major problem in fluorescence microscopy. It is deliberately exploited in techniques like FRAP and FLIP.

FRAP was developed in the 1970s, mainly by Axelrod[108][109], who originally utilized it to analyse diffusion in membranes[110]. Today it is a widely used method to reveal protein dynamics in membranes as well as in the cells' interior[111][112][113][114]. FLIP can be understood as a complementary technique to FRAP and has mainly been used to explore the connectivity between different subregions or compartments in cells[115][116].

Both techniques are based on the controlled bleaching of a subregion in the sample, combined with subsequent time-resolved monitoring of the fluorescence intensity of that sample. In this way, information about the dynamics of a fluorescently labelled structure can be extracted from imaging data.

3.5.1 Principles and Experimental Realization

The basic principle of FRAP and FLIP experiments is displayed in Fig. 3.6a. In both measurement techniques, initially a series of fluorescence images is acquired to serve as a reference value for the intensity in the sample. Subsequently a small, carefully selected subregion of this sample is illuminated by a focused excitation laser beam of high intensity. Exposure to high light intensity in the presence of molecular oxygen irreversibly damages the fluorophores inside the illuminated region, which interrupts their ability to repetitively emit fluorescence photons upon excitation. Those permanently damaged fluorophores stop contributing to the fluorescence from the bleached area. This process leads to a dark region in the sample. Depending on illumination intensity and exposure time the region can be bleached either completely or only to some extent.
Provided that the fluorescently labelled structures can move within the sample, the photo-bleached molecules will gradually be replaced by intact fluorophores from other regions in the sample after the bleaching event. This can be noticed as a gradual increase of fluorescence intensity in the bleached region, accompanied by a loss of fluorescence intensity in the surrounding sample. In order to analyse this process, a time series of images is taken at low excitation laser power after the bleaching event. An additional loss of fluorescence due to image acquisition after the initial bleaching event is to be avoided. Moderate levels of acquisition bleaching can, however, be corrected.

3.5.2 Analysis of FRAP and FLIP experiments

In the acquired image sequence a ROI is selected for evaluation, see Fig. 3.6a. In FRAP measurements, this is the ROI that was bleached during experiments. In FLIP it is different from the bleached ROI. For each image in the stack the fluorescence signal of the complete evaluation ROI is summed up to extract fluorescence recovery or loss, respectively, as a function of time (Fig. 3.6b and 3.6c).
The resulting curve can be used to gather information about molecule dynamics as well as their mobility in general: fluorescence recovery in FRAP experiments is supposed to reach a plateau intensity I_∞ after some time. If fluorescence intensity is normalized so that the initial, pre-bleach intensity equals 1 and the intensity immediately after the bleaching pulse equals 0,

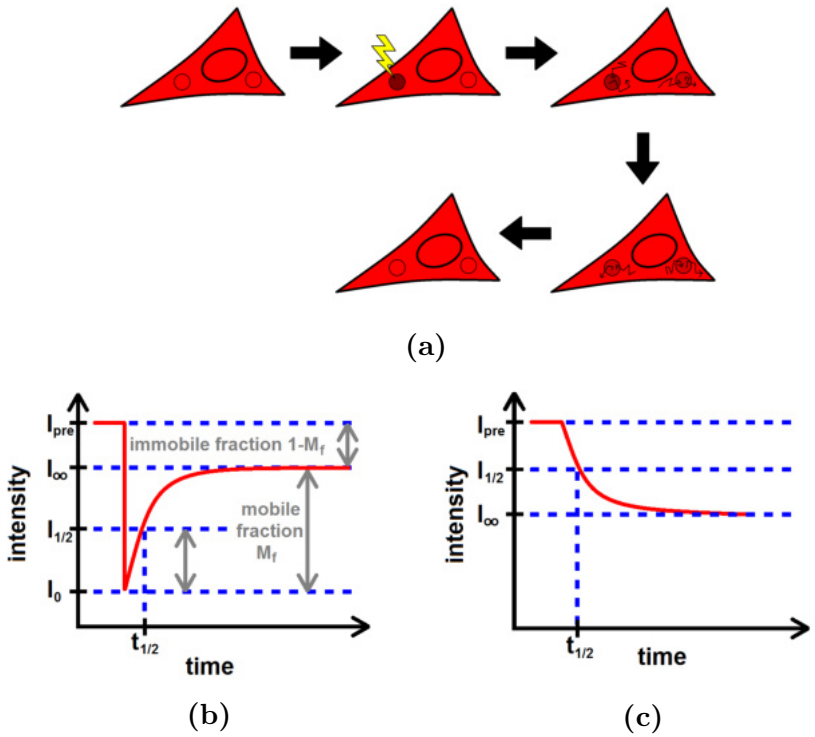

Figure 3.6: Principle of FRAP and FLIP. (a) In both FRAP and FLIP, initially a subregion of the sample is bleached at high intensity. Subsequently, the fluorescence recovery of that same region (FRAP) or the fluorescence loss in a second region (FLIP) is monitored as a function of time. (b) Typical FRAP curve. (c) Typical FLIP curve.

the ratio of plateau intensity I_∞ and the pre-bleach intensity I_{pre} renders the mobile and immobile fractions, $M_F = \frac{I_\infty}{I_{pre}}$ and $1 - M_F$, of the fluorescently labelled population. However, if the bleached area is large compared to the total sample volume, the overall loss of fluorescence must be corrected prior to evaluation in the recovery curve. The speed of fluorescence recovery in FRAP experiments is measured by the so-called half life $t_{1/2}$ (see Fig. 3.6b), which, by convention, refers to the time needed to recover to half the plateau intensity. In analogy, the half time of fluorescence loss in FLIP experiments can be defined as the time needed to reach an intensity level of $I_{1/2} = \frac{I_{pre}+I_\infty}{2}$.
In order to perform a meaningful analysis of FRAP data, the theoretical model for curve fitting must be chosen carefully: it is crucial to discriminate, for example, diffusion limited recovery from reaction limited recovery. However it must be taken into account that shape and size of the bleached region as well as of the analysed region can have a significant impact on acquired data. This can be quite challenging, as not only fluorophores in the focal plane are bleached but also those above and below. This bleached structure is generally assumed to have a conical shape. However, this assumption holds true only if objectives

with a low numerical aperture are used. If objectives with a high numerical aperture are used, the bleached volume's shape can be far more complex than the shape seen in the focal plane[99]. However, fluorescence regeneration can generally be considered to be transport limited if the half life is proportional to the size of the bleaching area.

3.6 Fluorescence Correlation Spectroscopy (FCS)

Fluorescence Correlation Spectroscopy (FCS) was invented in the early 1970s by Elson, Magde and Webb[117] [118]. In contrast to most other advanced fluorescence microscopy techniques, FCS focuses on analysing the fluctuations of recorded fluorescence intensity instead of fluorescence intensity itself. The method allows the analysis of processes on molecular level at fluorophore concentrations too high for techniques such as single particle tracking.

3.6.1 Principles and Experimental Realization

Similar to the other methods introduced in this chapter, FCS experiments are performed on a confocal microscope. In contrast to imaging-based techniques the confocal volume doesn't scan the sample but remains fixed (Fig. 3.7a). The recorded signal is the fluorescence intensity of this small stationary volume as a function of measurement time. As the confocal volume is open to the rest of the sample, individual molecules can move in and out of the confocal volume in the course of the measurement. In particular, the movement of fluorophores through the illuminated volume causes fluctuations in fluorescence intensity. The incoming signal is increased by means of an APD and translated into a photometric current which is recorded as a function of measurement time, thus rendering the time trace $I(t)$ (Fig. 3.7b).
An appropriate fluorophore concentration has to be maintained in the sample so that fluctuations in fluorescence intensity can be analysed. At high fluorophore concentrations the signal-to-noise ratio is high. Consequently fluctuations in fluorescence intensity are minute with regard to its mean value. At extremely low concentrations of less than a mean of one particle inside the confocal volume there is no guarantee that any signal at all can be detected. It can be shown that a mean concentration of one particle inside the confocal volume is ideal[118].

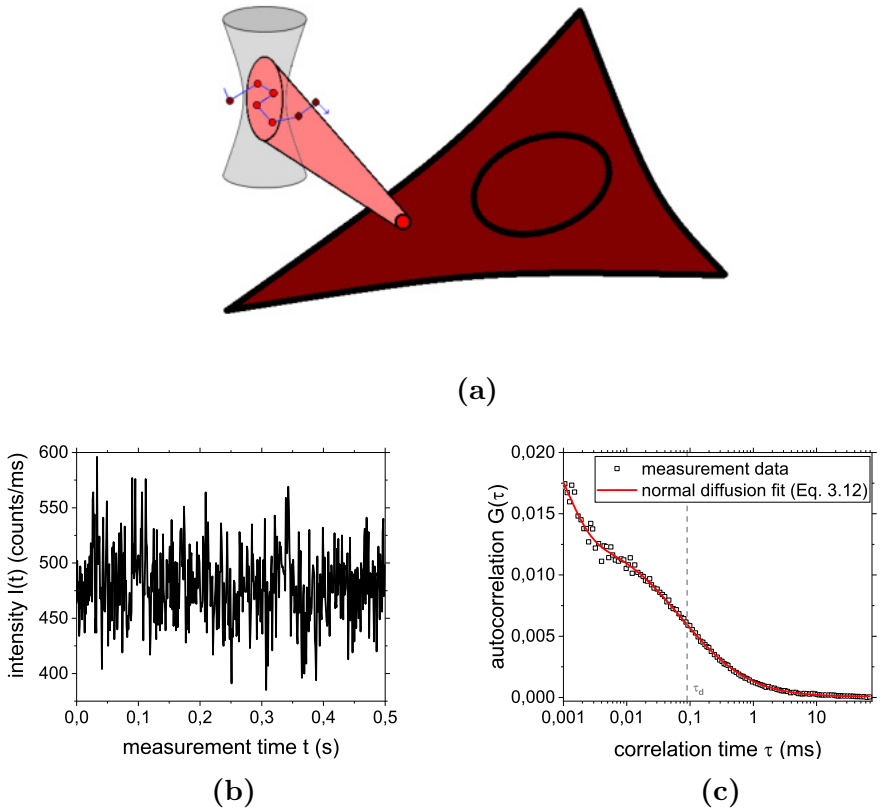

Figure 3.7: Principle of FCS. (a) Only a small region, corresponding to one confocal volume, is considered. This ROI remains stationary during the course of the measurement. (b) Fluorescence intensity I within the confocal volume is recorded as a function of time t. (c) The autocorrelation function $G(\tau)$ of this time trace is calculated. It can be fitted with the appropriate fit function to extract data such as diffusion times.

3.6.2 Evaluation of FCS Data

The recorded fluorescence intensity $I(t)$ can be written as the sum of its mean value and its fluctuations:

$$I(t) = \langle I \rangle + \delta I(t). \tag{3.10}$$

This can be used to calculate the autocorrelation function of the signal (see Fig. 3.7c)[94]:

$$G(\tau) + 1 = \frac{\langle I(t)I(t+\tau)\rangle}{\langle I(t)\rangle^2} = 1 + \frac{\langle \delta I(t)\delta I(t+\tau)\rangle}{\langle I(t)\rangle^2}. \tag{3.11}$$

It describes the probability of detecting a fluorophore at time τ that was already detected at time $\tau = 0$. If concentration fluctuations are governed

by normal diffusion of one tracer species, the autocorrelation function can be described by

$$G_{norm}(\tau) = \frac{1}{\langle N \rangle} \cdot \frac{1}{1 + \frac{\tau}{\tau_d}} \cdot \frac{1}{\sqrt{1 + \frac{\tau}{S^2 \tau_d}}} \tag{3.12}$$

where N denotes the average number of particles in the illuminated volume, S describes the elongation of confocal volume. The diffusion time $\tau_d = \frac{\omega_0^2}{4D_P}$ is the mean dwelling time of a fluorescent particle with the diffusion constant D_P inside a confocal volume with the radius ω_0 [94].
Anomalous diffusion, which has been reported to occur in cells, can be described by

$$G_{anom}(\tau) = \frac{1}{\langle N \rangle} \cdot \frac{1}{1 + \frac{\tau}{\tau_d}} \cdot \frac{1}{\sqrt{1 + (\frac{\tau}{S^2 \tau_d})^{\alpha}}} \tag{3.13}$$

where the scaling exponent α denotes the anomaly (see e.g. [2] [46] [48] [53]). Conformational fluctuations with the characteristic timescale τ_{fluc} of intramolecularly labelled FRET constructs can be described by

$$G_{fluc}(\tau) = 1 + \frac{1-p}{p} \cdot e^{-\frac{\tau}{\tau_{fluc}}} \tag{3.14}$$

where p represents the fraction of open strands [119] [120] [121].
These expressions are used to evaluate experimentally obtained autocorrelation functions by applying custom MATLAB fit routines.

3.7 Fluorescence Lifetime Measurements

Information about subcellular structures can also be gained by recording and analysing fluorescence lifetimes instead of or in addition to fluorescence intensities. The basic principle of lifetime measurements is shown in Fig. 3.8: the sample is illuminated with a pulsed laser of appropriate wavelength. Fluorophores in the sample emit photons which arrive at the detector a few nanoseconds after the initial laser pulse. A TCSPC unit ("time correlated single photon counting") records the arrival times τ_{arr} of the emitted fluorescence photons relative to the illumination laser pulse as well as relative to the beginning of the measurement. The histogram of arrival times is calculated. The shape of this histogram offers information on relaxation characteristics, i.e. the mean fluorescence lifetime. Information about fluorescence intensity can be gained by integrating the histogram.

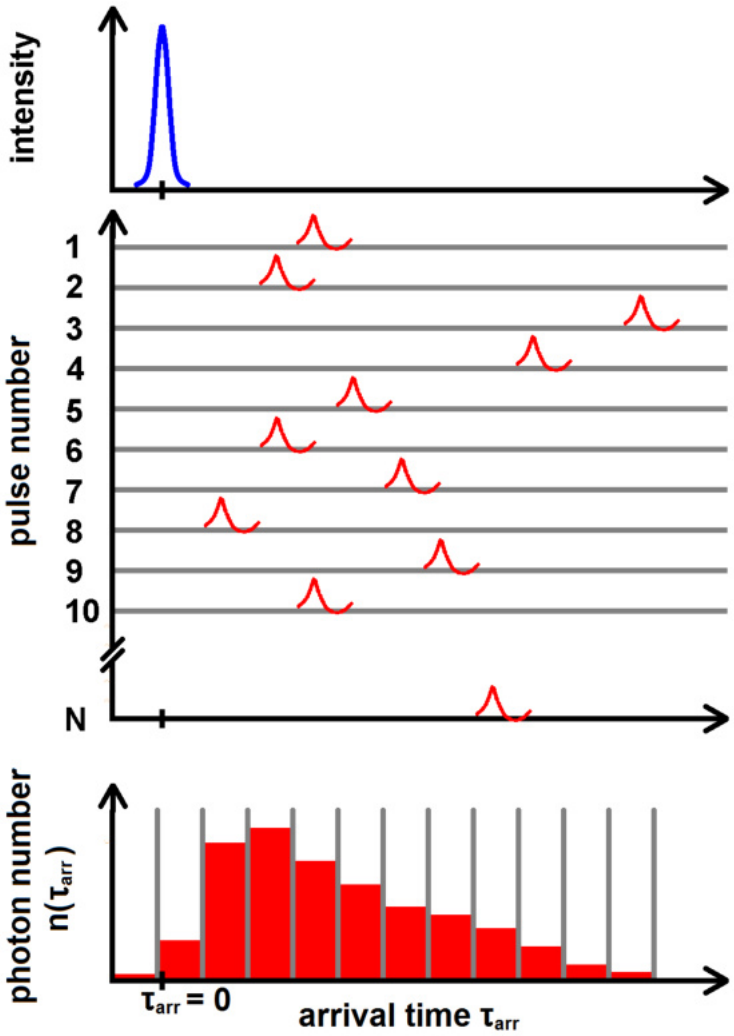

Figure 3.8: Basic principle of lifetime measurements. The sample is illuminated N times with a pulsed laser of appropriate wavelength (blue). A TCSPC unit records the arrival times τ_{arr} of individual photons (red) relative to the last illumination laser pulse. Subsequently the arrival time histogram is calculated from these data.

The method's main advantage over other fluorescence microscopy techniques is its relative insensitivity to limitations linked to fluorescence intensity. As fluorescence lifetime is independent of fluorescence intensity, the outcome of experiments is not influenced by measurement settings, neither by the local excitation intensity and fluorescence detection efficiency[122], the duration of exposure nor signal cross-contamination between donor- and FRET channel. Sample characteristics like spatially varying fluorophore concentrations and moderate levels of photobleaching do not corrupt lifetime analyses, either[123]. Nevertheless, fluorescence lifetime is determined by the fluorophore's surroundings. In FRET, for example, the presence of an acceptor molecule causes the donor molecule to lose its excited state energy considerably faster than with-

out the acceptor. So donor lifetime in the presence of FRET is shortened. Depending on the type of FRET sensor, lifetime analysis can provide information about either biochemical reactions or the physical properties of the sensor's surroundings. The sensor used in this work, fCrH2, is an intramolecularly labelled sensor which undergoes conformational changes depending on the local crowding state.
FRET efficiencies can be calculated from the excited state lifetimes of the donor molecules in the presence or absence of the corresponding acceptor molecules, τ_{DA} and τ_D, by[103]

$$E_{FRET} = 1 - \frac{\tau_{DA}}{\tau_D}. \tag{3.15}$$

In principle, FRET efficiencies can also be calculated from ratiometric FRET data. However, FRET efficiencies calculated from lifetime measurement data are considerably more accurate and require less calibrations than FRET efficiencies obtained by imaging-based techniques.

3.7.1 Fluorescence Lifetime Imaging Microscopy (FLIM)

Although the first instrument to measure fluorescence lifetimes was invented in 1959[124], it took another 30 years to develop true FLIM imaging[70] [125].
In the course of a FLIM measurement, see Fig. 3.9a, an area of the sample is scanned while recording arrival times. Since arrival times are recorded relative to illumination laser pulses as well as relative to the beginning of the measurement ("lab time"), each arrival time can be assigned to the locus the photon came from, i.e. the pixel in the FLIM image (which corresponds to a diffraction limited volume in the sample). The recorded dataset - the FLIM image - is a matrix with the first two dimensions corresponding to the x- and y-coordinate of the image. The third dimension contains the recorded lab time vs. arrival time vectors of the respective pixels (Fig. 3.9b).
After manually selecting a region (marked blue in Fig. 3.9a) of the FLIM image to be analysed, the histogram of arrival times is calculated either for each pixel or for the complete ROI (Fig. 3.9c). The histograms of these regions can be evaluated by single or double exponential curve fitting (see Sec. 3.7.3).

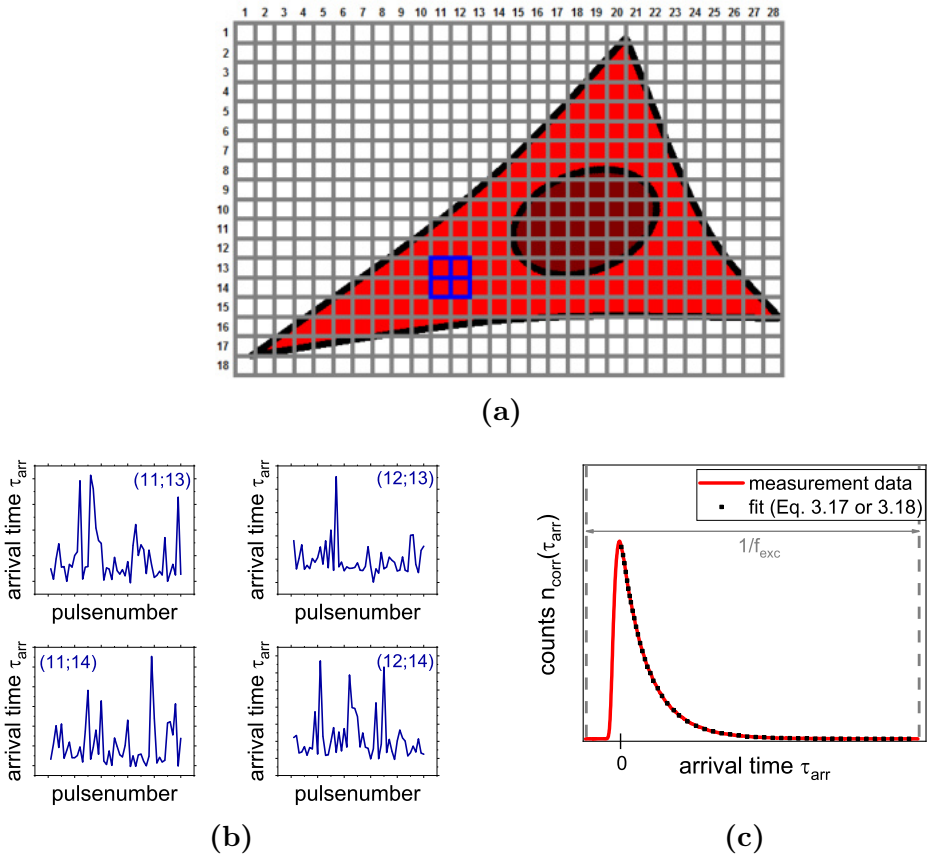

Figure 3.9: Principle of FLIM measurements. (a) TCSPC is performed while scanning the sample. ROIs to be analysed (blue) are selected after measurements. For each individual pixel a lab time vs. arrival time vector is recorded. (b) Arrival times τ_{arr} vs. pulse number for four pixels of the FLIM image. (c) Arrival time histograms can either be calculated from individual pixels or from a ROI containing several pixels. By means of curve fitting the fluorescence lifetimes can be extracted.

3.7.2 Fluorescence Lifetime Point Measurements (FLPM)

In contrast to FLIM, in FLPM only a few small ROIs in the sample are selected to record their fluorescence lifetimes (see Fig. 3.10a). The arrival times of fluorescence photons relative to the excitation laser pulse are recorded only for these spots. The resulting lab time vs. arrival time vectors contain information about the local intensity as well as the local mean fluorescence lifetime (Fig. 3.10b). These can be analysed via integration of the complete vector, or via conversion into an arrival time histogram (Fig. 3.10c) and subsequent fitting, respectively (see Sec. 3.7.3).

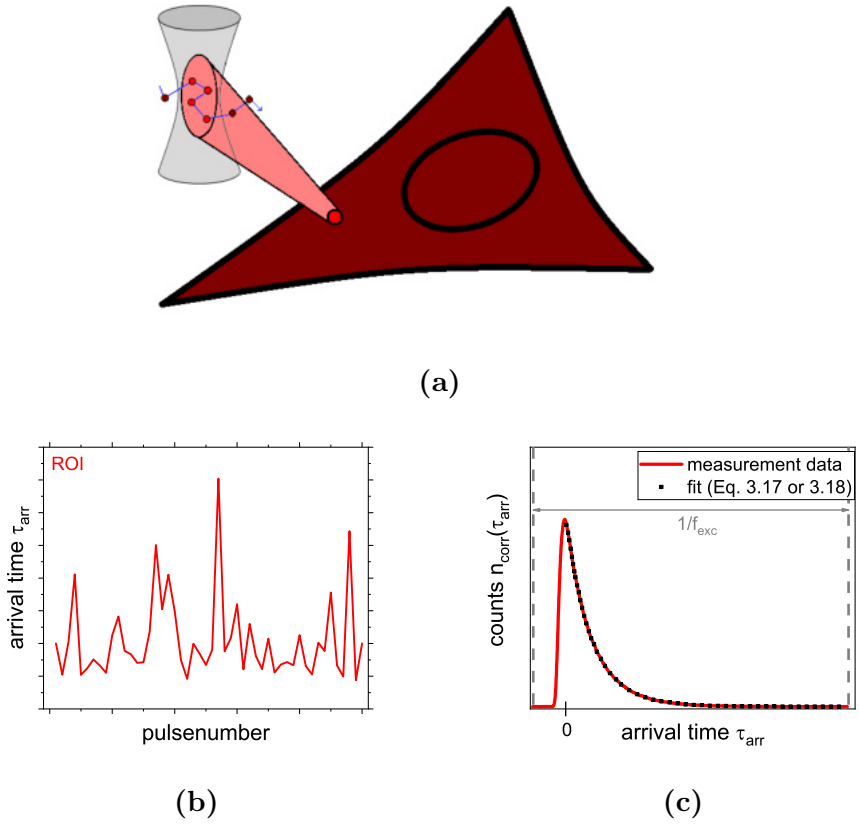

Figure 3.10: Principle of FLPM measurements. (a) TCSPC is performed on a small ROI in the sample. This ROI remains stationary during the course of the measurement. For this ROI a lab time vs. arrival time vector is recorded. (b) Arrival times τ_{arr} vs. pulse number of the recorded ROI. (c) The arrival time histograms can only be calculated for the ROIs selected during measurements. By means of curve fitting the fluorescence lifetimes can be extracted.

3.7.3 Evaluation of Fluorescence Lifetime Measurements

Both FLIM and FLPM measurements render a lab time vs. arrival time vector. They only differ in their spatial and temporal statistics. While FLPM measurements provide an excellent photon statistics per measurement locus (around 10^6 photons per locus), the number of measurement loci is limited and cannot be changed after measurements. In FLIM images, regions of interest can be chosen freely after measurements, but the photon statistics per pixel is considerably lower (typically 10^3 photons per pixel). For both methods, total acquisition time is limited by the time the cell remains in the focus without moving recognizably.

The evaluation performed in this thesis is based on an evaluation approach deduced by Andreas Veres[126] and Olivia Stiehl[127]. It was initially developed for a different set of samples, but for measurements using the same microscopy

setup. In order to evaluate lifetime measurements, at first, the measured lab time vs. arrival time vector is converted into a histogram: arrival times τ_{arr} are grouped into intervals of $\Delta\tau_{arr} = 16\,\text{ps}$. Then the frequency of photons per interval $n(\tau_{arr})$ is counted. However, due to long measurement times also unlikely arrival times, i.e. arrival times exceeding 20 ns, are registered. Therefore histograms have to be corrected prior to fitting (see Fig. 3.11). A phenomenological equation is used to calculate the corrected number of photons per arrival time interval $n_{corr}(\tau_{arr})$:

$$n_{corr}(\tau_{arr}) = n(\tau_{arr}) - \frac{2\Delta\tau_{arr}}{\Delta\tau_{arr} n_{bins} - \tau_{arr,low}} \cdot \sum_{i=\frac{\tau_{arr,low}}{\Delta\tau_{arr}}}^{n_{bins}=\frac{\tau_{arr,up}}{\Delta\tau_{arr}}} n(i). \tag{3.16}$$

In this equation, $\tau_{arr,low} = 22.4\,\text{ns}$ denotes the lower threshold of the interval used for background corrections, $n_{bins} = \frac{1}{f_{exc}\Delta\tau_{arr}} = 1562$ is the total number of bins. It is defined by temporal resolution $\Delta\tau_{arr} = 16\,\text{ps}$ and the laser's pulse frequency $f_{exc} = 40\,\text{MHz}$. The largest arrival time which can be measured is $\tau_{arr,up} = 25\,\text{ns}$, which simultaneously denotes the upper threshold of the correction interval.

After performing this background correction, the histogram's maximum is

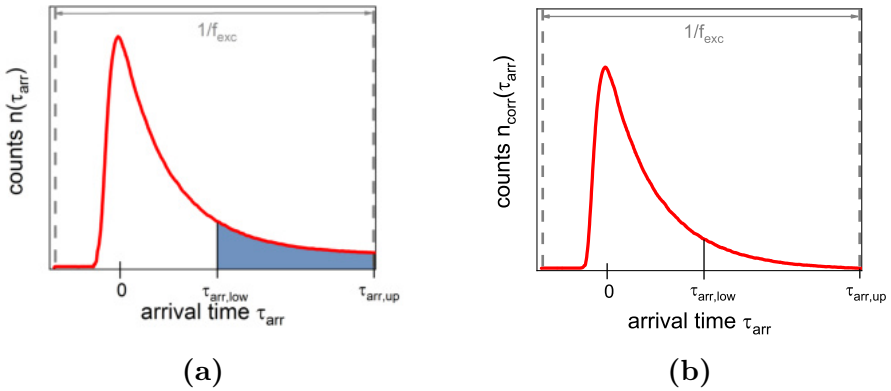

Figure 3.11: Principle of histogram correction in lifetime measurements. (a) Lifetime histogram prior to correction. The number of counts per interval between $\tau_{arr,low}$ and $\tau_{arr,up}$ (blue) is averaged. Twice the averaged number of counts is subtracted from the histogram to get the (b) corrected histogram.

determined. In theory this maximum corresponds to $\tau_{arr} = 0$. Since curve fitting of arrival time histograms is quite sensitive to the starting point of the fitted data range, the histogram's maximum and an interval of 150 subsequent time increments, i.e. $150 \cdot \Delta\tau_{arr} = 2.4\,\text{ns}$, is used as a starting point $\tau_{arr} = 0$. Thus fitting is repeated for 151 slightly different data ranges. In each fit, fit

results obtained for the previously evaluated data range are used as initial fit parameters.
Depending on whether the sample contains a single type of fluorophore or a FRET construct, curve fitting is performed either with a monoexponential

$$n(\tau_{arr}) = \alpha e^{-\frac{\tau_{arr}}{\tau_D}} \tag{3.17}$$

or a double exponential:

$$n\left(\tau_{arr}\right) = \alpha \left(f_{FRET} e^{-\frac{\tau_{arr}}{\tau_{DA}}} + \left(1 - f_{FRET}\right) e^{-\frac{\tau_{arr}}{\tau_D}} \right). \tag{3.18}$$

In these expressions, the multiplicative constant α depends on total photon numbers. f_{FRET} denotes the ratio of donor molecules undergoing FRET, τ_{DA} and τ_D are the fluorescence lifetimes of the donor molecule with and without the presence of an acceptor molecule, respectively.
For each of the 151 fits the residuals of fit function and data range are calculated. Further analysis is based on those fitting parameters for which the residuals between fit function and data are minimal.
If FLIM is performed on a FRET sensor, the fit results of donor lifetime with and without the presence of an acceptor molecule can be used to calculate the FRET efficiency:

$$E_{FRET} = 1 - \frac{\tau_{DA}}{\tau_D}. \tag{3.19}$$

3.8 Settings and Programs Used in this Thesis

3.8.1 Microscope and Experimental Settings

Microscope

All experiments discussed in this thesis were performed on a commercial Leica SP5 confocal laser scanning microscope equipped with a TSCPC unit by PicoQuant using a 63x/1.2NA water immersion objective. All experiments were performed at 37 °C using a custom-made incubator chamber. Details on the equipment are given in appendix B.

Settings for Imaging Experiments

In all imaging experiments in living cells, image acquisition was designed to respect the diffraction limit and to meet the Nyquist criterion for digital imaging. To ensure the comparability of all images, images of cells and lysates

were taken with 512×512 pixels or 1024×1024 pixels. Zoom was adjusted so that pixel sizes equalled 100.31 nm or 100.21 nm, respectively. All images were taken employing monodirectional scanning and photomultiplier tubes.
HeLa cells transfected with free EGFP were illuminated at 488 nm and fluorescence was detected in the range of 500 nm to 550 nm. The pinhole was set to one Airy unit to obtain an optically thin slice of specimen. Each pixel in an image corresponds to a diffraction-limited volume ('voxel'). Depending on image size, scanning frequencies were set to 200 lines per second or 100 lines per second to ensure equal exposure times per pixel in all images. Laser power and detector settings were adjusted to exploit the dynamic range of the photomultiplier without saturation effects.
Each FRAP series consisted of five frames acquired before bleaching, two frames of bleaching at full laser power (488 nm) and 70 frames after bleaching. Lag time between acquisition of individual frames was minimized at a scanning speed of 400 lines per second and image size of 1024×1024 pixels, i.e. time resolution between images was 2.578 s. To ensure bleaching of an optically thick slice of specimen, the pinhole was set to 4 Airy units.
For ratiometric FRET imaging of HeLa cells transfected with fCrH2, samples were illuminated at 488 nm, fluorescence was detected in the range of 500 nm to 550 nm and 600 nm to 700 nm. To ensure comparability of ratiometric FRET images, PMT voltages were set to 580 V in the green emission channel and 850 V in the red emission channel. Scanning frequencies were set to 400 lines per second or 800 lines per second, the pinhole was adjusted to 2 Airy units. A line average of 2 was employed in all images, i.e. each line was scanned two times and both lines averaged before proceeding to scanning the next line. Laser power was adjusted to exploit the dynamic range of photomultipliers without saturation effects.
HeLa cells transfected with Perceval HR were illuminated at 405 nm, 458 nm or 488 nm. To obtain similar absolute excitation powers, laser powers were adjusted to 5 % (405 nm), 22 % (458 nm) and 10 % (488 nm), respectively. For all illuminations, emission was detected in the range of 500 nm to 550 nm, PMT voltage was adjusted to ensure optimal use of the dynamic range of the photomultiplier without saturation effects and was held constant for all illuminations of the same cell. Images were scanned with a scanning speed of 400 lines per second and a line average of 2, the pinhole was set to 2 Airy units for all measurements.

Settings for FLIM Experiments

FLIM images were taken with 512×512 pixels, zoom was adjusted to achieve a pixel size of 100.31 nm. Samples were illuminated with a 470 nm pulsed laser with a pulse frequency of $f_{exc} = 40\,\text{MHz}$. Laser power was adjusted to minimize measurement time while staying below the recommended detection rate for lifetime measurements, $r_{det,max} \approx \frac{f_{exc}}{100} = 4 \cdot 10^5 \frac{\text{counts}}{s}$. Emitted photons were detected with an APD in the detection range of 500 nm to 550 nm. The pinhole was set to 1 Airy unit, image acquisition at a scanning speed of 400 lines per second was continued until a number of 2000 photons was registered in the brightest pixel, resulting in image acquisition times of ~ 10 min. Ratiometric FRET images were taken before and after FLIM imaging to ensure that cell movement or mitotic progression during image acquisition was negligible.

Settings for FLPM Experiments

In FLPM experiments, several modi operandi were followed: arrival times were recorded either for 5 s or 30 s per measurement locus. Depending on recording time per locus and cell cycle phase, various numbers of measurement loci were chosen. The exact combinations as well as the resulting total measurement times can be seen in table 3.1. Samples were illuminated with a 470 nm pulsed laser with a pulse frequency of $f_{exc} = 40\,\text{MHz}$. Laser power was adjusted to maximize photon counts while staying below the recommended detection rate for lifetime measurements, $r_{det,max} \approx \frac{f_{exc}}{100} = 4 \cdot 10^5 \frac{\text{counts}}{s}$. Emitted photons were detected with an APD in the detection range of 500 nm to 550 nm. The pinhole was set to 1 Airy unit. Ratiometric FRET images were taken before and after FLIM imaging to ensure that cell movement or mitotic progression during image acquisition was negligible.

Settings for FCS Experiments

FCS measurements were performed at 488 nm and 594 nm, respectively. Laser power was adjusted to maximize photon counts while not bleaching the sample. Fluorescence was detected with APDs in the range of 500 nm to 550 nm and 607 nm to 683 nm. Fluorescence intensity was recorded for 30 s per measurement locus, the pinhole was set to 1 Airy unit.

acquisition time per locus	loci per measurement	total measurement time
30 s	8 in cytoplasm **and** 6 in nucleoplasm	7 min
30 s	6 perpendicular to spindle axis **or** 6 parallel to spindle axis **or** 6 in periphery	3 min 3 min 3 min
5 s	10 in cytoplasm **and** 10 in nucleoplasm	1 min 40 s
5 s	10 perpendicular to spindle axis **or** 10 parallel to spindle axis **or** 14 in periphery	50 s 50 s 70 s

Table 3.1: Acquisition Times in FLPM-experiments

3.8.2 Analysis Programs

Imaging was performed using the built-in Leica LASAF Software (Version 2.7.3.9723). FLIM, FLPM and FCS measurements were performed by using the PicoQuant Symphotime Operation Software (Version 5.3.2.2) additionally. Analysis of FLIM data required the previous conversion from pt3 to ics data format, which was done using the pt32ics software by Verboogen et al.[128]. Data extraction from pt3 files for FLPM and FCS measurements was performed with the custom-made software workbench developed by Andreas Veres as part of his dissertation[126]. All further analyses were done in Matlab R2015b and Matlab R2018b with custom-made analysis routines. Plotting was accomplished in Origin2018 (Version 95E). False-colour fluorescence images were generated in Fiji (Version 2.0.0-rc-69/1.52p/Java 1.8.0_172).

Chapter 4

Cell Culture

In this chapter, all cell culture methods used in this work will be explained in detail. For a complete list of chemicals, equipment and their respective manufacturers see appendix B.

4.1 Culture of HeLa Cells

HeLa wild type cells of the Göteborg strain were grown in Cell Culture Flasks in D10 medium consisting of DMEM medium, supplemented with 10 % fetal calf serum, 100 µg/ml penicillin, 17 mM streptomycin and 10 mM glutamine at 37 °C and 5 % CO_2. Cells were passaged 2-3 times per week and used until the 25th-30th passage.

For microscopy, cells were plated in μ-Slide microscopy chambers and supplemented with transparent imaging medium consisting of MEM without phenol-red, 5% fetal calf serum and 50 mM HEPES.

4.2 Transfection of HeLa Cells

Cells were transiently transfected prior to measurements to obtain cells expressing fluorescent molecules. Transfection protocols are based on the respective manufacturers' protocols, but were optimized with respect to the particular requirements of cell type, plasmids and experiments.

4.2.1 Plasmids Used in this Work

Free Low-Expressing EGFP

A pCS2-based plasmid expressing EGFP under the control of a SRα promoter was used to characterize the heterogeneity of crowding states via imaging and FCS. Different from many other constructs, this particular plasmid expresses EGFP only on a comparatively low level. This low level is ideally suited for the experiments in this thesis. It is low enough to perform FCS measurements and, at the same time, high enough to allow imaging based techniques as well. The expressed EGFP molecules are unspecific, i.e. they do not bind to any particular substructure of the cell. The tertiary structure of EGFP as well as its excitation and emission spectra are shown in Fig. 4.1.

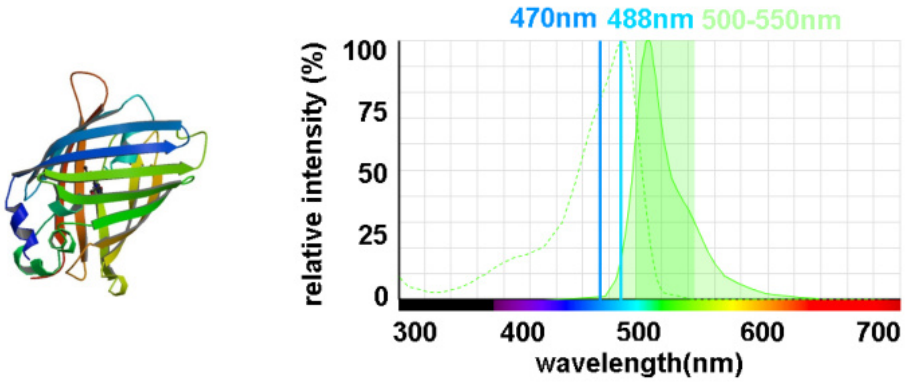

(a) **(b)**

Figure 4.1: EGFP. (a) Molecular structure. (b) Absorption and emission spectra with laser wavelengths and emission filter bandwidth used in this work. Figure (a) taken from [129]. Figure (b) generated with ThermoFisher Fluorescence Spectra Viewer [130].

fCrH2

fCrH2 is a synthetic crowding sensor based on a similar sensor initially developed by Boersma et al. [104] and modified by Sukenik et al. [105]. Different from the original sensor, fCrH2 uses AcGFP1 and mCherry as FRET pair (Fig. 4.2a). The excitation and emission spectra of fCrH2 are displayed in Fig. 4.2b. According to Sukenik et al. it undergoes a continuous structural change upon increase of crowder concentration. With increasing crowding levels, donor emission decreases whereas acceptor emission increases (Fig. 4.2c). Taken together, the FRET ratio rapidly responds to volume modulations in cells in a linear way (Fig. 4.2d).

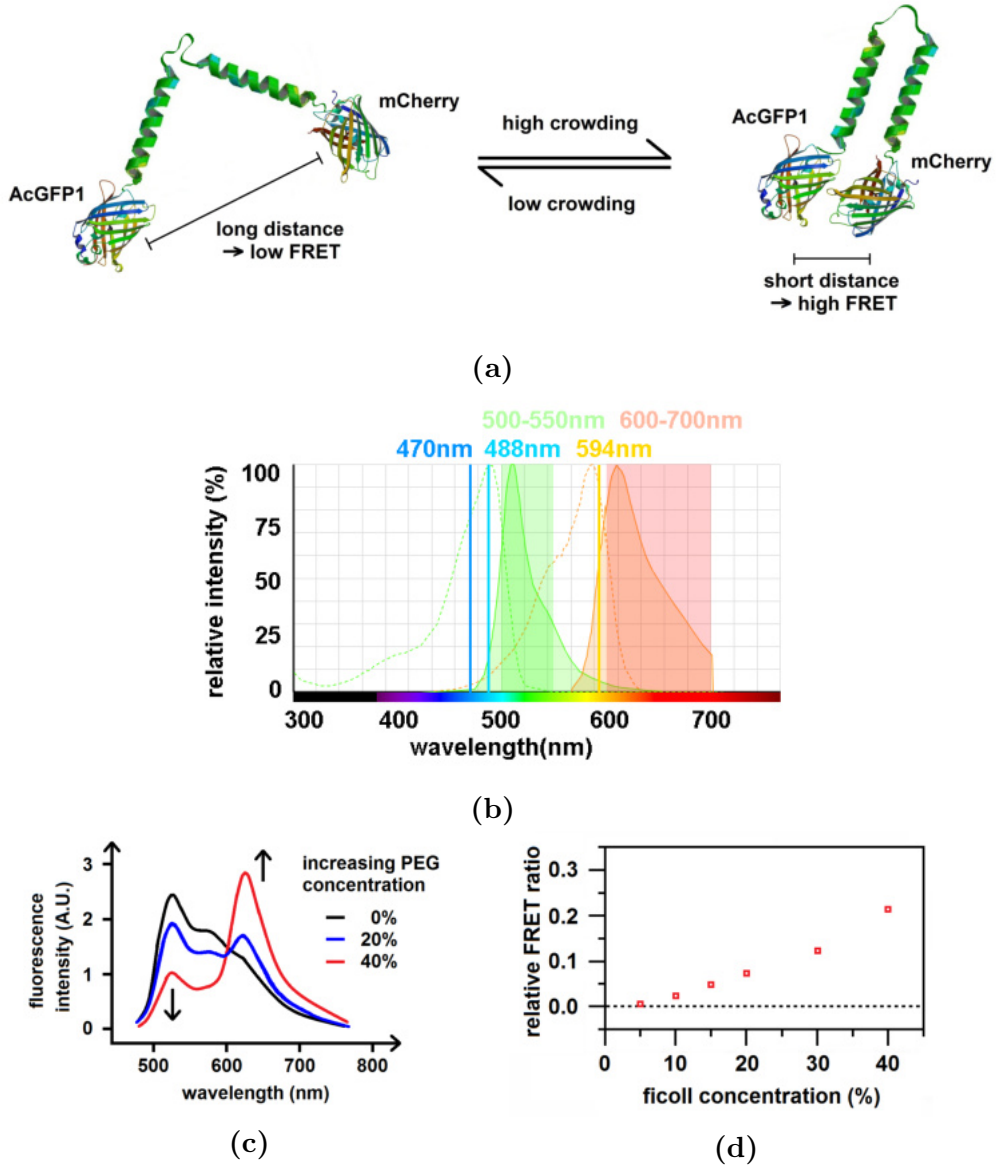

Figure 4.2: fCrH2. (a) Molecular structure of fCrH2. (b) Absorption and emission spectra with laser wavelengths and emission filter bandwidth used in this work. (c) Contribution of donor and acceptor to total fluorescence changes in response to increasing concentration of artificial crowder. (d) FRET ratio as a function of crowder concentration. In the range relevant for measurements in mammalian cells the dependence is approximately linear. Figure (a) generated using [129], [131] and [132]. Figure (b) generated with ThermoFisher Fluorescence Spectra Viewer [130]. Figure (c) inspired by [104]. Figure (d) inspired by [105].

PercevalHR

PercevalHR (Fig. 4.3a), developed by Tantama et al.[133], is a genetically encoded fluorescent biosensor susceptible to the local ATP:ADP ratio. Due to its high affinity to nucleotides it is constantly occupied by either ATP or ADP at physiological conditions. Its excitation spectrum has two distinct peaks that react differently to nucleotide binding (Fig. 4.3b): while ADP binding increases fluorescence at an excitation of 420 nm, ATP increases fluorescence at an excitation of 500 nm. At 455 nm the spectrum contains a fixed isosbestic point, i.e. fluorescence intensity at this excitation wavelength is independent of ATP:ADP levels.

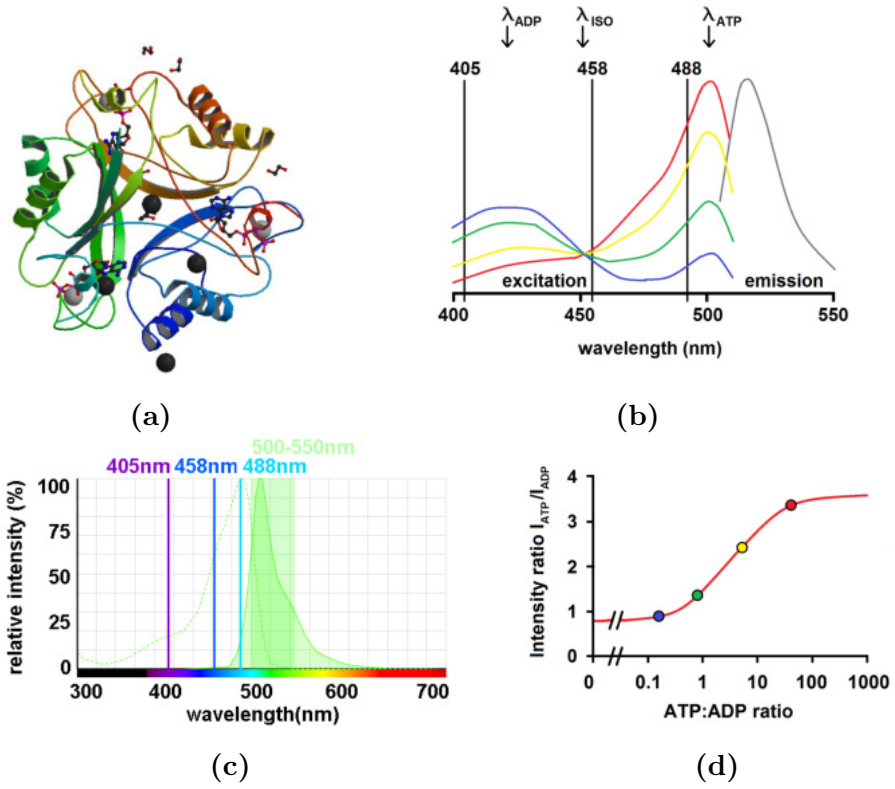

Figure 4.3: Perceval HR. (a) Molecular structure. (b) Principle of ATP:ADP sensitivity and laser lines used in this work. Absorption of excitation energy of specific wavelengths depends on local ATP:ADP concentration. Concentrations are colour-coded, colours match those used in (d). (c) Absorption and emission spectra with laser wavelengths and emission filter bandwidth used in this work. (d) Ratiometric signal as a function of ATP:ADP ratio. In the range relevant for measurements in mammalian cells (ATP:ADP ratios of about $[1, 100]$[133]) the dependence is approximately linear. Marked concentrations correspond to those displayed in (b). Figure (a) from[134]. Figure (c) generated with ThermoFisher Fluorescence Spectra Viewer[130]. Figures (b) and (d) inspired by[133].

Recording the fluorescence at high and low or, alternatively, at high and isosbestic wavelength and then taking the ratio of both channels is a way to analyse the intracellular ATP:ADP ratio independent of the absolute concentrations of sensor protein and nucleotides. It must be noted that, apart from intensity levels, the emission spectrum remains the same for all excitation wavelengths (Fig. 4.3c). In the ATP:ADP range relevant for measurements in mammalian cells, i.e. for ATP:ADP ratios of about $[1, 100]$[133], the relation between ATP:ADP ratio and the ratio of fluorescence intensities at high and low wavelengths is approximately linear (Fig. 4.3d). Moreover, PercevalHR has been shown not to buffer ATP or ADP[133].

4.2.2 Transfection of Free Low-Expressing EGFP with Peqfect

Transient transfection with EGFP was performed using Peqfect according to the manufacturer's protocol: 4 µl Peqfect were added to 200 µl supplement-free Opti-MEM GlutaMAX medium. After 5 min of incubation at room temperature, 2 µg DNA were added to the mixture. After another 30 min of incubation at room temperature, the complete mixture was added to the microscopy chamber containing cells seeded the day before and 1000 µl of fresh D10 medium. Measurements were performed after 24 h of incubation at 37 °C.

4.2.3 Transfections with Fugene 6

Transfection of Free Low-Expressing EGFP

Transient transfection with EGFP using Fugene 6 was performed according to the following, optimized protocol: 1.5 µl Fugene 6 were added to 50 µl supplement-free Opti-MEM GlutaMAX medium. After 5 min of incubation at room temperature 0.5 µg DNA were added to the mixture. After another 30 min of incubation at room temperature the complete mixture was added to the microscopy chamber containing cells seeded the day before and 1000 µl of fresh D10 medium. Measurements were performed after 24 h of incubation at 37 °C.

Transfection of Perceval

Transient transfection with PercevalHR using Fugene 6 was performed according to the following, optimized protocol: 3 µl Fugene 6 were added to 50 µl supplement-free Opti-MEM GlutaMAX medium. After 5 min of incubation

at room temperature 1 µg DNA were added to the mixture. After another 30 min of incubation at room temperature the complete mixture was added to the microscopy chamber containing cells seeded the day before and 1000 µl of fresh D10 medium. Measurements were performed after 24 h of incubation at 37 °C.

Transfection of fCrH2

Transient transfection with fCrH2 using Fugene 6 was performed according to the following, optimized protocol: 2.5 µl Fugene 6 were added to 50 µl supplement-free Opti-MEM GlutaMAX medium. After 5 min of incubation at room temperature 0.5 µg DNA were added to the mixture. After another 60 min of incubation at room temperature the complete mixture was added to the microscopy chamber containing cells seeded the day before and 1000 µl of fresh D10 medium. Measurements were performed after 24 h of incubation at 37 °C.

4.2.4 Transfection of fCrH2 with PolyPlus jetPrime

Transient transfection with fCrH2 using PolyPlus jetPrime was performed according to the following, optimized protocol: 2 µg of DNA were added to 150 µl PolyPlus jetPrime buffer. The mixture was vortexed for 10 s and centrifuged at 13.3 rpm for a few seconds. After adding 4 µl of PolyPlus jetPrime the mixture was vortexed and centrifuged again. After 10 min of incubation at room temperature the complete mixture was added to the microscopy chamber containing cells seeded the day before and 1000 µl of fresh DMEM medium. After 4 h of incubation at 37 °C, the medium was replaced by fresh D10 medium. Measurements were performed after another 20 h of incubation at 37 °C.

Transfection with PolyPlus jetPrime generates significantly higher transfection rates than transfection with either Peqfect or Fugene 6, but appears to be more invasive: cells treated with either Peqfect or Fugene 6 generally looked far more healthy than those treated with PolyPlus jetPrime. Since cells should be as close to their natural state as possible during single cell measurements, transfections for single cell measurements were performed with either Peqfect or Fugene 6. Preparation of lysates (protocol see Sec. 4.4), on the other hand, requires an as-high-as-possible transfection rate, whereas individual cells' states of health are not as crucial to the experimental procedure. Therefore, cells destined to be lysed were transfected with PolyPlus jetPrime.

Name	rotenone	oligomycin
C1	0.8	1.8
C2	0.6	1.5
C3	0.5	1.25
C4	0.4	1.0

Table 4.1: Final concentrations of rotenone and oligomycin used in apoptosis measurements. Concentrations are given in µM.

4.3 Special Treatments

Monitoring of changes in heterogeneity levels in cells subjected to stress conditions was achieved by treating cells according to the following protocols:

4.3.1 Treatments to Induce Osmolar Stress

Cells were generally cultured in isoosmolar media (0.3 Osm) to reproduce physiological conditions during cell growth and experiments. In order to induce hyperosmolar stress, isoosmolar imaging medium was mixed with sodium chloride (NaCl) to a final molarity of 0.8 Osm. To induce hypoosmolar stress, imaging medium was diluted with MilliQ water to a final molarity of 0.1 Osm.
After the onset of measurements the isoosmolar imaging medium was replaced either by hyperosmolar or hypoosmolar imaging medium. So measurements of cells could be taken by using the same cell both with and without treatment.

4.3.2 Treatments to Induce Apoptosis

Rotenone and Oligomycin

Rotenone and oligomycin dissolved in DMSO were added to transparent imaging medium to induce apoptosis in cells. Final concentrations of rotenone and oligomycin used in this work are given in table 4.1.
After the onset of measurements the imaging medium was replaced by imaging medium supplemented with rotenone as well as oligomycin. So measurements of cells could be taken by using the same cell both with and without treatment.

ATP Depletion via Sodium Azide and 2-Deoxy-D-Glucose

Cells were treated with sodium azide and 2-deoxy-D-glucose diluted in glucose free imaging medium to deplete them of ATP.

After the onset of measurements the imaging medium was replaced by imaging medium supplemented with sodium azide (NaN_3) at a final concentration of 10 mM and 2-deoxy-D-glucose at a final concentration of 6 mM. So measurements of cells could be taken by using the same cell both with and without treatment.

4.3.3 Depolymerization of Microtubules

Microtubules were depolymerized by adding nocodazole dissolved in imaging medium to a final concentration of 10 µM to cells seeded and transfected before. Measurements were performed after 10 min of incubation on ice and 15 min of incubation at 37 °C without another change of medium.

4.3.4 Synchronization of Cells for Measurements in Metaphase

For measurements in metaphase cells were synchronized with nocodazole: nocodazole was diluted in D10 to a final concentration of 49.5 nM and added to cells previously seeded and transfected. After 12 h to 18 h of incubation at 37 °C cells were washed 4 times with PBS. Then imaging medium was added. Measurements in metaphase were performed after 30 min of incubation at 37 °C.

4.4 Lysates

In order to produce cell lysates, cells were seeded and transfected in μ-Slide microscopy chambers (ibidi 2-well) and treated with M-PER Mammalian Protein Extraction Reagent. The cell culture medium was decanted and cells were washed once with PBS. The smallest volume of M-PER with lysis still being successful was found to be 200 µl per 2-well vial. This amount of M-PER was added to the cells and the chamber was shaken gently for 5 min. The resulting lysate was collected and transferred to a new, smaller microscopy slide (ibidi 8-well).

Part II

Characterizing Intracellular Heterogeneities on Multiple Lengthscales

Part II focuses on characterizing intracellular heterogeneities on several length-scales by various measurement methods:

Chapter 5 introduces the principal measurement and analysis methods used in all subsequent chapters of this part. The ratio of available volume fractions and their heterogeneity on the ROI-to-ROI scale as well as on the voxel-to-voxel scale is established by means of intensity-based fluorescence imaging in HeLa cells transfected with EGFP.

In chapter 6, ratiometric FRET imaging is performed in HeLa cells transfected with the FRET-based crowding sensor fCrH2. Thus overall crowding on the 5 nm-scale and its ROI-to-ROI heterogeneity can be analyzed.

In chapter 7, lifetime-based measurements in HeLa cells transfected with fCrH2 are used to further refine the results gained in chapter 6. The results of chapter 6 and chapter 7 are compared and briefly discussed.

Chapter 8 summarizes the results of several stress treatments performed on HeLa interphase cells. Depending on the specific treatment, either EGFP, fCrH2 or Perceval HR are transfected. Cellular stress responses are recorded by means of intensity-based fluorescence imaging, ratiometric imaging, ratiometric FRET or FCS.

In chapter 9, all results obtained in chapters 5 to 8 are summarized and discussed.

An overview of all lengthscales investigated in this thesis is given on p. 63.

An overview of all measurements, i.e. all combinations of cell cycle stages, treatments, fluorophores, observables and measurement techniques is given on p. 66.

Overview of Nomenclature, Observables, Lengthscales, and Measurements

Nomenclature

pixel	always refers to one pixel in an acquired image
voxel	always refers to the corresponding volume in the sample
comp	compartment: nucleoplasm/cytoplasm/spindle/periphery
$\mu(x) = \langle x \rangle$	mean of an observable x
$\sigma(x)$	standard deviation of an observable x
$\eta(x)$	heterogeneity of an observable x
$\delta(x)$	dispersion index of an observable x
$\mu_{ROI}(x)$	pixel-/voxelwise mean of x in one ROI
$\sigma_{ROI}(x)$	pixel-/voxelwise standard deviation of x in one ROI
$\eta_{ROI}(x)$	pixel-/voxelwise heterogeneity of x in one ROI
x_{comp}	mean of x in all ROIs in same compartment & cell
$\sigma(\mu_{ROI})$	standard deviation of μ_{ROI} in same compartment & cell
$\eta_{comp}(x)$	ROI-to-ROI heterogeneity in same compartment & cell
r	overall ratio of x between compartments in one cell
ρ	ratio of dispersion indices in a cell
$\langle x \rangle_{ens}$	ensemble average of observable x
$\langle x \rangle_{comp,ens}$	average of all ROIs in the same compartment in all cells
$\langle x \rangle_t$	temporal average of observable x

Overview of Observables

Observable	Description
I	intensity of EGFP proportional to available volume fraction φ lengthscale is determined by lengthscale of investigation
$\Theta = 1 - F_{FRET}$ $= \frac{D}{D+F}$	ratio of fCrH2 **not** undergoing FRET via FRET proportional to available volume fraction φ lengthscale is determined by lengthscale of investigation **and** Förster radius
$\Psi = 1 - E_{FRET}$ $= \frac{\tau_{DA}}{\tau_D}$	ratio of fCrH2 **not** undergoing FRET via FLIM proportional to available volume fraction φ lengthscale is determined by lengthscale of investigation **and** Förster radius
$\frac{ATP}{ADP}$	ATP:ADP level lengthscale is determined by lengthscale of investigation
$\frac{ATP}{ISO}$	ATP:isosbestic point level lengthscale is determined by lengthscale of investigation
τ	diffusion time, obtained via FCS
α	diffusion anomaly, obtained via FCS

Table 4.2: Overview of all fundamental observables investigated in this thesis.

Overview of Lengthscales

observable: $x: I, \Theta, \Psi, \frac{ATP}{ADP}, \frac{ATP}{ISO}$

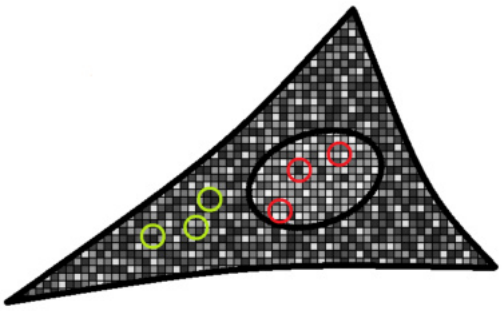

for each ROI:

$$\mu_{ROI,i}(x) = \frac{1}{n_{pixel}} \sum_{j=1}^{n_{pixel}} x_{pixel,j}$$

$$\sigma_{ROI,i}(x) = \sqrt{\frac{1}{n_{pixel}-1} \sum_{j=1}^{n_{pixel}} \left(x_{pixel,j} - \mu_{ROI,i} \right)^2}$$

$$\rightarrow \quad \eta_{ROI,i}(x) = \frac{\sigma_{ROI,i}}{\mu_{ROI,i}}$$

voxelscale heterogeneity
lengthscale: several hundred nm

for each compartment: Nucleus, Cytoplasm

$$x_{comp} = \langle \mu_{ROI} \rangle = \frac{1}{n_{ROI}} \sum_{i=1}^{n_{ROI}} \mu_{ROI,i}$$

$$\sigma(\mu_{ROI}) = \sqrt{\frac{1}{n_{ROI}-1} \sum_{i=1}^{n_{ROI}} \left(\mu_{ROI,i} - \langle \mu_{ROI} \rangle \right)^2}$$

$$\rightarrow \quad \eta_{comp} = \eta(\mu_{ROI}) = \frac{\sigma(\mu_{ROI})}{\langle \mu_{ROI} \rangle}$$

ROI-to-ROI heterogeneity
lengthscale: several µm

for each cell:

$$\rightarrow \quad r = \frac{x_{nuc}}{x_{cyto}} = \frac{\langle \mu_{ROI} \rangle_{nuc}}{\langle \mu_{ROI} \rangle_{cyto}}$$

overall ratio of observable
lengthscale : size of compartment

for each cell ensemble:

$$\langle \eta_{ROI} \rangle_{comp,ens} = \frac{1}{n_{ROI} \cdot n_{cells}} \sum_{l=1}^{n_{ROI} \cdot n_{cells}} \eta_{ROI,l}$$

$$\langle \eta_{comp} \rangle_{ens} = \frac{1}{n_{cells}} \sum_{k=1}^{n_{cells}} \eta_{comp,k}$$

ensemble averages

$$\langle r \rangle_{ens} = \frac{1}{n_{cells}} \sum_{k=1}^{n_{cells}} r_k$$

Overview of all Measurements in Cells

Treatment	Fluorophore	Method	Obs.	Pages
no treatment, interphase	EGFP	imaging	I	82-106
		imaging, TR	I	109-113 151-153
		FCS, TR	τ, α	181-185
	fCrH2	FRET	Θ	123-131
		FLIM	Ψ	135-140
		FLPM	Ψ	143-147
	Perceval HR	ratiom. im.	$\frac{ATP}{ADP}, \frac{ATP}{ISO}$	165-171
no treatment, metaphase	EGFP	imaging	I	82-106
	fCrH2	FRET	Θ	123-131
		FLIM	Ψ	135-140
		FLPM	Ψ	143-147
depletion of microtubules	EGFP	imaging	I	106-109
hyperosmolar stress	fCrH2	FRET, TR	Θ	153-158
hypoosmolar stress	fCrH2	FRET, TR	Θ	153-158
oxidative stress	fCrH2	FRET, TR	Θ	158-162
ATP depletion (rotenone + oligomycin)	Perceval HR	ratiom. im., TR	$\frac{ATP}{ISO}$	171-175
ATP depletion (sodium azide + 2-deoxy-D-gluc.)	Perceval HR	ratiom. im., TR	$\frac{ATP}{ADP}, \frac{ATP}{ISO}$	177-179
	EGFP	imaging, TR	I	179-181
		FCS, TR	τ, α	181-185

Table 4.3: Overview of all measurements in cells. TR: time-resolved.

Chapter 5

Characterizing Native Intracellular Crowding Levels and Crowding Heterogeneities via Intensity-based Imaging

→ *An overview of all lengthscales, observables and measurements in cells is given on p. 63-66. Ensemble statistics is summarized in appendix A.*

5.1 Motivation

Considering the importance of noise in biological processes in general[7] as well as the multi-scale nature of intracellular architecture, the assumption that crowding is homogeneous throughout the entire cell appears highly questionable. Indeed, as described in Sec. 2.2.2, a number of recent studies reported on non-negligible heterogeneities of intracellular transport processes. These might ultimately be caused by heterogeneities in the spatial organization of the protoplasm surrounding the tracer particles employed in the respective studies. Yet, the vast majority of researchers still follow the 'traditional' approach of data evaluation, i.e. they average over all data gathered from different loci within a cell. Thus, a potential spatial heterogeneity gets lost or, rather, included into the observable's error bars. For a sufficiently homogeneous sample this approach is perfectly acceptable. But in a complex specimen such as a living cell, the spatial heterogeneity of an observable might itself contain invaluable information.

As macromolecular crowding has a pronounced impact on virtually all intracellular processes, obviously a thorough characterization of intracellular crowding heterogeneities is needed. Particularly with regard to current advances in fields such as nanomedicine it is of crucial importance to understand how intracellular transport and reaction kinetics can vary even within one cell.
Previous works on the subject were based on measurements of transport processes, which might be influenced by other processes than mere crowding effects [53] [78] [80] [89].
This project aims at elucidating the spatial heterogeneity of cellular protoplasm in interphase and metaphase via a more static approach. Simple fluorescence imaging is used to characterize intracellular crowding heterogeneities on several lengthscales. Although the focus is on spatial heterogeneities, temporal heterogeneity is briefly discussed, too.

5.2 Definition of Heterogeneity Used in This Thesis

This thesis presents an attempt to quantify intracellular spatial heterogeneity on several lengthscales. An easy and straightforward method of doing so is calculating the coefficient of variation η. For any observable x it is defined as the ratio of its standard deviation and its mean value:

$$\eta(x) = \frac{\sqrt{\langle x^2 \rangle - \langle x \rangle^2}}{\langle x \rangle}. \tag{5.1}$$

Depending on the particular problem and the lengthscale investigated, x can represent various observables accessible via the respective measurement technique. In this chapter, for example, the spatial heterogeneity of the available volume fraction φ is deduced from the spatial heterogeneity of the local fluorescence intensity I.

5.3 Fundamental Relation between Crowding State and Measured Fluorescence Intensity

5.3.1 Intensity as a Function of Crowding

The fundamental idea for probing intracellular crowding heterogeneities via intensity-based imaging exploits the excluded volume effect. It is assumed that, in accordance with the laws of diffusion, chemically inert tracer particles in solution strive for a homogeneous distribution. Thus, from a macroscopic point of view, a solution of fluorescent particles would appear evenly stained. Putting a number of impenetrable obstacles into the solution would result in an increased effective concentration of tracer particles in the solution, whereas loci occupied by obstacles are free of tracers. In the macroscopic picture the solution would appear to be more brightly coloured but supplemented by some duller spots indicating the presence of obstacles.

It must, however, be taken into account that this pattern of measured fluorescence intensities does not only depend on the obstacles' size (relative to the fluorophores' size) but also on the lengthscale at which the sample solution is observed: consider, for example, a grid of 24×24 grid sites that are either black or white (see Fig. 5.1). When investigating this grid at maximum resolution, i.e. a resolution allowing to separate individual grid sites, each grid site has a value of either 0 (black) or 1 (white). When investigating the same grid at a resolution averaging over, for example, areas of 6×6 grid sites, the resulting areas ("measured pixels") have values between 0 and 1 - i.e. various grey scale values. Averaging over the complete grid of 24×24 grid sites again renders a grey value. Depending on the spatial distribution of black and white grid sites, the size of the region over whose grid sites the average is calculated can have a considerable influence on the obtained grey scale values: the more the distribution of individual grid sites is inhomogeneous, the more information gets lost when averaging over bigger regions. This principle is shown in Fig. 5.1: both grids in Fig. 5.1a and Fig. 5.1b consist of the same numbers of black and white grid sites. However, the pattern of grid sites is more homogeneous in Fig. 5.1a than in Fig. 5.1b. Averaging over areas of 6×6 grid sites renders a homogeneous grey value in all areas in Fig. 5.1a, but a new pattern of different grey scale values in Fig. 5.1b. When averaging over the complete box of 24×24

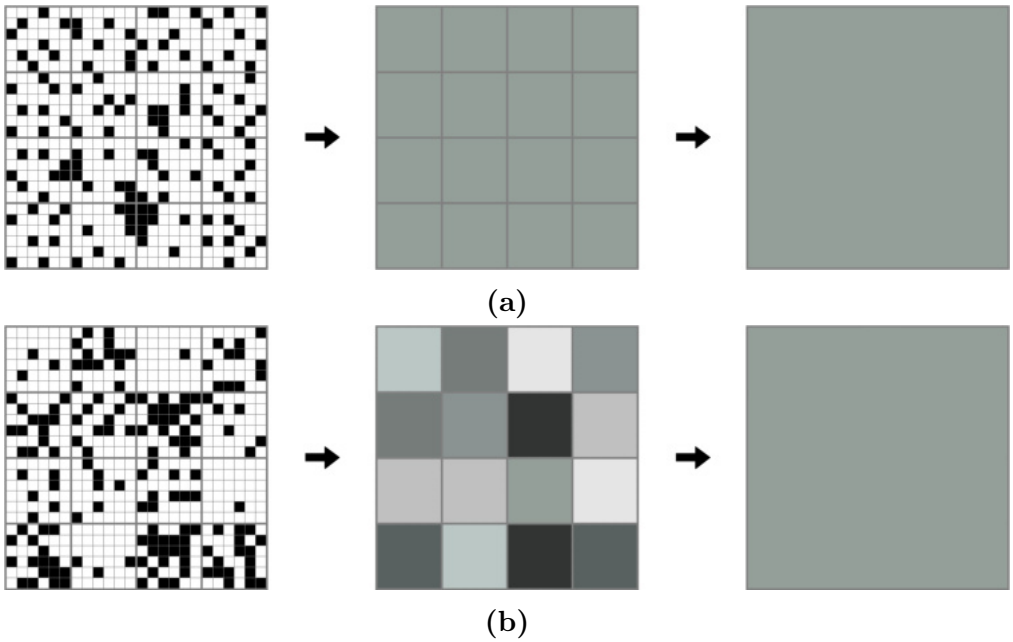

Figure 5.1: Fundamental relation between volume occupancy, heterogeneity and intensity on different lengthscales. (a) The sixteen 6x6 boxes display different patterns of occupied (black) grid sites, but they all contain the same ratio of occupied to non-occupied grid sites. On the lengthscale of 6x6 box to 6x6 box the sample therefore appears homogeneous, while on the lengthscale of individual grid sites it is heterogeneous. (b) The sixteen 6x6 boxes display different patterns of occupied grid sites as well as different ratios of occupied to non-occupied grid sites. Therefore the sample appears heterogeneous on both the small and the big lengthscale. However, these two heterogeneities are not necessarily the same. On the lengthscale of the complete sample, box (a) and box (b) are equivalent.

grid sites both, Fig. 5.1a and 5.1b, show the same grey scale value, as expected. So two samples showing equal intensities at a given resolution - or lengthscale - can be quite different from each other at another resolution/lengthscale.
Considering a complex multi-scale fluid like cellular protoplasm with obstacles of various sizes and shapes, one would expect an intricate pattern of regions coloured more or less brightly. Bright areas correspond to domains with many tracer molecules, i.e. a lower occupied/excluded volume fraction. Dull areas contain only few fluorophores which means that the local occupied/excluded volume fraction must be higher. By analysing the pattern of fluorescence intensities, it should be possible to gain information about local occupied/excluded volume fractions as well as their spatial variation.

5.3.2 Grid Box Simulation

A simple grid box simulation (principle shown in Fig. 5.2) can show that fluorescence intensity indeed reflects the local available volume fraction: cellu-

lar protoplasm is represented as a 3D matrix/grid box M of size $(10 \cdot r_0)^3$ with $r_0 = \frac{\lambda_{exc}}{2} \approx 240\,\text{nm}$. The length of individual grid sites is defined as $dx = dy = dz = 20\,\text{nm}$, resulting in a total number of $1.7 \cdot 10^6$ grid sites. Simplifying the simulation process, every grid site can either contain one unit of fluorophores or be devoid of them. In reality, a corresponding subvolume within a cell could, of course, contain varying amounts of fluorophores. Initially the occupied volume fraction Φ inside the grid box is set to zero, i.e. all matrix entries are set to one. For any chosen volume occupancy a percentage of grid sites corresponding to this particular occupied volume fraction is set to zero, representing the percentage of volume not available to fluorophores.

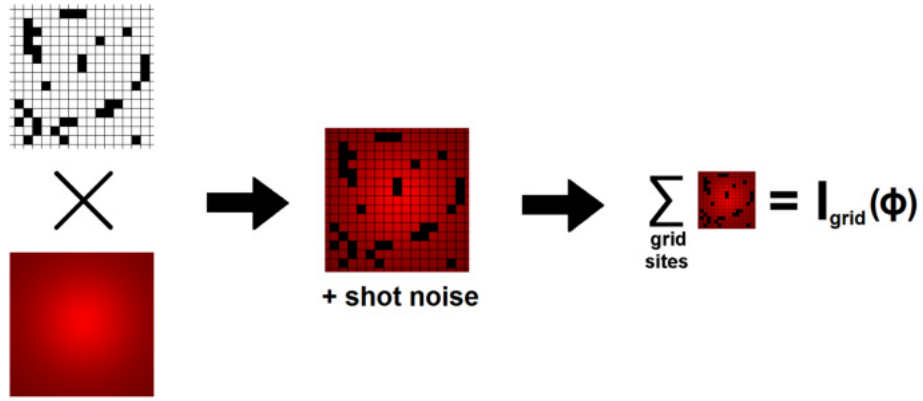

(a)

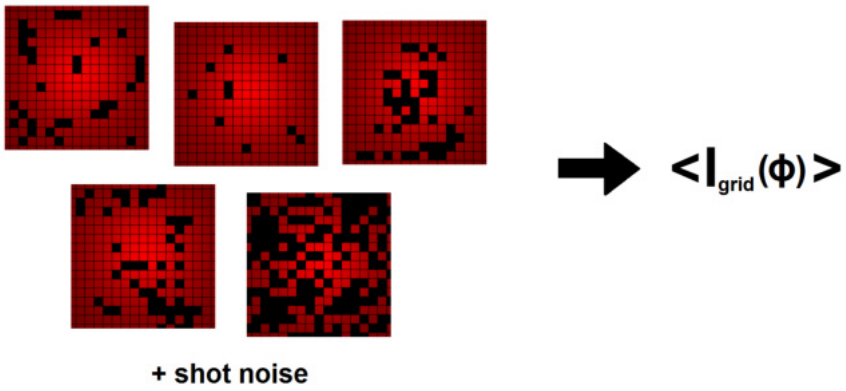

(b)

Figure 5.2: Grid box simulation. (a) A grid with a fraction Φ of occupied grid sites (black) is multiplied with a Gaussian beam profile (red). The sum of the resulting matrix represents the relative intensity displayed in one pixel as a function of occupied volume ϕ of the corresponding voxel within the sample. (b) Averaging over many grid boxes corresponds to the mean intensity of a ROI.

As the precise nature of occupation caused by surrounding molecules is not known, three different models of occupation are tested (see Fig. 5.3): to depict an occupation due to small molecules (corresponding to an ideal solution, i.e. occupation caused by other solvent molecules), all occupied grid sites are chosen randomly and immediately set to zero (Fig. 5.3a). In an attempt to describe a mixture of differently sized molecules, every grid site is assigned a probability p to be occupied when being chosen (Fig. 5.3d). Initially a probability $p = 0.05$ is assigned to all grid sites. As soon as a grid site is set to zero, the probability of the eight grid sites immediately surrounding this site to be occupied is set to 1. In order to represent occupation by bigger molecules, a grid site is chosen randomly and is set to zero together with its surrounding eight sites (Fig. 5.3b). Thereby the actual occupied volume fraction is increased by $9/(1.7 \cdot 10^6)\%$. In all three models grid sites can only be occupied once.

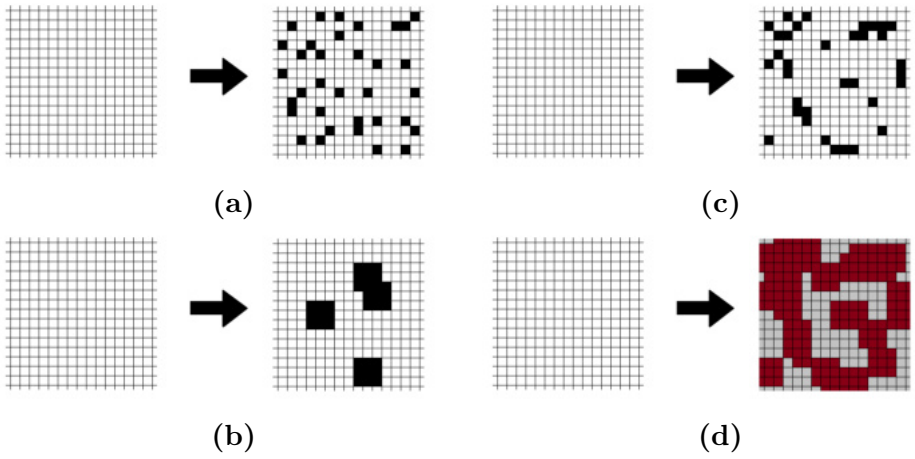

Figure 5.3: Different models of occupation. (a) Occupation by monomers. (b) occupation by big molecules. (c) Occupation by a mixture of differently sized molecules: grid box. (d) Occupation by a mixture of differently sized molecules: probability box.

In order to obtain the fluorescence intensity as a function of volume occupancy, the matrix is multiplied by a Gaussian beam profile G placed in the centre of the simulation volume:

$$M(\Phi) \circ G = \left(M^{\Phi}_{ijk} \cdot A \cdot e^{-\frac{2}{r_0^2} \cdot \left[\left(\left(i - \frac{I}{2}\right) dx \right)^2 + \left(\left(j - \frac{J}{2}\right) dy \right)^2 + \frac{\left(\left(k - \frac{K}{2}\right) dz \right)^2}{S^2} \right]} \right), \qquad (5.2)$$

with $I = J = K = \frac{10 \cdot r_0}{dx} = 120$ denoting the number of grid sites in each dimension, i, j, k being the actual position on the grid. The dimensionless shape

factor S describes the distortion of the confocal volume in axial direction compared to lateral directions. For this simulation it is set to be $S = 5$ to match the measurement setup used for fluorescence imaging. The intensity of the complete matrix as a function of the beam amplitude A is obtained by summing up all individual entries.

In all occupation models the effect of the grid's volume occupancy Φ on relative emitted intensity I_{grid} is tested for occupied volume fractions from $\Phi = 1\,\%$ to $\Phi = 100\,\%$ in $1\,\%$ steps. In order to improve run-time, the simulation box remains the same (i.e. all occupied grid sites stay occupied) while going from Φ_i to Φ_{i+1} and another $1\,\%$ of grid sites is set to zero according to the occupation rules described above. For statistical reasons, each simulation is repeated 300 times. For the purpose of depicting real fluorescence measurements more accurately, Poisson noise is applied to both the simulation matrix before summing up and the complete table of intensities as a function of occupied volume fractions by using the built-in MATLAB function *imnoise*:

$$\langle I_{grid}(\Phi)\rangle = \left\langle \text{imnoise}\left(\sum_{grid}\left[\text{imnoise}(M(\Phi)\circ G,'\text{poisson}')\right],'\text{poisson}'\right)\right\rangle . \tag{5.3}$$

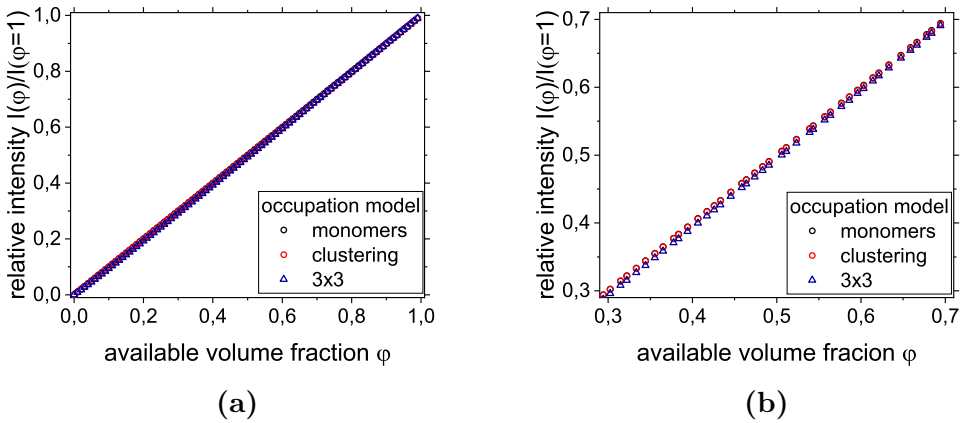

Figure 5.4: Relative emitted intensity as a function of available volume. Averaged result of 300 grid box simulations for (a) single voxel and (b) larger ROI. As expected, the fluorophores' relative emitted intensity $I(\varphi)/I(\varphi = 1)$ equals the available volume fraction φ. Results are independent of the chosen occupation model.

Fig. 5.4 shows that the relative fluorescence intensity is proportional to the available volume fraction $\varphi = 1 - \Phi$, which confirms the initial assumption that fluorescence intensity depends on crowding levels linearly. Please note that the result of one grid box simulation represents the fluorescence intensity

of one pixel as a function of the volume occupancy of the corresponding voxel in the sample (Fig. 5.4a). Trivially, however, the proportionality of relative intensity and available volume also holds true for larger areas, i.e. the sum of several pixels/grid boxes, which corresponds to a larger area in the focal plane of the sample (Fig. 5.4b).

5.3.3 Intensity as a Function of Particle Concentration and Instrument Settings

It might seem superfluous to specifically investigate the emitted intensity as a function of fluorophore concentration. However, one must bear in mind that measured intensities, i.e. ultimately pixel values, do not only depend on the corresponding voxel's fluorophore concentration in the sample but are influenced by instrument settings as well. To be more precise we have to state the fact that instrument settings might influence mean values and standard deviations of pixel values differently. For the purpose of testing this adjustable instrument settings were modified systematically in experiments with autofluorescent plastic slides ("chromaslides") and varying concentrations of the fluorescent dye Alexa488 dissolved in MilliQ water. Since both chromaslides and fluorophores can be expected to be homogeneous on the lengthscale of investigation, experimentally obtained standard deviations can be ascribed to the setup.

Scanning speed as well as image size were found to influence both recorded mean intensities and pixel-wise standard deviations (Fig. 5.5a and 5.5b). So depending on the settings, vastly different heterogeneity levels can be found in the same homogeneous sample. (Fig. 5.5d and 5.5e) As both parameters ultimately define illumination time per voxel, they were adjusted so that constant exposure time for all subsequent measurements could be guaranteed.

Naturally line and frame averages do not influence recorded mean fluorescence levels. They only influence standard deviations (Fig. 5.5c). However, thus also recorded heterogeneity levels depend on line and frame averages (Fig. 5.5f). One could argue that applying a high line or frame average would minimize noise originating from microscope components and, therefore, would yield more reliable results regarding the samples' native heterogeneities. However, averaging considerably increases image acquisition time. In view of the fact that all measurements are performed in living cells, long acquisition times should be avoided: cells continue their metabolic and/or reproductive activity during

measurements. So averaging over many lines/frames might mask actual heterogeneity levels by averaging over various temporally varying crowding states. Additionally, prolonged excitation can damage fluorophores permanently. In order to avoid these effects images were not averaged.

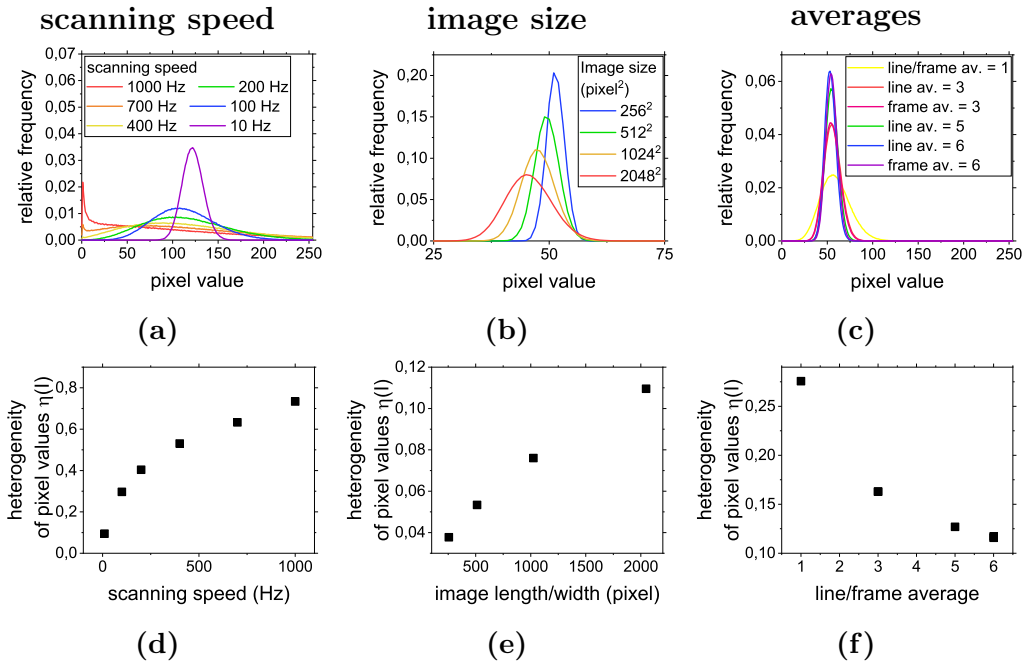

Figure 5.5: Influence of microscope settings on pixelwise intensity distributions. Measurements performed on chromaslides. (a) - (c) Distribution of pixel values. (d) - (f) Pixelwise heterogeneities $\eta(I)$. Heterogeneity $\eta(I)$ calculated according to Eq. 5.1. (a) + (d) Scanning speed. (b) + (e) Image Size. (c) + (f) Line/frame averages. Since microscope settings can have a significant impact on pixelwise heterogeneities obtained in the same (homogeneous) sample, scanning speed, image size and line/frame average, which together ultimately define illumination time per voxel, were adjusted to guarantee constant illumination times in all subsequent images.

Laser excitation power and photomultiplier bias voltage were found to influence both registered mean intensity and pixel-wise standard deviation and thus measured heterogeneity levels (see Fig. 5.6). So the best practice would be to define a set of standard imaging conditions to be used in all experiments. However, this is not possible for the given system: the expression levels of transfected EGFP in HeLa cells show a rather high variation. Yet the imaging approach to quantifying intracellular crowding heterogeneities depends on the analysis of pixel values of a given range. This causes the problem that laser excitation power and photomultiplier bias voltage cannot be held constant throughout measurements. For each individual cell they have to be adjusted to optimally exploit the dynamic range of the photomultiplier tube while avoiding saturation effects. Thus the precise influence of laser power and PMT voltage

on registered intensities has to be analysed. This is done by performing a set of simulations of pixel value distributions of homogeneous and inhomogeneous samples in ideal and realistic imaging conditions (see Fig. 5.7) and comparing their results to actual measurements performed on the given microscope (see Fig. 5.8).

Let us at first consider the simulation of a perfectly homogeneous sample (see Fig. 5.7a). In an ideal fluorescence imaging experiment (see Fig. 5.7c), the number of emitted photons k obtained from each voxel is defined by a Poissonian

$$p(k, \chi) = \frac{\chi^k}{k!} e^{-\chi}. \tag{5.4}$$

It can be shown that for this distribution the mean number of photons is given by $\langle k \rangle = \chi$, the variance by $\sigma^2(k) = \langle (k - \langle k \rangle)^2 \rangle = \chi$. The average number of emitted photons per voxel χ is, of course, determined by the average number of fluorescent molecules $\langle N \rangle$ in that volume as well as the fluorophores' quantum yield and the illumination intensity. So, in principle, we should find the relation $\langle k \rangle = \sigma^2(k) = \chi \propto \langle N \rangle \propto \langle c \rangle$. In this expression N denotes the number of fluorescent particles in a given volume, c the particle concentration.

When performing imaging experiments in solutions of fluorescent dyes, e.g. Alexa488, in water, however, the distribution of pixel values is markedly different from a Poissonian (see Fig. 5.8a): while the general shape of the distribution is clearly reminiscent of a Poissonian, the fundamental characteristic of Poissonian distributions, i.e. $\langle k \rangle = \chi = \langle (k - \langle k \rangle)^2 \rangle$, does not hold true for the given setup. For all measurements the variance of pixel values is considerably larger than the corresponding mean value. Yet the variance depends on the average in a linear fashion (see Fig. 5.9):

$$\sigma^2(I) = \xi^2 \cdot \mu(I). \tag{5.5}$$

The multiplicative prefactor ξ^2 depends on detector settings and is clearly larger than unity in all cases. The phenomenon itself can be attributed to the detector-dependent translation of photon counts via secondary electron multiplication to discrete fluorescence intensity values n performed by the image acquisition software. But also imperfections in photon detection might contribute to this scaling of variances.

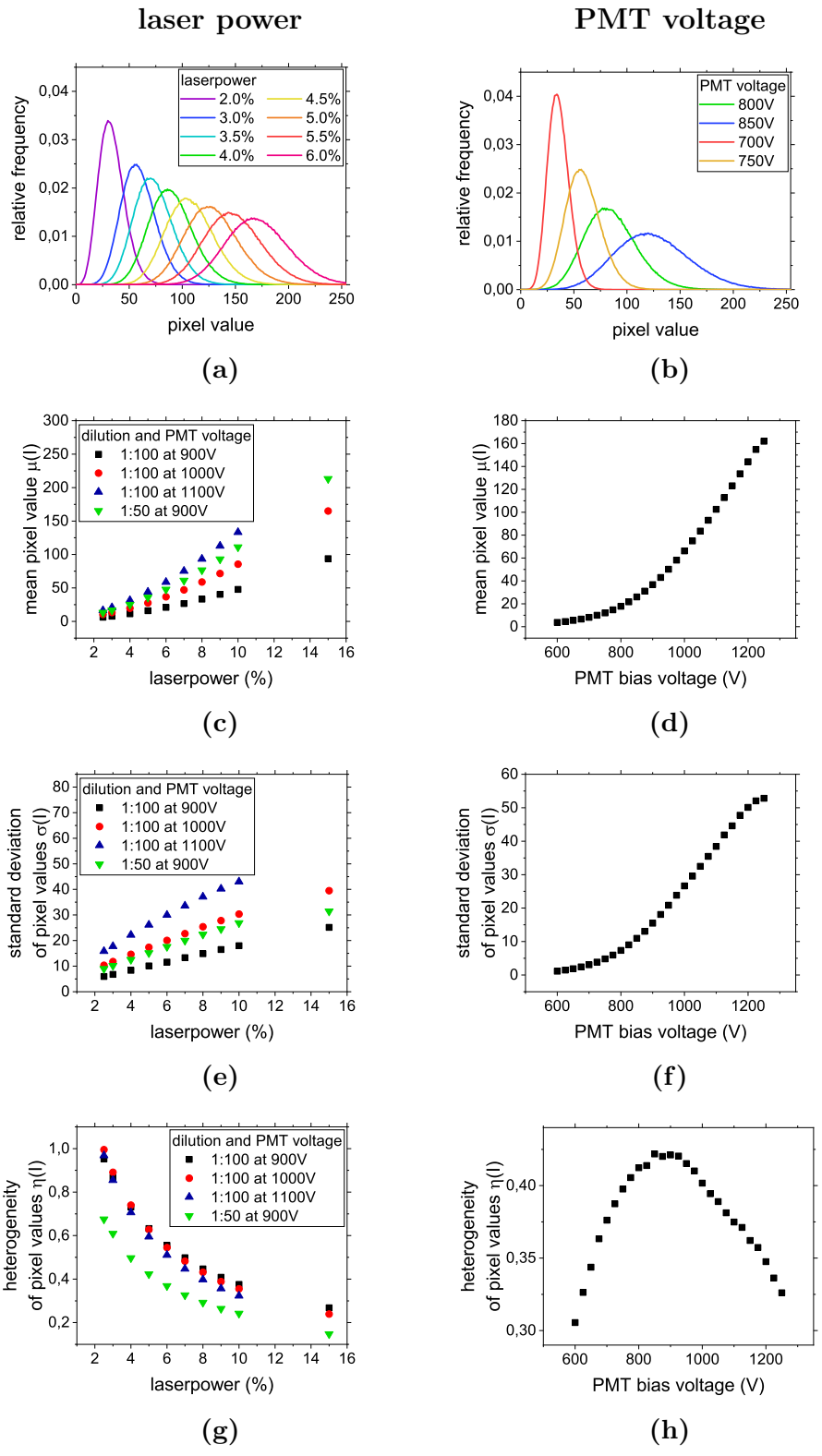

Figure 5.6: Influence of microscope settings on pixelwise intensity distributions. Left column: laser power. Right column: PMT bias voltage. (a) + (b) Distribution of pixel values obtained in chromaslides. (c) + (d) Mean $\mu(I)$, (e) + (f) standard deviation $\sigma(I)$ and (g) +(h) pixelwise heterogeneity $\eta(I)$ of pixel values. Heterogeneity $\eta(I)$ calculated according to Eq. 5.1. Measurements performed in fluorophore solutions of different concentrations in order to sample larger range of laser powers/PMT voltages. Although both settings have a profound impact on obtained heterogeneity values, they cannot be held constant.

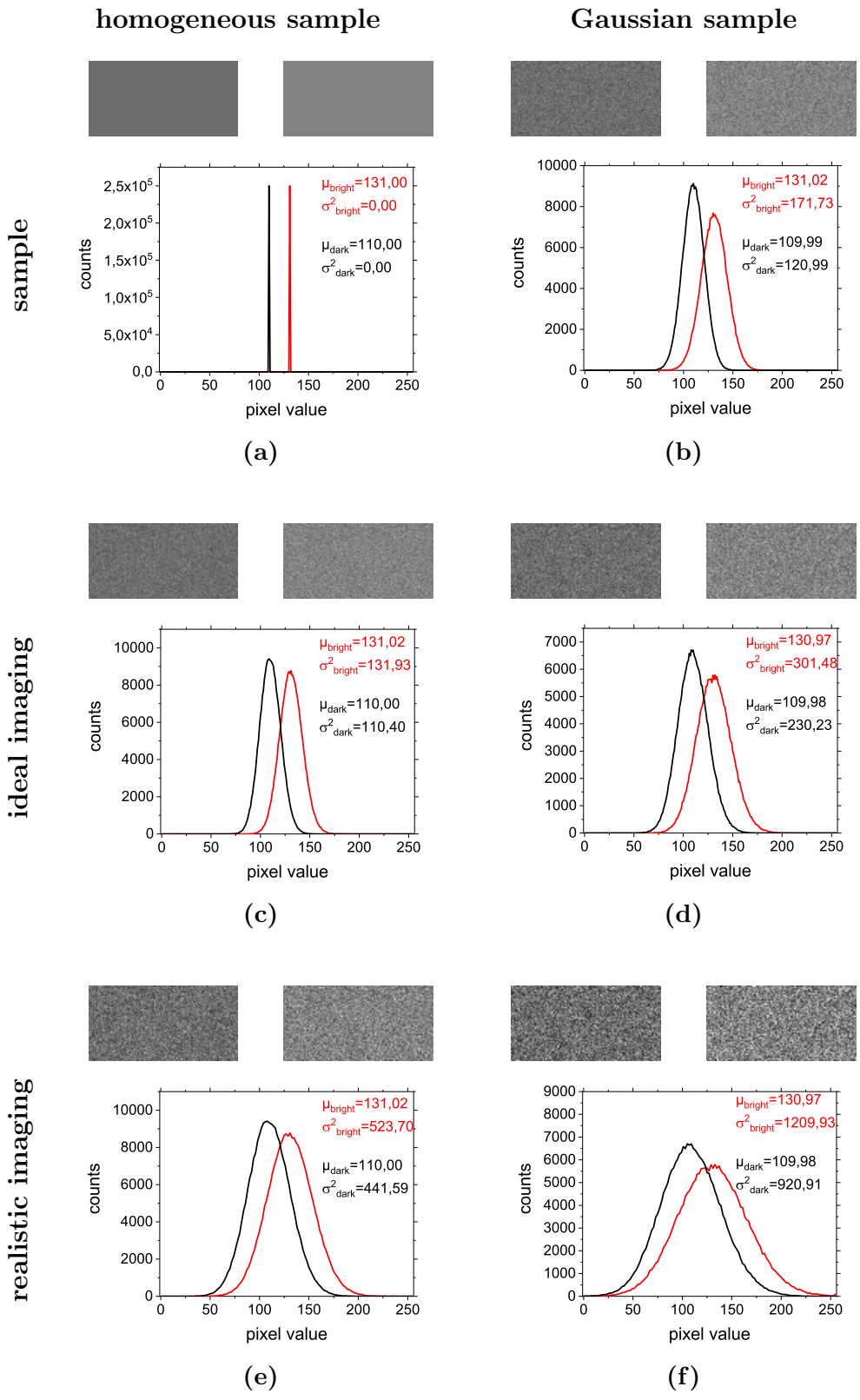

Figure 5.7: Simulation of pixel value distributions: homogeneous and inhomogeneous samples in ideal and realistic imaging conditions. Left: homogeneous sample. Right: Inhomogeneous sample with Gaussian distribution of pixel values. (a) + (b) Sample-inherent heterogeneity. (c) + (d) Ideal imaging conditions: Poisson noise. (e) + (f) Realistic imaging conditions: mapping algorithm. Grey areas: cut-out from simulated matrices.

In simulations, this can be modelled by means of a mapping algorithm. All pixel values n are transformed according to the following expression:

$$n = \xi(k - \langle k \rangle) + \langle k \rangle. \tag{5.6}$$

In this approach the mean pixel value remains unchanged, while the variance is stretched by a factor ξ^2:

$$\langle n \rangle = \langle k \rangle = \chi, \tag{5.7}$$

$$\sigma^2(n) = \langle (n - \langle n \rangle)^2 \rangle = \xi^2 \chi. \tag{5.8}$$

The resulting histogram retains a Poissonian shape, but is much broader than a 'true' Poissonian (see Fig. 5.7e).
Experimental data obtained in homogeneous samples can be reproduced almost exactly with this mapping algorithm as long as $\xi^2 > 1$: histograms of pixel values can be fitted very well with this model of a 'stretched', i.e. broadened Poissonian whereas the much slimmer 'true' Poissonian describes the data only very poorly (see Fig. 5.8a). However, the mapping algorithm is not suited to fit histograms of pixel values obtained in cells (see Fig. 5.8b). This indicates that cells indeed do contain an additional sample-inherent heterogeneity.

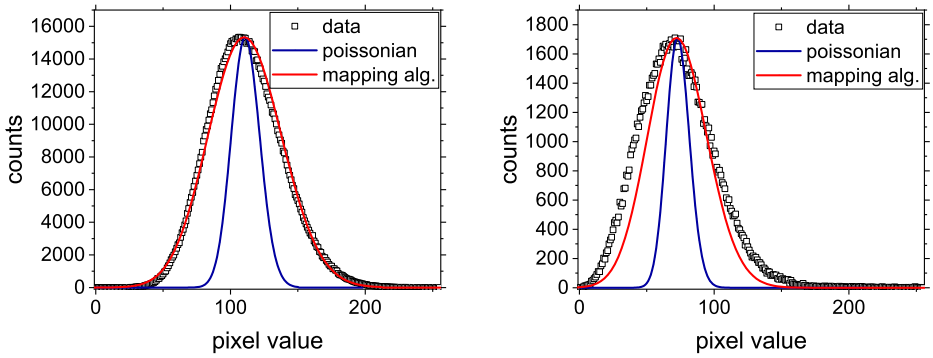

Figure 5.8: Comparison of measurement data, Poissonian and mapping algorithm. (a) The mapping algorithm described in the text is well suited to describe experimental data of solutions of Alexa488 in water. A Poissonian on the other hand describes experimental data even in homogeneous samples poorly. (b) In HeLa cells transfected with EGFP, neither a Poissonian nor the mapping algorithm can describe experimental data, hinting at an additional sample-inherent heterogeneity.

In inhomogeneous samples the spatial variation of units of volume below the diffraction limit accessible for fluorophores ultimately results in a spatially

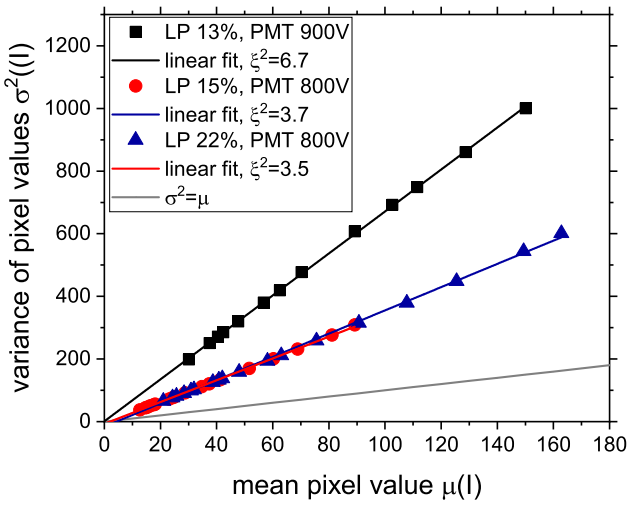

Figure 5.9: Pixelwise variance as a function of mean intensity. For homogeneous solutions of Alexa488 in MilliQ water at different concentrations, the pixelwise variance of intensity values $\sigma^2(n)$ is proportional to but does not equal the samples' mean intensity $\langle n \rangle$. The proportionality factor ξ^2 depends on PMT bias voltage (PMT) but not on excitation laser power (LP) and is generally > 1. The identity line $\sigma^2(n) = \langle n \rangle$ is added as a guide to the eye.

varying number of fluorescent particles per voxel. As shown before, the number of fluorophores per volume $\langle N \rangle$ is proportional to the accessible volume fraction ϕ:

$$\langle N \rangle \propto \phi. \tag{5.9}$$

Thus the mean fluorescence per voxel can be described as

$$\chi = A\phi \propto \langle N \rangle. \tag{5.10}$$

In this expression the prefactor A summarizes all proportionality factors.
For the purpose of simplification, in the simulation it is assumed that the accessible volume fraction can be described by a Gaussian probability distribution function with a mean accessible volume fraction ϕ_0 and a variance $\sigma^2(\phi) << \phi_0^2$ (see Fig. 5.7b). In perfect imaging conditions this would render a mean fluorescence intensity $\langle \chi \rangle = A\phi_0$ and a variance $\sigma^2(\chi) = A\sigma^2(\phi)$ (see Fig. 5.7d). Sampling such a specimen in more realistic measurement conditions, i.e. applying the mapping algorithm introduced in Eq. 5.6, 5.7 and 5.8, we find the mean and variance accessible via image analysis to be

$$\langle n \rangle = A\phi_0 \tag{5.11}$$

$$\sigma^2(n) = \xi^2(A\phi_0 + A^2\sigma^2(\phi)). \tag{5.12}$$

The resulting probability distribution function (see Fig. 5.7f) is well suited to describe experimentally obtained histograms of intracellular pixel values.
Eq. 5.12 can be utilized to extract the voxel-to-voxel heterogeneity of the accessible volume fraction in cellular compartments from imaging data. The exact analysis method is described in Sec. 5.6.
It must be noted that this setting-dependent scaling of pixel-wise variances only has an impact on pixel/voxel-wise heterogeneities. Intermediate length-scale heterogeneities can be calibrated with images acquired in homogeneous samples. This is discussed in more detail in Sec. 5.5.

It should be stressed that only photomultiplier settings have an effect on the prefactor ξ^2. Varying the laser illumination intensity at fixed detector settings does change mean value and variance of fluorescence intensities, but has no impact on their proportionality factor. The same holds true for varying the fluorophore concentration inside the sample. These results are displayed in Fig. 5.9.
Of course one could argue that the best measurement procedure would be to adjust PMT bias voltage to a fixed value and only vary laser illumination intensity. However, due to the extremely heterogeneous transfection levels of EGFP in HeLa cells, this would inevitably require using a very large interval of laser intensities. Yet the argon laser integrated in the measurement setup used in this thesis has been shown to remain stable only in a limited intensity range. Moreover, taking images at high laser power is likely to result in photobleaching of fluorophores or even in harming the cell itself.

5.3.4 Measuring Fluorescence Intensities in Cells

In this project, the genetically encoded fluorescent protein EGFP (enhanced green fluorescent protein) was used as a tracer particle. EGFP is a cylindrical protein with a chromophore in the centre of the cylinder[135]. The type of EGFP used here is not bound to any intracellular structure but diffuses freely in both cytoplasm and nucleoplasm. According to Swaminathan et al.[136] and Verkman et al.[137], it does not significantly interact with cellular components. As the molecule is quite small with a Stokes-radius of only 2.82 nm[138], it is able to diffuse rapidly in the cell[136]. Depending on the exact cell type, production of a fully functional EGFP molecule takes between one and several minutes[139]. After an incubation time of 24 h after transient transfection into HeLa cells it

is very likely to have adopted a more or less homogeneous distribution of individual molecules in the available volume fraction. Thus variations in local fluorescence intensities can be judged to be local excluded volume effects. In addition GFP is not particularly susceptible to photobleaching. So it is the perfect type of fluorophore to probe the surrounding environment via imaging. It should be noted that, in accordance with the resolution limit of confocal microscopy as well as the Nyquist criterion, zoom was adjusted so that pixel sizes equalled either 100.21 nm or 100.31 nm. This ensures comparability of all images.

5.4 Differences in Overall Crowding States between Compartments

When inspecting fluorescence images of HeLa cells transfected with free EGFP (Fig. 5.10a) it is particularly striking that the average fluorescence intensity seems to be higher in the nucleoplasm than in the cytoplasm. The mere visual impression can be confirmed quantitatively by plotting an averaged line profile of fluorescence intensities of both compartments (Fig. 5.10e). This profile shows that fluorescence is higher in the nucleoplasm than in the cytoplasm, on average about 30 %. Plotting the distribution of pixel-wise fluorescence values per compartment (Fig. 5.10g) is an additional way of showing a considerably higher mean fluorescence intensity in the nucleus.
Strangely enough, however, a similarly biased distribution of fluorescence intensities can be observed in metaphase cells (Fig. 5.10b), where fluorescence in the spindle region is markedly higher than in the spindle periphery. With regard to nuclear envelope breakdown in early prometaphase this observation is really remarkable: all intracellular constituents - or, at least, all those small enough - are expected to mix freely in the absence of a diffusion barrier. Yet fluorescence line profile (Fig. 5.10f) as well as the distribution of pixel-wise fluorescence values (Fig. 5.10h) establish the average fluorescence intensity in the spindle region to be about 15 % to 20 % higher than in its periphery.

EGFP has been reported to be biochemically inert and to possess no nuclear localization sequence[140]. Thus directional transport between nucleoplasm and cytoplasm is rather unlikely.
Of course there might be a fraction of immobile EGFP molecules bound to one of the nucleoplasmic constituents. The most likely binding partner would

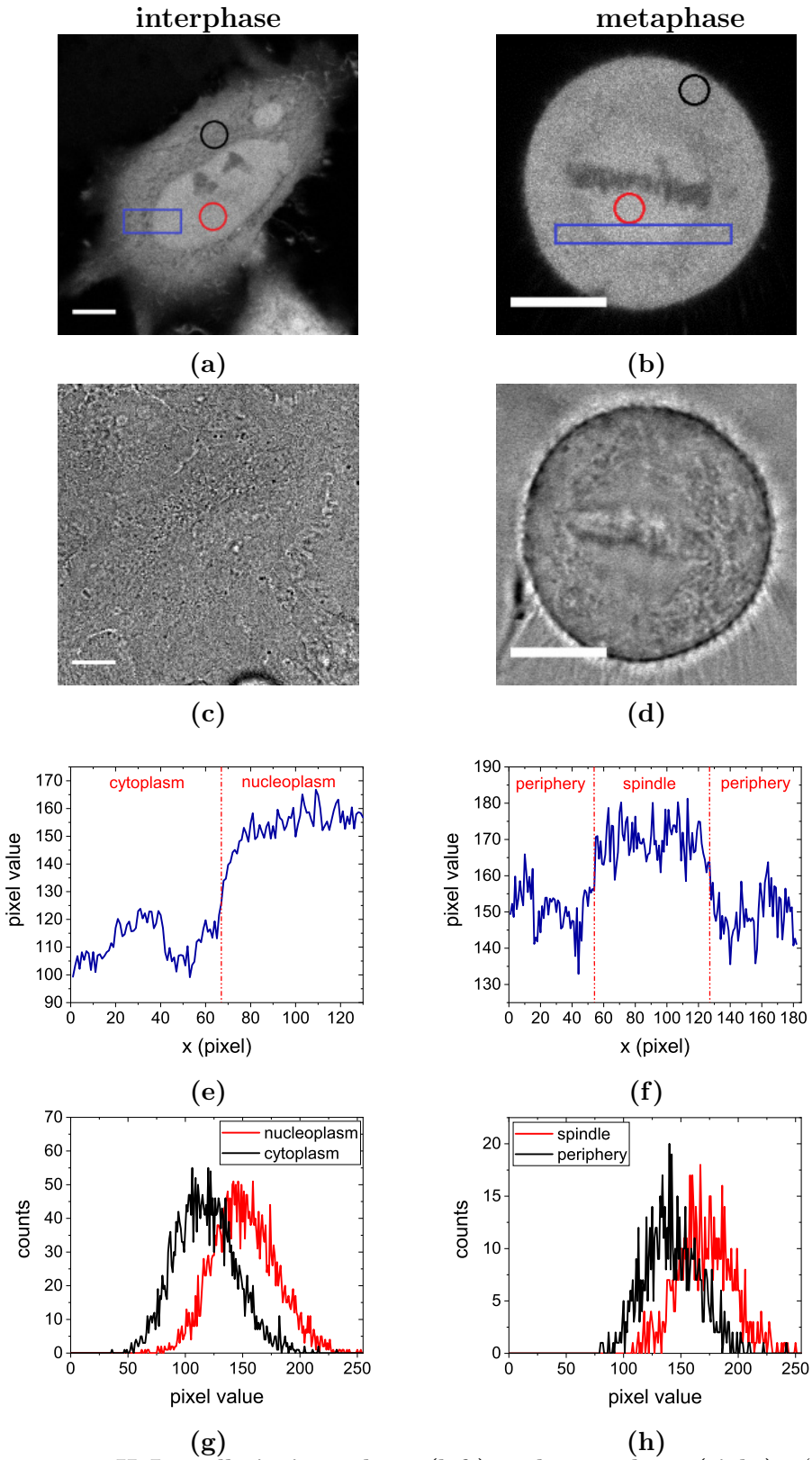

Figure 5.10: HeLa cells in interphase (left) and metaphase (right). (a) + (b) Fluorescence images. Nucleus and spindle feature a higher fluorescence intensity than cytoplasm and periphery. (c) + (d) Transmission images. (e) + (f) Line profiles of rectangular regions marked in (a) and (b) (taken along horizontal direction x and averaged over vertical direction). Pixel values are higher in nucleus and spindle than in cytoplasm and periphery. (g)+(h) Histograms of pixel values in circular ROIs marked in (a) and (b). Scalebar 10 µm.

be DNA. Together with a constant concentration of EGFP molecules diffusing freely in both cytoplasm and nucleoplasm this would result in an increase in absolute concentration of fluorophores in the nucleus. But this would not provide an explanation for the increased level of fluorescence in the spindle region during metaphase, where condensed chromatin is clearly visible as a dark, i.e. non-fluorescent region localized in only a comparatively small part of the spindle region.
It might be possible that a fraction of EGFP is bound to decondensed DNA in interphase cells but detaches prior to entry into mitosis or during chromatin condensation. This could explain the increased fluorescence level in interphase nuclei as well as in the metaphase spindle region. This assumption is true provided that the contiguous nucleocytoplasmic fluid does not mix completely before metaphase.
A number of FRAP experiments was performed on interphase cells to test whether the nucleus does feature such a fraction of immobilized EGFP molecules. A region in the nucleus was bleached at high laser power. The subsequent fluorescence recovery in the nucleus as well as the simultaneous fluorescence loss in the cytoplasm was being monitored for 3 min. With the standard imaging conditions used in this project the minimum time resolution that could be realized is 1 image per 2.578 s. In order to limit the influence of z-directional diffusion on FRAP recovery, the confocal pinhole was set to 4 AU. In this way a thick section of the sample can be bleached.
Please note that FRAP experiments cannot easily be performed in metaphase cells since mitotic cells are considerably more vulnerable than interphase cells. Usually they are destroyed during illumination at high laser power even after short measurement times.

When bleaching only a small region inside the nucleus two equilibration processes take place in the cell: first, fluorescence levels are equilibrated inside the nucleus. Subsequently the ratio of fluorescence levels between nucleus and cytoplasm is re-established. Mixing within the nucleus is generally completed within the first two images, i.e. within 2.5 s to 5 s. This demonstrates, in accordance with previous FRAP studies, that EGFP diffuses freely within both compartments[136] [135] [141] [142] [143] [144]. In contrast to intranuclear mixing, equilibration between cytoplasm and nucleoplasm takes considerably more time (see Fig. 5.11). The same tendency was observed by Wei et al.[140] for EGFP in COS7 cells. When bleaching the complete nucleus, only the second equilibration process is visible, of course. In 1975 Paine et al.[145] discovered that

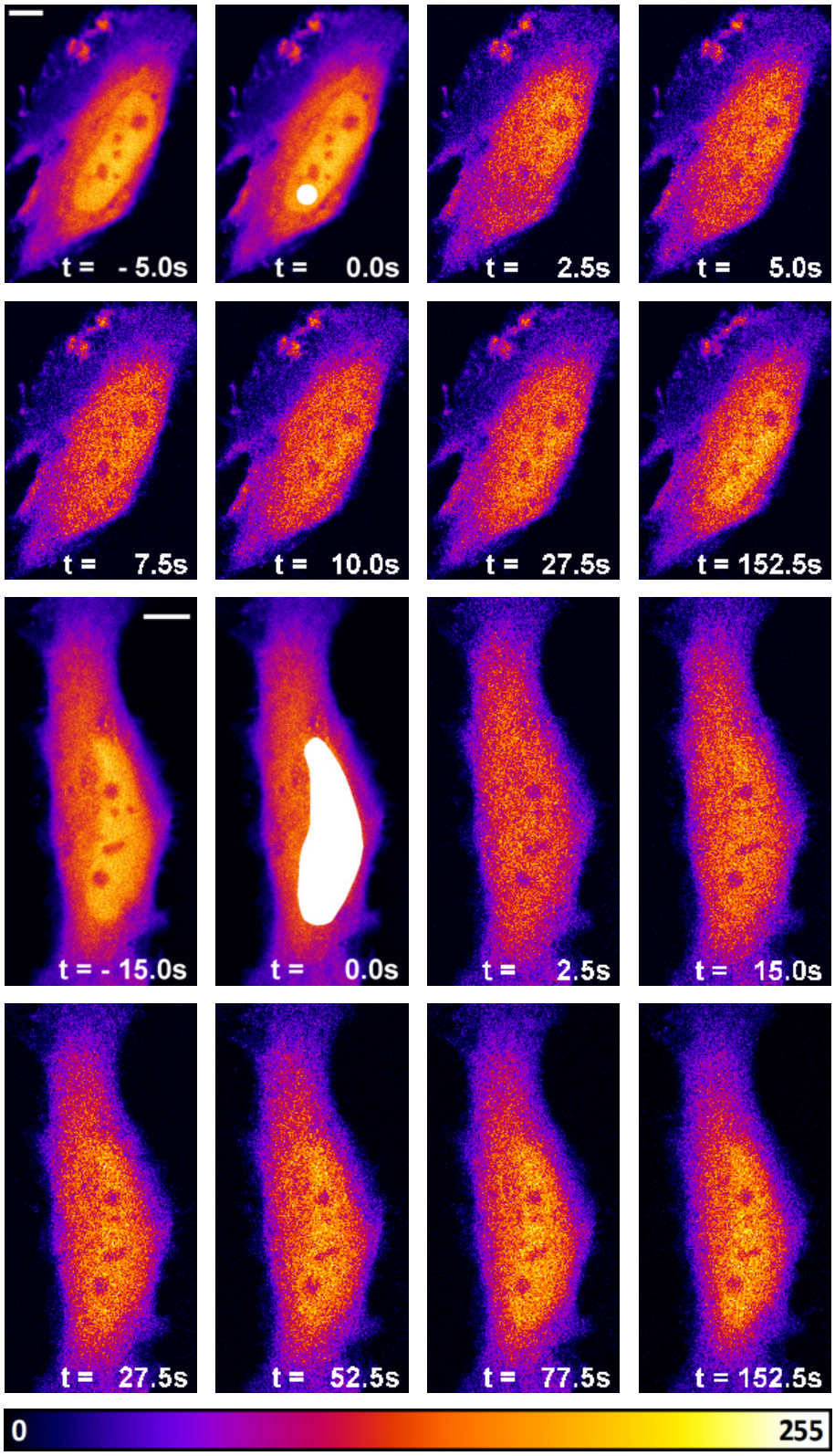

Figure 5.11: False colour images of FRAP series. 1st and 2nd row: only a small, circular ROI (white) is bleached. Equilibration within the nucleus is accomplished in less than 10 s. Restoring the initial ratio of fluorescence levels between compartments takes much longer. 3rd and 4th row: in order to avoid additional effects by intranuclear equilibration the whole nucleus (white) is bleached. Scalebar 10 µm.

the nuclear envelope is a substantially more effective transport barrier than cytoplasm of similar thickness is. Thus transit through the nuclear membrane constitutes the rate limiting factor in diffusion between both compartments. Although Paine et al. demonstrated this for the diffusion of dextran in *Rana pipiens* oocytes, the nuclear envelope ultrastructure is conserved extraordinarily even among phylogenetically distant species[145]. Moreover, similar results were found for a number of different tracer molecules and cell types in more recent studies: Mohr et al.[146] describe that passive translocation through nuclear pore complexes is slowed down at least 10-fold for GFP-sized proteins in HeLa cells. In contrast to that, according to Guigas et al.[59] diffusion of gold nanoparticles in the nucleoplasm and cytoplasm of HeLa cells differs only by a factor < 2. Ribbeck et al.[147] claim that passive diffusion through NPCs is fast for small molecules, but becomes restricted and inefficient as the diffusing objects approach a size limit of 20 kDa to 40 kDa, with 27 kDa-sized EGFP lying well within this range. Timney et al.[148] state that NPCs in *Saccharomyces cerevisiae* form a soft barrier to passive diffusion that intensifies gradually with increasing molecular mass – a tendency that was also described by Paine et al.[145] for *Rana pipiens*. Wei et al.[140] found that diffusion is slowed down 100-fold at the nuclear envelope boundary compared to diffusion within the nucleus or cytoplasm in COS7 and HEK 293 cells. So both compartments have been mixed well long before equilibration between nucleus and cytoplasm takes place.

While fluorescence equilibration by diffusion within a compartment after bleaching events is usually described by an infinite series solution[108], fluorescence recovery in the nucleus represents restricted diffusion between two well-mixed compartments. Thus recovery kinetics is strongly influenced by the nuclear membrane's permeability properties due to a finite number of nuclear pore complexes. According to Svoboda et al.[149] and Majewska et al.[150] this kind of fluorescence kinetics can be described by a single-exponential decay. If, however, protoplasmic diffusion significantly affected nuclear entry, a higher order equation would be necessary to describe fluorescence recovery/loss. The greater the influence of such intracompartmental diffusion, the worse a single exponential can describe nucleocytoplasmic tracer movement. The same, of course, holds true for replacement of immobilized bleached molecules.

Indeed, a monoexponential fit function is well-suited for reproducing fluorescence recovery in the nucleoplasm and fluorescence loss in the cytoplasm of HeLa cells after bleaching the complete nucleus. Fluorescence loss in the cy-

toplasm and fluorescence recovery in the nucleoplasm were fitted independent of each other with the single exponential function

$$F_{norm,comp}(t) = F_{norm,comp}(\infty) + A_{comp} \cdot \exp\left[-\frac{t}{\tau_{comp}}\right]. \tag{5.13}$$

In this equation τ_{comp} is the characteristic time scale of recovery, A_{comp} is the intensity of the mobile fraction of molecules, $F_{norm,comp}(\infty)$ denotes the fluorescence level in the respective compartment long after the bleaching event. $F_{norm,comp}(t)$ is the sum of all pixel values inside the respective compartment, normalized on the fluorescence emitted by the complete cell:

$$F_{norm,comp}(t) = \frac{F_{comp}(t)}{F_{cell}(t)} = \frac{\sum_{comp} I_{pixel}(t)}{\sum_{cell} I_{pixel}(t)}. \tag{5.14}$$

Of course, after normalizing the fluorescence signal per compartment on the whole cell's fluorescence, compartment-wise analysis of time scales of fluorescence kinetics might seem redundant. After all, loss of fluorescence in one out of two compartments must necessarily equal fluorescence gain/recovery in the other compartment. Therefore, time scales should automatically be the same in both compartments. However, due to experimental constraints such as bleaching of a large fraction of the cell's volume as well as limitations of the measurement setup, normalization of the fluorescence signal prior to analysis cannot be avoided. Nevertheless, successful fitting of both fluorescence loss and recovery serves as a control. Obtaining the same results in both fit processes confirms the fact that the whole process can, indeed, be described by a single exponential fit function.

Half times $t_{1/2,comp} = \ln 2 \cdot \tau_{comp}$ of fluorescence kinetics were found to be virtually the same in both compartments of individual cells: although half times varied significantly between cells ($\langle \tau_{1/2,both} \rangle = (51 \pm 21)\,\mathrm{s}$ for both compartments), the difference between compartments in the same cell was on average only $\left\langle \left| \frac{\tau_{1/2,nuc} - \tau_{1/2,cyto}}{\tau_{1/2,nuc}} \right| \right\rangle = (0.38 \pm 0.34)\,‰$.

It must be noted that corresponding half times in both compartments do not completely exclude the possibility of an immobile fraction of EGFP in the nucleus. Fluorophores bound to a nuclear constituent could, of course, gradually be exchanged by fluorophores in the mobile fraction. However, the time scale of this replacement process would have to be close to the time scale of membrane translocation or much faster to be completely masked in fluorescence recovery curves. It stands to reason to assume that the characteristic

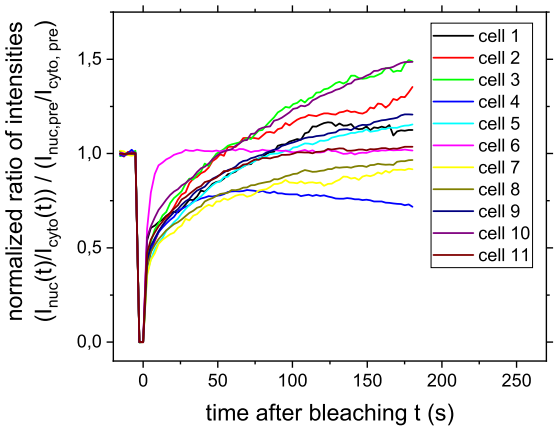

(a)

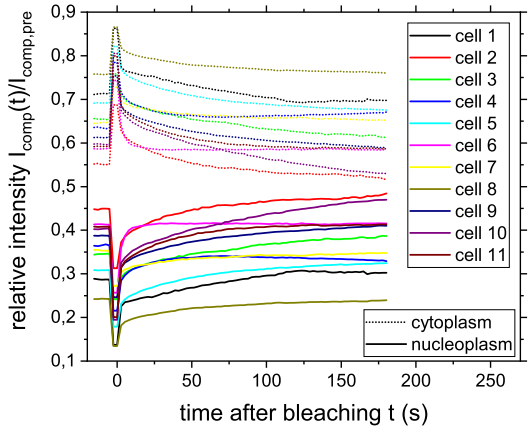

(b)

Figure 5.12: Evolution of fluorescence intensities during FRAP experiments. (a) Relative ratio of fluorescence intensities in nucleoplasm and cytoplasm, normalized on initial ratio. (b) Relative nucleoplasmic and cytoplasmic fluorescence intensity, normalized on total cellular intensity.

time scale of replacement should be the same in all cells. However, depending on nucleus size and shape, half times of fluorescence recovery and loss varied considerably throughout the investigated cell ensemble (see appendix A). While this variation would be expected for recovery/loss purely depending on diffusion, it excludes substitution of immobile EGFP at the time scale of membrane translocation events. Substitution at a much faster time scale also appears questionable. Moreover, the initial ratio of fluorescence intensities between nucleoplasm and cytoplasm is in most cases re-established within 3 min after bleaching, which can be seen when plotting the evolution of either compartment-wise intensities (see Fig. 5.12a) or the ratio of compartment-wise

intensities (see Fig. 5.12b) relative to pre-bleaching levels. Hence, there is no indication for an immobilized EGFP pool leading to an elevated nuclear fluorescence.

So, in accordance with the initial assumptions, differences in fluorescence intensities are very likely to be caused by differences in crowding levels between the compartments. In view of the fact that illumination and detection settings necessarily have to be the same for both compartments within one cell, the ratio r of mean fluorescence intensities I_{comp} between both compartments can serve as an estimate for the ratio of average accessible volume fractions ϕ_{comp}:

$$r = \begin{cases} \frac{I_{nuc}}{I_{cyto}} = \frac{\phi_{nuc}}{\phi_{cyto}} & \text{for interphase,} \\ \frac{I_{spin}}{I_{per}} = \frac{\phi_{spin}}{\phi_{per}} & \text{for metaphase.} \end{cases} \tag{5.15}$$

The indices *nuc*, *cyto*, *spin* and *per* indicate nucleus, cytoplasm, spindle and spindle periphery, respectively.

Basically there are two ways of determining mean fluorescence intensities per compartment: either selecting the complete compartment and calculating its average pixel value, or selecting a number of small ROIs inside a compartment and calculating their average pixel value. The advantage of calculating the mean of a complete compartment lies in the fact that no information gets lost during averaging. However, this method has some flaws that are difficult to avoid: especially in interphase cells it is often difficult to discern the cell boundary. Interphase cells are of a roughly triangular, trapezoid or spindle-like shape with a centre thickness of several 10 µm. However, cell thickness decreases considerably towards the border of a cell attached to the surface of a culture dish. Consequently this border region contains comparatively few fluorophores. Thus it appears dull and has only a low contrast to the background. Moreover, this decrease in section thickness and fluorescence levels might have a negative impact on analysis results as there is no way to use the photomultiplier's dynamic range optimally in dull border area and the bright centre at the same time. An additional aspect is the fact that HeLa cells are epithelial cells most suitably grown in a nearly confluent monolayer. If two cells with similar expression levels of EGFP grow in close proximity, it can be hard to discern where exactly the cell membranes are. A similar problem arises at the nuclear boundary: in general the nucleus can easily be identified

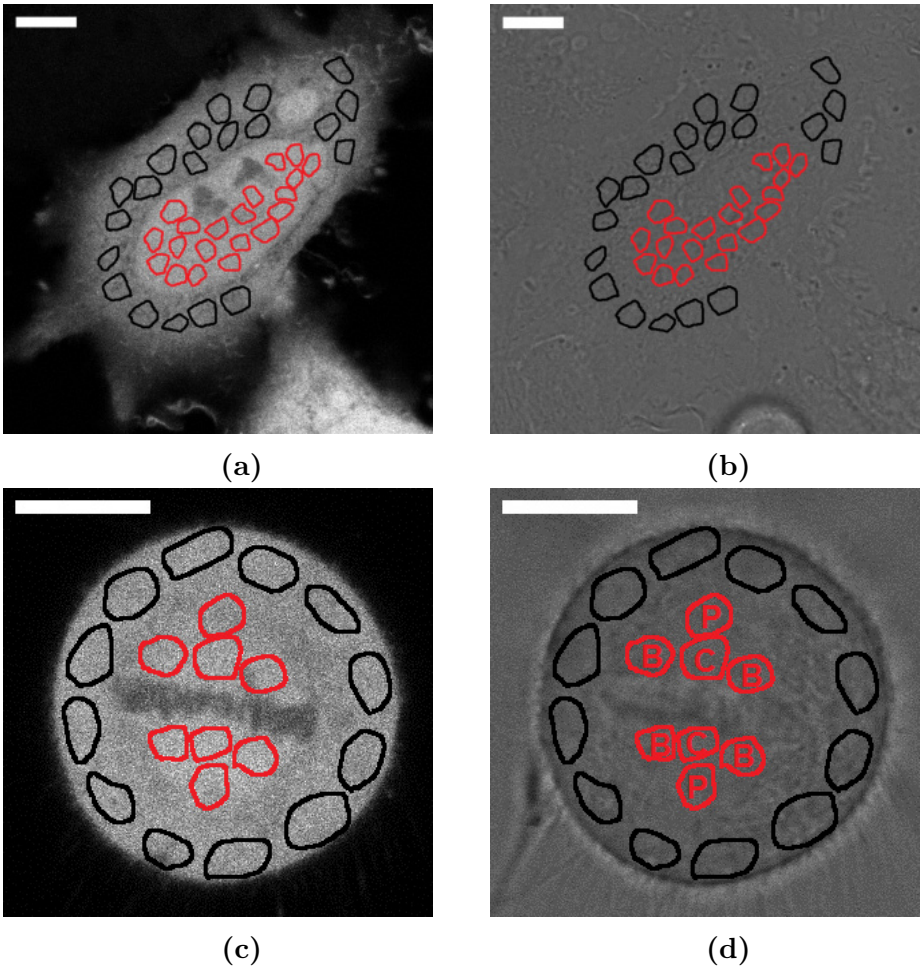

Figure 5.13: Distribution of ROIs selected in HeLa cells. (a) Fluorescence and (b) Transmission image of interphase cell. 20 ROIs per compartment (red: nucleus, black: cytoplasm) are selected for further analysis. Within the compartments, ROIs are selected randomly in a way that no structure visible to the naked eye lies within a ROI. (c) Fluorescence and (d) Transmission image of metaphase cell. 8 ROIs in the spindle (red) and 12 ROIs in the spindle periphery (black) are selected for further analysis. Selection of ROIs always follows the pattern shown in this image. P, C and B in (d) signify pole, centre and border positions used in spatially resolved analysis of spindle region. Scalebar 10 µm.

in interphase cells. It is, however, error-prone to select the exact location of the nuclear membrane at the resolution reached in the given setup. Due to the cells' circular shape it is easy to recognize the boundary between cell and background in metaphase cells. Once again, however, it is hard to locate the exact border between spindle area and periphery. Moreover, it is a matter of debate whether such a 'hard' border actually exists.

However, in interphase cells as well as in metaphase cells it is no problem to identify smaller subregions clearly located in one of the two compartments. Therefore, in order to analyse mean crowding levels in cellular compartments, only small subregions were selected that could be assigned to one of the com-

partments without any doubt. Due to cell geometry 20 ROIs were chosen both in nucleoplasm and cytoplasm in all interphase cells. In metaphase cells 8 ROIs were selected inside the spindle region and 12 ROIs in the periphery (Fig. 5.13). All regions were selected by hand with a custom MATLAB routine. During selection special attention was given to choose regions that met the following standards: they were completely inside the respective compartment and did not feature any conspicuous large structure (such as nucleoli in interphase nuclei, DNA in metaphase spindles). In addition to that they well represented the cell (i.e. no conspicuously bright or dull regions) and were of roughly the same size (usually $20 - 25$ pixels squared).
Subsequently the average fluorescence of the complete ensemble of ROIs in one compartment of one cell was calculated. Average values per compartment were compared within the same cell by building the ratio r of both compartments according to Eq. 5.15. Finally, ratios per cell could be compared within the cell ensemble.

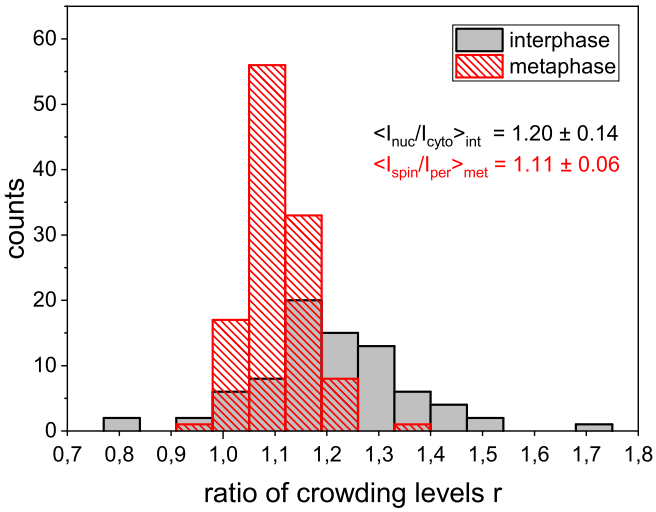

Figure 5.14: Ratio of overall crowding levels in interphase and metaphase cells. 79 interphase cells and 116 metaphase cells were recorded. Ratios calculated according to Eq. 5.15. Angle brackets signify ensemble averages ± ensemble standard deviations.

Plotting the distribution of fluorescence ratios (see Fig. 5.14) reveals the accessible volume fraction for EGFP to be about 20 % higher in the nucleoplasm than in the cytoplasm.
At first glance this might seem counter-intuitive due to the nucleus being densely packed with decondensed chromatin. But it confirms the results previously found by Guigas et al.[59]. While analysing the diffusion of inert gold

nanoparticles in cellular protoplasm by means of FCS they observed slight differences in diffusion characteristics between cytoplasm and nucleoplasm. In their measurements the anomaly factor α for subdiffusive behaviour was consistently smaller in the cytoplasm than in the nucleoplasm. The anomaly factor α was established by Weiss et al.[48] to be a measure for crowding levels. In a series of FCS experiments in cells and dextran solutions, as well as by means of simulations, they showed that low anomaly factors α indicate high levels of macromolecular crowding and vice versa. Moreover they were able to show that treatments to disrupt intracellular architecture on the scale of 100 nm to several micrometres do not alter the subdiffusive nature of cytoplasmic passive transport.
In accordance with these results we can state that crowding levels appear to be higher in the cytoplasm than in the nucleoplasm of physiological HeLa cells. Most likely this can be attributed to the presence of organelles in the cytoplasm. Membrane-enclosed organelles can be expected to be completely excluded for small molecules, thus already constituting a comparatively large excluded volume fraction in itself. Moreover, according to Nguyen et al.[151] a large fraction of proteins is found almost exclusively in the cytoplasm. Thus rise is given to a more dense packing of the cytoplasm than the nucleoplasm. So a higher excluded volume fraction is more probable in the cytoplasm than in the nucleoplasm.

Comparing spindle region and spindle periphery metaphase cells, similar to interphase cells, display differences in fluorescence levels, and, consequently in crowding states. Comparing both "compartments" in one cell and plotting the ensemble distribution of both ratios, we find the accessible volume fraction for EGFP to be about 10 % higher in the spindle region than in the spindle periphery. This hints at a continued zoning of former nucleus and former cytoplasm even after nuclear envelope breakdown.
Although there is no evidence for a physical barrier between spindle and spindle periphery, cellular constituents do not mix freely throughout the cell but remain separate, at least partly. This is especially true for large intracellular constituents such as organelles. As shown in Fig. 2.3 many organelles are located solely in the spindle periphery during mitosis. Only some structures, such as Golgi apparatus and nuclear envelope, fragment and subsequently spread in the complete cell. Considering these very characteristic and widely conserved localization patterns of various organelles during mitosis, it appears justified to

regard spindle and spindle periphery as separate compartments with distinct crowding levels although they lack a separating membrane.
Indeed it was proposed in previous studies that some form of compartmentalization remains even after nuclear envelope breakdown: the mitotic spindle matrix as a distinct biochemical milieu that differs considerably from the surrounding spindle periphery was suggested as early as 1967[152]. Initially it was thought to be a stationary substrate that stabilizes the spindle[153]. Recent studies suggest a more dynamic spindle matrix: after the nuclear envelope being - at least in part - recycled into the ER, the ER could serve as an organelle exclusion envelope[115] [154] similar to that reported in *Drosophila melanogaster*[155]. While the sheet-like mitotic ER cannot be considered to be a general diffusion barrier such as the interphase nuclear envelope, a simple size-exclusion barrier was proposed to be sufficient to maintain spatial differences in obstacle concentration even after nuclear envelope breakdown[36] [156]. Similar results were reported for *Caenorhabditis elegans* embryos[157].
Nevertheless it must be stressed that at least some mixing of former nucleoplasm and cytoplasm does take place after nuclear envelope breakdown: the mean ratio of crowding levels in both compartments is closer to unity for metaphase cells ($\langle r \rangle_{met} = 1.11 \pm 0.06$) than for interphase cells ($\langle r \rangle_{int} = 1.20 \pm 0.15$), hinting at a more similar texture in the different parts of mitotic nucleocytoplasmic fluids than in the clearly distinct interphase protoplasms.
It is a matter of particular interest to compare absolute crowding levels in interphase and metaphase compartments. This procedure could help to find out whether the pronounced change in ratios of crowding levels between compartments is completely caused by partial mixing of both types of protoplasm after nuclear envelope breakdown. This change in ratios could also be caused by changes in overall cell volume. However, it was not possible to extract absolute crowding levels with the method described above. Artefacts such as bleaching, phototoxicity and rapid evaporation of immersion and imaging media prevented monitoring the same cell in interphase and metaphase with the available setup.

5.5 Heterogeneity of Crowding States on Intermediate Lengthscales

When looking at ensemble distributions of crowding ratios in interphase and metaphase cells (see Fig. 5.14), apart from different mean ratios another characteristic trait attracts attention. For both cell cycle phases a large number of cells was recorded (79 interphase cells, 116 metaphase cells) to satisfy statistics. The distribution of interphase crowding ratios is, however, much broader than that of metaphase crowding ratios: although mean crowding ratios differ by less than 10 %, the standard deviation of crowding ratios in interphase cells is almost 2.5 fold larger than the standard deviation in metaphase cells. This shows that the ratio of fluorescence levels between both compartments varies much more in interphase cells than in metaphase cells. This, in turn, hints at a higher heterogeneity of crowding levels in at least one of the interphase compartments.

It is possible that cell ensembles feature a significant cell-to-cell heterogeneity of crowding levels. Due to restrictions stemming from the analysis method itself, it is, however, not possible to investigate cell-to-cell variations in absolute crowding levels. In order to do this, images of cells would have to be acquired at exactly the same illumination and detection settings. In principle it is possible to define a set of standard instrument settings and select only cells fitting the conditions for imaging. But it cannot be guaranteed that standard instrument settings really produce exactly the same measurement conditions. This is especially true when imaging is performed on several days of measurement. As a result of highly diverse transfection and protein expression levels, it is not possible to find a statistically relevant number of cells suitable for image acquisition with exactly the same instrument settings in one sample. So only the intracellular spatial heterogeneity of crowding levels can be analysed in this work.

A simple way to get a first clue about a possible intracellular spatial heterogeneity of crowding is a mere looking at images of HeLa cells transfected with free EGFP (see Fig. 5.10a and Fig. 5.10b). Apart from their overall fluorescence levels metaphase cells do not seem to display any marked differences between spindle region and spindle periphery. In contrast to that, interphase cells do: in most interphase cells the cytoplasm does not only appear darker than the nucleoplasm but also displays a much more speckled pattern of brighter and duller areas. Fluorescence in the nucleus appears much more homogeneous.

In order to quantify intracellular compartment-wise heterogeneity levels on an intermediate lengthscale, i.e. on a lengthscale of several micrometres, the previously introduced coefficient of variation (see Eq. 5.1) was used. To this end, again the $n = 20/12/8$ ROIs per compartment were used that had been selected to calculate the overall crowding state per compartment. Inserting the average $\langle \mu_{ROI} \rangle$ and standard deviation $\sigma(\mu_{ROI})$ of all mean intensities per ROI μ_{ROI} obtained in the same cell into Eq. 5.1 renders the ROI-to-ROI heterogeneity η_{comp} of a specific compartment *comp*:

$$\eta_{comp} := \eta(\mu_{ROI}) = \frac{\sigma(\mu_{ROI})}{\langle \mu_{ROI} \rangle} = \frac{\sqrt{\frac{1}{n-1} \sum_{i=1}^{n} (\mu_{ROI,i} - \langle \mu_{ROI} \rangle)^2}}{\frac{1}{n} \sum_{i=1}^{n} \mu_{ROI,i}}. \tag{5.16}$$

Thus cell-wise ROI-to-ROI heterogeneities can be calculated for all compartments. It must be stressed that these intermediate lengthscale heterogeneities can be considered to be absolute heterogeneities. Fluorescence intensities are governed by cellular fluorophore concentration as well as illumination and detection settings. However, all settings are conserved for the ROIs in one cell. Furthermore, both, mean value $\langle \mu_{ROI} \rangle$ and standard deviation $\sigma(\mu_{ROI})$, depend on fluorescence intensity in the same way. So imaging-dependent prefactors cancel out in the intermediate lengthscale heterogeneity per compartment η_{comp}, leaving only the sample-inherent heterogeneity.

Yet, a lower threshold should be defined below which heterogeneities are considered to be insignificant. The relative standard error of individual regions' mean fluorescence intensities $s_{ROI} = \frac{\sigma_{ROI}(I)}{\sqrt{N}\mu_{ROI}}$ can serve as a first estimate for this lower threshold. In this expression, $\sigma_{ROI}(I) = \sqrt{\frac{1}{N-1} \sum_{i=1}^{N} (I_i - \mu_{ROI})^2}$ denotes the pixel-wise standard deviation of intensity values of a ROI consisting of N pixels. Although there is some variation between compartments (exact values are given in appendix A), mean and median standard errors are close to 1 % for all compartments and cells. So intermediate lengthscale heterogeneities in cells exceeding a level of 1 % could be classified as significant. Another way of estimating a lower boundary is repeating the analysis method described above for measurements obtained in homogeneous samples. To this end images of varying concentrations of Alexa488 dissolved in MilliQ water were taken and evaluated. The mean heterogeneity of homogeneous samples obtained in this way was $\eta_{Alexa488} = (1.78 \pm 0.59)\,\%$. This percentage is slightly larger but still consistent with the first estimate. So 2 % was chosen to be the

lower threshold above which heterogeneities obtained in cellular compartments are considered to be significant.

One might ask why a spatial heterogeneity would exist at all in homogeneous samples at the given lengthscale. After all, fluorophore solutions should strive for a homogeneous distribution of fluorophores and solvent molecules according to the laws of diffusion. Moreover, fluorophore solutions were thoroughly vortexed immediately before measurements. Imaging was completed before any significant sedimentation of fluorophores was likely to occur. Although Alexa488, which in this case is attached to dextran, might form aggregates of several molecules, the rather small size of 10kDa-dextran [158] makes an influence of aggregation on the observed lengthscale rather unlikely - after all, a single voxel describes a volume of $(100\,\mathrm{nm})^3$. It is more likely that the measured inhomogeneities in homogeneous samples are caused by the measurement process itself. As described in Sec. 5.3, measured pixelwise intensities depend on instrument settings as well as on statistical effects of detection instruments. Taking into consideration that also excitation illumination might fluctuate minutely, it stands to reason that homogeneous samples display a measurable - albeit small - heterogeneity.

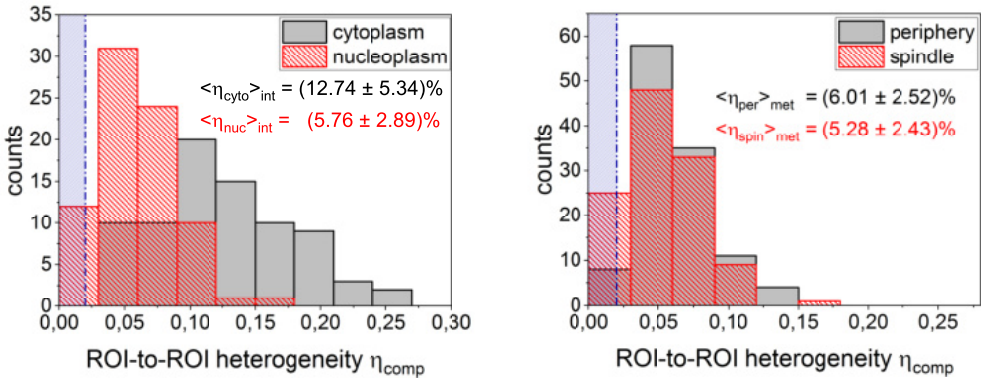

(a) **(b)**

Figure 5.15: ROI-to-ROI heterogeneities of available volume fractions. (a) Results of 79 interphase cells. (b) Results of 116 metaphase cells. Lower significance level (blue) obtained by evaluation of fluorophore solutions. Angle brackets signify ensemble averages ± ensemble standard deviations.

With regard to the established lower boundary of 2 % all mean heterogeneities per compartment and even the vast majority of cellular heterogeneities are significant: intermediate lengthscale heterogeneities range from 0 % to 20 % for nucleoplasm, spindle and spindle periphery. Cytoplasmic heterogeneities can reach even higher levels in a few cases. The respective distributions as well

as all ensemble means and standard deviations are shown in Fig. 5.15. Confirming the visual impression from fluorescence images (see Fig. 5.10a), the cytoplasm is, indeed, much more heterogeneous than the other compartments: with an average intermediate lengthscale heterogeneity of $(12.7 \pm 5.3)\,\%$ its heterogeneity level is about twofold higher than that of other compartments. This can be explained in terms of intracellular architecture and composition: while the nucleus is densely packed with DNA and other (macro)molecules, the diversity of molecule species is considerably higher in the cytoplasm[159]. Considering the size-distribution of objects populating the cytoplasm, we can also expect it to have a more complex organization than the nucleoplasm, most probably on several length scales. Regarding this complex multi-scale nature of intracellular architecture it is not surprising to find a higher ROI-to-ROI heterogeneity in the cytoplasm: bigger organelles such as the Golgi cannot be distinguished faithfully in HeLa cells transfected with free EGFP, but can, in principle, constitute much of an individual evaluation ROI. So ROIs containing much of a big organelle would appear considerably darker than ROIs containing primarily cytosol.
As anticipated from visual impressions, crowding heterogeneities in metaphase are virtually the same in both compartments (Fig. 5.15b). One could argue that, similar to interphase cells, crowding is somewhat more heterogeneous in the spindle periphery than in the spindle itself. This would be completely reasonable since, similar to interphase cells, the majority of organelles is located in the spindle periphery whereas the spindle itself features mostly smaller structures. However, measured heterogeneity levels are as high as 2 % even in homogeneous samples. So the difference in heterogeneity levels between both compartments can hardly be considered to be significant. Moreover, the distributions of compartment-intrinsic heterogeneities are quite similar. So we can conclude that crowding heterogeneities are the same in spindle as well as in spindle periphery, despite their different overall crowding levels.
Peculiarly, the average heterogeneity levels of nucleoplasm, spindle and spindle periphery are nearly the same.

Finally, with regard to results obtained by Pawar et al.[82], an attempt was made to analyse a possible pattern of heterogeneity levels inside the spindle region. Pawar et al. performed spatially resolved FCS measurements parallel and perpendicular to the spindle axis of mitotic cells. They found that macromolecules display an anisotropically varying diffusion characteristics inside the

spindle region. With diffusion being less anomalous along the spindle axis, as compared to perpendicular directions, diffusion along the spindle axis is clearly favoured.

In an attempt to mimic their experiments with an imaging approach, ROIs inside the spindle were selected according to the pattern shown in Fig. 5.13. To ensure comparability of all individual measurements, all fluorescence intensities per ROI μ_{ROI} in one cell were normalized by this particular cell's average fluorescence intensity inside the spindle region $\langle \mu_{ROI} \rangle_{spin}$. Then ROIs were sorted according to their relative position in the spindle, to be more precisely, their position near spindle centre, spindle border or spindle pole (see Fig. 5.13d).

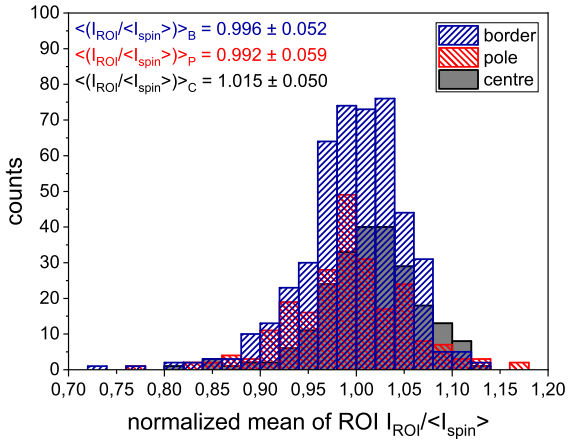

Figure 5.16: Spatially resolved analysis of the spindle region Relative mean fluorescence values per ROI μ_{ROI}/μ_{spin} sorted according to their relative position within the spindle. Result of 116 metaphase cells. Angle brackets signify ensemble averages ± ensemble standard deviations.

As can be seen in Fig. 5.16 these relative fluorescence intensities display rather similar distributions within the cell ensemble. So on the ROI-to-ROI lengthscale, none of the three positions investigated can be viewed to be more or less crowded than the rest of the mitotic spindle. One might argue that the centre position, which seems to have a slightly higher intensity, might be less crowded than the pole and border positions. After all, at least the density of spindle microtubules is lower in the spindle centre than close to the spindle poles. In addition to that, crowding at the spindle centre would be less influenced by objects in the spindle periphery than crowding at pole or border positions. It is, however, open to dispute whether the slightly higher average of relative fluorescence intensity at the spindle centre can be viewed as significant, es-

pecially when taking into account the considerably high ensemble variation. After all, all ensemble means lie well within each other's standard deviations (see Fig. 5.16).

5.6 Voxel-wise Heterogeneity of Crowding States

When going beyond intermediate lengthscales we have to take account of the influence of illumination laser power and photomultiplier bias voltage on mean fluorescence values and their pixel-wise variance. So sample-inherent contributions have to be separated from setting-dependent contributions to heterogeneity values. The principle of this calculation process is displayed in Fig. 5.17. It is based on simulation results obtained in chapter 5. As shown in Sec. 5.3.3 the relation between pixel-wise variance $\sigma^2_{ROI}(I)$ and mean value $\mu_{ROI}(I)$ can be described as

$$\sigma^2_{ROI}(I) = \xi^2(\mu_{ROI}(I) + A^2\sigma^2_{ROI}(\varphi)) = \xi^2(A\varphi_{0,ROI} + A^2\sigma^2_{ROI}(\varphi)). \quad (5.17)$$

Here $\mu_{ROI}(I) = A\varphi_{0,ROI} = A\mu_{ROI}(\varphi)$ is determined by the local mean accessible volume fraction φ. $A^2\sigma^2_{ROI}(\varphi)$ reflects its local spatial variation. Due to experimental constraints the instrument settings and, consequently, the multiplicative factor ξ^2 could not be held constant for all measurements. Trivially, however, all instrument settings remain the same for all ROIs within one image. So ξ^2 and A are constant for all ROIs in the same image. What is more, assuming a Gaussian distribution of the local accessible volume fraction, $A^2\sigma^2_{ROI}(\varphi)$ can be expected to deviate randomly and unbiasedly from the mean over all ROIs in the same sample. So the unknown prefactor ξ^2 can be obtained by fitting the data pairs $(\mu_{ROI}(I), \sigma^2_{ROI}(I))$ of all ROIs in the same compartment of the same cell with a linear function

$$\sigma^2_{ROI}(I) = \xi^2_{fit} \cdot (\mu_{ROI}(I) + \beta_{fit}). \quad (5.18)$$

The scaled offset β_{fit} reflects the average local heterogeneity of the accessible volume fraction, $\beta_{fit} = \langle A^2\sigma^2_{ROI}(\phi)\rangle_{ROIs}$. The factor A includes parts dependent on the setup as well as parts dependent on crowding. The general prefactor ξ^2_{fit}, however, is only determined by measurement settings. As both compartments are necessarily imaged at the same illumination and detection

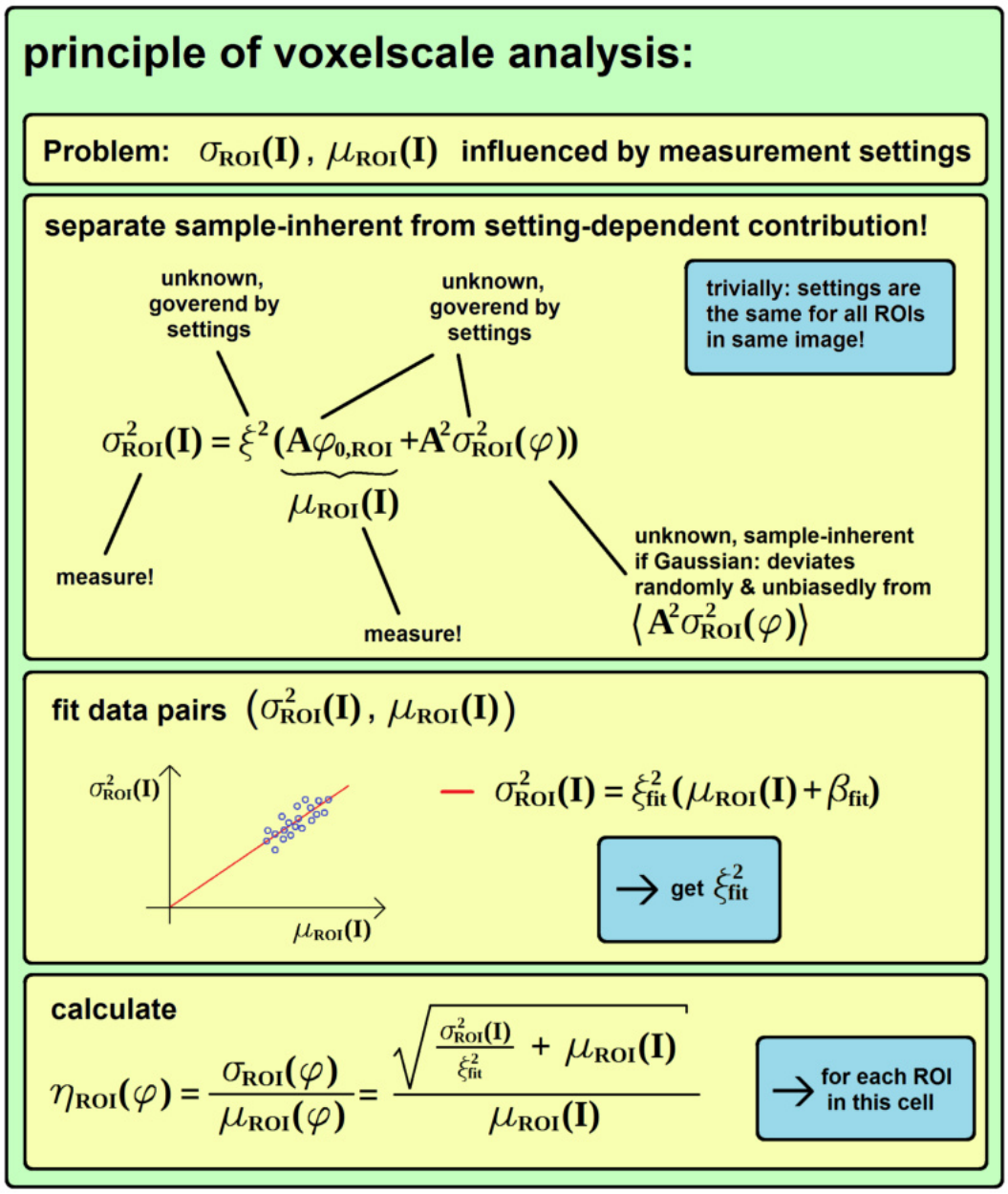

Figure 5.17: Principle of voxelscale analysis. Sample-inherent and setting-dependent contributions to pixel-wise heterogeneity of intensity values have to be separated in order to obtain the voxel-wise heterogeneity of crowding states.

settings, it is sufficient to fit only the data pairs of one compartment and to use the fit results for further evaluation of both compartments of the same cell. Due to geometric reasons, in metaphase cells the number of ROIs selected in both compartments was not the same. In order to achieve a better fit quality the ensemble of data pairs selected in the spindle periphery was used to determine the prefactor ξ^2_{fit}. For the sake of better comparability of data evaluation the ensemble of data pairs selected in the cytoplasm was used in interphase

cells. Fitting was performed in MATLAB following the robust nonlinear least-squares method with bisquare weighing. In order to ensure good fit quality, fitting was repeated up to 8000 times. Fit quality was further controlled by the built-in MATLAB option *exitflag*, only results with positive exitflags were taken into further consideration. But for all that, results obtained in this way have to be read carefully, as, in each cell, there are only 20/12 data pairs available for fitting.
After determining the prefactor ξ_{fit}^2 and solving Eq. 5.17 for $A\sigma_{ROI}(\varphi)$ the voxel-wise heterogeneity of the accessible volume fraction can, according to Eq. 5.1, be estimated as

$$\eta_{ROI}(\varphi) = \frac{\sigma_{ROI}(\varphi)}{\mu_{ROI}(\varphi)} = \frac{A\sigma_{ROI}(\varphi)}{A\varphi_{0,ROI}} = \frac{\sqrt{\frac{\sigma_{ROI}^2(I)}{\xi_{fit}^2} - \mu_{ROI}(I)}}{\mu_{ROI}(I)}. \tag{5.19}$$

Please note that this evaluation has to be repeated for each individual cell, as experimental settings and, in consequence of this, ξ^2 and A differ from cell to cell.

Of course also in this case a lower threshold should be defined above which heterogeneity levels can be considered to be significant. For this purpose the same evaluation method was applied to data gathered in homogeneous dye solutions. Different concentrations of Alexa488 dissolved in MilliQ water were imaged under the same imaging conditions. The complete series of images was repeated for several typical measurement settings. Only images with mean fluorescence intensities (i.e. pixel values) in the range $[50, 150]$ were considered to be apt for analysis by means of fitting, because mean fluorescence values in cells usually were in that range. In order to circumvent the problems of few data pairs available for fitting, all data pairs from images taken at the same instrument settings were treated as one data set for fitting. Heterogeneity levels of the accessible volume fraction were calculated according to Eq. 5.19. Since the vast majority of calculated heterogeneity levels of homogeneous fluorophore solutions was below 3 % this value was chosen as a lower cut-off level. So intracellular heterogeneity levels on the voxel-lengthscale can be considered to be significant as soon as they exceed 3 %.

Fig. 5.18a and Fig. 5.18b display the distribution of intracellular crowding heterogeneities on the voxel-lengthscale as well as their ensemble means and

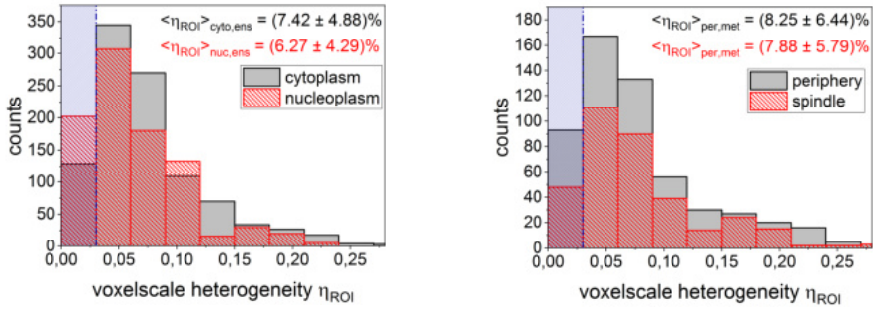

(a) **(b)**

Figure 5.18: Voxelscale heterogeneities of EGFP (a) Results of 79 interphase cells. (b) Results of 116 metaphase cells. Lower significance level obtained via evaluation of fluorophore solutions. Angle brackets signify ensemble averages ± ensemble standard deviations.

standard deviations. Most of the heterogeneity values obtained in cells are above the significance level. However, there is no apparent difference in heterogeneity levels between compartments, especially when taking into account the rather large ensemble heterogeneity. All compartments feature mean heterogeneities around 7 %. The distribution of local heterogeneity values is very similar, too. Moreover, heterogeneity levels on the voxel-scale, i.e. on the scale of a few 100 nm, do not appear to change after entry into mitosis. So the major structural changes cells undergo in the process of reproduction appear to take place either on bigger or on considerably smaller lengthscales. In addition to that, the obvious differences in protoplasmic content, most prominently those between nucleoplasm and cytoplasm, do not appear to have an impact on voxel-wise heterogeneity levels. So we can establish the average voxel-wise heterogeneity to be about 7 % in all compartments.

It should be emphasized that in contrast to heterogeneity levels on intermediate lengthscale the results for voxel-to-voxel lengthscale are quite vague. Additional fluctuations are most likely to be introduced to the method when fitting with only a small number of data pairs. Fitting was performed for one compartment only and the prefactor ξ^2_{fit} was subsequently used to evaluate the other compartment. A more accurate result might be obtained by fitting both compartments separately until a value for ξ^2_{fit} is found that is adequate to describe both data sets well. But it must be noted, though, that data sets from both compartments cannot be fitted together as the factor A does not only depend on measurement settings but also on crowding properties in the respective compartments.

Another way to roughly estimate heterogeneity levels in cellular compartments on the voxel-scale is to compare indices of dispersion between compartments. This technique has the advantage that it doesn't require data fitting. So additional uncertainties introduced via data fitting are avoided. The index of dispersion of a variable x is defined as

$$\delta(x) = \frac{\langle (x - \langle x \rangle)^2 \rangle}{\langle x \rangle} = \frac{\sigma^2(x)}{\mu(x)}. \tag{5.20}$$

Inserting the relation between variance and mean for imaging data as it was established previously, the index of dispersion for intracellular compartments becomes

$$\delta_{ROI}(I) = \frac{\sigma^2_{ROI}(I)}{\mu_{ROI}} = \xi^2 \left(1 + \frac{A\sigma^2_{ROI}(\phi)}{A\mu_{ROI}(\phi)}\right) = \xi^2(1 + \delta_{ROI}(\phi)). \tag{5.21}$$

Necessarily the setup-dependent prefactor ξ^2 is the same for both compartments of one cell. So it cancels out when taking the ratio of mean indices of dispersion per compartment of the same cell

$$\rho(I) = \frac{\langle \delta_{ROI}(I) \rangle_{nuc,cell}}{\langle \delta_{ROI}(I) \rangle_{cyto,cell}} = \frac{1 + \langle \delta_{ROI}(\phi) \rangle_{nuc,cell}}{1 + \langle \delta_{ROI}(\phi) \rangle_{cyto,cell}}. \tag{5.22}$$

In the vast majority of cells this ratio of mean dispersion indices of intensities is < 1. It is easy to show that the ratio $\rho(I)$ underestimates the ratio of mean dispersion indices of accessible volume fractions $\rho(\phi) = \frac{\langle \delta_{ROI} \rangle_{nuc,cell}}{\langle \delta_{ROI} \rangle_{cyto,cell}}$ by adding zero and rearranging the equation:

$$\begin{aligned} \rho(I) &= \frac{1 + \langle \delta_{ROI} \rangle_{nuc,cell}}{1 + \langle \delta_{ROI} \rangle_{cyto,cell}} \\ &= \frac{1 + \langle \delta_{ROI} \rangle_{nuc,cell}}{1 + \langle \delta_{ROI} \rangle_{cyto,cell}} + \frac{\langle \delta_{ROI} \rangle_{nuc,cell}}{\langle \delta_{ROI} \rangle_{cyto,cell}} - \frac{\langle \delta_{ROI} \rangle_{nuc,cell}}{\langle \delta_{ROI} \rangle_{cyto,cell}} \\ &= \frac{\langle \delta_{ROI} \rangle_{nuc,cell}}{\langle \delta_{ROI} \rangle_{cyto,cell}} + \frac{\langle \delta_{ROI} \rangle_{cyto,cell} - \langle \delta_{ROI} \rangle_{nuc,cell}}{(1 + \langle \delta_{ROI} \rangle_{cyto,cell}) \langle \delta_{ROI} \rangle_{cyto,cell}}. \end{aligned} \tag{5.23}$$

As both $\langle \delta_{ROI} \rangle_{cyto,cell}$ and $\langle \delta_{ROI} \rangle_{nuc,cell}$ are larger than one also the denominator $(1 + \langle \delta_{ROI} \rangle_{cyto,cell}) \langle \delta_{ROI} \rangle_{cyto,cell}$ exceeds unity. The experimentally obtained result $\rho(I) = \frac{1 + \langle \delta_{ROI} \rangle_{nuc,cell}}{1 + \langle \delta_{ROI} \rangle_{cyto,cell}} < 1$ implies that $\langle \delta_{ROI} \rangle_{cyto,cell} > \langle \delta_{ROI} \rangle_{nuc,cell}$, so the numerator $\langle \delta_{ROI} \rangle_{cyto,cell} - \langle \delta_{ROI} \rangle_{nuc,cell}$ is positive. Therefore in all cases the following expression holds true:

$$1 > \rho(I) = \frac{1 + \langle \delta_{ROI} \rangle_{nuc,cell}}{1 + \langle \delta_{ROI} \rangle_{cyto,cell}} > \frac{\langle \delta_{ROI} \rangle_{nuc,cell}}{\langle \delta_{ROI} \rangle_{cyto,cell}} = \rho(\phi). \tag{5.24}$$

So the ratio of dispersion indices $\rho(I)$ underestimates the real difference in voxel-scale crowding dispersion indices between compartments.

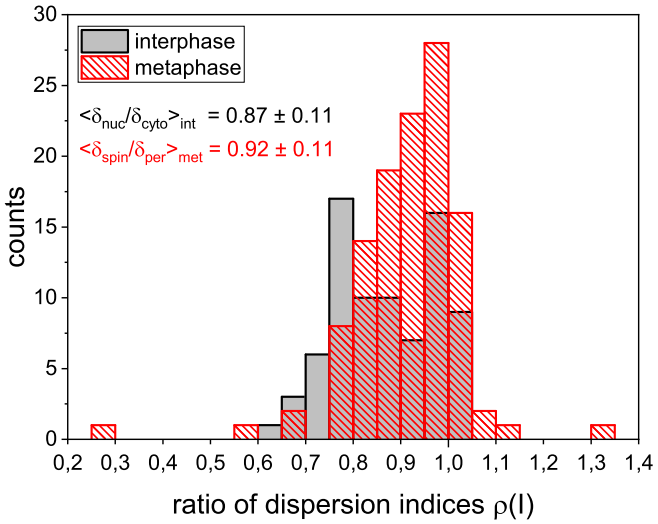

Figure 5.19: Ratio of dispersion indices ρ. Results of 79 interphase cells and 116 metaphase cells. Angle brackets signify ensemble averages ± ensemble standard deviations.

Distributions of both interphase and metaphase ratios, ρ_{int} and ρ_{met}, are shown in Fig. 5.19. The mean ratio of dispersion indices in interphase cells was found to be $\langle\rho\rangle_{int} = \langle\delta_{nuc}/\delta_{cyto}\rangle_{int} = 0.87 \pm 0.11$. In metaphase cells the ratio was found to be $\langle\rho\rangle_{met} = \langle\delta_{spin}/\delta_{per}\rangle_{met} = 0.92 \pm 0.11$. This might be interpreted as an indication that heterogeneity levels on the voxel-to-voxel scale differ between compartments as well. A considerably higher heterogeneity of crowding in the cytoplasm (as compared to the nucleoplasm) and an at least somewhat higher heterogeneity of crowding in the spindle periphery (as compared to the spindle itself) would confirm the previous results for intermediate scale heterogeneities. It must, however, be emphasized that the index of dispersion itself is not dimensionless, as opposed to the coefficient of variation that was previously used to characterize crowding heterogeneities. What is more, in imaging experiments the pixel-to-pixel variance of fluorescence intensities depends on the mean pixel value in a linear way. So the ratio of dispersion indices does not only reflect the differences in heterogeneity levels between the compartments but also their differences in fluorescence intensity levels. Remembering that our first observation was exactly that striking difference in fluorescence intensity levels between the compartments, it must be taken into consideration that the difference in heterogeneity levels is rather negligible.

Yet, the experimentally obtained ratio of dispersion indices does not equal the inverse of the ratio of mean fluorescence values. This confirms the assumption that there is, at least to some degree, a heterogeneity on the voxel-to-voxel-scale in living cells. It is, however, not possible to draw any definite conclusion whether these heterogeneities are the same in all compartments or whether they differ in some ways.

Finally, voxelscale heterogeneity values per ROI obtained in metaphase cells were sorted according to their relative position within the spindle. All values were obtained by data fitting, so any known influence of absolute intensity has already been eliminated. Thus there is no need to normalize ROI-wise heterogeneity values on the cell's mean heterogeneity value. Nevertheless, no obvious difference in heterogeneity values or distributions could be observed between spindle pole, centre and border positions (see Fig. 5.20). Since the voxelscale heterogeneity was found to be very similar in all compartments, this is no surprise.

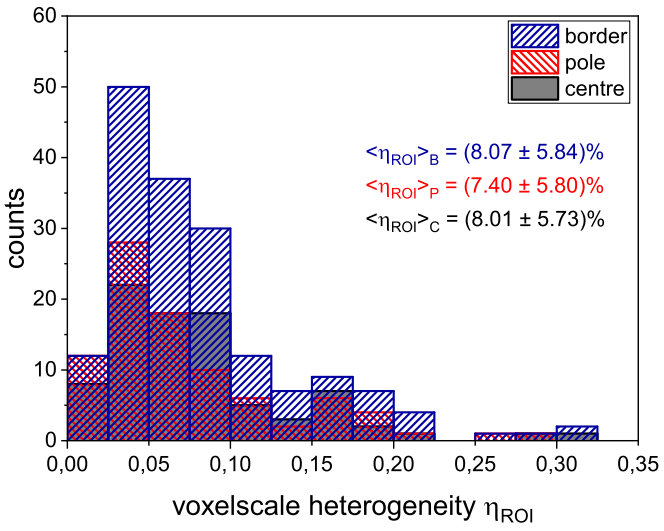

Figure 5.20: Spindle spatially resolved: voxelscale heterogeneity values per ROI. Results of 116 metaphase cells. Angle brackets signify ensemble averages ± ensemble standard deviations.

5.7 Further Characterization of Intracellular Crowding Levels

5.7.1 Intracellular Heterogeneity in Cells Without Microtubules

In order to investigate a possible influence of the cytoskeleton on intracellular heterogeneity levels, HeLa cells were treated with nocodazole (protocol see Sec. 4.3.3). This drug is known to prevent polymerization of microtubules[160]. Measurements and analysis on all lengthscales were performed following the method used in untreated cells. However, as this protocol served only as a test measurement, a much smaller ensemble of only 11 cells was investigated.

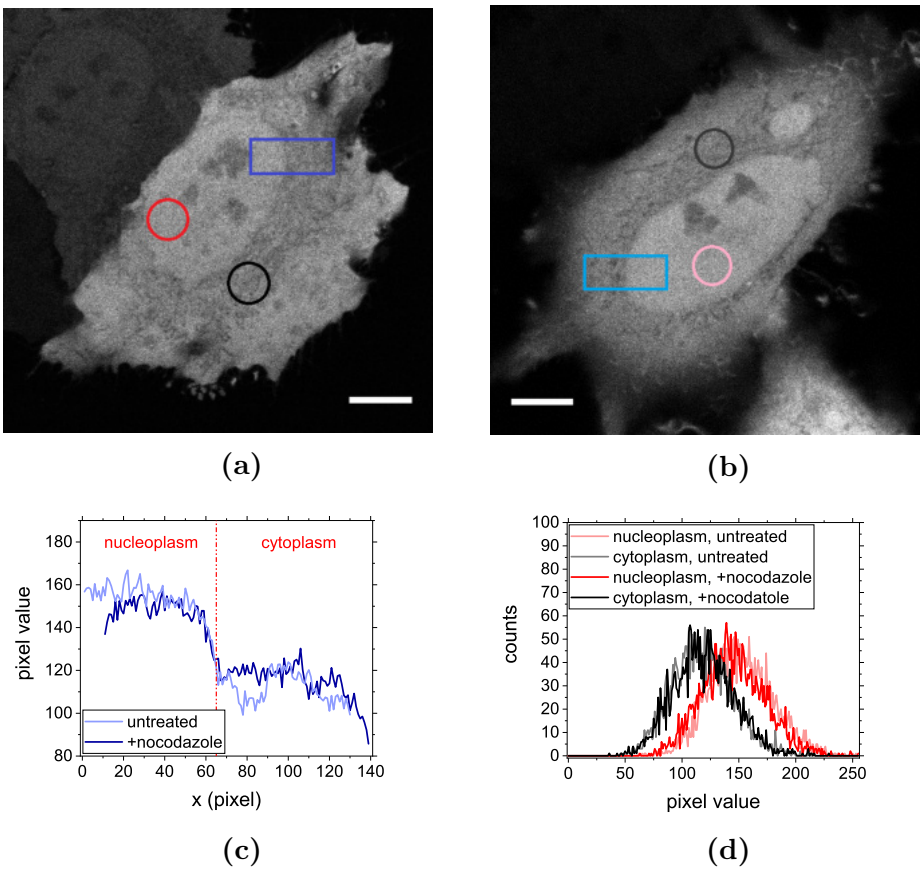

Figure 5.21: Comparison of HeLa wildtype cell and HeLa cell treated with nocodazole. (a) Cell treated with nocodazole. (b) Wildtype Cell. (c) Plotprofiles of rectangular ROIs in both images. (d) Histograms of circular ROIs in both images. Profiles are taken along horizontal direction x and averaged over all pixels in vertical direction. There are no obvious differences between both cells. Scalebar 10 µm.

An image of a cell treated with nocodazole is displayed in Fig. 5.21a. Visible to the naked eye there is no obvious difference between physiological cells (Fig. 5.21b) and cells treated with nocodazole. This first impression is confirmed when we consider the plotprofile (Fig. 5.21c) and histograms (Fig. 5.21d) of nucleus and cytoplasm. Plotprofile as well as histograms show a rather strong resemblance to those obtained in untreated cells.

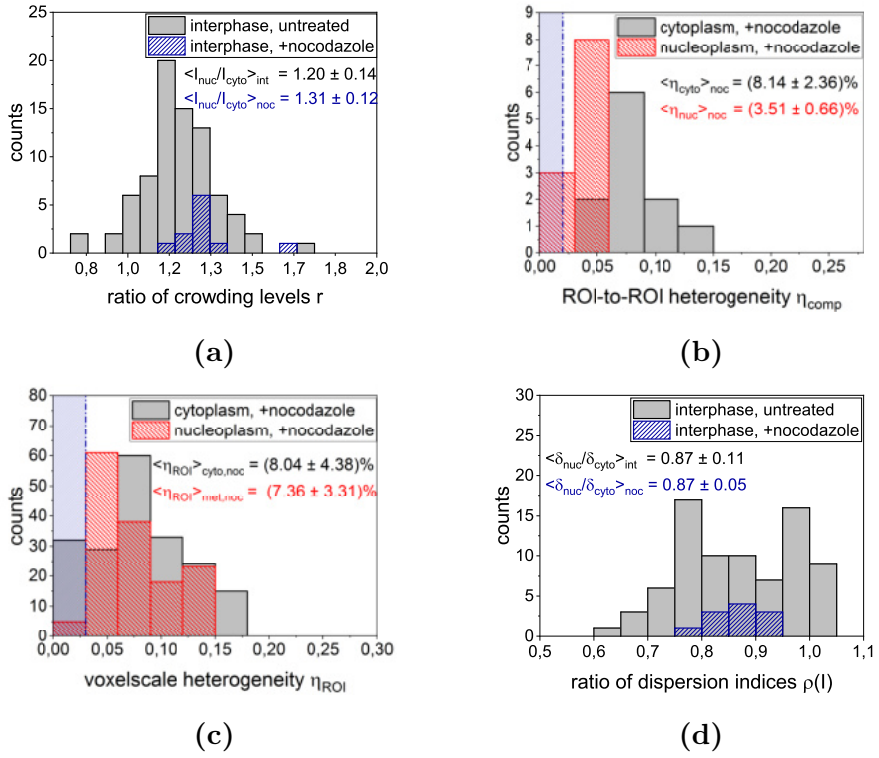

Figure 5.22: Comparison of crowding ratios and heterogeneities on all length-scales in HeLa wildtype and HeLa treated with nocodazole. Results of 79 native interphase cells and 11 interphase cells treated with nocodazole. (a) Crowding Ratios. (b) ROI-to-ROI heterogeneities. (c) Voxelscale heterogeneities. (d) Ratio of Dispersion Indices. Angle brackets signify ensemble averages ± ensemble standard deviations.

The distributions of crowding ratios as well as ensemble means and standard deviations of untreated cells and cells treated with nocodazole are displayed in Fig. 5.22a. The ratio of overall crowding levels was found to be somewhat higher in nocodazole treated cells ($\langle r \rangle_{noc} = 1.3 \pm 0.1$) than in untreated cells ($\langle r \rangle_{int} = 1.2 \pm 0.1$). This suggests that the difference in crowding levels between nucleus and cytoplasm is even more pronounced in nocodazole treated than in untreated cells, with the cytoplasm being more crowded than the nucleoplasm. However, both ratios lie within each other's standard deviations. Besides, it must be noted that in contrast to normal interphase cells, the ensemble of

nocodazole treated cells analysed was very small. So the perceived difference in overall crowding ratios might be a misconception due to the small ensemble size.

The same holds true for ROI-to-ROI heterogeneities (see Fig. 5.22b): at first glance both, distribution and ensemble mean of compartment-wise ROI-to-ROI heterogeneities, seem to differ between wildtype cells and nocodazole treated cells: in both compartments heterogeneities in nocodazole-treated cells are smaller ($\langle\eta_{cyto}\rangle_{noc} = (8.14 \pm 2.36)\,\%, \langle\eta_{nuc}\rangle_{noc} = (3.51 \pm 0.66)\,\%$) than in untreated cells ($\langle\eta_{cyto}\rangle_{int} = (12.74 \pm 5.34)\,\%, \langle\eta_{nuc}\rangle_{int} = (5.76 \pm 2.89)\,\%$), while the general tendency $\eta_{cyto} > \eta_{nuc}$ still holds true. Moreover, the ensemble distributions of heterogeneities appear to be less wide in both compartments than they are in untreated cells. In fact the histograms of nocodazole treated cells lie entirely within those of untreated cells. So, considering the small ensemble size, no definite conclusion can be drawn whether cells depleted of microtubules differ significantly in their crowding levels or crowding heterogeneities.

On the voxel-to-voxel level (see Fig. 5.22c), cells with and cells without microtubules appear to feature the same heterogeneity levels. Since interphase and metaphase cells did not show any obvious difference on that lengthscale, this is rather unlikely to be merely an effect of ensemble sizes. Interestingly there doesn't seem to be any difference between the ratio of dispersion indices in cells depleted of microtubules and in physiological cells (Fig. 5.22d). The ratio of overall crowding levels, on the other hand, which is equivalent to the ratio of mean intensities, appears to be somewhat different in both populations. This might serve as a confirmation that the ratio of dispersion indices indeed does allow drawing conclusions on differences in voxelscale heterogeneities in both compartments, even though it is not dimensionless.

Ultimately, no definite conclusion can be drawn whether the microtubule skeleton has an influence on intracellular heterogeneity levels at the investigated lengthscales or not. In order to decide whether the perceived differences in overall crowding ratios and ROI-to-ROI heterogeneities are in fact significant a large ensemble of cells treated with nocodazole would have to be measured and analysed It was decided not to include such extensive measurements into this thesis, as other aspects of intracellular heterogeneity such as FRET-based measurements and time-resolved measurements in cells exposed to stress were considered to be more promising.

5.7.2 Temporal Evolution of Intracellular Heterogeneities

In order to characterize the multi-scale intracellular heterogeneity of HeLa interphase cells in greater detail, a test measurement was performed in which the same cell was monitored for 31 min. During this period the cell was repeatedly imaged at the same imaging conditions. All analyses were performed in analogy to measurements previously described. The same ROIs were analysed at all time steps.
In addition to studying the temporal evolution of intracellular observables, their temporal heterogeneities η_t were calculated:

$$\eta_t(x) = \frac{\sigma_t(x)}{\mu_t(x)}, \tag{5.25}$$

with $\sigma_t(x) = \sqrt{\langle x^2 \rangle_{time} - \langle x \rangle_{time}^2}$ being the temporal standard deviation and $\mu_t(x) = \langle x \rangle_{time}$ the temporal mean of the observable x. The timescale of temporal heterogeneities is, of course, governed by total measurement duration and temporal resolution, i.e. the length of time increments between two subsequent images in a series.

Fig. 5.23 displays the evolution of intracellular intensity levels and heterogeneities as well as their respective ratios for two series. The first series (left column) covers a measurement time of approximately one minute, with images taken every 2.575 s. The second series (right column) covers a measurement time of 30 min at a temporal resolution of 30 s.
In both series, the intensity levels stay virtually the same throughout the course of the measurement - there is no evidence of bleaching. Consequently, there were only slight variations in the ratio of overall crowding levels. In fact its temporal heterogeneity is below 1 % for short measurement times and below 4 % for long measurement times. The rather large dip in intensities in Fig. 5.23b can be attributed to a slight focal drift, which unfortunately cannot be avoided in long term measurements with the given measurement setup. Excluding the drift region from evaluation results in the fact that the temporal heterogeneity of overall crowding ratios decreases to 1.45 %. Interestingly, the ensemble heterogeneity of interphase crowding ratios is much higher (12.34 %). So apparently the ensemble heterogeneity of overall crowding ratios in interphase cells is not caused by temporal variation. It rather seems to be a distinct feature of the cells. However, no definite conclusion can be drawn since these

measurements only cover a small fraction of HeLa cells' 24 h-cell-cycle. It would be most interesting to cover the whole cell cycle, especially in the same cell. However, due to substantial focal drift and increasing CO_2-concentration during long term measurements this cannot be achieved with the measurement setup available for this thesis.

The temporal heterogeneity of intracellular ROI-to-ROI heterogeneities is much more pronounced than the temporal heterogeneity of crowding ratios. Nevertheless it is still much lower than the ensemble heterogeneity of intracellular ROI-to-ROI heterogeneities in interphase cells. The exact values are displayed in table 5.1. Moreover, at least for short measurement times, there is no general trend in either compartment-wise ROI-to-ROI heterogeneities nor their ratio. For long measurement times there seems to be a decrease in the ratio of ROI-to-ROI heterogeneities, which can be seen even after excluding the drift part. It remains to be analysed whether this tendency is a mere side-effect of focal drift or, indeed, caused by intracellular processes. As already mentioned, it is difficult to monitor the same cell for long time periods. In order to thoroughly investigate the evolution of ROI-to-ROI heterogeneities, a large set of interphase cells of all cell cycle stages would have to be measured for periods of 30 min to 60 min. This would, however, require at measurement setup allowing to control O_2 and CO_2 levels and without suffering from focal drift.

ensemble heterogeneity interphase cells	temporal heterogeneity $\delta t = 2.575\,\mathrm{s}$, $T = 65\,\mathrm{s}$	temporal heterogeneity $\delta t = 30\,\mathrm{s}$, $T = 3\,\mathrm{min}$
$\eta_{int}(\eta_{cyto}) = 41.94\,\%$	$\eta_t(\eta_{cyto}) = 5.76\,\%$	$\eta_t(\eta_{cyto}) = 24.87\,\%$ (18.65 %)
$\eta_{int}(\eta_{nuc}) = 50.22\,\%$	$\eta_t(\eta_{nuc}) = 11.41\,\%$	$\eta_t(\eta_{nuc}) = 20.09\,\%$ (11.86 %)
$\eta_{int}(\frac{\eta_{nuc}}{\eta_{cyto}}) = 51.71\,\%$	$\eta_t(\frac{\eta_{nuc}}{\eta_{cyto}}) = 11.55\,\%$	$\eta_t(\frac{\eta_{nuc}}{\eta_{cyto}}) = 18.09\,\%$ (20.56 %)

Table 5.1: Comparison of temporal heterogeneity and ensemble heterogeneity of ROI-to-ROI heterogeneities. Values in parentheses signify temporal heterogeneities excluding the drift part.

On the voxel-to-voxel scale neither the compartment-wise heterogeneities nor their ratio show any tendency to evolve over time. This holds true for short as well as for long measurement times. There might be a slight deflection in both nucleoplasmic and cytoplasmic voxelscale heterogeneities during focal drift. However, the eye can easily be deceived. Neither does their ratio show any general tendency to evolve over time. This, however, doesn't come as a surprise, since voxelscale heterogeneities were already found to be very similar in interphase as well as metaphase cells.

Similar to ROI-to-ROI heterogeneities the temporal heterogeneity of voxelscale spatial heterogeneities is much smaller than the ensemble heterogeneity of interphase voxelscale heterogeneities. This supports the theory that the ensemble heterogeneity is not caused by intracellular cell cycle variations but by differences between individual cells. The exact values are displayed in table 5.2. Interestingly, in both series the mean voxelwise heterogeneity per compartment is larger in the cytoplasm than in the nucleoplasm. This confirms the observation that the previously described trend of the cytoplasm being more heterogeneous than the nucleoplasm can also be seen on the voxelscale. An extensive set of measurements would be necessary to analyse whether these results are genuine or a special property of this individual cell.

ensemble heterogeneity interphase cells	temporal heterogeneity $\delta t = 2.575\,\mathrm{s}$, $T = 65\,\mathrm{s}$	temporal heterogeneity $\delta t = 30\,\mathrm{s}$, $T = 3\,\mathrm{min}$
$\eta_{cyto}(\eta_{ROI}) = 65.70\,\%$	$\eta_t(\langle\eta_{ROI}\rangle_{cyto}) = 12.81\,\%$	$\eta_t(\langle\eta_{ROI}\rangle_{cyto}) = 9.45\,\%$ $(9.03\,\%)$
$\eta_{nuc}(\eta_{ROI}) = 68.39\,\%$	$\eta_t(\langle\eta_{ROI}\rangle_{nuc}) = 21.92\,\%$	$\eta_t(\langle\eta_{ROI}\rangle_{nuc}) = 13.46\,\%$ $(11.55\,\%)$

Table 5.2: Comparison of temporal heterogeneity and ensemble heterogeneity of voxelscale heterogeneities. Values in parentheses signify temporal heterogeneities excluding the drift part.

In summary, overall crowding levels as well as voxel-wise heterogeneities do not appear to change during the cell cycle. In contrast, the ratio of compartment-wise ROI-to-ROI heterogeneities might evolve. However, the test measurement performed in this thesis does not allow making any definite deduction about the evolution of intracellular spatial heterogeneities on either lengthscale. A proper characterization of cell cycle dependent variations in spatial heterogeneities would require more extensive measurements and is not part of this thesis.

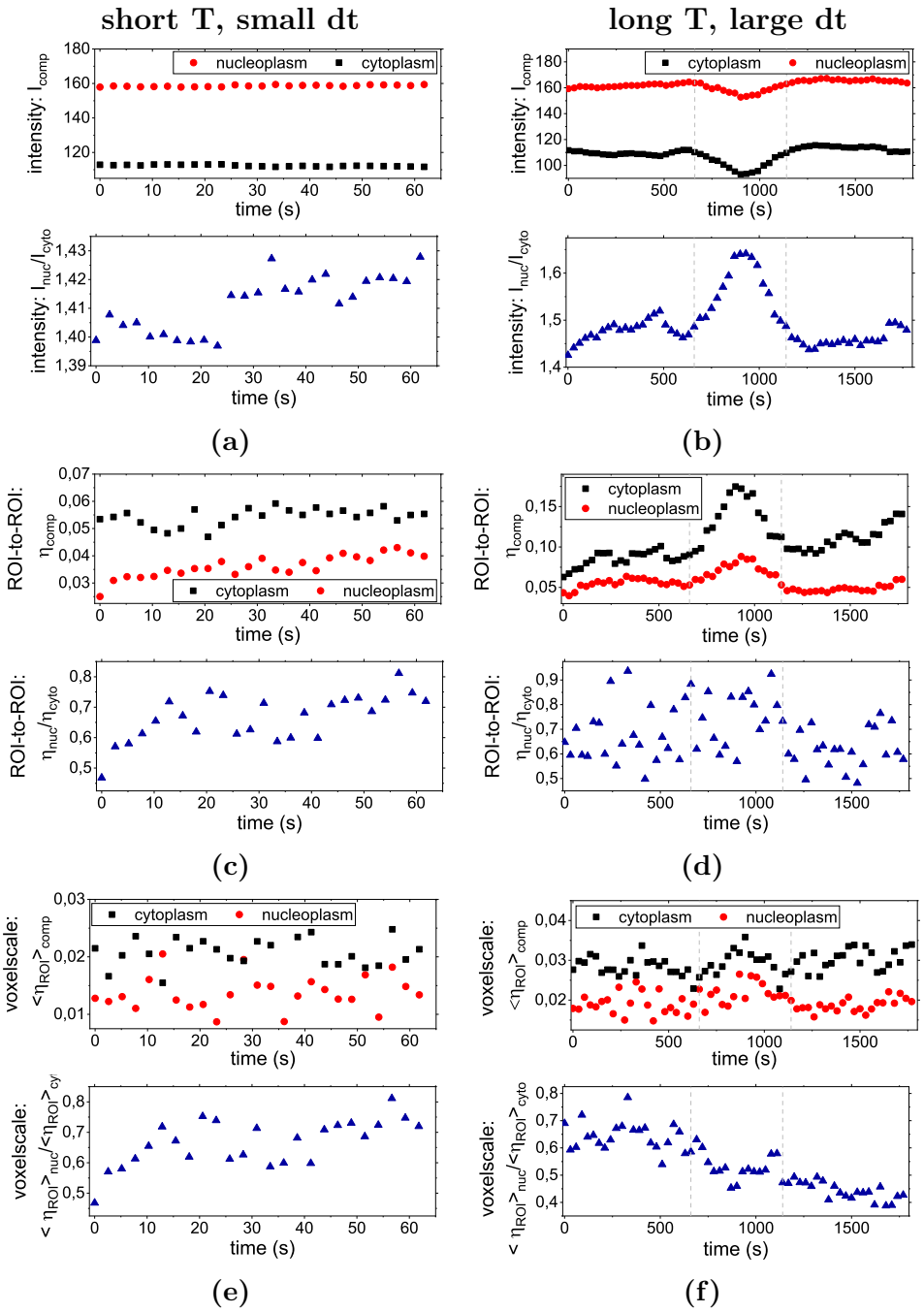

Figure 5.23: Temporal evolution of crowding levels and heterogeneities. Left column: short measurement time at high temporal resolution. Right column: long measurement time at low temporal resolution. Dashed lines indicate start and end of a period of stage drift as identified in the acquired images. (a) + (b) Intensity levels + ratio. (c) + (d) ROI-to-ROI heterogeneities + ratio. (e) + (f) Voxelscale heterogeneities + ratio.

5.7.3 Additional Analysis Approaches

Spatial Correlation of Pixelwise Intensity Values

In order to check whether pixelwise intensity levels are correlated, the spatial correlation of intensity values per pixel was manually calculated for short distances (see Fig. 5.24a). To this end, the ROIs previously selected for heterogeneity analyses were divided into subROIs of 21 × 21 pixels, i.e. a maximum distance of 10 pixels from the centre pixel of each subROI was considered for correlations. Then for each distance d from the centre pixel the mean product of pixel values of centre pixel and pixel at distance d was calculated. This value represents the spatial correlation $C_{subROI}(d)$ of distance d of this particular subROI. This procedure was repeated for the complete ROI (i.e. all pixels with a minimum distance of 10 pixels from the ROI's boundary served as centre pixels). Subsequently the mean of all subROI-correlations $\langle C_{subROI}(d)\rangle$ was calculated.
The result is shown in Fig. 5.24b for a representative ROI. As can be seen, the pixelwise intensity values are not spatially correlated.

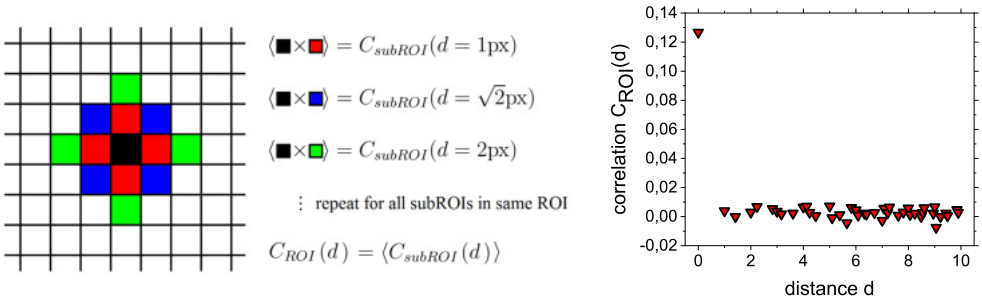

(a) **(b)**

Figure 5.24: Spatial correlation of pixelwise intensity values. (a) Principle of manual calculations. (b) Averaged correlation for a representative ROI. Clearly the pixelwise intensity is not spatially correlated.

Edge Filters and Fractal Analysis

In an attempt to characterize the internal structure of cellular protoplasms more thoroughly, various edge filters (ImageJ) were applied to images of cells. However, neither within raw images nor within thresholded images any kind of edges could be identified. Similarly, results obtained by means of multifractal analysis in FracLac (ImageJ) were inconclusive. Most probably, free EGFP is not suitable for these types of analyses. Thus results are not shown.

5.8 Summary and Discussion

In chapter 5, intracellular crowding levels and intracellular crowding heterogeneities on several lengthscales were analysed in interphase and metaphase cells by means of a simple, intensity-based imaging approach.
The cytoplasm of interphase HeLa cells was found to be more crowded than their nucleoplasm. These observations straightforwardly confirm results obtained by previous studies[59] [48], which, primarily, had been based on diffusion. Furthermore, it could be established that the difference in crowding states between compartments is conserved even after nuclear envelope breakdown: the spindle periphery is more crowded than the spindle region, although there is no evidence of a membranous barrier between both regions. However, at least some mixing between former cytoplasm and former nucleoplasm does take place, as spindle and periphery feature more similar crowding levels than nucleoplasm and cytoplasm. Unfortunately it was not possible to gather information about absolute crowding levels within the compartments. It would be most interesting to investigate how, within both compartments, absolute crowding levels change upon entry into mitosis. This remains to be done in a future project.

In addition to characterizing overall crowding ratios, the heterogeneity of crowding levels within nucleoplasm, cytoplasm, spindle and spindle periphery was described on two lengthscales.
HeLa cells were found to feature significant heterogeneity levels in all compartments. This confirms a number of recent studies[36] [64] [75] [80] [81] [85] [86]. However, results in this thesis are obtained in a more direct way, as previous studies were generally based on simulations and diffusion experiments. Different to previous studies on the subject, in this thesis metaphase cells were analysed as well.
On the ROI-to-ROI lengthscale, the interphase cytoplasm is more heterogeneous than the nucleoplasm. This is most likely due to the multi-scale nature of cytoplasmic architecture, i.e. its complex composition of membrane-bound organelles and macromolecules of various sizes. Different from that, the nucleoplasm is more homogeneous. Once again this can be explained in terms of macromolecular composition: there are no membrane-bound organelles, and the number of large proteins in the nucleoplasm is smaller than in the cytoplasm[151]. In metaphase cells, spindle and spindle periphery feature very similar levels of ROI-to-ROI heterogeneity, with the periphery being only slightly

more heterogeneous than the spindle region. Interestingly, spindle region, spindle periphery and interphase nucleoplasm display very similar levels of heterogeneity.
On the voxel-to-voxel lengthscale, all compartments, i.e. nucleoplasm, cytoplasm, spindle region and spindle periphery show roughly the same levels of heterogeneity. However, sample-intrinsic heterogeneity levels are only accessible in an indirect way, i.e. by fitting of small ensembles of data pairs. This is due to a significant impact of measurement settings on pixelwise intensity levels as well as their pixelwise standard deviation. Because of these small ensembles available for fitting, voxelscale heterogeneity values have to be considered to be rather vague.

Overall crowding levels as well as heterogeneity levels on both lengthscales appear to be time-invariant, at least for measurement durations of up to 30 min. However, characterizing cell cycle dependent variations in spatial heterogeneities would require extensive measurements in all cell cycle stages, which is not part of this thesis.
The same holds true for test measurements performed in cells depleted of microtubules. The influence of the microtubule skeleton on crowding ratio and heterogeneity levels in interphase cells is quite small, if it even exists. So a large number of measurements would be required to determine its significance. Within the spindle region, neither the mean intensity per ROI nor the voxelscale heterogeneity per ROI appear to follow a specific pattern.

So, in summary, so far we can state that on intermediate lengthscales the interphase cytoplasm is more crowded and more heterogeneous than the interphase nucleoplasm. After nuclear envelope breakdown both compartments equilibrate to some degree, but can still be discriminated. On the voxel-to-voxel scale, all compartments appear to show roughly the same spatial heterogeneity.

Chapter 6

Going Beyond the Diffraction Limit: Characterizing Native Intracellular Crowding Levels and Crowding Heterogeneities via FRET-based Imaging

An overview of all lengthscales, observables and measurements in cells is given on p.63-66. Ensemble statistics is summarized in appendix A.

6.1 Motivation

Up to now this thesis has been characterizing intracellular crowding heterogeneities on the lengthscale of complete compartments, on the lengthscale of several microns as well as on the lengthscale of several hundred nanometres. Now getting insights into even smaller lengthscales is to be the centre of attention. All images were taken at a pixel size of 100 nm. In accordance with Abbe's limit of resolution in combination with the Nyquist criterion for resolution in digital images this is the smallest lengthscale accessible via conventional fluorescence microscopy techniques. Yet characterizing the accessible volume's heterogeneity on the voxel-to-voxel scale via standard fluorescence imaging techniques is challenging as it is. Moreover the results we get in doing so are not, by any means, satisfying.
This is why a different approach to describing intracellular heterogeneity levels via imaging is tested: instead of the 'conventional' fluorophore EGFP previ-

ously utilized now the FRET-based crowding sensor fCrH2 is used as an indicator of local crowding levels. Thus a characterization of intracellular crowding levels and crowding heterogeneities below the diffraction limit can be achieved.

6.2 Relation between Crowding State, Fluorescence Intensity and FRET Ratio

The sensor fCrH2 is an intramolecularly labelled, genetically encodable biomolecule which uses AcGFP1 and mCherry as a FRET pair. The fluorophores are located at opposing ends of a conformationally flexible domain. This flexible part of the molecule assumes a more condensed conformation when free volume decreases. In turn this leads to a decreased distance between N and C terminus of the protein, which ultimately increases FRET efficiency.
The sensor was introduced by Boersma et al.[104] and modified by Sukenik et al.[105]. Both groups tested the molecule extensively. They reported that the effect of self-association and aggregation of the sensor as well as that of direct chemical interactions between sensor and surrounding cell protoplasm is negligible. In addition, they proved that the conformational change is reversible, continuous and linearly responds to volume modulation. What is more, in chapter 10 of this thesis the sensor will be shown to require active pushing by its surroundings to assume its closed state. So the FRET efficiency of fCrH2 indeed reflects only the local excluded volume fraction.

In experiments with HeLa cells transfected with EGFP, fluorescence intensity was proportional to the local accessible volume fraction. When working with a FRET-based crowding sensor, the fluorescence signal is governed by two factors: on the one hand, similar to EGFP, the total fluorescence signal depends on the local number of fluorophores. Of course this in turn reflects the local available volume fraction on a lengthscale bigger than the sensor itself. On the other hand, the fluorescence ratio between AcGFP1 and mCherry depends on the occurrence of FRET. Since FRET efficiency scales inversely with the 6th power of the donor-to-acceptor proximity (see Eq. 3.4), this fluorescence ratio reacts extremely sensitively to smallest changes in distance. For the FRET pair AcGFP1 and mCherry the Förster radius, i.e. the characteristic distance where FRET efficiency reaches 50 %, is approximately 5.1 nm[99]. If donor and acceptor molecules are separated by more than approximately 10 nm it can

be assumed that FRET does not occur anymore. So FRET efficiency can be used as an observable to characterize the intracellular crowding state and its heterogeneity below the diffraction limit.

The crucial point in this approach is separating FRET-dependent from particle-number-dependent contributions to total fluorescence. This can easily be achieved by performing ratiometric FRET imaging (see Sec. 3.4). In this technique a sample containing a FRET sensor is illuminated only with the donor excitation wavelength - 488 nm in the case of fCrH2 - whereas fluorescence is registered simultaneously both in the donor and the acceptor emission range. Registered fluorescence in the donor channel D stems from all donor molecules that are excited but do not perform FRET. Registered fluorescence in the acceptor channel during donor excitation F, on the other hand, is caused by the acceptor of all sensor molecules that do perform FRET. It is tacitly assumed that all sensor molecules are equally probable to assume a condensed conformation at a given crowding level. So, in principle, the fraction of molecules performing FRET F_{FRET} can be extracted from total fluorescence intensities via

$$F_{FRET} = \frac{F}{D + F}. \tag{6.1}$$

As $D + F$ represents the total number of sensor molecules, F_{FRET} is independent of absolute sensor concentration.
It must, however, be noted that F_{FRET} obtained by ratiometric imaging does not represent the FRET efficiency E_{FRET} by any means. This is caused by constraints in the experimental procedure. As described in Sec. 5.3.3, illumination and detection settings influence the registered absolute fluorescence values in a complex way. In the case of ratiometric imaging, fluorescence is registered in two channels, i.e. in two different ranges of wavelengths and by two different detectors. Both detectors are photomultipliers of the same type. Nevertheless, they cannot be assumed to show exactly the same dependence between detector settings (i.e. photomultiplier bias voltage), registered mean and pixelwise variance of fluorescence levels. In principle, it is possible to extensively test both detectors with the same set of homogeneous fluorescent samples, e.g. dye solutions or even chromaslides. However, Woehler et al.[161], as well as Neher et al.[162], stated that variances introduced by photomultipliers depend not only on bias voltage but also on wavelength. Moreover, fluorescence intensity in the FRET/Acceptor channel was found to be much lower than in the donor channel. This holds true even for direct acceptor illumination. Therefore, in order

to fully exploit the dynamic range of the photomultiplier, the photomultiplier bias voltage for detection in the FRET channel has to be set to a considerably higher level than in the donor channel. So it is not possible to achieve exactly the same behaviour in both detectors. Consequently, the FRET ratio F_{FRET} is biased due to measurement settings. In contrast, the FRET efficiency E_{FRET} is a property of the employed FRET sensor. This means that by definition it is independent of measurement settings and procedure. It is, however, not as easily accessible via FRET imaging as the FRET ratio. Nevertheless, an estimate for spatially varying crowding levels can be obtained by means of ratiometric FRET imaging, even if only the FRET ratio F_{FRET} is accessible.

It should be noted that in the previously performed 'traditional' imaging approach fluorescence intensity is proportional to the local *accessible* volume fraction φ. The FRET ratio of fCrH2 F_{FRET}, however, depends on the local *excluded* volume fraction ϕ in a linear way:

$$F_{FRET} = m\phi + y_0. \tag{6.2}$$

The slope m and offset y_o of this expression have to be found by calibration experiments performed on FRET sensors in crowded solutions at defined crowding levels. In order to ensure better comparability between results obtained in FRET experiments and results obtained in intensity-based imaging experiments in the previous chapter, $\Theta := 1 - F_{FRET}$ is chosen as an observable instead of F_{FRET}. Θ represents the fraction of molecules *not* undergoing FRET. It can be shown to depend linearly on the available volume fraction φ:

$$\Theta = 1 - F_{FRET} = m(1-\phi) + (1 - m - y_0) =: m\varphi + \hat{y_0}. \tag{6.3}$$

Thus, following the definition of any observable's heterogeneity given in Eq. 5.1, the heterogeneity of Θ is

$$\eta(\Theta) = \frac{\sigma(\Theta)}{\mu(\Theta)} = \frac{\sigma(\varphi)}{\mu(\varphi) + \hat{y_0}/m}. \tag{6.4}$$

The slope m and offset $\hat{y_0}$ remain unknown: it was not possible to perform calibration experiments in solutions of artificial crowders such as dextran or ficoll at defined concentrations. Despite optimizing transfection protocols, transfection rates were too low to obtain sufficiently high fluorescence rates after mixing lysates with artificial crowders. However, building on experimental

results describing the relation between absolute crowding level and measured FRET efficiency obtained by Sukenik et al. (fig. 2.A in[105]), we can estimate $m \in [0;1]$ and $\hat{y_0}/m > 0$. By means of a simple simulation, it can be shown that with these boundary conditions $\eta(\Theta)$ depends on $\eta(\varphi)$ in a roughly linear way: matrices with entries following a Gaussian distribution around a pre-set mean in the range $[0.2, 0.8]$ were used to calculate actual means and standard deviations of matrix entries. Since this approach is similar to intensity-based imaging experiments, means, standard deviations and heterogeneities of matrix entries obtained in this way represent heterogeneities of the available volume fraction: $\mu(\varphi)$, $\sigma(\varphi)$ and $\eta(\varphi)$. The unknown factor $\hat{y_0}/m$ was set to 100 different values in the range $[0.1, 10]$, so that $10 \cdot \hat{y_0}/m$ was equidistant. With these values a set of heterogeneities of Θ could be calculated according to Eq. 6.4. Plotting $\eta(\Theta)$ as a function of $\eta(\varphi)$ with these boundary conditions shows that both variables still show a roughly linear dependence (representative results are given in Fig. 6.1). So mean values and heterogeneities of Θ can be compared to the results in HeLa cells expressing EGFP established in chapter 5.

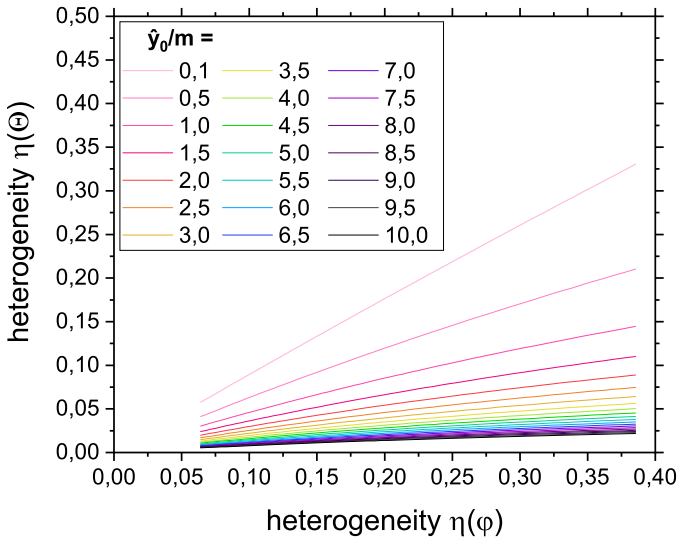

Figure 6.1: The heterogeneity of Θ is roughly proportional to the heterogeneity of the available volume fraction φ. Data were acquired by simulation of a 500×500-matrix of random numbers uniformly distributed around a pre-set mean value. $\eta(\Theta)$ was calculated for 100 equidistant values of $\hat{y_0}/m \in [0.1, 10]$.

Due to the ratiometric analysis approach, however, it is not possible to characterize the voxel-to-voxel heterogeneity of crowding via ratiometric FRET imaging. As described above, the pixelwise variance of the fluorescence sig-

nal is determined by Eq. 5.12. Of course, this holds true for both detection channels, donor D and FRET F, albeit with different proportionality factors $\xi_{D,F}$:

$$\sigma_D^2(D) = \xi_D^2(\mu_D(D) + A_D^2\sigma^2(\varphi)), \tag{6.5}$$
$$\sigma_F^2(F) = \xi_F^2(\mu_F(F) + A_F^2\sigma^2(\varphi)). \tag{6.6}$$

When taking the ratio of two quantities containing statistical errors, the uncertainty of the resulting function depends on the initial uncertainties of numerator and denominator, respectively. Calculating the propagation of uncertainty for the particular example $\Theta = 1 - E_{FRET} = 1 - \frac{F}{D+F} = \frac{D}{D+F}$ renders

$$\sigma^2(\Theta) = \left(\frac{\partial\Theta}{\partial\mu_D}\cdot\sigma_D\right)^2 + \left(\frac{\partial\Theta}{\partial\mu_F}\cdot\sigma_F\right)^2. \tag{6.7}$$

For homogeneous samples, this is

$$\begin{aligned}\sigma_{hom}^2(\Theta) &= \frac{\mu_F^2}{(\mu_D+\mu_F)^4}\xi_D^2\mu_D + \frac{\mu_D^2}{(\mu_D+\mu_F)^4}\xi_F^2\mu_F \\ &= \frac{\mu_F\mu_D}{(\mu_D+\mu_F)^4}\left(\xi_D^2\mu_F + \xi_F^2\mu_D)\right).\end{aligned} \tag{6.8}$$

For inhomogeneous samples, i.e. samples featuring a sample-inherent variance $\sigma^2(\varphi)$, Eq. 6.7 becomes

$$\begin{aligned}\sigma_{inhom}^2(\Theta) &= \frac{\mu_F^2}{(\mu_D+\mu_F)^4}\xi_D^2(\mu_D + A_D^2\sigma^2(\varphi)) + \frac{\mu_D^2}{(\mu_D+\mu_F)^4}\xi_F^2(\mu_F + A_F^2\sigma^2(\varphi)) \\ &= \frac{\mu_F\mu_D}{(\mu_D+\mu_F)^4}\left(\xi_D^2\mu_F + \xi_F^2\mu_D)\right) + \frac{\sigma^2(\varphi)}{(\mu_D+\mu_F)^4}\left(\xi_D^2\mu_F^2A_D^2 + \xi_F^2\mu_D^2A_F^2\right) \\ &= \sigma_{hom}^2(\Theta) + \delta_{inhom}^2(\Theta).\end{aligned} \tag{6.9}$$

It must be assumed that the sample-inherent variance $\sigma^2(\varphi)$ is represented differently in donor and FRET channels, so $A_D^2 \neq A_F^2$. Thus it is not possible to extract the actual voxel-wise crowding-heterogeneity from ratiometric images. Due to the fact that $\sigma^2(\Theta)$ depends on the inverse fourth power of total fluorescence intensity $\mu_D + \mu_F$, it is not feasible either to perform calibration measurements in homogeneous samples. In order to achieve this calibration an individual calibration image for every possible inherent fluorescence intensity would be required. Therefore, crowding states on the 5 nm-lengthscale are only analysed on the compartment level and on the ROI-to-ROI level.

Yet, taking a pixel-wise ratio of fluorescence images can be influenced severely by noise originating from microscope components. As mentioned in Sec. 5.3.3, averaging over several images is a possible way of decreasing this noise, albeit at the cost of temporal resolution. Photobleaching becomes more probable, too, when applying high frame or line averages. However, errors introduced by division by small numbers were considered to be the more severe problem in FRET experiments. Therefore a line average of $LA = 2$ was chosen for all images.
In order to ensure comparability of all ratiometric FRET measurements, PMT voltages were held constant at 580 V in the range of 500 nm to 550 nm (donor channel) and at 850 V in the range of 600 nm to 700 nm (acceptor/FRET channel) throughout all measurements. These settings were heuristically found to suit a large fraction of cells expressing fCrH2. So cells were selected for measurements according to their compatibility to these measurement settings. Since the ratio of overall crowding levels in the compartments as well as crowding heterogeneities on the intermediate lengthscale are relative observables, most setup influences cancel out in their calculation.

6.3 Overall Crowding States on the 5 nm-Lengthscale

At first, let us again consider fluorescence images as well as ratiometric FRET images of HeLa cells in interphase and metaphase (Fig. 6.2a to 6.2d). In fluorescence images of interphase cells, the nucleus can easily be distinguished from the surrounding cytoplasm due to its considerably lower fluorescence intensity in both channels. It is not clear why sensor expression levels are that different in both compartments. However, it is consistent with previous works of other groups who used fCrH2 in various cell types[104] [105]. It is possible that the sensor features a cytoplasmic localization signal or cannot pass freely through the nuclear envelope into the nucleus.

In order to get more reliable data from nuclear regions, only cells with a comparatively high fluorescence signal in the nucleus were selected for imaging. Of course, following this procedure only a small part of the whole cell population is sampled. Nevertheless, this selection process is inevitable to get any result at all from the nuclear region. As mentioned above, even during acceptor illu-

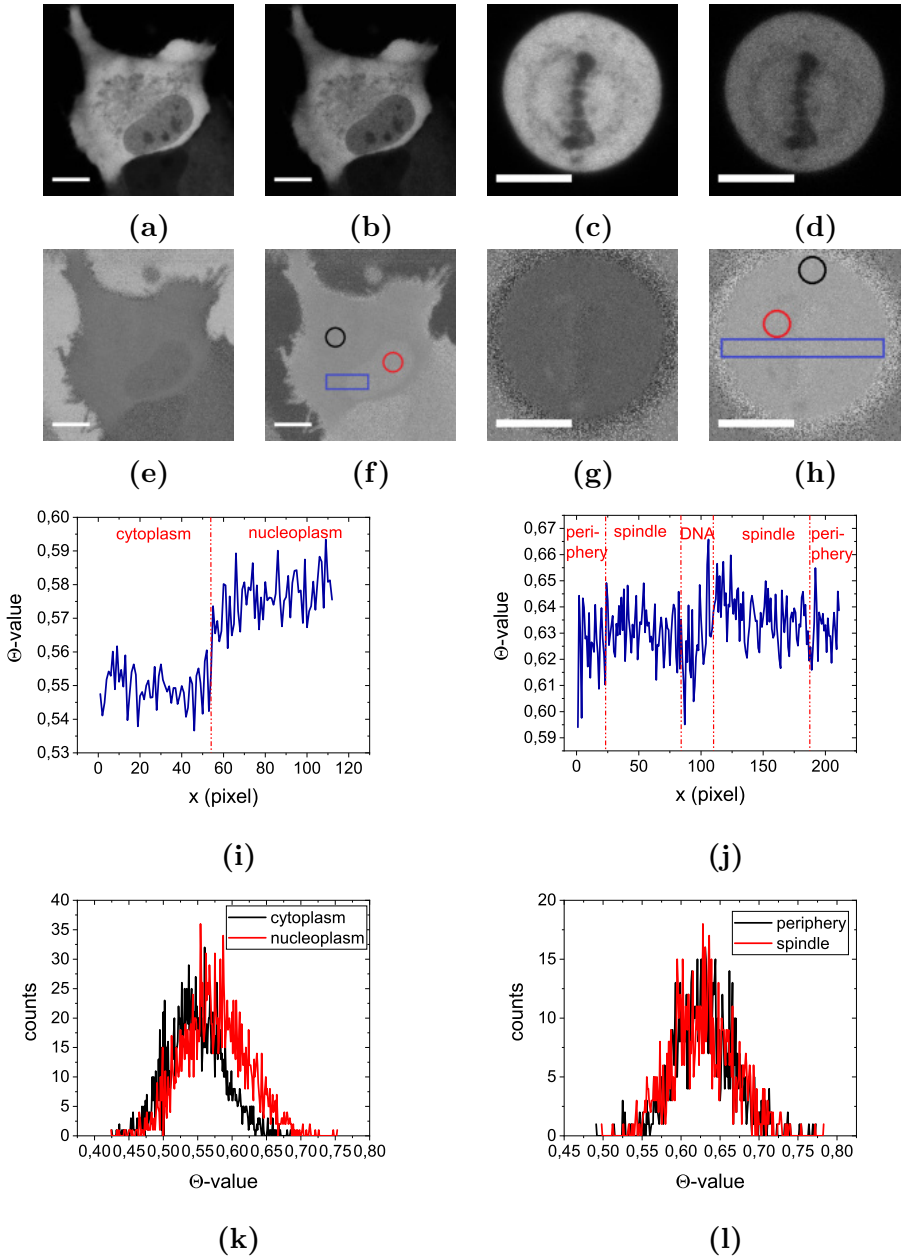

Figure 6.2: HeLa cells transfected with fCrH2 in interphase (left) and metaphase (right). (a) and (c) Donor images. (b) and (d) FRET images. (e) and (h) E_{FRET} images. (f) and (g) Θ images. Neither E_{FRET} nor Θ images show any obvious pattern within the compartments. (i) and (j) Plotprofiles for rectangular ROIs marked in Θ images. Profiles are taken along horizontal direction x and averaged over all pixels in vertical direction. (k) and (l) Histograms for circular ROIs marked in Θ images. Scalebar 10 µm.

mination fluorescence intensity is much lower in the acceptor/FRET channel. Ratiometric imaging requires dividing the FRET image through the sum of FRET and donor images. So regions with low fluorescence intensities in the cell should be avoided in order to limit errors introduced by division by small numbers. That is why only those cells were considered for further analysis

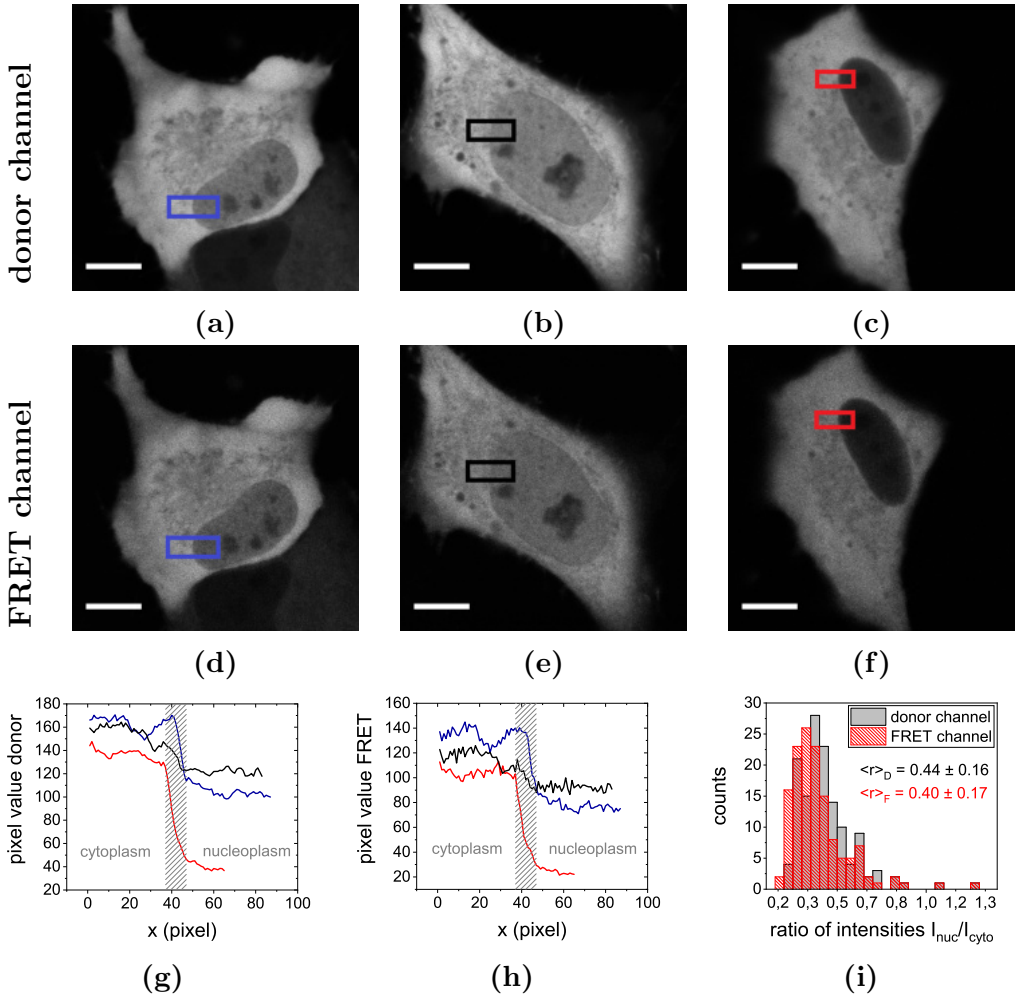

Figure 6.3: Nuclear expression levels of fCrH2 throughout the cell ensemble. (a, b, c, g) Donor channel. (d, e, f, h) FRET channel. (a) + (d) Cell with nucleus of intermediate intensity. (b) + (e) Cell with bright nucleus. (c) + (f) Cell with dark nucleus. (g) + (h) Fluorescence intensity profiles of the ROIs marked in figures a-f. Profiles are taken along horizontal direction x and averaged over all pixels in vertical direction. (i) In order to get more reliable data from nuclear regions, only cells in which nuclear fluorescence in the donor channel reached at least one fifth of cytoplasmic fluorescence were considered for further analysis. Fluorescence ratios were in the range of 0.25 to 0.65 in the majority of analysed cells. Scalebar 10 µm.

whose nuclear fluorescence in the donor channel reached, at least, one fifth of cytoplasmic fluorescence levels in the same channel (see Fig. 6.3). In the vast majority of cells the ratio of fluorescence levels between compartments was between 0.25 and 0.65 (see Fig. 6.3i).

When comparing donor and FRET images of the same interphase cell (see Fig. 6.2a and 6.2b), both images appear to be very similar. In particular, there are no prominent regions in which the local intensity pattern is clearly different in FRET and donor channel. This first impression gained by mere

sight is supported by the ratiometric image (see Fig. 6.2e): cytoplasm as well as nucleoplasm appear quite homogeneous. However, both compartments can still be distinguished: the FRET ratio is somewhat higher in the cytoplasm than in the nucleoplasm.
As mentioned above, rather than evaluating the FRET ratio F_{FRET} directly, analysing $\Theta = 1 - F_{FRET}$ should be aimed at (see Fig. 6.2f). In contrast to F_{FRET}, Θ depends linearly on the accessible volume fraction. So results obtained for Θ as an observable can be compared to the results previously obtained in cells expressing EGFP more easily. Of course, values for Θ are somewhat higher in the nucleoplasm than in the cytoplasm (see Fig. 6.2i and Fig. 6.2k).
In metaphase cells, however, spindle region and spindle periphery can only be distinguished in the fluorescence images (Fig. 6.2c and Fig. 6.2d). Just as in cells expressing EGFP, fluorescence intensity is somewhat higher in the spindle region than in the spindle periphery. So after nuclear envelope breakdown fCrH2 molecules spread in the cell according to the same principle as EGFP does: the local number of molecules primarily depends on the amount of accessible volume. However, in the ratiometric image (Fig. 6.2g) as well as in the Θ-image (Fig. 6.2h, line profile in Fig. 6.2j, histograms see Fig. 6.2l) the mitotic compartments look very much the same - this hints at equal crowding levels on the 5 nm-scale.

In analogy to our evaluation of EGFP data, the mean value of Θ of 20 ROIs in both nucleoplasm and cytoplasm or of 8 ROIs in the spindle region and 12 ROIs in the spindle periphery is calculated:

$$r = \begin{cases} \frac{\Theta_{nuc}}{\Theta_{cyto}} \approx \frac{\phi_{nuc}}{\phi_{cyto}} & \text{for interphase,} \\ \frac{\Theta_{spin}}{\Theta_{per}} \approx \frac{\phi_{spin}}{\phi_{per}} & \text{for metaphase.} \end{cases} \tag{6.10}$$

The distributions of the ratios of Θ of both compartments per cell are displayed in Fig. 6.4, together with ensemble means and standard deviations. Confirming the visual impression, crowding levels on the 5 nm-scale are the same in spindle region and spindle periphery of mitotic cells. Their compartment-wise ratio is $\langle r \rangle_{met} = 1.001 \pm 0.004$. In interphase cells, crowding levels are very similar, too, with a ratio of $\langle r \rangle_{int} = 1.054 \pm 0.035$. This might hint at a slightly higher accessible volume fraction, i.e. slightly lower crowding levels, in the nucleus. However, considering the low intensity levels of fluorescence both in donor and FRET/acceptor channel in the nucleus, we have to be careful not to jump to

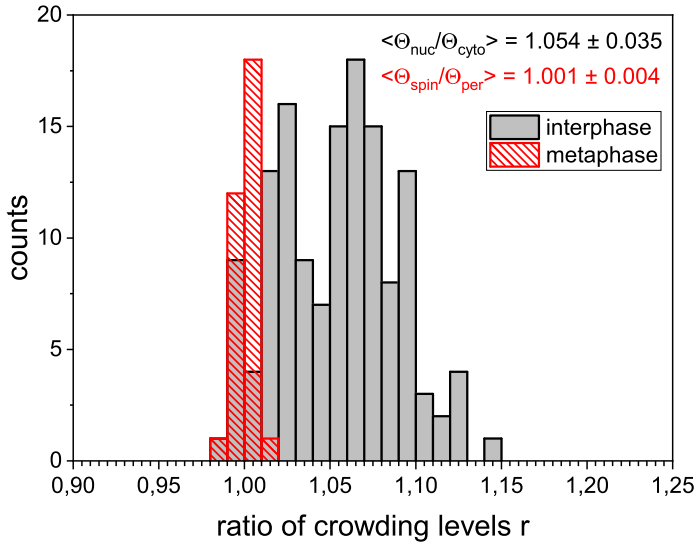

Figure 6.4: Ratio of overall crowding levels obtained via ratiometric FRET imaging. Ratios are calculated according to Eq. 6.10. Both ratios are close to one. However, interphase ratios are higher and scatter more widely throughout the ensemble. Angle brackets signify ensemble averages ± ensemble standard deviations.

conclusions: the slight difference in overall crowding levels might as well be caused by the lower signal-to-noise ratio of fluorescence values in both channels which in turn causes a much higher level of noise in ratiometric images. The difference in accessible volume fractions might in fact be marginal, if it exists at all. This is especially true since fCrH2 is known to react extremely sensitive even to small changes in local available volume.

6.4 ROI-to-ROI Heterogeneity of Crowding States on the 5 nm-Lengthscale

The fluorescence images of both donor and FRET channel (Fig. 6.2a to 6.2d) look similar to fluorescence images obtained in EGFP cells: metaphase cells do not show any obvious differences in spindle region and spindle periphery apart from their overall fluorescence levels. On the other hand, in interphase cells cytoplasmic fluorescence appears much more speckled than nucleoplasmic fluorescence, even though cytoplasmic fluorescence is much brighter. This confirms our previous results on the crowding heterogeneity on the ROI-to-ROI scale. However, in the ratiometric images all compartments appear to be quite homogeneous (Fig. 6.2e to Fig. 6.2h). Nevertheless, just as in EGFP cells, the distribution of ratios of mean Θ per compartment is much broader in

interphase cells than in metaphase cells (Fig. 6.4), indicating either a higher ensemble heterogeneity in interphase cells or a higher ROI-to-ROI heterogeneity in at least one interphase compartment. This characteristic feature is even more pronounced in fCrH2 cells than in EGFP cells.

In order to thoroughly characterize the ROI-to-ROI heterogeneity of crowding states on the 5 nm-scale, the coefficient of variation was calculated according to Eq. 5.1 for the same 20/12/8 ROIs per compartment that had been used to calculate the overall crowding state on this lengthscale. The results for interphase and metaphase cells are shown in Fig. 6.5. In contrast to bigger lengthscales, ROI-to-ROI heterogeneity levels on the 5 nm-scale are quite similar in nucleoplasm and cytoplasm. The same holds true for metaphase cells: ROI-to-ROI heterogeneity levels are in the same range for both spindle region and spindle periphery. However, ROI-to-ROI heterogeneities are somewhat lower in metaphase cells than in interphase cells.

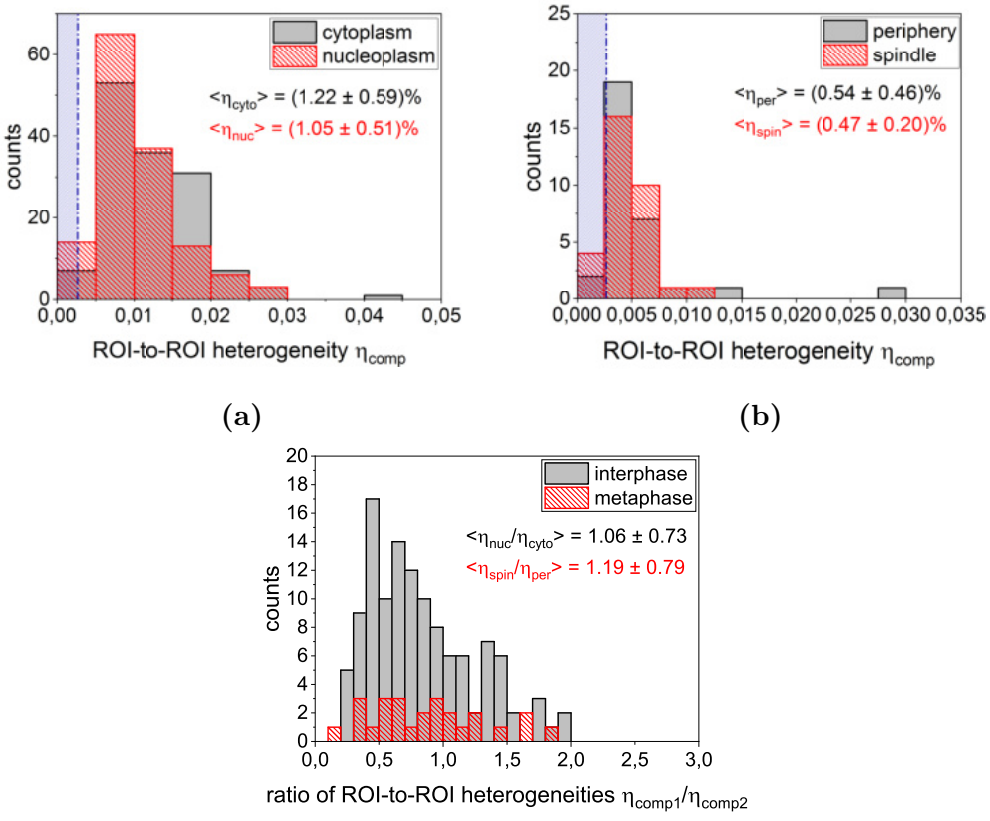

Figure 6.5: ROI-to-ROI heterogeneity levels of Θ obtained in HeLa cells transfected with fCrH2. (a) Interphase cells. (b) Metaphase cells. (c) Cell-wise ratios of both compartments in interphase and metaphase cells. Angle brackets signify ensemble averages ± ensemble standard deviations. Thresholds obtained via measurements in cell lysates.

Of course, a lower threshold should be defined, above which heterogeneity levels can be considered to be significant. Since in the case of fCrH2 we are considering ratiometric FRET data, neither chromaslides nor dye solutions can be used to this end. So a series of experiments on lysates of HeLa cells expressing fCrH2 was performed. Cell lysates cannot be considered to be as homogeneous as a dye solution since it cannot be verified whether really all membranes were lysed completely. Yet they are the most suitable sample available to calibrate ROI-to-ROI heterogeneity levels in ratiometric FRET imaging data. By analogy to our previous strategy for imaging cells, equal measurement conditions were set when taking images in lysates. Subsequently the ROI-to-ROI heterogeneity was calculated for 20 ROIs in the lysate. Thus the lower threshold was found to be $\langle \eta_{lys} \rangle = (0.27 \pm 0.04)\,\%$.

The vast majority of ROI-to-ROI heterogeneities in interphase cells are above this threshold value. However, these heterogeneity levels are surprisingly low with averages of $\langle \eta_{nuc} \rangle = (1.05 \pm 0.51)\,\%$ and $\langle \eta_{cyto} \rangle = (1.22 \pm 0.59)\,\%$, respectively. Heterogeneity levels in metaphase cells are even lower with averages of $\langle \eta_{spin} \rangle = (0.47 \pm 0.20)\,\%$ and $\langle \eta_{per} \rangle = (0.54 \pm 0.46)\,\%$. As expected, also a spatially resolved analysis of the spindle region (Fig. 6.6) does not yield any further information about the local heterogeneity of crowding states during metaphase.

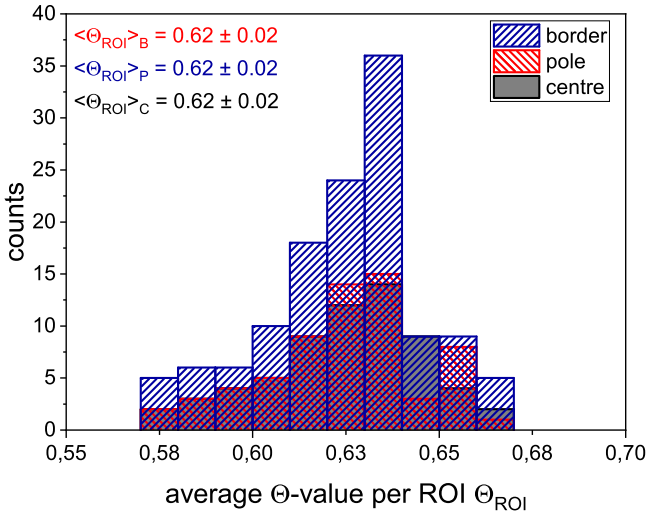

Figure 6.6: Spatially resolved analysis of the spindle region. Average Θ values per ROI sorted according to their relative position within the spindle. Angle brackets signify ensemble averages ± ensemble standard deviations.

Of course, these low heterogeneity values might be caused by a number of side-effects of the employed measurement technique that cannot be avoided in ratiometric FRET experiments:

1. In interphase cells there is a pronounced difference in expression levels of fCrH2 in the nucleoplasm and cytoplasm. Only those cells were selected for imaging that displayed a comparatively high fluorescence intensity in the nucleus, i.e. at least approximately one fifth of cytoplasmic fluorescence. Yet this marked difference in fluorescence intensity might still introduce some error into FRET ratios via division by small numbers.

2. As was demonstrated in Sec. 6.2, the pixel-to-pixel variance of ratiometric images in a rather complex way depends on instrument settings, sample-inherent spatial heterogeneities as well as local absolute fluorescence values. It was tacitly assumed that this pixel-to-pixel variance does not influence ROI-to-ROI heterogeneities. This cannot easily be verified. However, by means of analysing a few randomly selected test images, alternative approaches to obtaining FRET ratios were tested: for the analysis described above, FRET ratios were calculated pixel-wise. Subsequently the average of the respective ROI was calculated. Now, ROI-wide averages of donor and FRET intensities were calculated for the same ROIs. Then the FRET ratio of the ROI was calculated from these averaged intensity values. Mean FRET ratios per ROI obtained by both methods showed differences of only 1 %. This confirms results obtained by Sukenik et al.[105]. So probably the effect of pixel-to-pixel variance on ROI-to-ROI heterogeneities can, indeed, be neglected.

3. On account of performing all measurements at the same instrument settings, all values obtained for crowding levels and crowding heterogeneities can be compared. However, as mentioned above, FRET ratios as well as values for Θ do not represent an absolute measure for crowding levels. With the available equipment, fCrH2 could not be purified to perform calibration measurements to characterize its signal as a function of absolute crowding levels. Moreover, while the heterogeneity of Θ is proportional to the heterogeneity of φ, the proportionality constant remains unknown. Therefore, the true level of crowding heterogeneity might be masked in our measurements.

In addition to previous analyses also the cell-wise ratio of compartment-wise ROI-to-ROI heterogeneities was calculated (see Fig. 6.5c). Thus the proportionality constant cancels out. Ratios of compartment-wise ROI-to-ROI heterogeneities are widely distributed within the cell ensemble with ensemble means of $\langle \eta_{nuc}/\eta_{cyto} \rangle = 1.06 \pm 0.73$ in interphase and $\langle \eta_{spin}/\eta_{per} \rangle = 1.19 \pm 0.79$ in metaphase. This supports the view that indeed true levels of ROI-to-ROI heterogeneities are at least partially underestimated when choosing a ratiometric imaging approach.

Since results obtained in this chapter are not satisfying and, in addition, difficult to interpret, the next chapter will show a different strategy used to characterize crowding levels and crowding heterogeneities below the diffraction limit.

6.5 Summary and Discussion

The results obtained by ratiometric FRET imaging in HeLa cells expressing fCrH2 suggest that on the 5 nm-scale the ratios of compartment-wise overall crowding levels are close to unity in both interphase and metaphase cells. Moreover, ROI-to-ROI heterogeneity levels are very low in all compartments. In fact, single cell ROI-to-ROI heterogeneity levels do not exceed 4.5 %, ensemble averages are below 2 % in all compartments.
It is possible that crowding states are very similar as well as nearly homogeneous in all compartments throughout the cell cycle. After all, small proteins tend to be present in both nucleus and cytoplasm of interphase cells[151] [159]. However, differences in both crowding states and crowding heterogeneities between compartments might be masked in the ratiometric imaging approach: while $\eta(\Theta)$ is proportional to $\eta(\varphi)$, the proportionality constant cannot easily be obtained. Moreover, different PMT bias voltages have to be chosen for donor and FRET channels, which introduces different levels of shot noise to fluorescence images. In traditional fluorescence intensity based imaging approaches this detector noise can be neglected for the most part, a fact which was discussed in detail in chapter 5. It might, however, critically adulterate ratiometric imaging results while calculating the pixel-wise ratio of two defective images. So, particularly with regard to the pronounced differences in expression levels in interphase nucleus and cytoplasm, results obtained via ratiometric FRET imaging have to be interpreted very carefully.

Chapter 7

Characterizing Intracellular Crowding Levels and Crowding Heterogeneities Via Lifetime Measurements

An overview of all lengthscales, observables and measurements in cells is given on p. 63-66. Ensemble statistics is summarized in appendix A.

7.1 Motivation

In chapter 6 an attempt was made to characterize crowding levels and crowding heterogeneities on scales below the diffraction limit by means of ratiometric FRET imaging. However, ratiometric FRET imaging suffers from a number of measurement constraints. In this chapter another property of fluorophores will be exploited to gain insight into the nature of crowding on the 5 nm-scale: fluorescence lifetime. In FRET, there are two ways an excited donor molecule can relax to the ground state: it can either lose its energy by emission of a fluorescence photon or by non-fluorescent energy transfer to the acceptor molecule. When plotting the histogram of fluorescence arrival times after a short excitation laser pulse, these two relaxation processes are visible in a two-component decay.
FRET efficiency can be extracted via the ratio of fluorescence lifetimes in the presence (τ_{DA}) and absence (τ_D) of the acceptor molecule[103]:

$$E_{FRET} = 1 - \frac{\tau_{DA}}{\tau_D}. \tag{7.1}$$

Given that overall photon statistics is sufficient to allow a reliable fit, the obtained FRET efficiency is independent of fluorescence intensity levels as well as detector settings. So it is possible to circumvent the experimental problems encountered in chapter 6. Since FRET efficiency responds linearly to changes in the occupied volume fraction ϕ,

$$\Psi = 1 - E_{FRET} = \frac{\tau_{DA}}{\tau_D} \propto \varphi \tag{7.2}$$

is used as an observable. Please note that, in constrast to ratiometric imaging, in lifetime experiments FRET efficiency is directly accessible. So Ψ is similar, but not equivalent to the previously used observable Θ.

7.2 Fluorescence Lifetime Imaging Measurements (FLIM)

7.2.1 Method

The basic principle of FLIM experiments is described in Sec. 3.7.1. This description also includes examples of images of lifetime-pulsenumber vectors and a lifetime histogram with fit.
Similar to intensity-based and ratiometric imaging approaches, FLIM images of complete cells were taken with the same pixelsize as before. For subsequent analysis, 20 ROIs per compartment were selected in interphase cells. In metaphase cells, 8 ROIs in the spindle region and 12 ROIs in the spindle periphery were selected according to the previously introduced pattern (see Fig. 5.13d in chapter 5). For every ROI the histogram of all photon arrival times of all pixels was calculated. After performing a background correction according to the principles described in Sec. 3.7.3, this histogram was fitted with a function for two-component decay:

$$n(\tau) = \alpha(f_{FRET} e^{-\frac{\tau_{arr}}{\tau_{DA}}} + (1 - f_{FRET}) e^{-\frac{\tau_{arr}}{\tau_D}}). \tag{7.3}$$

In this way, values for donor lifetimes in the presence (τ_{DA}) and absence (τ_D) of the acceptor molecule can be obtained. Calculating Ψ_{ROI}, i.e. the fraction of donor molecules not undergoing FRET in this ROI, is based on these values. In order to reduce the number of free parameters in fitting, prior to lifetime measurements in cells expressing fCrH2 a number of lifetime measurements was performed in interphase cells expressing only EGFP. In these cells, arrival

time histograms were calculated for 20 ROIs in the nucleoplasm and cytoplasm. These histograms were fitted with a function describing a single-exponential decay, i.e. relaxation only by emission of fluorescence photons:

$$n(\tau) = \alpha e^{-\frac{\tau_{arr}}{\tau_D}}. \tag{7.4}$$

The resulting τ_D was averaged and $\langle\tau_D\rangle = 2.3\,\text{ns}$ was used as a start value for fitting two-component decay in cells expressing fCrH2. As an upper and lower limit for τ_D, $\langle\tau_D\rangle \pm \sigma(\tau_D) = (2.3 \pm 0.2)\,\text{ns}$ was chosen.
Samples were illuminated with a 470 nm pulsed laser at a pulse frequency of 40 MHz. Laser excitation intensity was adjusted for each individual cell, so that the photon countrate was maximal while still staying below the recommended detection rate for lifetime measurements, $r_{det,max} \approx \frac{f_{exc}}{100} = 4 \cdot 10^5 \frac{counts}{s}$. Still, this procedure resulted in image acquisition times of approximately 10 min per cell. In order to ensure measurement quality, fluorescence intensity images were taken before and after FLIM imaging. These images were used to check whether the cell moved or changed its shape during FLIM image acquisition time. Only FLIM measurements where neither movement nor change of shape could be identified were considered to be adequate for further analysis.

7.2.2 Overall Crowding States and ROI-to-ROI Heterogeneity on the 5 nm-Lengthscale

By analogy with the experiments and analyses in HeLa cells expressing EGFP, overall crowding levels on the 5 nm-scale are determined first. To this end, the average fraction of molecules not undergoing FRET $\langle\Psi_{ROI}\rangle_{comp}$ was calculated from all ROIs in the same compartment and compared to the average of the other compartment:

$$r = \begin{cases} \frac{\Psi_{nuc}}{\Psi_{cyto}} \approx \frac{\phi_{nuc}}{\phi_{cyto}} & \text{for interphase,} \\ \frac{\Psi_{spin}}{\Psi_{per}} \approx \frac{\phi_{spin}}{\phi_{per}} & \text{for metaphase.} \end{cases} \tag{7.5}$$

The ensemble distribution as well as its mean and standard deviation are displayed in Fig. 7.1a.

Similar to the results obtained in ratiometric FRET imaging, the average ratios were close to unity both in interphase ($\langle r\rangle_{int} = 0.96 \pm 0.17$) and metaphase ($\langle r\rangle_{met} = 1.02 \pm 0.18$). It is debatable whether interphase ratios being slightly

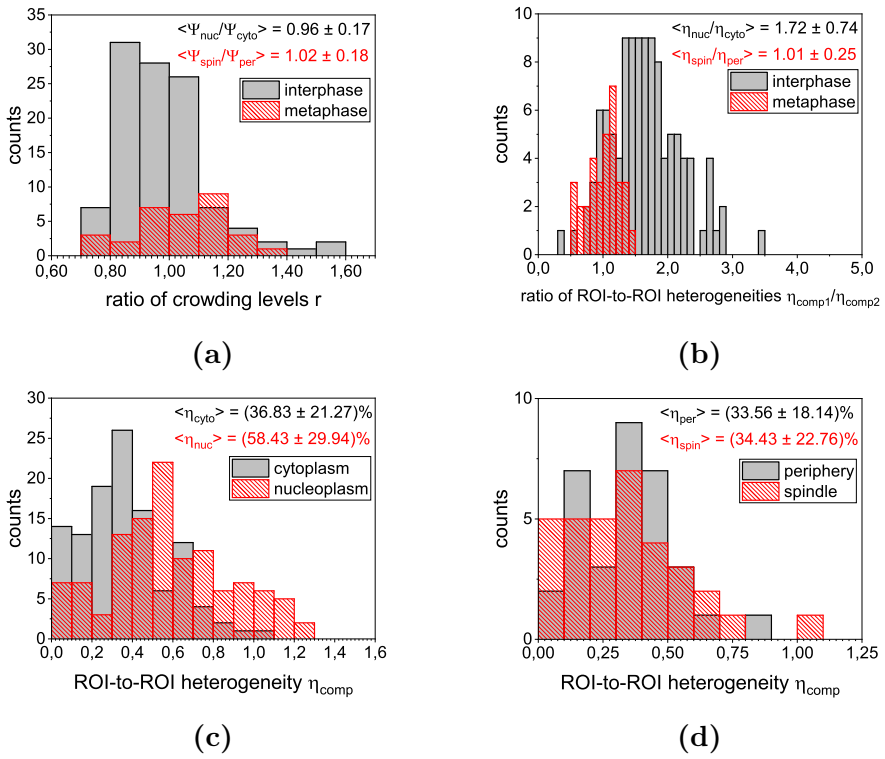

Figure 7.1: Results of FLIM analysis. (a) Ratio of overall crowding levels, calculated according to Eq. 7.5. (b) Ratio of ROI-to-ROI heterogeneities. (c) ROI-to-ROI heterogeneities in interphase. (d) ROI-to-ROI heterogeneities in metaphase. Angle brackets signify ensemble averages ± ensemble standard deviations.

farther from unity in both methods can be considered to be significant. However, we must be aware of the fact that the distribution of individual ratios per cell is much broader in FLIM results than in ratiometric FRET imaging results.

This is also mirrored in the ROI-to-ROI heterogeneities of crowding states on the 5 nm-scale in both interphase and metaphase cells. In order to calculate the cells' ROI-to-ROI heterogeneities per compartment the average and standard deviation of all ROIs in the same compartment was used, a method already used in intensity-based imaging. The ensemble-wide distributions of heterogeneities are displayed in Fig. 7.1c and 7.1d.

It is striking to see how much average heterogeneities obtained in FLIM images differ from those obtained in ratiometric FRET imaging: average ROI-to-ROI heterogeneities in ratiometric FRET imaging are well below 2 % in all compartments, whereas in FLIM they are clearly above 30 %. While cytoplasm, spindle and spindle periphery display similar heterogeneity levels of (37.83 ± 21.27) %, (34.43 ± 22.76) % and (33.56 ± 18.14) %, respectively, the average ROI-to-ROI heterogeneity level in the interphase nucleus is as high as (58.43 ± 29.94) %. In

most compartments, individual cells can reach heterogeneity levels exceeding even 100 %. The ensemble distribution of individual heterogeneity levels of all compartments but the spindle periphery is broader in FLIM data than in ratiometric imaging data.
The ratio of intermediate heterogeneities (see Fig. 7.1b) in interphase cells is $\langle \eta_{nuc}/\eta_{cyto} \rangle_{FLIM} = 1.71 \pm 0.74$, which is much farther from one than the ratio obtained in ratiometric imaging ($\langle \eta_{nuc}/\eta_{cyto} \rangle_{FRET} = 1.06 \pm 0.73$). Different from that, in metaphase cells the ratio of intermediate heterogeneities obtained in FLIM experiments is $\langle \eta_{spin}/\eta_{per} = \rangle_{FLIM} = 1.01 \pm 0.25$, which is closer to one than the ratio obtained in ratiometric imaging, $\langle \eta_{spin}/\eta_{per} \rangle_{FRET} = 1.19 \pm 0.76$.

How can it be that crowding heterogeneities, though obtained in the same system, differ so much? There are several possible explanations for this phenomenon:

1. Ratiometric FRET imaging results heavily depend on imaging settings. Since it was not possible to perform a proper calibration, only the FRET ratio was accessible in FRET imaging experiments, but not the FRET efficiency. Thus, variation in crowding ratios throughout the cell ensemble is probably masked by setup-dependent factors. In contrast, FLIM imaging is implemented via a TCSPC unit, i.e. the considerable impact of photomultiplier bias voltage on recorded fluorescence values is avoided. Especially in FLIM imaging and subsequent lifetime analysis of photon arrival time histograms only one detection channel is required. This is opposed to the combination of detection channels required for ratiometric imaging techniques. Moreover, in FLIM experiments the FRET efficiency is directly accessible. Based on these considerations FLIM results could be regarded as the more reliable data set.

2. While FLIM is relatively independent of detection settings, analysis of FLIM images is based on fitting arrival time histograms. However, in contrast to "traditional" analyses of FLIM experiments, only comparatively small ROIs are selected for analysis. So averaged photon statistics of individual histograms is as low as $2.5 \cdot 10^5 - 3.1 \cdot 10^5$ photons per histogram in cytoplasm, spindle and spindle periphery. Histograms of nuclear ROIs have an even worse photon statistics. On average only $1.5 \cdot 10^5$ photons per histogram were registered. This makes analysis by fitting quite unreliable. However, it is not easy to obtain better photon statistics. Selection of large ROIs for analysis suffers from the problems already

experienced in intensity-based and ratiometric imaging techniques: often exact boundaries between compartments cannot be clearly identified. This problem is even more prevalent in FLIM data: in FLIM images of cells expressing fCrH2, the exact boundary e.g. between nucleus and cytoplasm is often even harder to discern than in fluorescence images of cells expressing EGFP. This is why FLIM images were compared to intensity-based fluorescence images during selection of ROIs. However, intensity-based fluorescence images (in which the nucleus can easily be detected) cannot be used directly to select ROIs for the FLIM image: due to limitations of the measurement setup, FLIM and fluorescence images are not congruent. What is more, they are not merely shifted against each other but distorted, which can be seen in Fig. 7.2. So superposition of both images is difficult to achieve. This implies that a selection of large ROIs for FLIM analyses is impossible.

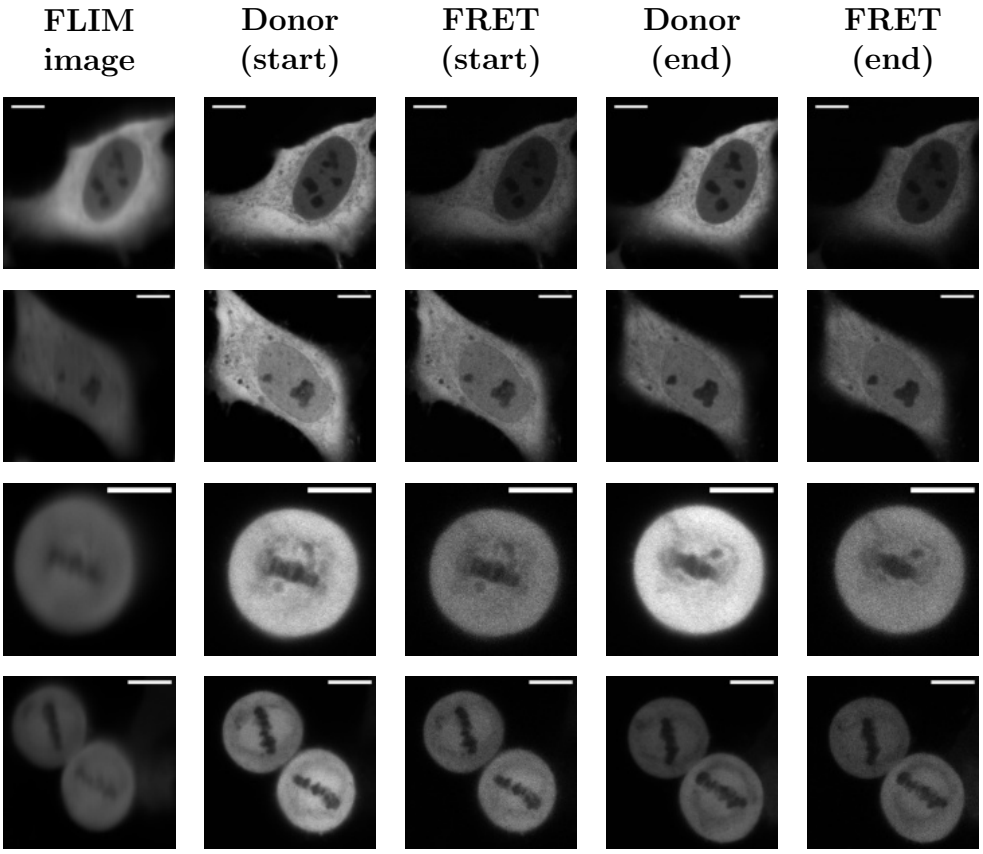

Figure 7.2: Issues in FLIM imaging and data evaluation. FLIM images (column 1) as well as fluorescence images of the same cell before (columns 2 and 3) and after FLIM imaging (columns 4 and 5), in Donor (columns 2 and 4) and FRET channel (columns 3 and 5). FLIM images and fluorescence images are not congruent. Cellular boundaries, e.g. between nucleoplasm and cytoplasm, are much harder to discern in FLIM images than in corresponding fluorescence images. Scalebars 10 µm.

The second method to obtain better photon statistics is to prolong acquisition times. However, with the statistics used so far image acquisition times were already approximately 10 min per image. Since all experiments were performed in living cells, measurement times cannot be prolonged arbitrarily. Even at acquisition times of 10 min a considerable number of cells moved during measurements. This is even more severe in metaphase cells, which move or change their overall shape much faster than interphase cells. Moreover, the longer the image acquisition time, the more involuntary bleaching can occur within the sample. In principle this problem could be avoided by sampling a smaller region within the cell instead of monitoring the complete cell. This, however, would limit spatial resolution severely. Since it was the aim of this thesis to find estimates of intracellular spatial heterogeneities in different compartments and at varying lengthscales, only FLIM images of complete cells were acquired, despite all side-effects. As a consequence, FLIM results have to be regarded as inherently error-prone and should always be used in combination with data obtained by other experimental techniques.

3. Due to long image acquisition times necessary to obtain the required photon statistics for FLIM analysis, cells were often bleached considerably. This can distort evaluation results. But, of course, bleaching would be expected to affect all parts of the cell with equal probability.

4. Finally it must be mentioned that recently some issues with the detection setup were discovered: in FLIM images of lysates made from HeLa cells expressing fCrH2, i.e. in homogeneous solutions of fCrH2, a number of localized inhomogeneities can be seen in both red and green detection channels. So far, it has not been possible to identify their origin. However, these inhomogeneities seem to have an impact only on measurements performed in samples of very low intensity. In order to decrease image acquisition time only very bright cells were selected for imaging. At any rate, no trace of this characteristic intensity pattern could be detected in FLIM images of fluorescent cells. Therefore it is assumed that possible flaws in the detection unit do not significantly alter the results of crowding and heterogeneity analysis. Nevertheless, this possibility cannot be ruled out completely. In particular, it was not possible to perform adequate control measurements in lysates containing fCrH2: even after optimizing sample preparation protocols with respect

to transfection as well as expression rates of fCrH2, lysates were generally not intensive enough to allow analysis of FLIM experiments by data fitting. At very low acquisition countrates, measurement time would have to be prolonged to several hours to get photon statistics sufficient for analysis via fitting. At such long image acquisition times, however, a considerable amount of sensor molecules is bleached. Moreover, lysates are significantly less crowded than physiological cells, as they actually do contain not only cellular constituents but also a substantial amount of lysis reagent. Unfortunately, it is rather challenging to extract this lysis reagent from the mixture. Thus fCrH2 in lysates can be expected to behave in a way quite different from its behaviour in cells, as noticeably less instances of FRET should occur in the lysate.

Unfortunately it was not possible to analyse the heterogeneity of crowding on a lengthscale smaller than the ROI-to-ROI level. Even at image acquisition times of 10 min and more, photon statistics did not allow pixel-wise fitting of lifetime histograms. In order to find the smallest possible lengthscale allowing lifetime histograms to be analysed successfully, images were binned repeatedly: lifetime histograms were calculated for 2×2 pixels, subsequently for 4×4 pixels, etc. However, it was found that the smallest number of pixels to be binned in order to be able to fit the resulting lifetime histogram corresponds roughly to the typical ROI size used in previous analysis, i.e. $(20\text{pixel} - 25\text{pixel})^2$. So the ROI-to-ROI level constitutes the smallest lengthscale at which FLIM images can be analysed.

A spatially resolved analysis of the spindle region (Fig. 7.3), executed in analogy with the analysis already performed in FRET experiments, did not yield any further information. At all positions within the spindle, ensemble means of Ψ are slightly higher than 40 %. Moreover, the ensemble distributions of Ψ are very similar for all positions.

7.2.3 Conclusion

In summary, ratios of total crowding levels seem to be close to unity. However, no definite conclusion can be drawn concerning intracellular heterogeneity levels. In data obtained via FLIM measurements not only the average heterogeneity levels differ extremely, but the distributions of heterogeneity levels are very wide as well.

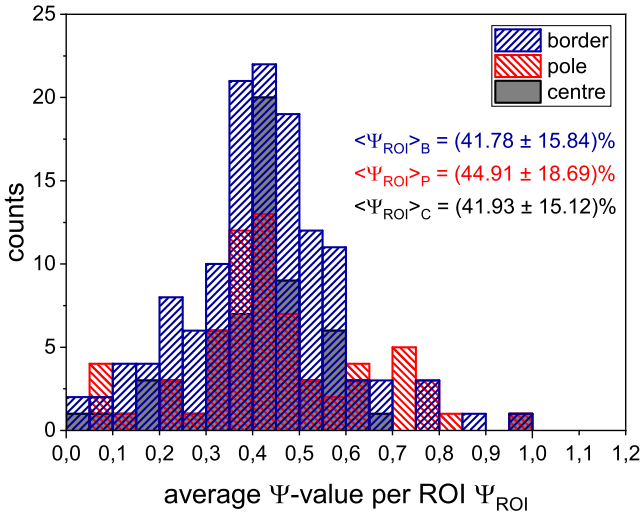

Figure 7.3: Spatially resolved analysis of the spindle region in FLIM experiments. Distributions are very similar for all positions within the metaphase spindle. Angle brackets signify ensemble averages ± ensemble standard deviations.

There are a number of factors that are likely to have an impact on analysis results in ratiometric FRET and FLIM experiments. The most substantial influences are probably the influence of photomultiplier settings in ratiometric FRET and the comparatively low photon statistics in FLIM. However, ultimately it cannot be decided which results should be considered to be more reliable.

Therefore yet another fluorescence microscopy technique was applied in order to gain insight into intracellular crowding levels and crowding heterogeneities on the 5 nm-scale: Fluorescence Lifetime Point Measurements.

7.3 Fluorescence Lifetime Point Measurements (FLPM)

7.3.1 Method

Fluorescence Lifetime Point Measurements have several advantages over FLIM measurements. The main difference in experimental implementation is recording fluorescence photons only at a few measurement loci rather than in the complete sample. This approach makes the whole experimental procedure much more tolerable for the cell. Especially photodamage is greatly reduced in FLPM experiments, as only measurement loci are illuminated. In addition,

limiting the acquisition area automatically decreases total data acquisition time. Thus, in FLIM experiments measurement loci can be sampled for a much longer period of time than individual pixels, while, at the same time, total measurement time can be kept considerably shorter. In this way a very good photon statistics per measurement locus can be achieved without inflicting any apparent damage upon the cell.
Comparing FLPM and FLIM, the major disadvantage of FLPM lies in the fact that ROIs have to be selected prior to measurements and cannot be changed afterwards. So spatial resolution is already being defined during experiments. Nevertheless a balance has to be found between number of measurement loci and acquisition time per locus to limit total measurement time. This is especially important in metaphase cells which tend to change their shape quite fast. Neither should interphase cells be subjected to measurements for more than a few minutes, a fact which is due to cellular movement as well as focus instability. In this work, two strategies were tested: arrival times were recorded either for 5 s or 30 s per locus. Depending on recording time per locus and on cell cycle phase, various numbers of measurement loci were chosen. The exact combinations as well as the resulting total measurement times are displayed in table 3.1 in chapter 3.8.1. Their spatial distribution within cells is displayed in Fig. 7.4.
Of course diffraction-limited measurement loci in FLPM experiments are considerably smaller than ROIs marked for analysis in imaging-based experiments. Yet they are distributed within the cell in a way similar to the distribution of ROIs in fluorescence and FLIM images. Therefore, the locus-to-locus heterogeneity of FLPM data can be considered to be equivalent to the ROI-to-ROI heterogeneity obtained in FLIM experiments. Therefore the term "ROI-to-ROI heterogeneity" will be used for the locus-to-locus heterogeneity in the subsequent sections.
Arrival time histograms obtained in FLPM measurements are analysed exactly in the same manner as those obtained in FLIM experiments.

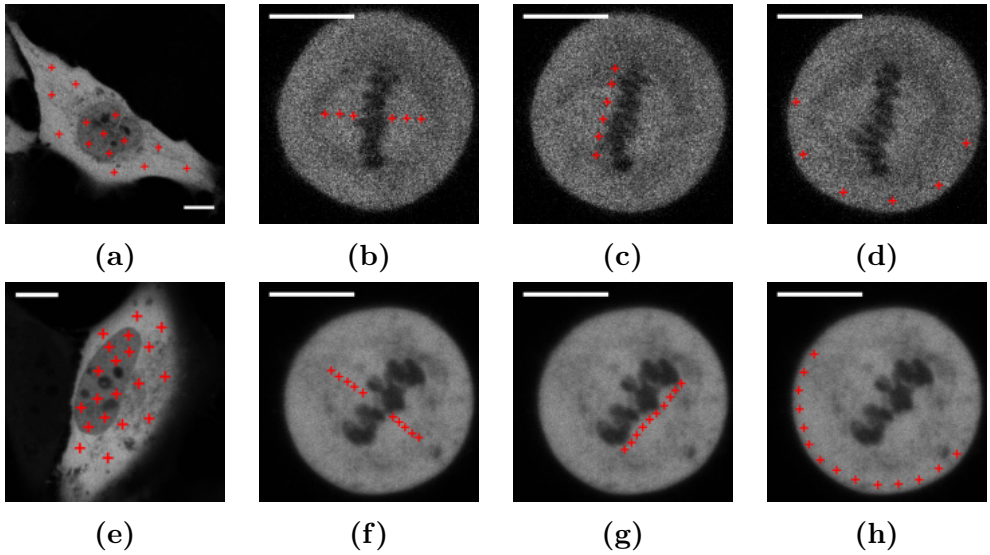

Figure 7.4: FLPM measurements - distribution of measurement loci. Top row: measurement time of 30 s per locus. Bottom row: measurement time of 5 s per locus. (a) + (e) Randomly distributed loci in interphase cells. (b) + (f) Parallel direction in metaphase spindle. (c) + (g) Perpendicular direction in metaphase spindle. (d) + (h) Spindle periphery. Scalebars 10 µm.

7.3.2 Overall Crowding States and ROI-to-ROI Heterogeneity on the 5 nm-Lengthscale

For both modi operandi, many measurement loci at short acquisition times as well as fewer measurement loci at longer acquisition times, the average ratio of compartment-wise average crowding levels was close to unity. The results are displayed in Fig. 7.5. The ratios in interphase and metaphase cells are nearly equal for the short time/many points-strategy, $\langle r \rangle_{int} = 1.008 \pm 0.057$ and $\langle r \rangle_{mit} = 1.011 \pm 0.061$. In the long time/few points mode, however, the interphase ratio is farther from unity than the metaphase ratio with $\langle r \rangle_{int} = 1.071 \pm 0.065$ and $\langle r \rangle_{mit} = 1.006 \pm 0.089$. Taken together with the results obtained via FLIM and ratiometric imaging, this might hint at a slightly more pronounced difference in crowding levels in interphase cells. Thus crowding levels would mirror, albeit much less pronounced, the tendency observed on the larger lengthscale tested by EGFP. However, the differences in crowding ratios on the 5 nm-scale are so small that they cannot be interpreted as significant, a fact which is especially true as it was not possible to perform adequate calibration measurements, e.g. in lysates or in polymer solutions containing purified fCrH2-molecules.

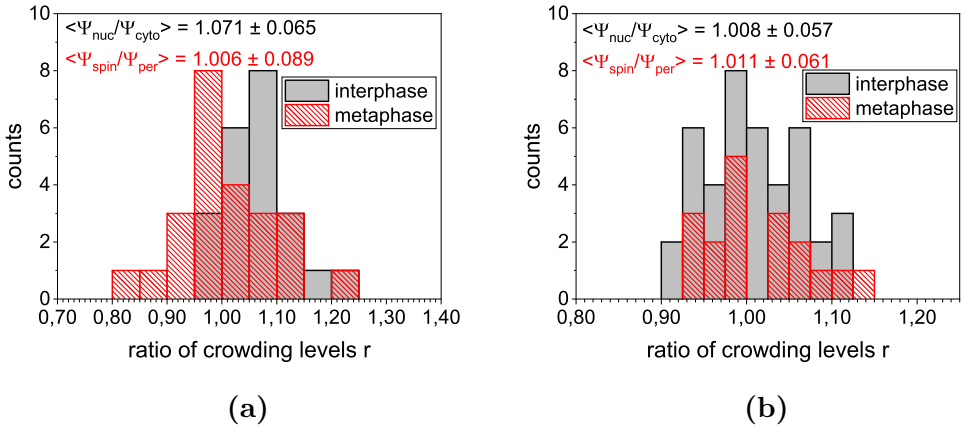

Figure 7.5: Overall crowding ratios obtained via FLPM. (a) Long measurement time but few measurement loci. (b) Short measurement time but many loci. Angle brackets signify ensemble averages ± ensemble standard deviations.

With respect to ROI-to-ROI heterogeneity levels both measurement strategies yield very similar results (see Fig. 7.6). For all compartments, heterogeneity levels are close to 10 %. Since heterogeneity levels in the spindle are slightly higher than in the periphery for many loci at short measurement times, but slightly lower for few loci at long measurement times, it seems reasonable to state that in metaphase cells ROI-to-ROI heterogeneities on the 5 nm-scale are the same in both compartments. Interestingly, in interphase cells ROI-to-ROI heterogeneities are slightly higher in the nucleoplasm than in the cytoplasm for both measurement modes. This is different from results at larger lengthscales, obtained in HeLa cells expressing EGFP. Of course it is quite possible that crowding heterogeneities show different tendencies on different lengthscales. However, this could also be a side-effect of the considerably lower expression level of fCrH2 in the interphase nucleus as compared to the cytoplasm. While fluorescence lifetime itself is, of course, independent of sensor concentration, fluorophore number does influence photon statistics and hence fit quality and reliability. So it is assumed that crowding heterogeneity is also the same in both compartments in interphase cells.
Assuming equal heterogeneity levels on the 5 nm-scale for all compartments is also supported by the distributions of compartment-wise heterogeneity levels across the cell ensemble. For all compartments and both measurement methods, individual heterogeneity levels are within the same range.

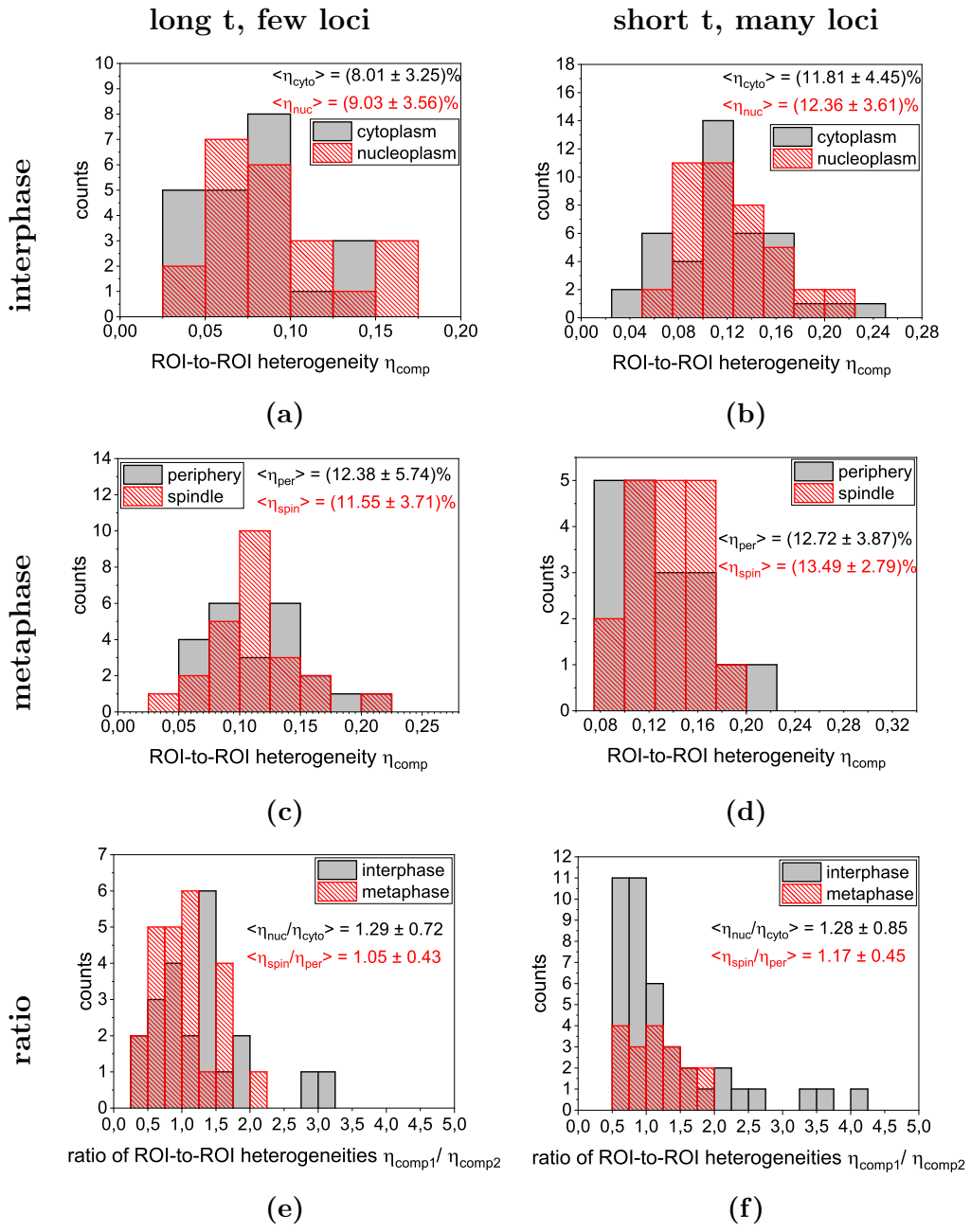

Figure 7.6: Intermediate heterogeneities obtained via FLPM. (a) Long measurement time but few loci in interphase cells. (b) Long measurement time but few loci in metaphase cells. (c) Short measurement time but many loci in interphase cells. (d) Short measurement time but many loci in metaphase cells. (e) Long measurement time but few loci, cell-wise ratio of compartment-wise heterogeneities in both interphase and metaphase cells. (f) Short measurement time but many loci, cell-wise ratio of compartment-wise heterogeneities in both interphase and metaphase cells. Angle brackets signify ensemble averages ± ensemble standard deviations.

The distribution of measurement loci parallel and perpendicular to the spindle axis (see Fig. 7.4) allows for an even finer spatial resolution within the metaphase spindle. However, in neither measurement mode any obvious functional patterning of more and less crowded regions could be observed (see Fig. 7.7). Since spatially resolved analyses of the metaphase spindle on larger lengthscales didn't yield any information, this result is not surprising.

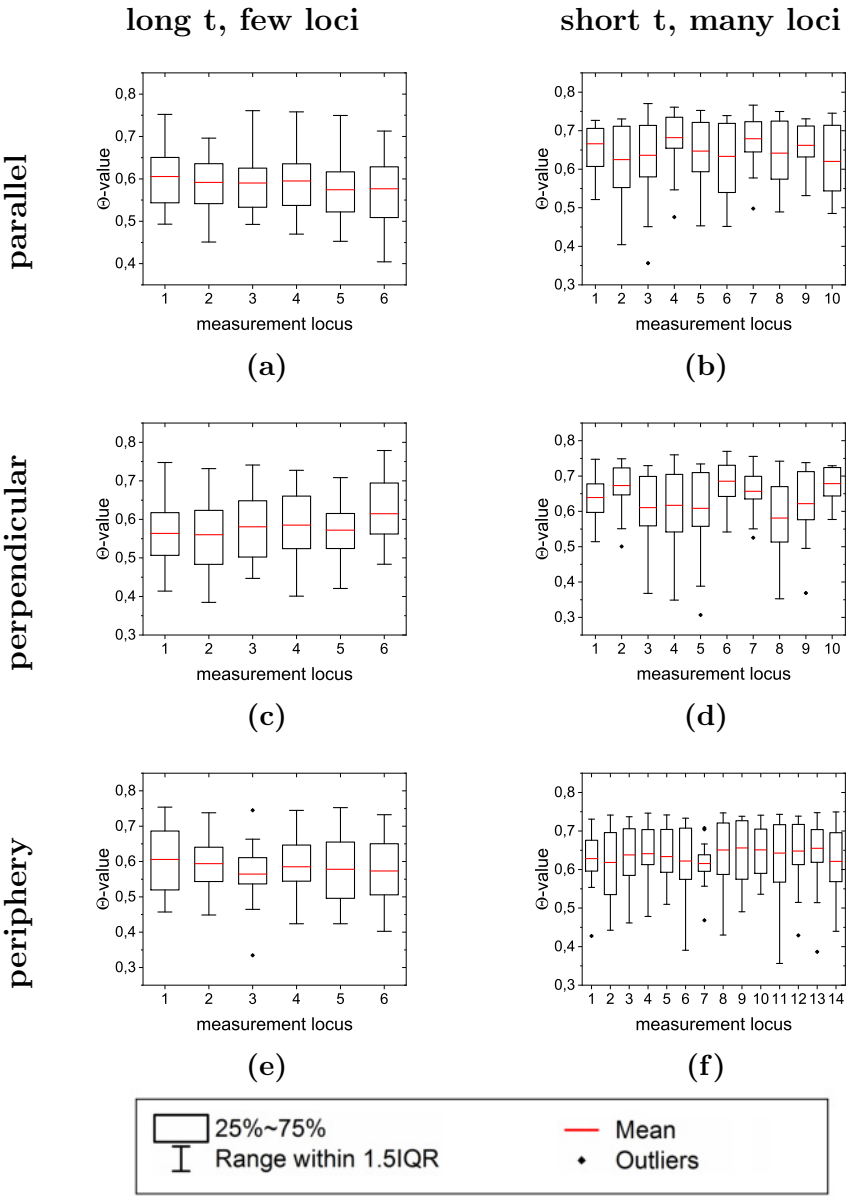

Figure 7.7: Spatially resolved analysis of the spindle region. Left column: long measurement times but few loci. Right column: short measurement times but many loci. (a) + (b) Measurement direction parallel to spindle. (c) + (d) Measurement direction perpendicular to spindle. (e) + (f) Spindle Periphery. Boxes represent all values within the interquartile range IQR. Whiskers indicate values within 1.5 interquartile ranges. Outliers were automatically discerned by ORIGIN2018.

7.3.3 Conclusion

In summary, FLPM experiments as well support the statement that crowding levels on the 5 nm-scale are very similar or even equal in both compartments in interphase cells as well as in metaphase cells.
Average heterogeneity levels are close to 10 % in all compartments. This is in stark contrast to ratiometric FRET imaging data, where average heterogeneity levels were found to be below 2 %, as well as FLIM data, where heterogeneity levels were found to be above 30 %. However, as FLPM neither suffers from susceptibility to detection settings (as ratiometric FRET imaging does) nor from unreliable fit results due to insufficient photon statistics (as FLIM does), FLPM is considered to be the most trustworthy method to characterize crowding on the 5 nm-scale.
This leads to the conclusion that below the diffraction limit crowding levels as well as crowding heterogeneities are very similar in all compartments. This is independent of cell cycle phase.
The absolute values obtained for heterogeneity levels in all compartments differ, at least at first glance, significantly from those obtained by Stiehl et al.[64]. By performing spatially resolved FCS and FLIM experiments, they basically probe the ROI-to-ROI heterogeneity on lengthscales below the diffraction limit, too. From anomaly factors and sensor fluorescence lifetimes they extrapolate to ROI-to-ROI heterogeneities of crowding levels. However, results obtained in this thesis differ from those obtained by Stiehl et al. in two major points: first, Stiehl et al. directly calculate ensemble heterogeneities from all measurement loci within all cells. In contrast to this method, in this thesis the focus is primarily on intracellular heterogeneity, the subject of intercellular heterogeneities is only briefly touched. Moreover, as a general rule ensemble averages are calculated using intracellular averages. Secondly, Stiehl et al. actually calculate the heterogeneity of the occupied volume fraction, whereas in this thesis generally the heterogeneity of the available volume fraction (or an observable linearly depending on it) is investigated. Since occupied and available volume fraction add up to one, their heterogeneities are related like

$$\eta(\varphi) = \left(\frac{1}{\mu(\varphi)} - 1\right)\eta(\phi). \tag{7.6}$$

The dependence on mean values cannot easily be eliminated from this equation. What is more, on the 5 nm-scale only a variable linearly depending on but not equivalent to the available volume fraction was accessible. So values obtained

in this thesis cannot directly be compared to those established by Stiehl et al. Therefore, in spite of their obvious discrepancy, both results do not necessarily exclude each other.

Chapter 8

Intracellular Crowding Levels and Crowding Heterogeneities During Stress Treatments

An overview of all lengthscales, observables and measurements in cells is given on p. 63-66. Ensemble statistics is summarized in appendix A.

8.1 Motivation

The previous three chapters aimed at characterizing intracellular crowding levels and crowding heterogeneities on various lengthscales in physiological cells in interphase and metaphase. The insights gained in these chapters can possibly be used in simulations of intracellular transport processes of particles, e.g. medical agents. In view of recent advances in fields like nanotechnology, nanomedicine or controlled release studies, more detailed knowledge about protoplasmic architecture on several lengthscales and its impact on intracellular processes will facilitate targeting individual locations in cells to treat diseases in a highly specialized manner [14] [15] [16]. Yet the fact should be considered that crowding levels, as well as crowding heterogeneities, could vary depending on the cell's state of health. The most prominent example of this phenomenon is osmolar stress: depending on the osmolarity of their surroundings, cells can rapidly change their shape and volume: uptake of water leads to a decreased overall crowding level, whereas dispensing water leads to an increased overall crowding level. Up to now no data have been available that indicate whether this change in overall crowding levels has any impact on crowding heterogeneities. In case of any impact of volume changes on crowding hetero-

geneities, crowding as well as heterogeneity levels in simulations would have to be adjusted dynamically to the cell's state of health in order to describe e.g. transport of medical agents adequately. The following chapter aims at identifying whether various kinds of stress treatments do influence crowding levels or heterogeneities or whether these observables remain robust under stress conditions.

8.2 Standard Experimental Procedure for all Time-Resolved Measurements During Stress Treatments

In order to check how cells react to stress treatments with respect to their crowding levels and crowding heterogeneities, cells expressing EGFP, fCrH2 or PercevalHR were subjected to one of five treatments: inducing either hyperosmolar, hypoosmolar or oxidative stress, depleting the cell of ATP or inducing apoptosis. The standard measurement procedure was to take an image of a physiological cell in isoosmolar standard imaging medium. Subsequently the medium was substituted by a special medium adapted to the respective treatment with the help of a pipette. The moment the medium was changed was defined as "time 0". After refocusing, time-resolved imaging was performed. The image acquired prior to treatment was assigned to "time 0" even though it was taken a few seconds before exchange of medium.
Depending on the expressed fluorescent protein, either 'traditional' fluorescence imaging or ratiometric imaging was performed. Please note that, due to their fairly long acquisition times, lifetime-based techniques could not be applied to perform stress measurements. With metaphase cells being much more vulnerable than interphase cells, all stress measurements were performed in interphase cells.
Image series were analysed according to the techniques described in chapters 5 and 6. However, only 10 ROIs per compartment were selected for analysis: depending on the respective treatment, cells can undergo substantial changes in shape and size. Thus it can be challenging or even impossible to select 20 ROIs within one compartment that do not overlap and are of similar size as those used in previous experiments. Reducing the total number of ROIs selected per compartment to 10 allows to draw the same number of non-overlapping, similarly sized ROIs in all images of the same series. The notable exception

to this rule are the control measurements performed in cells transfected with EGFP, which were already discussed in chapter 5 and will be displayed again in Sec. 8.3.1 of this chapter.
In order to enhance comparability of individual measurements, time-resolved results of each image series were divided by the values obtained in the first image of the same series, i.e. the one without treatment. Ensemble averages were taken after normalization.

8.3 Various Treatments and their Results

8.3.1 Control Measurements

Test measurements concerning a possible temporal evolution of overall crowding levels and their spatial heterogeneities have already been discussed in Sec. 5.7.2. Analysing absolute crowding ratios and heterogeneities leads to the conclusion that crowding levels and heterogeneities appear to vary only insignificantly in time. This holds true for measurement times of up to 30 min. In this chapter these test measurements can serve as a control.
However, in this chapter, as a matter of principle, only relative data are displayed and discussed: prior to averaging over several individual measurements, all results obtained in the same measurement are normalized on the initial levels of the respective observable, i.e. on the values obtained in the same cell before exposure to stress treatments. In order to improve comparability of measurements with and without treatments, the results discussed in Sec. 5.7.2 are displayed again in Fig. 8.1, but normalized on their initial values.

	relative intensity	relative ROI-to-ROI heterogeneity	relative voxelscale heterogeneity
nucleoplasm	0.30 %/2.19 %	11.41 %/20.09 %	21.92 %/13.47 %
cytoplasm	0.44 %/5.34 %	5.76 %/24.87 %	12.81 %/9.45 %
ratio	0.69 %/3.66 %	11.55 %/18.09 %	30.42 %/16.64 %

Table 8.1: Temporal heterogeneity of HeLa cell without treatment. First value: short measurement time at high temporal resolution. Second value: long measurement time at low temporal resolution. The drift part was excluded before calculating temporal heterogeneities.

Just as in Sec. 5.7.2 the left column of Fig. 8.1 displays results for a comparatively short measurement time at high temporal resolution, the right column displays results for a long measurement time at lower temporal resolution.

Of course, temporal heterogeneity is independent of normalization. As a reminder, temporal heterogeneities obtained for all observables in both time series (excluding the drift part that occurred during long measurement time) are repeated in table 8.1.

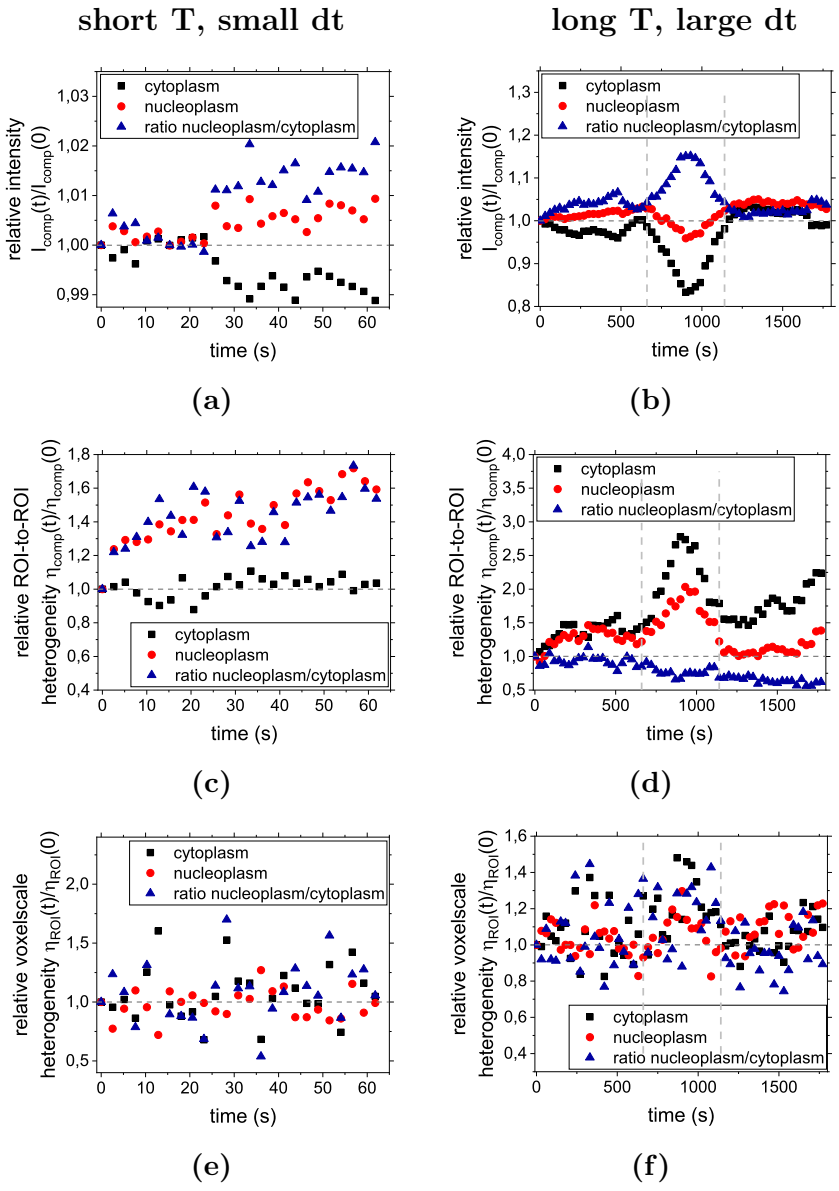

Figure 8.1: EGFP normalized without treatment. Left column: short measurement time at high temporal resolution. Right Column: long measurement time at low temporal resolution. The part between dashed lines could be identified as stage drift. (a) + (b) Relative intensity levels + ratios. (c) + (d) Relative ROI-to-ROI heterogeneity levels + ratios. (e) + (f) Voxelscale heterogeneity levels + ratio.

8.3.2 Osmolar Stress

Changes in osmotic pressure are a type of stress routinely encountered by some mammalian cell types, most notably kidney cells[163]. However, hyperosmotic stress has also been linked to several inflammatory disorders[164]. Cells respond to fluctuations in extracellular osmolarity by rapid volume changes driven by exchange of water with the surrounding medium[165][166][167][168][169]: due to water efflux cells subjected to hyperosmolar stress shrink. Cells subjected to hypoosmolar stress increase in size due to water influx. Thus the total volume can change by up to 30 %[165][166][167]. As volume change by means of water influx/efflux doesn't require more than approximately 1 s to 100 s, regulatory mechanisms to counterbalance volume changes are rarely initiated[163][170]. So volume change immediately after exposure to hypo-/hyperosmolar media represents a purely physico-chemical effect. After about 100 s regulatory mechanisms such as activation of enzymes, chaperones or synthesizing channels[163][170] initiate a gradual recovery of the isoosmolar configuration.
Of course, water influx or efflux significantly alters the concentration of all molecule species within cellular protoplasm[165][168][169]. Consequently, also the overall crowding level is expected to change in response to volume modulation. Studies on cellular responses to osmotic pressure in chondrocytes[171][172] suggest that nucleus and cytoplasm do not contribute equally to this overall change in volume. However, currently a similar study in HeLa does not exist. Up to the present it has not been identified whether the ratio of crowding levels in nucleoplasm and cytoplasm changes during water exchange. Additionally, until now no data on the intracellular heterogeneity of cells subjected to osmolar stress has been available. Therefore a number of time-resolved imaging experiments was performed in HeLa cells exposed to hyper- or hypoosmolar imaging medium, respectively. In order to induce hyperosmolar stress in cells, sodium chloride (NaCl) was added to standard imaging medium (0.3 Osm) until an osmolarity of 0.8 Osm was reached. To induce hypoosmolar stress, standard imaging medium was diluted with MilliQ water to a final osmolarity of 0.1 Osm. Since water is very small compared to other cellular constituents and makes up most of the native cell interior[22], changes were expected to take place predominantly on the nanometre scale. So cells were transfected with the FRET-based crowding sensor fCrH2.

By analogy with chapters 6 and 7, the ratio of molecules not undergoing FRET, $\Theta = 1 - F_{FRET} = \frac{D}{F+D}$, was used as an observable. It must be noted that, just as in physiological cells, absolute values of crowding levels cannot be determined since proper calibration measurements are not possible. However, all cells were analysed in their physiological state first and under stress conditions subsequently. Thus, relative changes in Θ over the course of the experiment can serve as an indicator of the changes in intracellular available volume fractions. Still, a relative change in Θ of 30 % does not necessarily represent a relative change in the available volume fraction φ of 30 %, as Θ also depends on measurement settings (see chapter 6.2). Therefore time-resolved ratiometric FRET experiments allow only general statements about the nature of crowding states and crowding heterogeneities in response to osmolar pressure.
It should be taken into consideration that the problems encountered in the analysis of ratiometric FRET images in physiological cells in chapter 6 also hold true during stress treatments. Due to the comparatively low expression level of fCrH2 in the nucleus, imaging-related errors might be disproportionally high in data obtained in this compartment. So especially the evaluation of nuclei during water uptake might be compromised: due to the increase in nuclear volume the initially fairly low concentration of fluorophores gets even more diluted. Thus the signal-to-noise ratio in both acquisition channels gets even worse. However, due to the long acquisition times lifetime-based measurement techniques cannot be utilized during osmolar stress treatments. So crowding on the 5 nm-lengthscale in cells subjected to stress treatments is only accessible via ratiometric FRET imaging.
Cells subjected to hyperosmolar stress respond with a rapid efflux of water, i.e. with a decrease in volume. So overall crowding is expected to increase. Consequently available volume fractions and hence Θ are expected to decrease. Cells subjected to hypoosmolar stress increase their volume by water influx. So crowding levels are expected to decrease, whereas the available volume fraction and hence Θ should increase.

Indeed, Θ can be observed to drop rapidly in both compartments immediately after switching from isoosmolar imaging medium to hyperosmolar imaging medium (see Fig. 8.2a). As is to be expected the available fraction decreases in both nucleoplasm and cytoplasm during exposure to hyperosmolar pressure. However, after about 50 s to 100 s relative available volume fractions reach a plateau value with the cytoplasmic level differing more from the native level

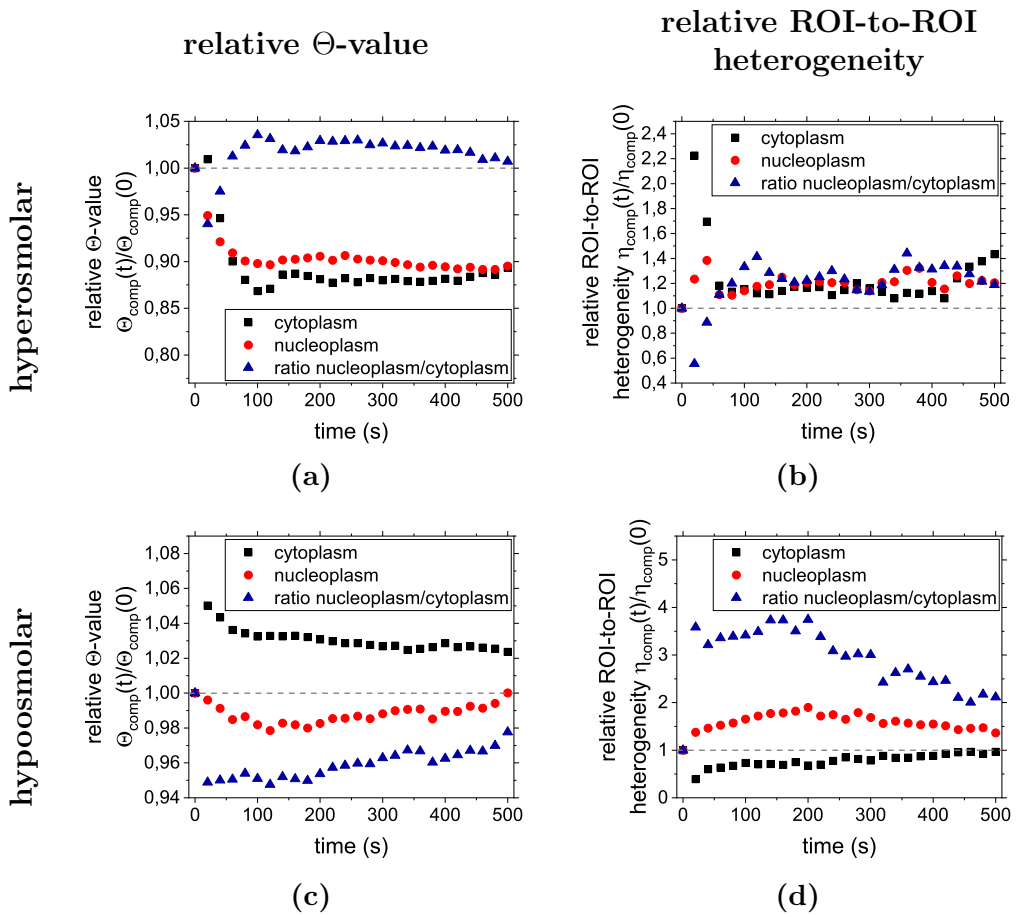

Figure 8.2: Changes in overall crowding states and ROI-to-ROI heterogeneities in response to osmolar stress treatments. (a) Overall crowding levels in cells subjected to hyperosmolar stress. (b) ROI-to-ROI heterogeneities in cells subjected to hyperosmolar stress. Averaged result of 11 cells. (c) Overall crowding levels in cells subjected to hypoosmolar stress. (d) ROI-to-ROI heterogeneities in cells subjected to hypoosmolar stress. Averaged result of 15 cells.

than the nucleoplasmic level. The whole process is mirrored in an increase in the ratio of relative available fractions, i.e. an increase in the ratio of Θ after about 50 s, followed by a slow decrease of the ratio until the initial ratio is reached again. So the initial ratio of available volume fraction between interphase compartments is gradually restored, although the plateau levels of Θ do not seem to change much in the course of about 400 s. In conclusion, there seems to be some exchange, probably of water, between nucleoplasm and cytoplasm, while overall available volume fractions remain decreased due to water efflux.

Under hyperosmolar pressure both compartments respond in the same way. Available volume fractions in cells subjected to hypoosmolar stress behave differently (see Fig. 8.2c): as is to be expected, available volume fractions in the cytoplasm increase immediately after switching from isoosmolar to hypoosmo-

lar imaging medium, i.e. Θ increases as a function of time. After approximately 50 s, available volume fractions in the cytoplasm start to decrease gradually. However, initial levels are not reached again within a measurement time of 10 min. By analogy with hyperosmolar stress response, this can be explained by the following scenario: a rapid influx of water immediately after exposure to hypoosmolar medium is followed by the somewhat slower regulatory response initiated to restore isoosmolar architecture. Contrary to expectations, available volume fractions in the nucleoplasm appear to decrease rapidly immediately after exchange of media. After about 100 s a slow increase in available volume fractions takes place until the initial value is reached again after about 7 min. Consequently, the ratio of relative available volume fractions decreases rapidly immediately after exchange of media. This is followed by a gradual increase in the ratio of available volume fractions after about 100 s. Yet, the initial ratio is not quite reached again during measurement time.

The remarkable disparity of cellular responses to hypo- and hyperosmolar stress, respectively, is, to some degree, also mirrored in the time course of ROI-to-ROI heterogeneities during osmolar stress treatments. Changes in ROI-to-ROI heterogeneities are parallel in the nucleoplasm and cytoplasm during exposure to hyperosmolar pressure (see Fig. 8.2b). Yet they are in opposite direction during exposure to hypoosmolar pressure (see Fig. 8.2d).

Consistent with the results obtained in physiological cells, the ROI-to-ROI heterogeneity of the available volume fraction in cells subjected to hyperosmolar stress is generally somewhat higher in the cytoplasm than in the nucleoplasm (data not shown). But the fact remains that the ratio of heterogeneity levels is close to one, a fact which is the rule in physiological cells. After onset of stress treatment the relative heterogeneity level increases in both compartments by about 20 %. The same holds true for the ratio of relative heterogeneity levels. Despite the gradual recovery of the ratio of relative available volume fractions during the same time after this initial increase the heterogeneity levels as well as their ratio stay more or less the same for the complete experiment.

It is interesting to note that cells subjected to hypoosmolar stress again behave quite differently. Immediately after exposure to hypoosmolar medium, the ROI-to-ROI heterogeneity of the available volume fraction rapidly decreases in the cytoplasm, while it simultaneously increases in the nucleoplasm. This results in a striking behaviour: during exposure to hypoosmolar pressure ROI-to-ROI heterogeneity levels in the nucleoplasm exceed those in the cytoplasm (not shown). After approximately 50 s in the cytoplasm and approximately

200 s in the nucleoplasm these trends are reversed: ROI-to-ROI-heterogeneities slowly go back towards initial levels. Yet, physiological heterogeneity levels are only reached in the cytoplasm during measurement time, heterogeneity in the nucleus stays considerably elevated. In general, independent of the direction of change, changes in heterogeneity seem to be slower in the nucleoplasm than in the cytoplasm. It might be possible that native heterogeneity levels return to their initial values in the nucleoplasm as well during continued exposure to hypoosmolar pressure, albeit after a longer time. The whole process is mirrored in the ratio of relative ROI-to-ROI heterogeneities of the available volume fraction: after a pronounced and fast increase during the first ~ 100 s, the ratio gradually decreases towards the physiological level. But the initial ratio is not reached any more during a measurement time of 10 min.

How can this striking behaviour be explained? In principle, hyperosmolar stress shrinks the nucleus which assumes a convoluted shape. Hypoosmolar stress causes the nucleus to swell and assume a smooth, globular shape. So it is reasonable to assume that nuclear crowding increases under hyperosmolar stress conditions and decreases under hypoosmolar stress conditions. In turn this would be visible in the experiments as a decrease in the available volume fraction in the nucleus while being exposed to hyperosmolar stress. Exposure to hypoosmolar stress would lead to an increase in the available volume fraction in the nucleus. The results obtained for cells subjected to hyperosmolar stress match that assumption. The response observed under hypoosmolar pressure, however, demands an explanation.

Intranuclear architecture differs from cytoplasmic architecture in its basic organization: while the cytoplasm features a multitude of membrane-bound vesicles, the dominant structures in the nucleoplasm are macromolecular aggregates. These aggregates consist mainly of decondensed chromatin binding to the nuclear envelope either directly or via other proteins[173]. In interphase cells, each chromosome occupies a distinct subvolume of the nucleus[174]. These subvolumes are separated and penetrated by the inter-chromatin domain, a network of chromatin-free channels which terminate at nuclear pore complexes[175] [176]. Sub-nuclear bodies such as nucleoli, speckles or Cajal bodies are usually found in the inter-chromatin domain as they are size-excluded from territories of dense chromatin[177]. The territories of decondensed chromatin are sustained by excluded volume effects and have been found to dissolve in dilute buffer[178] [179] [180].

During exposure to hypoosmolar pressure, the cell rapidly takes up water from the surrounding medium in an attempt to compensate the concentration gradient of osmotically active particles at least partially. In the cytoplasm this water uptake results in the reduction of absolute crowding levels, i.e. an increase in the available volume fraction, as many bigger structures are membrane-bound organelles which are not affected by water uptake. In the nucleoplasm, however, an initial increase in volume, i.e. a decrease in the occupied volume fraction, initiates further decondensation of chromatin, i.e. a further deorganization of the chromosome territories. However, DNA molecules can be expected to remain intact in spite of water uptake, as hypoosmolar stress is a widely occurring phenomenon.
In this thesis, cells subjected to osmolar stress were observed to recover gradually after their initial stress response. But the decondensation of chromosomes can easily result in a higher excluded volume fraction and hence a lower available volume fraction on the 5 nm-scale, even though the absolute nuclear volume is increased. Moreover, nuclear swelling is ultimately limited by nuclear lamina located in the nuclear membrane, since nuclear lamina cannot be stretched indefinitely. In combination, chromatin decondensation and limited nuclear swelling result in a nonlinear relation between the inverse cell volume and osmotic pressure, which is proportional to macromolecule concentration and, hence, crowding. Different from that, under hyperosmotic pressure nuclear crowding levels are inversely proportional to the nuclear volume[171].

8.3.3 Oxidative Stress

Oxidative stress refers to the inability of a cell to detoxify oxidizing molecule species and to repair the damage inflicted upon cellular components by these molecules. In healthy eukaryotic cells most oxidative molecules are rapidly destroyed by cellular defence mechanisms. Moreover, damages induced by oxidative stress are continuously repaired[181]. Yet an increased production of reactive oxidizing species as well as defect or inefficient antioxidant defence mechanisms can harm the cell or even a multicellular organism severely[182].
Oxidative stress can damage all intracellular components. In humans, it is thought to play a role in a vast number of diseases, including neurodegenerative diseases such as Parkinson's disease[183] and Alzheimer's disease[184], cardiovascular diseases such as atherosclerosis[185] or heart failure[186] as well as male infertility[187] [188] and age-related development of cancer[189] [190]. Most

long-term effects of oxidative stress are caused by base damage and strand breaks in DNA[191]. Thus, oxidative stress can ultimately be mutagenic[189]. It is interesting to note that oxidative stress has been found to trigger apoptosis and necrosis[192] as well as to suppress apoptosis[189] [193] [194]. Similarly, it has been found to play a role in premature ageing[195] as well as to be involved in lifespan extension[196] and prevention of ageing[197].

On the other hand, reactive oxygen species are crucial in naturally occurring intracellular processes such as redox signalling. Moreover, the immune system uses the toxic properties of reactive oxygen species to damage and ultimately kill pathogens[198] [199].

So basically the state of health of a particular cell depends on its ability to maintain a balance between production and consumption of reactive oxygen species in which at least small perturbations can rapidly be overcome. Oxidative stress has even been proposed to have played a major role in the evolution of eukaryotes: the biologically induced generation of oxygen in the earth's atmosphere approximately 2.5 billion years ago is thought to have been highly toxic to the surrounding organisms. So the selective pressure to thrive under oxidative stress might, amongst other environmental stresses, have driven the evolution of a lineage of archaea into the first eukaryotes to facilitate repair of damages induced by oxidative stress[200] [201] [202].

A natural source of reactive oxygen species is a leakage of activated oxygen from mitochondria during oxidative phosphorylation. In experiments oxidative stress can easily be induced by treating the cells with medium supplemented with oxidizing molecules such as hydrogen peroxide (H_2O_2).

As oxidative stress supposedly plays a role in numerous diseases, a precise characterization of crowding states under stress conditions as opposed to physiological conditions might provide a deeper understanding of these diseases as well as facilitate the development of new drugs. Until now, however, data has not been available that illustrates the influence oxidative stress exerts on crowding levels or on the heterogeneity of crowding. In this work, a number of cells was subjected to oxidative stress by treatment with hydrogen peroxide. As known short-term effects of reactive oxygen species are at the level of single molecules, it was decided to test the effects of oxidative stress on crowding and its heterogeneity on the 5 nm-scale. Therefore cells were transfected with the FRET-based crowding sensor fCrH2.

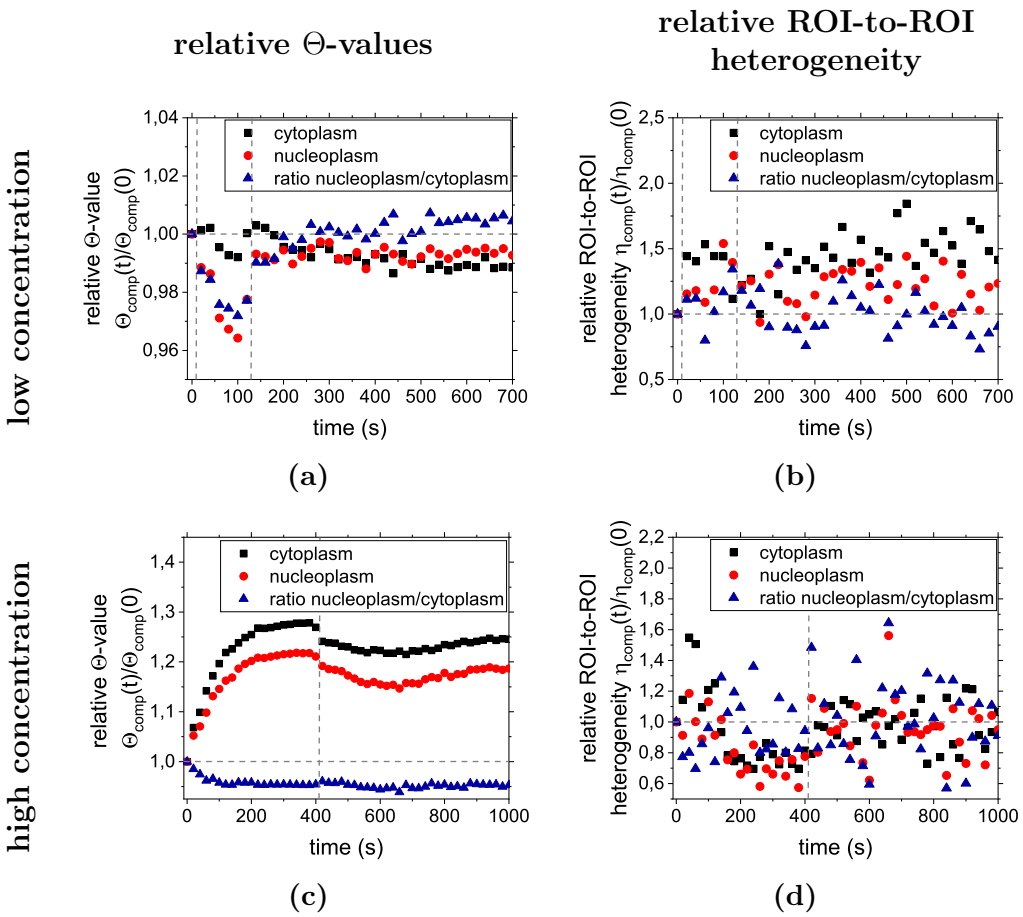

Figure 8.3: Changes in overall crowding states and ROI-to-ROI heterogeneities in response to oxidative stress treatments. (a) + (b) Exposure to moderate levels of oxidative stress. Averaged result of 3 cells. (c) + (d) Exposure to high levels of oxidative stress. Averaged result of 3 cells. (a) + (c) Relative FRET ratios. (b) + (d) Relative ROI-to-ROI heterogeneities.

Even though only a small set of test measurements could be performed for this thesis, it was found that changes in overall crowding levels clearly depend on hydrogen peroxide concentration. Following the approach described by Stiehl[127], the first two cells were treated with imaging medium supplemented with 0.3 mM hydrogen peroxide. A third cell was treated with imaging medium supplemented with 0.6 mM hydrogen peroxide. Since these cells responded in very much the same way, subsequently all three of them are treated as one population, i.e. as "cells subjected to low levels of oxidative stress". Their overall crowding ratios (Fig. 8.3a) virtually do not change during a measurement time of 11 min. The prominent dip during the first 2 min can be attributed to focal drift: in image series, the microscope used for these measurements very often shows an out-of-focus drift within the first few images, immediately followed by a drift in the opposite direction until the initially selected focal plane is

reached again. Until now the reason for this characteristic drift event hasn't be found. So, as a rule, measurements suffering from this drift event are not considered for further evaluation. In this case only a very small set of test measurements was performed. So excluding measurements in which focal drift occurred from further analysis was not viable. As crowding levels and ratio after the drift event stay constant and are at virtually the same level as before treatment, it can only be assumed that no significant change in crowding levels and ratios occurs within these 2 min.

The second group of cells, likewise consisting of only three individual cells, was treated with a considerably higher concentration of hydrogen peroxide - approximately 180 mM. At this concentration, in both compartments the available volume fraction significantly increases immediately after exposure to medium containing hydrogen peroxide (Fig. 8.3c). Within 4 min a relative increase of 20 % is reached in the nucleoplasm, a relative increase of 28 % is reached in the cytoplasm. Thus the ratio of available volume fractions decreases immediately after initial exposure. After this rapid response, both relative crowding levels as well as their ratio stay constant until the end of the measurement. The small drop in relative crowding levels after 6.5 min is solely due to insufficient measurement statistics: while values in the interval 0.0 min to 6.5 min represent the average of three individual measurements, only one of these measurements continues after 6.5 min.

In contrast to this striking reaction, at least to high concentrations of oxidative stress, neither of the compartments shows any distinct response to treatments on the ROI-to-ROI scale. Consequently also the ratio of ROI-to-ROI heterogeneities remains constant throughout the course of the measurement. This holds true for exposure to both high and low concentrations of hydrogen peroxide (Fig. 8.3d and 8.3b)

One could argue that, compared to exposure to osmolar stress, ROI-to-ROI heterogeneities under oxidative stress conditions do change significantly. After all, relative changes are in the same range as in osmolar stress conditions. However, in cells subjected to osmolar stress the ROI-to-ROI heterogeneity shows a rather distinct curve progression with little point-to-point variation. In contrast to that, data on ROI-to-ROI heterogeneities during exposure to oxidative stress are extremely noisy. Of course this might simply be caused by inadequate statistics. Noise levels could decrease significantly if a larger number of measurement series were taken and evaluated. However, with the data situation being as it is, ROI-to-ROI heterogeneities are preliminarily interpreted

not to change significantly. This is especially backed up by the conspicuous lack of change during the vast increase of compartment-wise Θ-levels at high concentrations of hydrogen peroxide at the begin of exposure. In contrast to that, ROI-to-ROI heterogeneities in cells subjected to osmolar stress mirrored the time course of Θ-levels, albeit in the opposite direction.
So damage caused by oxidative stress seems to be fairly homogeneous within one compartment. Moreover, overall crowding levels appear to be affected only at high levels of oxidative stress. In this case, the cytoplasm shows a stronger reaction than the nucleoplasm. Due to the small number of measurements, however, these results should be treated as preliminary.
It would be interesting to investigate the causes of the difference in relative changes in crowding levels in nucleus and cytoplasm at high levels of oxidative stress. For example it could be due to a lower vulnerability of nuclear constituents to reactive oxygen species, better or faster repair and defence mechanisms in the nucleus or simply the cytoplasm and nuclear membrane serving as a protective layer between the nucleoplasm and the surrounding, hydrogen peroxide-enriched medium. This, however, remains to be analysed in future work on the topic.

8.3.4 Treatments Impairing ATP Regeneration

Adenosine triphosphate (ATP) is frequently referred to as a "molecular unit of currency" for intracellular energy transfer[203]. It provides the energy required for many energy-consuming processes in living cells, such as chemical synthesis of proteins. During metabolic processes it is dephosphorylated to form either adenosine diphosphate (ADP) or adenosine monophosphate (AMP). Both are considerably lower in energy than ATP. Subsequently, ADP or AMP, respectively, is regenerated to ATP either in the cytosol during glycolysis or in mitochondria as part of the electron transport chain. A third pathway of ATP regeneration which is located in the nucleoplasm was recently proposed by Wright et al.[204]. It was established that each day the human body recycles the equivalent of its own body weight in ATP[205]. ATP:ADP ratios in healthy mammalian cells can range from 1 to more than 100[206] [207] [208] [209].
Decreased levels of intracellular ATP contents - and, respectively, increased levels of intracellular ADP or AMP contents - might be associated with a number of diseases in humans, such as fibromyalgia[210], myalgic encephalomyelitis/chronic fatigue syndrome[211] [212] [213] and dysfunction of retinal cells due to increased oxidative stress damage[214].

In experiments, the regeneration of ATP can easily be manipulated by means of chemical inhibitors, such as rotenone, oligomycin, several fungicides, antibiotics, azides and carbon monoxide. Most of them inhibit a specific complex which participates in the respiratory chain in mitochondria. In this thesis, two combinations of substances were used to manipulate ATP recycling: sodium azide and 2-deoxy-D-glucose (p. 57 et seq.) as well as rotenone and oligomycin (p. 57 et seq.).
Cells were either transfected with EGFP or with Perceval HR. EGFP was employed to investigate possible effects of ATP depletion on the compartment-wise crowding states and their heterogeneities. Perceval HR is a ratiometric sensor that, depending on the combination of illumination settings (405 nm and 488 nm or 458 nm and 488 nm), reflects the local ATP:ADP or ATP:isosbestic point ratio, respectively. For a more detailed description of Perceval HR and the relation between adenosine phosphate concentrations and emitted intensity, see Sec. 4.2.1. An example of a cell transfected with Perceval HR is displayed in Fig. 8.4.

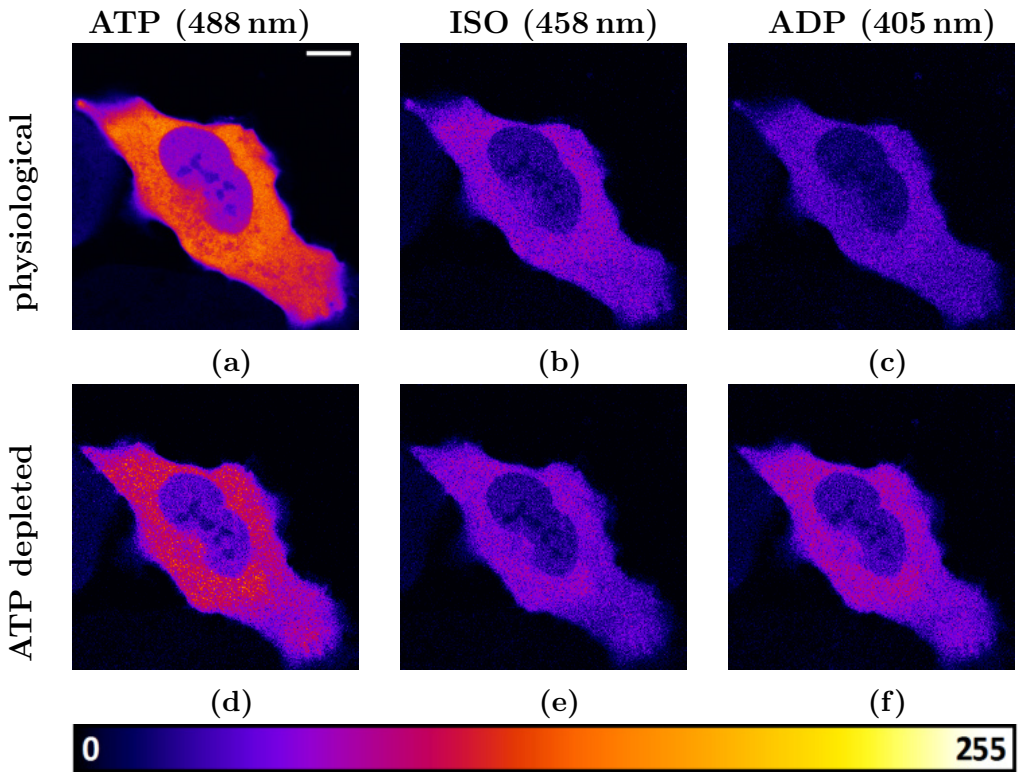

Figure 8.4: Cell transfected with Perceval HR during ATP depletion. Top row: before ATP depletion. Bottom row: 25 min after onset of ATP depletion with sodium azide and 2-deoxy-D-glucose. (a) + (d) ATP-excitation. (b) + (e) Isosbestic point excitation. (d) + (f) ADP excitation. Scalebar 10 µm. False colour images, colour signifies intensity.

Evaluation was done in analogy to previous experiments in HeLa cells transfected with EGFP or fCrH2: 20 ROIs per compartment per interphase cell were selected. For each ROI the mean ATP:ADP ratio as well as the mean ATP:isosbestic point ratio was calculated. The mean values per ROI were used to calculate the mean ratio per compartment (ATP:ADP$_{comp}$ and ATP:ISO$_{comp}$) as well as the ROI-to-ROI heterogeneity per compartment (η_{comp}(ATP:ADP) and η_{comp}(ATP:ISO)). Similar to previous analyses, the cell-wise ratios of mean ATP:ADP/ATP:isosbestic point levels were calculated according to

$$r = \begin{cases} \frac{ATP{:}ADP_{nuc}}{ATP{:}ADP_{cyto}} & \text{for ATP:ADP levels} \\ \frac{ATP{:}ISO_{spin}}{ATP{:}ISO_{per}} & \text{for ATP:isosbestic point levels.} \end{cases} \tag{8.1}$$

In addition, the cell-wise ratios of ROI-to-ROI heterogeneities were calculated according to

$$r_\eta = \begin{cases} \frac{\eta_{nuc}(ATP{:}ADP)}{\eta_{cyto}(ATP{:}ADP)} & \text{for ATP:ADP levels} \\ \frac{\eta_{spin}(ATP{:}ISO)}{\eta_{per}(ATP{:}ISO)} & \text{for ATP:isosbestic point levels.} \end{cases} \tag{8.2}$$

It must be mentioned, however, that in contrast to cells transfected with EGFP, cells transfected with Perceval HR can only be evaluated at two length-scales. As this sensor relies on a ratiometric analysis method an analysis of the voxel-to-voxel heterogeneity is not possible: as mentioned in chapter 5.3.3 the pixel-wise variance of fluorescence intensity can be described by Eq. 5.12. All detection channels operated at exactly the same settings. Additionally the excitation laser beams were adjusted to emit at the same absolute laser power. Thus the proportionality factor ξ can be assumed to be the same in all detection channels. So the pixel-wise variance is

$$\sigma^2_{ATP}(I_{ATP}) = \xi^2 \ (\mu_{ATP}(I_{ATP}) + \sigma^2_{ATP}(sample)), \tag{8.3}$$

$$\sigma^2_{ADP}(I_{ADP}) = \xi^2 \ (\mu_{ADP}(I_{ADP}) + \sigma^2_{ADP}(sample)), \tag{8.4}$$

$$\sigma^2_{ISO}(I_{ISO}) = \xi^2 \ (\mu_{ISO}(I_{ISO}) + \sigma^2_{ISO}(sample)), \tag{8.5}$$

for ATP-, ADP- and isosbestic point channels, respectively. The signal investigated in this work is either the local ATP:ADP ratio or the local ATP:isosbestic point ratio, which is given by the pixel-wise ratio $r_{px} = I_{ATP}/I_{ADP/ISO}$. By

propagation of uncertainty the variance of r_{px} within a ROI is given by

$$\sigma^2(r) = \left(\frac{\partial r}{\partial \mu_{ATP}} \cdot \sigma_{ATP}\right)^2 + \left(\frac{\partial r}{\partial \mu_{ADP/ISO}} \cdot \sigma_{ADP/ISO}\right)^2. \tag{8.6}$$

In a perfectly homogeneous sample, i.e. a sample lacking any inherent variance $\sigma^2_{ATP}(sample)$, $\sigma^2_{ADP/ISO}(sample)$ of the fluorophore distribution, this is

$$\sigma^2_{hom}(r) = \xi^2 \left(\frac{\mu_{ATP}}{\mu^2_{ADP/ISO}} + \frac{\mu^2_{ATP}}{\mu^3_{ADP/ISO}}\right) = \xi^2 \frac{r(1+r)}{\mu_{ADP/ISO}}. \tag{8.7}$$

In an inhomogeneous sample, Eq. 8.6 changes to

$$\begin{aligned}
\sigma^2_{inhom}(r) &= \xi^2 \frac{1}{\mu^2_{ADP/ISO}} \left(\mu_{ATP} + \sigma^2_{ATP}(sample)\right) + \\
&+ \xi^2 \frac{\mu^2_{ATP}}{\mu^4_{ADP/ISO}} \left(\mu_{ADP/ISO} + \sigma^2_{ADP/ISO}(sample)\right) \\
&= \xi^2 \frac{r(1+r)}{\mu_{ADP/ISO}} + \xi^2 \frac{\left(\sigma^2_{ATP}(sample) + r^2 \sigma^2_{ADP/ISO}(sample)\right)}{\mu^2_{ADP/ISO}} \\
&=: \sigma^2_{hom}(r) + \delta^2_{inhom}(r).
\end{aligned} \tag{8.8}$$

So similar to FRET-based ratiometric imaging, it is not possible to separate the sample-inherent voxel-wise heterogeneity of ATP:ADP and ATP:isosbestic point ratios from setup- and intensity-dependent factors in ratiometric imaging data. Additionally the complex relation between the measured variance $\sigma^2(r)$, the ATP:ADP or ATP:isosbestic point ratio itself and the observables of individual channels prevents a calibration of the absolute ATP:ADP and ATP:isosbestic point heterogeneities by means of, for example, cell lysates.
Therefore, similar to FRET-based experiments, the ATP:ADP and ATP:isosbestic point ratio is only analysed on the compartment levels and on the ROI-to-ROI levels. Again, for all images a line average of $LA = 2$ was chosen in order to decrease, at least to some extent, a possible influence of instrument settings on results at these lengthscales.

ATP:ADP and ATP:Isosbestic Point Ratios in Physiological Cells

Prior to ATP depletion measurements, images in all three illumination modes, 405 nm, 458 nm and 488 nm, were taken in cells not subjected to any stress treatment. This was done in order to establish the mean ATP:ADP ratios

and ATP:isosbestic point ratios per compartment as well as their respective ROI-to-ROI heterogeneities for physiological HeLa cells.

Averaged ATP:ADP and ATP:Isosbestic Point Ratio. Although distributions of ATP:isosbestic point ratios in nucleoplasm and cytoplasm are very similar (Fig. 8.5b), in the majority of cells the ATP:isosbestic point ratio is higher in the nucleoplasm than in the cytoplasm (Fig. 8.5d). The average cell-wise ratio of compartment-wise ATP:isosbestic point ratios was found to be $\langle r \rangle_{int} = 1.03 \pm 0.04$. At the same time, in all cells the ATP:ADP ratio is somewhat higher in the nucleoplasm than in the cytoplasm. The cell-wise ratio of compartment-wise ATP:ADP ratios was found to be $\langle r \rangle_{int} = 1.09 \pm 0.04$ (Fig. 8.5c). This is also visible in the distributions of ATP:ADP ratios per compartment (Fig. 8.5a). The fact that this ratio between compartments is somewhat farther from one than the ratio of ATP:isosbestic point ratios indicates that also ADP levels differ between nucleoplasm and cytoplasm. ADP levels appear to be somewhat lower in the nucleoplasm than in the cytoplasm. Yet the different cell-wise ratios of compartment-wise ratios might also be influenced by measurement settings: the isosbestic point of Perceval HR is located at 455 nm. However, an excitation of this particular wavelength is not possible in the given setup. Therefore, experiments were performed at an excitation wavelength of 458 nm. While, at first glance, a deviation of only 3 nm from the ideal excitation wavelength appears to be negligible, one must keep in mind that the maximum of ATP-dependent emission is already located at ~ 500 nm. So it is possible that the excitation wavelength lying in the ATP-dependent part of the spectrum has a non-negligible effect on the obtained ratiometric data in spite of its closeness to the isosbestic point. This effect might well influence the ratio of ATP:isosbestic point levels between cytoplasm and nucleoplasm.
In addition to that, it must be noted that neither the obtained ATP:ADP ratio nor the obtained ATP:isosbestic point ratio should be interpreted to directly represent the actual value of the respective variable. While all images are obtained at exactly the same detection settings, the excitation wavelength is different for all three images. The absolute laser intensity arriving at the sample plane was measured for all laser lines to find a setting where incoming laser intensity is the same for all three images. Yet, measuring laser intensity with a photometer is a rather imprecise method, all the more so since the sensor of the available photometer cannot be built into the beam path but

has to be held by hand. Due to generally low transfection rates in spite of protocol optimization it was also not possible to perform any calibration measurement in cell lysates, e.g. by adding defined amounts of ATP or ADP to the lysate. When comparing the ATP:ADP ratios in interphase cells obtained in this work with the data gathered by Tantama et al.[133], this discrepancy between measured values and actual ATP:ADP ratios becomes especially clear: in this work fluorescence ratios in the range of $5-9$ were obtained for both compartments. Yet, according to Tantama et al. a ratio of fluorescence signals higher than 4 is not obtained at all. Most likely this discrepancy in results can be attributed to the differing setups. Therefore, the obtained ATP:ADP ratios and ATP:isosbestic point ratios should rather be considered to show general tendencies instead of absolute values. So the only possible conclusion from the available data is the fact that the ATP:ADP ratio is higher in the nucleoplasm than in the cytoplasm.

This result as is is somewhat surprising. The major ATP recovery pathways take place in the cytoplasm. Maintenance of nuclear ATP:ADP levels primarily relies on transport between nucleoplasm and cytoplasm. So one would expect ATP:ADP levels to be higher in the cytoplasm than in the nucleus. Interestingly, Imamura et al.[215] indeed found ATP:ADP levels to be slightly higher in the cytoplasm than in the nucleoplasm. Yet, while they also used HeLa cells in their experiments, the employed sensor was different from the one used in this work. In particular, while Perceval HR is expressed both in the cytoplasm as well as in the nucleoplasm of HeLa cells, albeit at somewhat different expression levels, the sensor used by Imamura et al. is mainly distributed in the cytoplasm. Therefore they fused a nuclear localization signal to their sensor. They did, however, not investigate whether this addition to the molecule alters the susceptibility of the sensor to the local ATP:ADP level in any way. They found the ATP:ADP levels to be considerably lower inside mitochondria than in cytoplasm and nucleoplasm. This is somewhat counterintuitive since mitochondria are a major locus of ATP production inside the cell. Of course, ATP could be transported out of mitochondria quite fast so that ADP could be enriched within mitochondria, while ATP would be enriched in their immediate surroundings.
On the other hand, a more recent study by Wright et al.[204] suggests the existence of a nuclear metabolic pathway generating ATP via the hydrolysis of poly(ADP-ribose) and ADP-ribose. This pathway is supposed to be essential

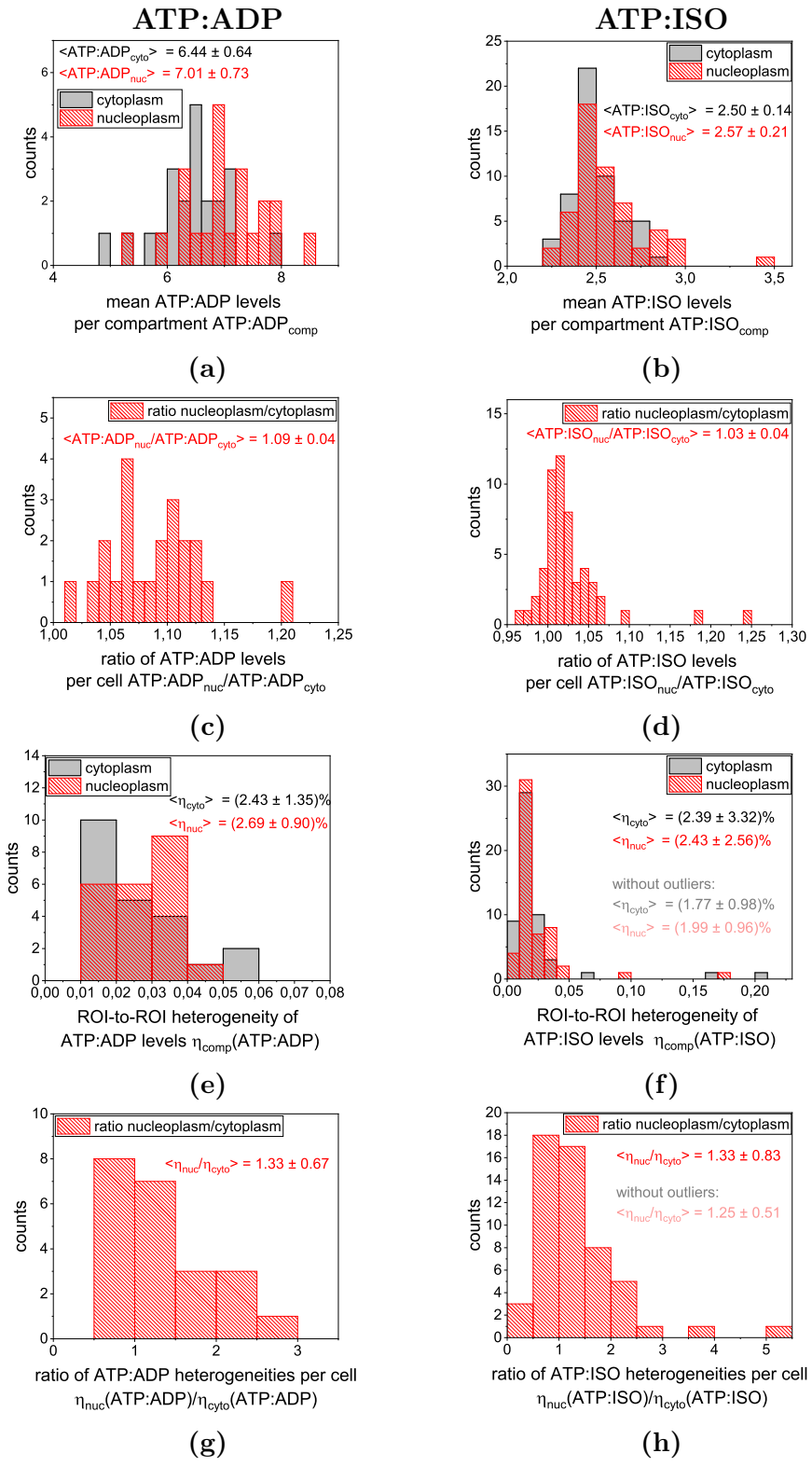

Figure 8.5: ATP:ADP and ATP:isosbestic point ratios in physiological cells. Left column: ATP:ADP ratio. Right column: ATP:isosbestic point ratio. (a) + (b) Overall ratios per compartment. (c) + (d) Cell-wise ratios of average energy ratios per compartment. (e) + (f) Compartment-wise ROI-to-ROI heterogeneity of energy ratios. (g) + (h) Cell-wise ratio of compartment-wise ROI-to-ROI heterogeneities. Angle brackets signify ensemble averages ± ensemble standard deviations. Data on ATP:ADP ratio: Result of 22 cells. Data on ATP:ISO ratio: Result of 54 cells.

for several biochemical processes located in the nucleus, such as chromatin remodelling or transcriptional regulation. Moreover, while Wright et al. mainly focused on the changes of compartment-wise ATP:ADP levels in response to hormone-treatments, their data also suggest the ATP:ADP ratio in the nucleus to be higher than in the cytoplasm even before treatments. However, Wright et al. performed their experiments on breast cancer cells whereas in this thesis HeLa cells were used. So a direct comparison of the results should be treated with caution.
The different ATP:ADP or ATP:isosbestic point ratios in nucleus and cytoplasm might also be a side-effect of the different transfection levels in both compartments. This disparity in expression levels is not as pronounced as it is in cells transfected with fCrH2. Yet it might be enough to introduce random errors into the results obtained in the less intensive nuclei via division by small numbers.
Finally, it is possible that the cytoplasm simply harbours more sites of high energy-consumption. If this was the case, metabolic turnover of ATP, ADP and AMP could be faster in the cytoplasm, resulting in - at least locally - lower ATP:ADP levels.

ROI-to-ROI Heterogeneity of ATP:ADP and ATP:Isosbestic Point Ratios. Independently of the observable, i.e. the ATP:ADP ratio or the ATP:isosbestic point ratio, the ROI-to-ROI heterogeneity is quite low in both compartments. The average ROI-to-ROI heterogeneity of the ATP:ADP ratio was found to be $(2.4 \pm 1.3)\,\%$ in the cytoplasm and slightly higher, $(2.7 \pm 0.9)\,\%$ in the nucleoplasm (Fig. 8.5e). Averaged results are even more similar when the ATP:isosbestic point ratio serves as an observable: here ROI-to-ROI heterogeneities of $(2.4 \pm 3.3)\,\%$ in the cytoplasm and $(2.4 \pm 2.5)\,\%$ in the nucleoplasm are reached (Fig. 8.5f). Taking only the respective distributions of compartment-wise ROI-to-ROI heterogeneities into consideration, it appears to be justified to regard both compartments as rather equally heterogeneous.
It is interesting to note that in about 2/3 of the cells the ATP:ADP ratio is a little more heterogeneous in the nucleus than in the cytoplasm. Yet about 1/3 of the cell ensemble displays exactly the opposite behaviour. The ensemble mean of compartment-wise ratios of ATP:ADP heterogeneities is 1.33 ± 0.67 (Fig. 8.5g). A very similar result is found for the ratio of ATP:isosbestic point heterogeneities. Here the ensemble average is 1.33 ± 0.83 (Fig. 8.5h). Although the distributions of compartment-wise ROI-to-ROI heterogeneities look very

similar, this fact appears to reflect the intercellular rather than the intracellular variation.

The ensemble variation of ATP:ADP heterogeneities is, however, in the same range as ensemble heterogeneities in cells transfected with EGFP or fCrH2: ensemble-wise heterogeneities were found to be about 33 % in the nucleoplasm and about 56 % in the cytoplasm. The ensemble heterogeneity of the cell-wise ratio of compartment-wise ROI-to-ROI heterogeneities is about 50 %.

When using the ATP:isosbestic point ratio as an observable, ensemble wide heterogeneities are extremely high: levels of about 139 % in the cytoplasm and about 105 % in the nucleoplasm are reached. This amounts to an ensemble heterogeneity of the ratio of nucleoplasmic to cytoplasmic heterogeneity levels of 63 %. At first glance, these values are surprisingly high, especially when taking into consideration the rather similar ensemble averages. However, these can easily be explained: the ensemble of cells imaged at ATP and isosbestic point wavelengths is considerably larger than that imaged at ATP and ADP wavelengths: 54 versus 22 cells. A more direct comparison of ATP:ADP and ATP:isosbestic point results can be achieved when only analysing the (sub)ensemble of 22 cells in which images at all three excitation wavelengths were acquired. In this ensemble, ATP:isosbestic point ROI-to-ROI heterogeneities were found to be (1.49 ± 0.53) % in the cytoplasm and (1.63 ± 0.54) % in the nucleoplasm, which amounts to ensemble heterogeneities of 36 % and 33 %, respectively. The average ratio was found to be 1.16 ± 0.38, which results in an ensemble heterogeneity of 33 %. Differences in these values from those obtained for the ATP:ADP ratio can be attributed to systematic aberrations due to the different measurement settings as well as to stochastic influences from the setup.

Considering the complete ensemble of cells imaged at ATP and isosbestic point excitation wavelengths, a few outliers in the ROI-to-ROI heterogeneity attract attention. After removing them, ensemble averages as well as ensemble heterogeneities are similar to values obtained in the sub-ensemble in both imaging modes: ensemble averages of (1.77 ± 0.98) % in the cytoplasm and (1.99 ± 0.96) % in the nucleoplasm render ensemble heterogeneities of 55 % and 48 %, respectively. Then the ratio of compartment-wise ROI-to-ROI heterogeneities is 1.25 ± 0.51, resulting in an ensemble heterogeneity of 41 %. However, the reasons for outliers in these specific cells cannot be ascertained: both ATP and isosbestic point images do not differ visually from other images, the ratiometric images are not conspicuous either. Interestingly, an outlier in

ROI-to-ROI heterogeneity in any of the compartments does not necessarily coincide with an outlier in the respective overall ATP:isosbestic point ratio. Since all outliers appear in the sub-population imaged only in ATP and isosbestic point mode, it cannot be tested whether they represent a characteristic feature of the sample or a random error due to the measurement technique.
So, with regard to the quite unintuitive observable, it appears questionable to simply remove outliers. After all, they might represent an actual feature of the cell population: cells were not synchronized. So presumably within one sample all cell cycle phases are present in equal fractions. Probably the total amount of energy needed within one cell doesn't vary that much over the course of one complete cell cycle. Yet, it appears reasonable to assume that the spatial distribution of loci needing much energy varies considerably throughout the cell cycle: each cell cycle phase is characterized by a number of distinct biochemical processes that must be completed prior to progression into the next cell cycle phase. The vast majority of these biochemical reactions should either generate or consume energy, resulting in locally varying ATP:ADP ratios. As the cell progresses through interphase, presumably the 'hotspots' of ATP consumption and production change temporally. Thus the heterogeneity of ATP:ADP ratios on several lengthscales might potentially be altered. So the broad distribution of ROI-to-ROI heterogeneities throughout the cell ensemble might simply reflect the distribution of morphologically undistinguishable cell cycle phases in a non-synchronized cell population.
It would be interesting to test the hypothesis of temporal variation of ATP:ADP heterogeneities. To do so one cell would have to be imaged repeatedly until completing a whole cell cycle. As discussed earlier, it is difficult to achieve this aim with the equipment available for this thesis .

ATP Depletion via Rotenone and Oligomycin

Rotenone prevents the transport of electrons in complex I of the respiratory chain. This interferes with NADH, thus hindering ATP production[216]. As a side-effect, cellular oxygen is reduced, which results in the creation of reactive oxygen species[217]. Furthermore, rotenone also suppresses the assembly of microtubules[218]. However, moderate levels of ATP can still be produced in complex II of the respiratory chain (see Fig. 8.6).
Oligomycin blocks a subunit of ATP synthase, which significantly slows down electron transport[219] [220]. Yet, with the help of uncoupling proteins electron

transport does not stop completely.[221]. Nevertheless, oxidative phosphorylation of ADP is largely suppressed.

In combination, rotenone and oligomycin impede ATP regeneration but do not stop it. In particular, cytosolic production of ATP during glycolysis is not affected by this treatment. Nevertheless, apoptosis is induced. So most cells die within 1 h.

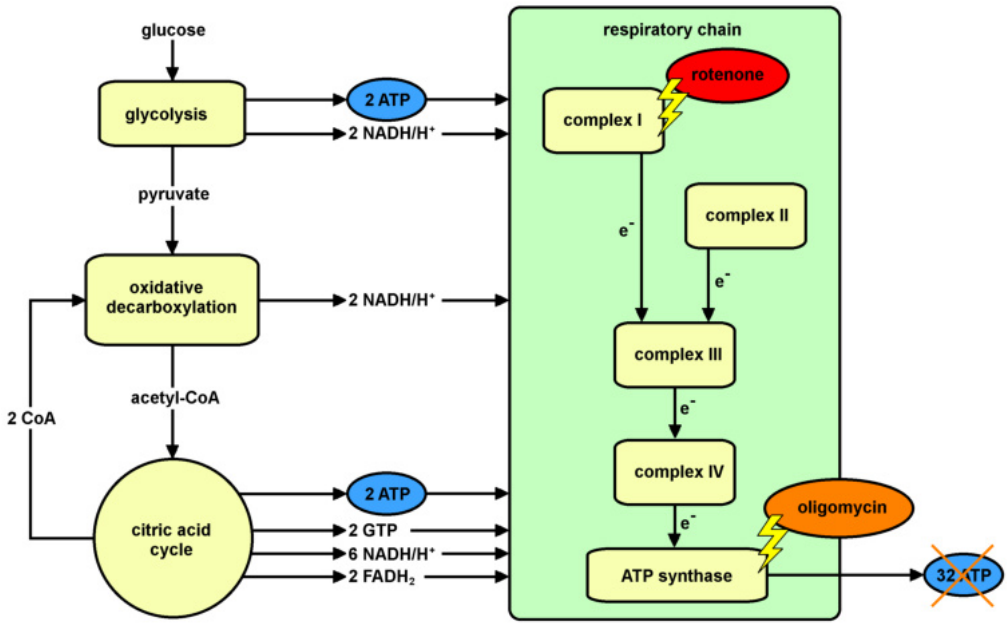

Figure 8.6: Impact of rotenone and oligomycin treatment on cellular ATP regeneration. While rotenone completely blocks complex-I-activity, complex II still works. Oligomycin blocks a subunit of ATP synthase, however, due to uncoupling proteins, oxidative phosphorylation is not completely stopped. ATP production in glycolysis and citric acid cycle is not hindered. Therefore, ATP regeneration is significantly impaired but does not stop completely.

ATP depletion experiments using rotenone and oligomycin were performed on cells transfected with Perceval HR. In all measurements, images were taken at excitation wavelengths of 458 nm and 488 nm, respectively. So, in all images, the ATP:isosbestic-point ratio served as an observable.

Rotenone and oligomycin were used in four different concentrations:

Name	rotenone (µM)	oligomycin (µM)
C1	0.8	1.8
C2	0.6	1.5
C3	0.5	1.25
C4	0.4	1.0

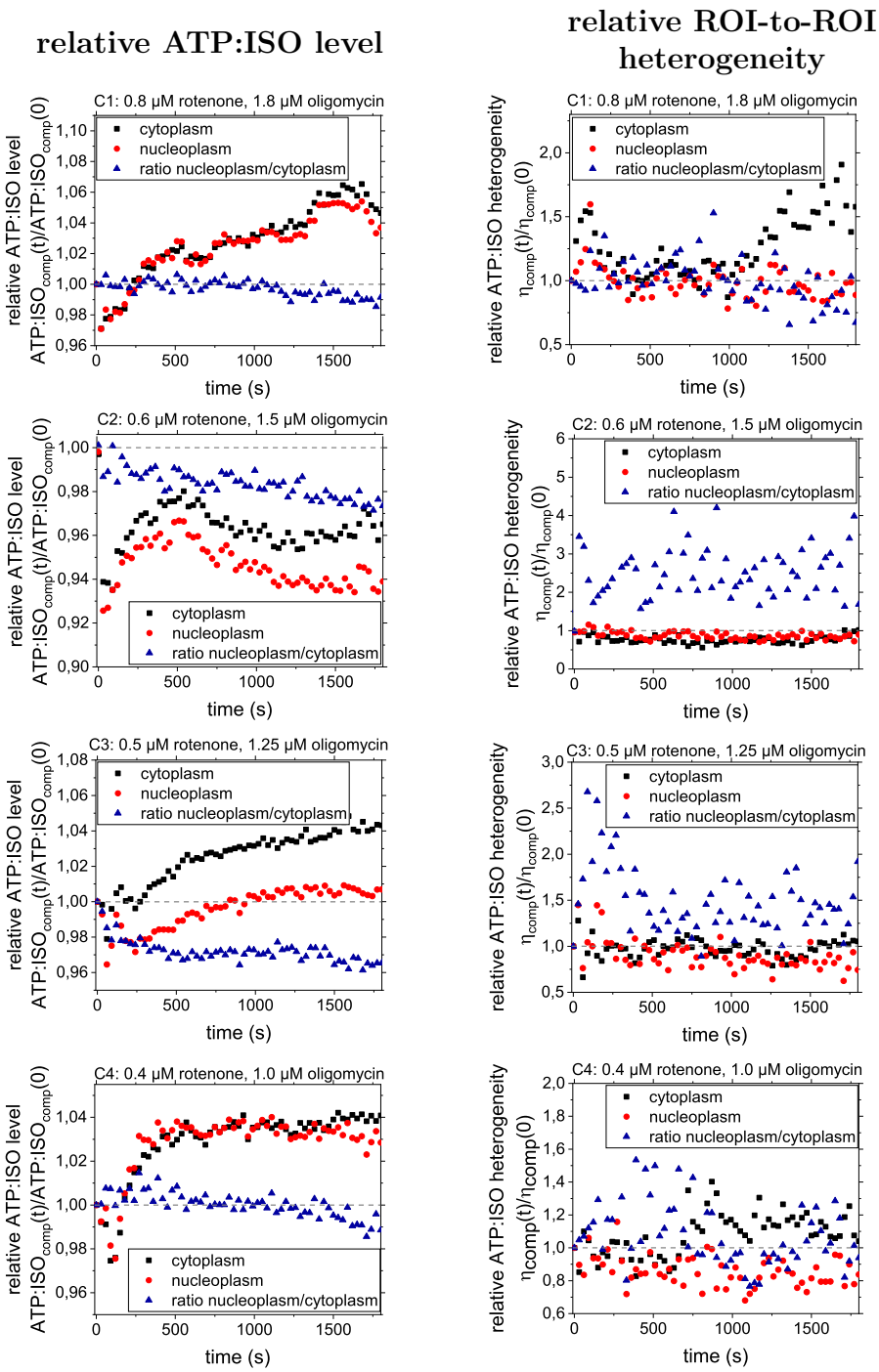

Figure 8.7: ATP depletion via rotenone and oligomycin at four different concentrations. Left column: relative ATP:isosbestic point levels and ratios. Right column: relative ATP:isosbestic point heterogeneities and their ratio. Exact concentrations of rotenone and oligomycin are given on p. 172. Each diagram shows averaged results of 8 cells.

Evolution of Compartment-Wise ATP:Isosbestic Point Ratios. Although several concentrations of rotenone and oligomycin were tested, all cells responded in a very similar way (Fig. 8.7). In all samples, relative ATP:isosbestic point ratios drop immediately after exchange of media, followed by

an initially quite fast recovery. However, in most cells ATP:isosbestic point ratios exceed initial ratios after a short time in both compartments. After about 10 min plateaued values are reached in both compartments in all measurements. Interestingly, while ATP:isosbestic point ratios evolve in parallel in both compartments, compartment-wise ratios decrease slowly at a constant rate throughout all measurements. This is independent of the direction compartment-wise ROI-to-ROI heterogeneities evolve in at a particular time. This behaviour might be explained as follows: as shown in the description given above, treating cells by combining rotenone and oligomycin impedes mitochondrial ATP regeneration, but does not completely stop it. Moreover, cytosolic and - if they exist - nucleosolic pathways of ATP production[204] are not influenced directly. So the immediate drop in ATP:isosbestic point levels upon exchange of media might reflect the loss of the majority of mitochondrial ATP production. However, only a short period of time later cytosolic and nucleosolic ATP regeneration is upregulated to compensate for that deficiency. Nevertheless, rotenone and oligomycin do trigger apoptosis. This apparently impacts ATP regulation within the cell, as cytosolic/nucleosolic mechanisms of ATP regeneration generally overcompensate the loss of mitochondrial ATP regeneration. So final, i.e. plateaued ATP:isosbestic point levels after exposure to rotenone and oligomycin generally exceed initial levels in both compartments. Interestingly, neither the relative amplitudes of ATP:isosbestic point ratios nor the velocity of change after exchange of media depend on rotenone and oligomycin concentrations. At all concentrations, the half time of recovery is approximately 200 s.
However, cytosolic ATP production seems to be faster or more efficient than nucleosolic ATP production. This is mirrored in the gradual decrease of compartment-wise ratios of ATP:isosbestic point ratios at all concentrations.
It would be interesting to test the hypothesis of increased cytosolic ATP regeneration after exposure to rotenone and oligomycin. As in the cytosol ATP can only be produced by means of glycolysis, this would be mirrored in an increased consumption of glucose by the cell. So monitoring glucose levels in the surrounding medium, e.g. by using Benedict's solution[222], would be an easy approach. However, assays containing Benedict's solution have to be heated in order to observe colour changes. So it would be required to plate cells in a vessel big enough to allow repeated removing of small amounts of medium during the course of one measurement. It might also be required to use medium containing less glucose than the standard imaging medium used

in this thesis. According to a manufacturer's testimonial, Benedict's solution has a detection limit of 0.01 % glucose in water[223]. However, since Benedict's solution is a classical indicator test, it might be difficult to quantify glucose levels. So this method can probably serve only as a general test whether glucose levels change significantly during apoptosis after rotenone and oligomycin treatment or not.
Another approach could be monitoring intracellular ATP:ADP levels and intracellular glucose levels simultaneously. Garrett et al.[224] developed a genetically encoded FRET-based pH-insensitive glucose indicator protein. It uses CFP and YFP as a FRET pair, so it is, in principle, possible to use it in combination with Perceval HR. However, CFP and GFP have a considerable spectral overlap. So data would certainly suffer from spectral bleed-through. Moreover, in addition to the two images needed for ratiometric imaging with Perceval another two images would be required to perform ratiometric FRET to monitor glucose levels. Taking four images per time increment would necessarily impair temporal resolution.

Evolution of Compartment-Wise ROI-to-ROI Heterogeneities. With regard to their compartment-wise ROI-to-ROI heterogeneities cells respond very similarly in all experiments: irrespectively of the concentration levels of rotenone and oligomycin, heterogeneity levels do not appear to change significantly in any of the compartments (Fig. 8.7). Although at individual measurement points ROI-to-ROI heterogeneities can differ from initial values by 50 %, temporal variation between time increments is rather large. This is similar to results obtained in cells exposed to oxidative stress. In view of this high level of noise, ROI-to-ROI heterogeneities are interpreted as invariant under rotenone and oligomycin treatments. Consequently also the ratio of compartment-wise ROI-to-ROI heterogeneities is interpreted not to change during the course of the measurement. So ATP:isosbestic point levels appear to be quite uniform throughout the cell. This might be due to the wide distribution of mitochondria in interphase cells. Moreover, cytosolic/nucleosolic ATP production is most probably spatially homogeneous.

ATP Depletion via Sodium Azide and 2-Deoxy-D-Glucose

Sodium azide blocks the binding site of oxygen of cytochrome-c-oxidase[225]. Thus mitochondrial production of ATP is completely stopped, which ulti-

mately causes cell death.

2-deoxy-D-glucose is an analogon for glucose[226]. It competitively inhibits glucose-6-phosphate-isomerase which cannot metabolize the molecule[227] [228]. While 2-deoxy-D-glucose-6-Phosphate accumulates, cellular ATP levels decrease, as ATP producing steps of glycolysis cannot be performed any more[226]. As a side effect, 2-deoxy-D-glucose promotes the production of reactive oxygen species as well as autophagy[226] [227].

In combination, sodium azide and 2-deoxy-D-glucose completely stop the cell's ability to regenerate ATP in cytoplasm (Fig. 8.8). This is particularly effective if the treatment is combined with the use of glucose-free media, which was done in this work. By analogy with experiments on the effects of partial ATP depletion by means of rotenone and oligomycin, the effects of total cytoplasmic ATP depletion on intracellular ATP:ADP levels and their heterogeneity were tested in cells transfected with the ratiometric ATP:ADP sensor Perceval HR. In addition to that, possible effects of intracellular ATP depletion on intracellular crowding levels and crowding heterogeneities were investigated by way of fluorescence imaging as well as by means of FCS in HeLa cells transfected with free, low-expressing EGFP.

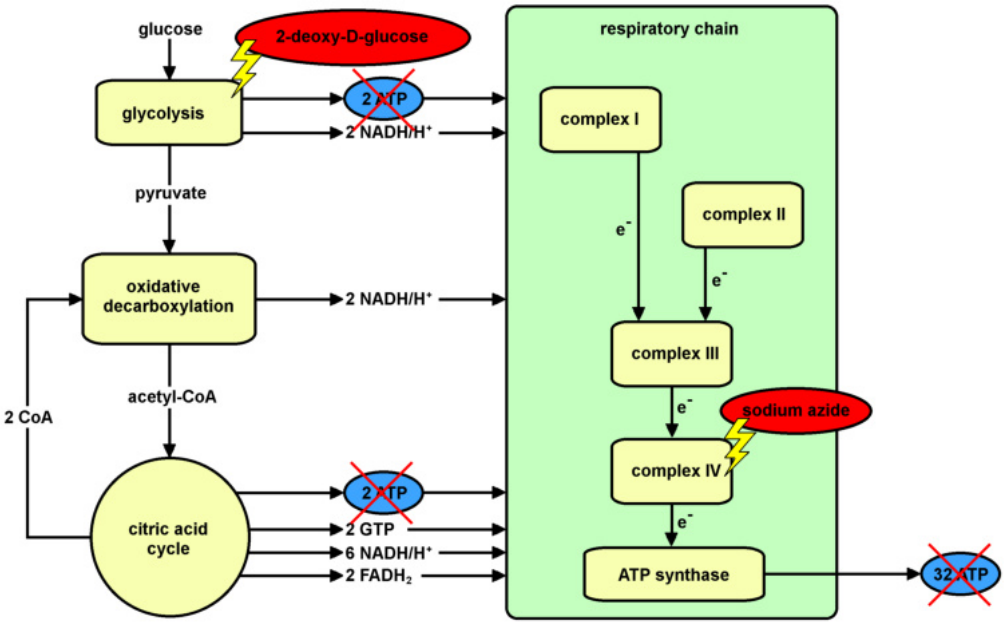

Figure 8.8: Impact of sodium azide and 2-deoxy-D-glucose treatment on cellular ATP regeneration. Sodium azide irreversibly blocks complex IV of the respiratory chain, which completely stops mitochondrial ATP production. At the same time, 2-deoxy-D-glucose inhibits cytosolic ATP production. Therefore, ATP regeneration is completely stopped.

Ratiometric Imaging Experiments in Cells Transfected with Perceval HR. In all ratiometric measurements, three images per cell were taken with excitations of 405 nm, 458 nm or 488 nm, respectively. So in all images both ATP:ADP ratio and ATP:isosbestic-point ratio could be analysed.

Being exposed to sodium azide and 2-deoxy-D-glucose ATP:ADP levels immediately start dropping rapidly in both cytoplasm and nucleoplasm (Fig. 8.9a), a process which was to be expected. After about 5 min a lower plateau value is reached in both compartments. It is kept for the rest of the experiment. At this plateaued value, in both compartments ATP:ADP levels are only about 25 % of their initial value.
At the same time, the ratio between compartments of the ATP:ADP ratio decreases by about 10 %. Since the initial ratio of ATP:ADP levels between nucleoplasm and cytoplasm is about 1.09, both compartments completely equilibrate in less than 5 min.
These tendencies are found as well when analysing the ATP:isosbestic-point ratio (Fig. 8.9c). ATP:isosbestic point levels drop to approximately 65 % of their initial values immediately after exposure to sodium azide and 2-deoxy-D-glucose. Simultaneously the ratio between compartments assimilates. However, intercompartmental equilibration is slower than in the ATP:ADP measurement mode. This is due to the fact that the ATP:isosbestic point ratio mirrors only the decrease of ATP levels, while the ATP:ADP ratio reflects the simultaneous increase of ADP levels as well.
A more detailed examination of the evolution of ATP:ADP and ATP:isosbestic point levels might allow drawing more deductions about the individual development of ATP and ADP levels in both compartments. But the differences in evolution of velocities are very small and, most probably, not significant. Calculating the actual ATP:isosbestic point ratio would be a more direct way of investigating ADP levels. However, if for all three excitation wavelengths the same measurement settings are chosen, i.e. the same PMT bias voltages and the same absolute laser powers, fluorescence intensity is perceptibly lower in the ADP and isosbestic point images, as excitation wavelengths are not ideally suited to GFP. So, in order to reduce errors introduced by low fluorescence intensities, imaging would have to be performed either at higher bias voltages or at higher laser powers. In principle both settings can be changed. But then a direct comparison with images taken in the ATP channel would be impossible.

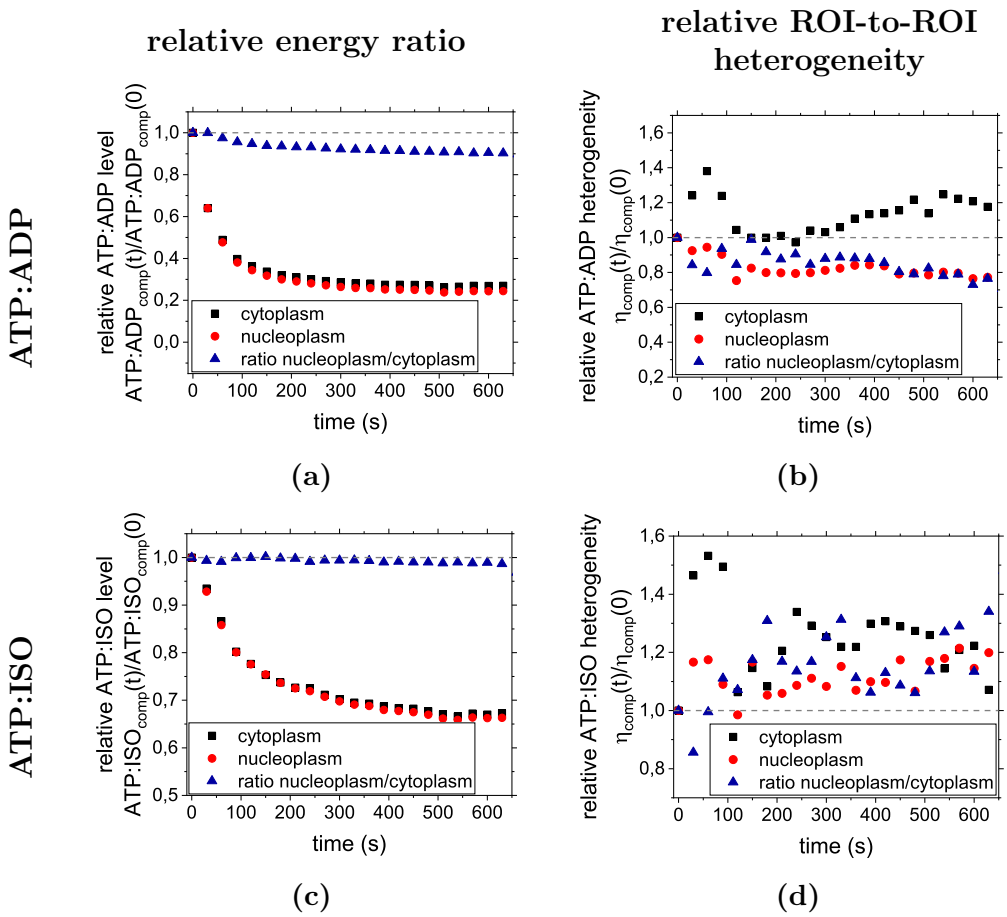

Figure 8.9: ATP Depletion via sodium azide and 2-deoxy-D-glucose in cells expressing Perceval HR. (a) Relative ATP:ADP levels and their ratio. (b) Relative ROI-to-ROI heterogeneities of ATP:ADP levels and their ratio. (c) Relative ATP:isosbestic point levels and their ratio (d) Relative ROI-to-ROI heterogeneities of ATP:isosbestic point levels and their ratio. Averaged results of 22 cells.

The ROI-to-ROI heterogeneity of ATP:ADP ratios (see Fig. 8.9b) or ATP: isosbestic-point ratios (see Fig. 8.9d), respectively, might change during ATP depletion: the heterogeneity of ATP:isosbestic ratios in both compartments could be interpreted to increase. However, temporal variation of both, nucleoplasmic and cytoplasmic ROI-to-ROI heterogeneity, is quite high. So it is highly debatable whether the changes in heterogeneity levels should be considered to be significant. Similarly, the heterogeneity of ATP:ADP ratios could be interpreted to increase in the cytoplasm and to decrease in the nucleoplasm. However, the ROI-to-ROI heterogeneity of the ATP:ADP ratio in the cytoplasm features a rather high temporal heterogeneity that does not seem to depend on absolute ATP:ADP levels in the same compartment. Nucleoplasmic ROI-to-ROI heterogeneity of the ATP:ADP ratio evolves more distinctly. However, in comparison with the very pronounced response of absolute

ATP:ADP ratios, changes of the nucleoplasmic ROI-to-ROI heterogeneity still appear rather small. So ATP depletion and ADP increase are preliminarily interpreted to happen quite homogeneously within both compartments. It remains to be analysed in further projects whether this interpretation is valid indeed.

Imaging Experiments in Cells Transfected With EGFP. It could be established that the applied ATP depletion protocol results in a constant low level of ATP:ADP after only 5 min. In addition to describing the temporal evolution of ATP:ADP and ATP:isosbestic point levels as well as their heterogeneities, a possible influence of the same treatment on intracellular crowding levels and crowding heterogeneities was investigated. In order to accomplish this, images were acquired in HeLa cells transfected with EGFP during ATP depletion. Analysis followed the same routine that was established in chapter 5, but in a time-resolved manner.

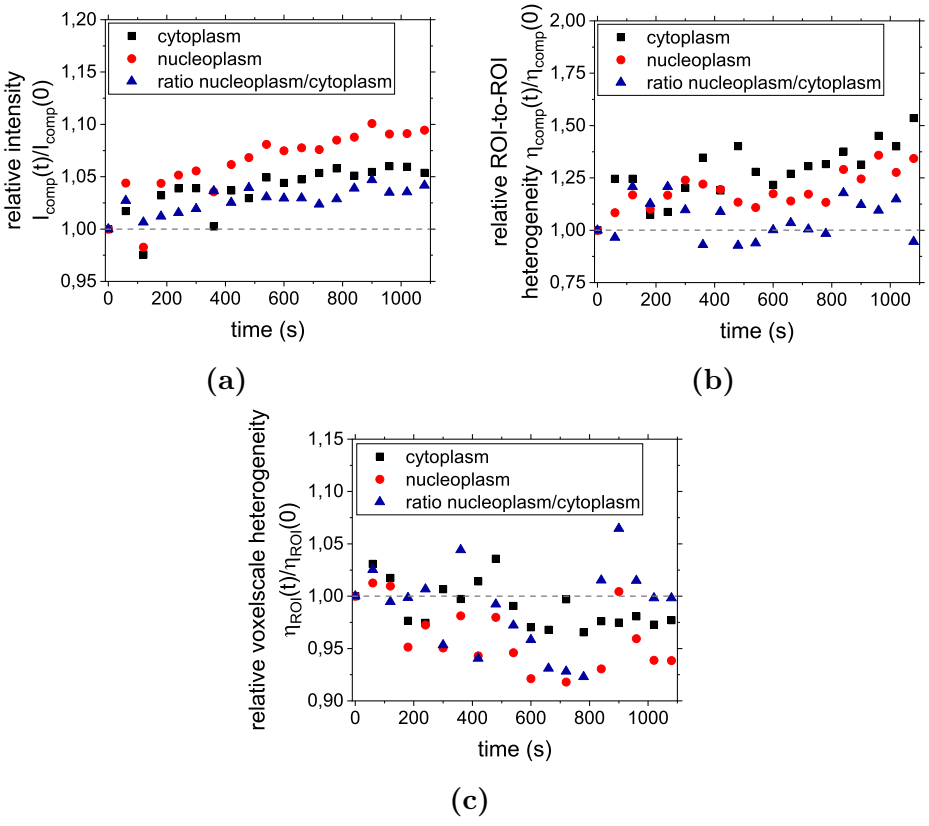

Figure 8.10: ATP Depletion via sodium azide and 2-deoxy-D-glucose in cells expressing free EGFP. (a) Relative intensities and their ratio. (b) Relative ROI-to-ROI heterogeneities and their ratio. (c) Relative voxelscale heterogeneities and their ratio. Averaged results of 19 cells.

After the onset of ATP depletion the overall available volume fraction increases a little in both nucleoplasm and cytoplasm (Fig. 8.10a). Notably the absolute ratio of available volume fractions remains constant at a value of ~ 1.38 throughout the course of the experiment, i.e. for up to 20 min (data not shown). By naked eye, an increase in the cells' surface is not visible. Yet, similar to cells exposed to osmotic pressure, volume changes are likely to predominantly take place in height. The exact mechanism behind the increase in available volume fractions is not clear, however. Several inhibitors of ATP regeneration pathways are known to produce reactive oxygen species as a side-effect. As oxidative stress induced a similar effect, i.e. an increase in available volume in both compartments, this might also be the explanation for the change in crowding levels during ATP depletion. Of course, during oxidative stress treatment also the ratio of available volume fractions between both compartments changed. Yet, if ATP depletion indeed results in oxidative stress there are still two major differences between this experiment and the previously performed oxidative stress measurements: for one thing, cells in oxidative stress measurements were exposed to medium containing H_2O_2, i.e. to an oxidative environment primarily outside the cell. During ATP depletion oxidative molecule species would be generated directly in the cell. In this case the nucleus would not experience any protection by the surrounding cytoplasm. The second difference is the lengthscale at which the cellular response is investigated. Oxidative stress measurements were performed in cells transfected with fCrH2. So all results obtained in these measurements ultimately describe what happens on the 5 nm-scale. In the case at hand, cells are transfected with EGFP. So the cell's response to the treatment is monitored on a much larger lengthscale. Thus oxidative stress induced by lack of ATP appears to be a possible explanation for increased available volume fractions. Additionally, increased available volume fractions in the nucleoplasm could be caused by condensation of chromatin, a process that usually occurs during apoptosis[229]. Structural changes in the cytoplasm of apoptotic cells include, for example, fragmentation of the cytoskeleton's microfilaments, swelling and partial redistribution of Golgi apparatus and endoplasmic reticulum as well as permeabilization of lysosomes and vacuolation of mitochondria[230]. These processes could well be responsible for the observed evolution of available volume fractions. Nevertheless, considering the test measurement in a HeLa cell transfected with EGFP but not subjected to any kind of treatment (see Sec. 8.3.1), it is debatable whether the observed changes are even significant.

The available volume fraction might change in both compartments. However, neither the ROI-to-ROI heterogeneity (Fig. 8.10b) nor the voxel-wise heterogeneity (Fig. 8.10c) display any significant variation during ATP depletion. In addition to that, their compartment-wise ratios remain constant throughout the course of the experiment. Temporal changes in the ROI-to-ROI heterogeneity are even less pronounced than in the control measurement without treatment. Whether this decreased temporal variation of ROI-to-ROI heterogeneities is purely a side-effect of measurement statistics or whether it is caused by slowed-down metabolism after ATP depletion remains to be analysed in further projects. From the data gathered in this thesis only one possible conclusion can be drawn: whatever mechanism causes the available volume fractions to increase as ATP levels sink, it is not confined to any particular location inside the cell but seems to be quite homogeneous throughout the cell.

FCS Experiments in cells transfected with EGFP. By analogy to imaging experiments, FCS measurements were performed in the cytoplasm and nucleoplasm of HeLa cells. However, FCS measurements require a comparatively long acquisition time of 30 s per measurement locus. So only one locus per compartment was measured as a function of time. Initially a time trace was acquired in the nucleus and in the cytoplasm of an untreated cell. After changing from standard imaging medium to glucose-free medium supplemented with sodium azide and 2-deoxy-D-glucose, time traces were acquired in the same cell once per minute for a period of 30 min. Autocorrelation curves were calculated in WORKBENCH and analysed with a custom MATLAB fit routine assuming anomalous diffusion of one component (Eq. 3.13). Thus, values for the anomaly exponent α and for the mean residence time τ_d were acquired for each cell as a function of time. In addition, a control measurement was performed in which the cell was not treated with ATP depleting chemicals.

In the control measurement, diffusion time as well as anomaly exponent display a rather large variation (see Fig. 8.11a and 8.11b). However, on average diffusion times are higher in the cytoplasm than in the nucleoplasm, while anomaly exponents are on average higher in the nucleoplasm than in the cytoplasm. So diffusion in the nucleus can be considered to be less anomalous and somewhat faster than in the cytoplasm. This observation confirms previous data found for the diffusion of small tracer particles in mammalian cells, e.g. results found

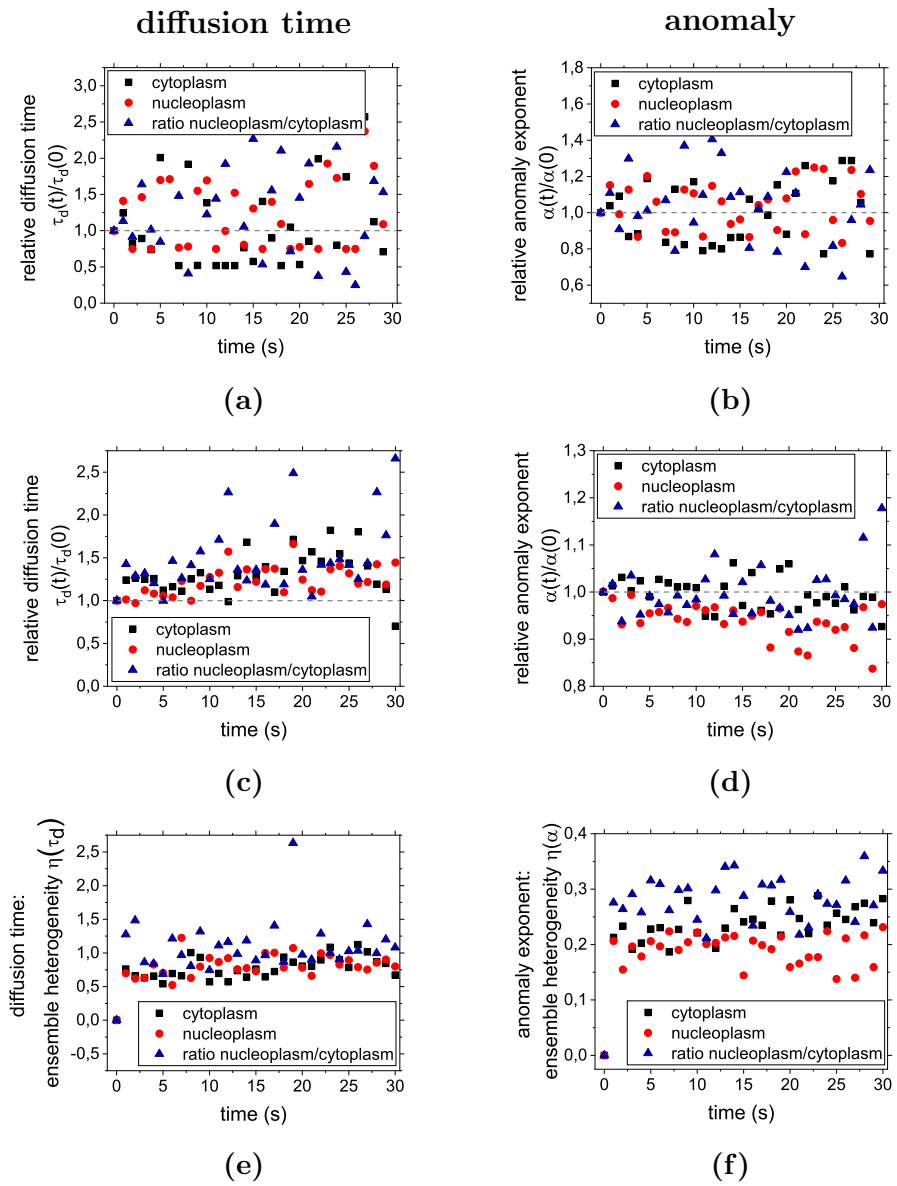

Figure 8.11: FCS measurements in untreated cell and cells transfected with EGFP and treated with sodium azide and 2-deoxy-D-glucose. (a) Diffusion time in untreated cell. (b) Anomaly exponent in untreated cell. (c) Diffusion time during ATP depletion. (d) Anomaly exponent during ATP depletion. (e) Ensemble heterogeneity of diffusion times during ATP depletion. (f) Ensemble heterogeneity of anomaly exponents during ATP depletion. Data during ATP depletion: Averaged results of 32 cells.

in two studies by Guigas et al.[59] [231]. Moreover, since anomalous diffusion of tracer particles is associated with the crowding level of the surrounding medium, it further supports the results described earlier in this work of the nucleoplasm being less crowded than the cytoplasm in interphase HeLa cells. As was to be expected, there is neither an evolution of diffusion times nor an evolution of anomaly exponents throughout the measurement. Temporal heterogeneity of diffusion times is as high as $\langle \eta_{nuc}(\tau_d) \rangle_t = 38\,\%$ in the nucleus and $\langle \eta_{cyto}(\tau_d) \rangle_t = 60\,\%$ in the cytoplasm. Temporal heterogeneities of anomaly exponents were found to be $\langle \eta_{nuc}(\alpha) \rangle_t = 13\,\%$ in the nucleus and $\langle \eta_{cyto}(\alpha) \rangle_t = 17\,\%$ in the cytoplasm. These values are considerably higher than those found by Stiehl et al. in the same system[64]. However, due to the time-resolved measurement mode in this thesis, only one measurement locus per compartment could be selected. Moreover, only one representative control measurement was performed. So, in this thesis, the calculated heterogeneity is based on a much smaller ensemble of measurement results. Considering the fact that the analysis of FCS data relies on fitting a complex function to a curve obtained in a highly heterogeneous system, temporal heterogeneities might well decrease considerably as statistics improve.

In cells exposed to sodium azide and 2-deoxy-D-glucose, anomaly exponents appear to remain at their physiological level in both compartments (Fig. 8.11d). They vary temporally by less than 10 %. This is even less than temporal variation in the control measurement. Of course, statistics is worse in the control measurement. Diffusion times in both compartments could be argued to increase slightly during ATP depletion (Fig. 8.11c). So diffusion would be somewhat slowed-down in an ATP-depleted environment. In principle, this would be in line with the results obtained by Parry et al.[78] who found that cellular metabolism constitutes a fluidizing effect on bacterial cytoplasm. Consequently, silencing cellular metabolism would 'solidize' cellular protoplasm, thus slowing down diffusion. However, the time-dependent change during ATP-depletion is rather minor for both variables, especially when considering the rather large cell-to-cell variation of both variables (Fig. 8.11e and Fig. 8.11f) as well as the rather large temporal fluctuations. Temporal heterogeneity of diffusion times during ATP depletion is about 27 % in both compartments, whereas temporal heterogeneity of diffusion times in the control measurement is at 39 % in the nucleoplasm and as high as 60 % in the cytoplasm. So, similar to anomaly exponents, temporal heterogeneity levels of diffusion times during

ATP depletion are smaller than temporal heterogeneity levels without treatment. In conclusion, changes in diffusion times during ATP depletion are most probably not significant. This is even more apparent when comparing these results to those obtained by Pawar et al.[82]: residence times and anomaly exponents obtained with the same setup and the same cell type, albeit in a different cell cycle phase, varied as much inside the same cell and at the same time while depending only on the relative position inside the mitotic spindle. Moreover, when looking at the temporal variation of either residence time or anomaly exponent in only one cell, the tendencies of increasing τ_d and decreasing α virtually disappear (not shown). So ATP depletion seems to have no major influence on the diffusion characteristics of EGFP in cells. Since Parry et al.[78] also found that the impact of fluidization caused by cellular metabolism depends on tracer particle size, the apparent lack of a cellular response in diffusion characteristics to ATP depletion is perfectly reasonable: according to Parry et al., large tracer particles are much more affected than small particles. A lower threshold in tracer size at about 30 nm to 40 nm is proposed, with smaller tracer particles not being affected at all by cytoplasm fluidization. Their experiments were performed in *Escherichia coli* and *Caulobacter crescentus*, i.e. in bacteria, unlike the mammalian HeLa cells used in this work. Yet a similar behaviour might apply to HeLa. It remains to be analysed whether ATP depletion has any significant impact on the diffusion of larger particles, such as gold particles or peroxisomes.

Conclusion. In summary, these results suggest that apart from the obvious depletion of ATP and accompanying increase in ADP levels, sodium azide and 2-deoxy-D-glucose do not appear to significantly impact the investigated observables. ATP:ADP heterogeneity as well as ATP:isosbestic point heterogeneity are preliminarily interpreted to not show a significant response to ATP depletion. Similarly, intracellular crowding levels as well as heterogeneities appear not to change during ATP depletion. While crowding levels might decrease slightly according to imaging results, they seem to increase slightly according to FCS results. So it appears to be justified to interpret crowding levels as more or less constant in spite of energy loss.

8.4 Summary

In summary, overall available volume fractions change significantly during osmolar as well as oxidative stress treatment. Hyperosmolar stress causes the cell to shrink, resulting in decreased available volume fractions in both nucleus and cytoplasm. Hypoosmolar stress causes the cell to expand, consequently increasing the available volume fraction in the cytoplasm. Available volume fractions in the nucleoplasm decrease, a fact which is most likely caused by stabilizing effects of nuclear lamina as well as by chromatin decondensation. High levels of oxidative stress result in prominently increased available volume fractions in both nucleoplasm and cytoplasm. However, apparently neither low levels of oxidative stress nor ATP depletion via sodium azide and 2-deoxy-D-glucose have any effect on available volume fractions.

As was to be expected, ATP:ADP levels as well as ATP:isosbestic point levels decrease rapidly immediately after exposure to sodium azide and 2-deoxy-D-glucose until a lower level is reached which remains constant for the rest of the experiment. During partial ATP depletion with rotenone and oligomycin, however, ATP:isosbestic point levels recover quickly after an initial major drop. At their subsequent plateaued value they even exceed initial levels.

In contrast to these very characteristic responses of overall available volume fractions and energy levels, intracellular heterogeneities appear to remain robust in most stress treatments that were probed in this thesis. Significant changes in heterogeneity levels of available volume fractions were only found in cells subjected to osmolar stress, where they evolve in directions opposite to the respective available volume fraction's in the same compartment. Oxidative stress as well as ATP depletion caused by sodium azide and 2-deoxy-D-glucose do not appear to impact heterogeneity levels of available volume fractions.

Heterogeneity levels of the ATP:ADP and ATP:isosbestic point ratios might change during ATP depletion caused by exposure to sodium azide and 2-deoxy-D-glucose, but not during partial ATP depletion caused by exposure to rotenone and oligomycin.

Chapter 9

Characterizing Intracellular Heterogeneities on Multiple Lengthscales: Summary, Discussion and Outlook

In spite of a number of experimental constraints, intracellular crowding levels and their heterogeneities were successfully characterized on multiple lengthscales. An overview of all results obtained in physiological cells is given in Fig. 9.1. It was found that, at least in the particular strain of HeLa cells employed in this thesis, overall crowding levels are generally about 20 % higher in the cytoplasm than in the nucleoplasm of interphase cells. Moreover, cytoplasmic crowding heterogeneity on intermediate lengthscales, i.e. on the ROI-to-ROI level, exceeds nucleoplasmic crowding heterogeneity: values obtained in the cytoplasm are, on average, twice as high as those obtained in the same cell's nucleoplasm ($\langle\eta_{cyto}\rangle_{int} = 12.7\,\%, \langle\eta_{nuc}\rangle_{int} = 5.8\,\%$). On the voxel-to-voxel lengthscale, i.e. on the lengthscale of several hundred nanometres, this disparity seems to vanish ($\langle\eta_{ROI}\rangle_{cyto} = 7.4\,\%, \langle\eta_{ROI}\rangle_{nuc} = 6.3\,\%$). Voxel-to-voxel heterogeneities might still be somewhat higher in the cytoplasm than in the nucleoplasm. However, owing to difficulties in separating sample-inherent heterogeneities from heterogeneities introduced by the measurement process, these results have to be interpreted with care.

When going below the classical resolution limit, measurement results critically depend on the employed measurement technique: while overall crowding levels were universally found to be very similar in cytoplasm and nucleoplasm,

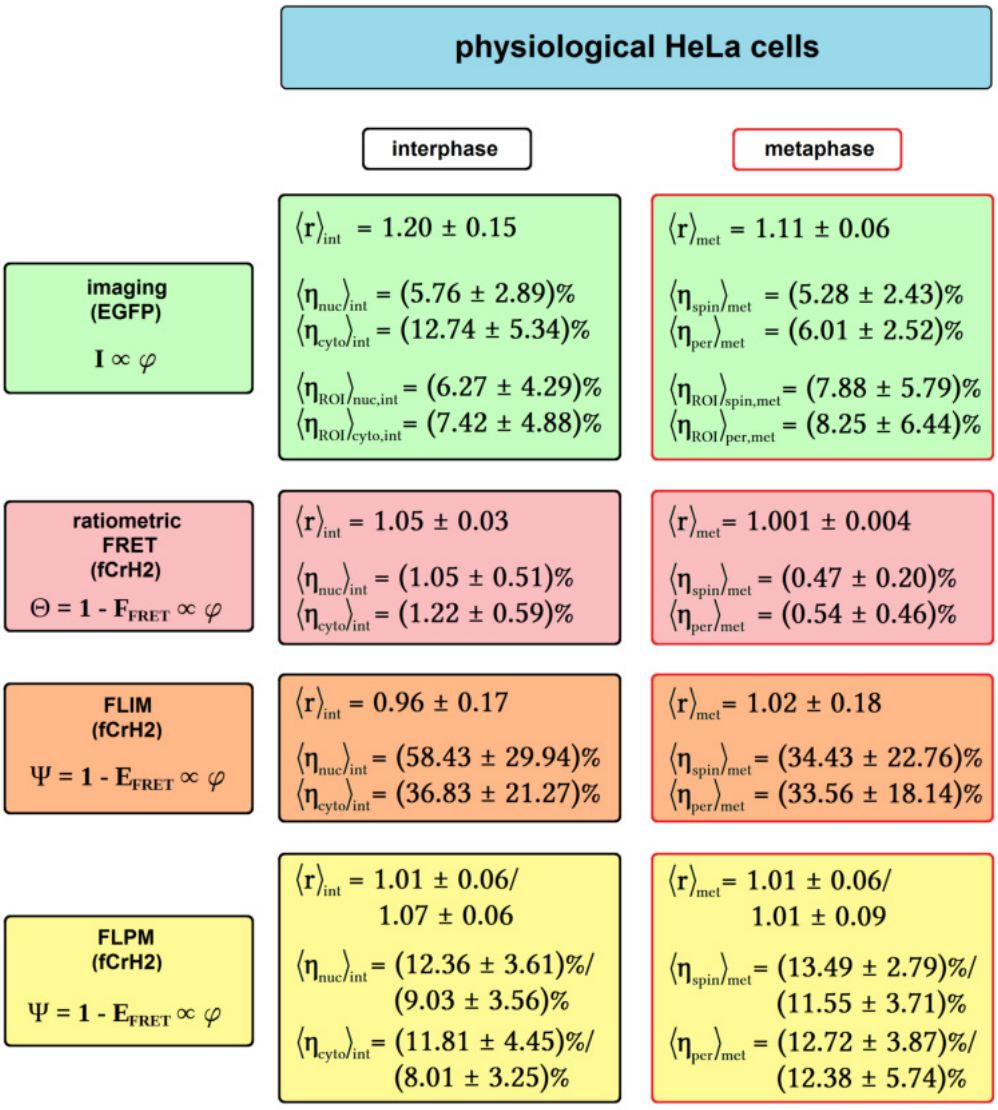

Figure 9.1: Overview: crowding levels and heterogeneities on multiple length-scales in interphase and metaphase cells.

ROI-to-ROI heterogeneity levels on the 5 nm-scale varied from 1 % to 60 % between methods. In FLPM experiments, which should be considered to be more reliable than either FLIM or ratiometric FRET imaging experiments, both, cytoplasmic and nucleoplasmic heterogeneity levels, were found to be about 10 %.
The temporal evolution of crowding levels and heterogeneities could only be probed for comparatively short measurement times. On this scale, however, they appear to remain constant. Depleting interphase cells of their microtubule skeleton does not appear to change neither overall crowding levels nor their heterogeneities significantly.

In metaphase cells, spindle area and spindle periphery are, according to current knowledge, not separated by any membrane or similar structure. Nevertheless, these two areas can be viewed as separate compartments. While the difference is not as pronounced as it is in interphase cells, the former cytoplasm retains its higher crowding level to some degree: crowding in the spindle periphery is about 10 % higher than in the spindle area. However, on all lengthscales crowding heterogeneities appear to be very similar in both compartments ($\langle\eta_{per}\rangle_{met} = 6.0\,\%, \langle\eta_{spin}\rangle_{met} = 5.3\,\%, \langle\eta_{ROI}\rangle_{per} = 8.3\,\%, \langle\eta_{ROI}\rangle_{spin} = 7.9\,\%$). Moreover, heterogeneity levels in spindle and spindle periphery on lengthscales below a few hundred nanometres are basically the same as those obtained in interphase cells. Spatially resolved analyses of the spindle region did not provide any further information on any lengthscale.

So, in short, crowding levels and intermediate lengthscale heterogeneities differ between nucleoplasm and cytoplasm. After nuclear envelope breakdown some mixing between former nucleoplasm and former cytoplasm takes place. However, spindle and spindle periphery retain at least some degree of dissimilarity. So it is legitimate to view spindle and spindle periphery as contiguous, but individual compartments even after nuclear envelope breakdown.
On lengthscales below a few hundred nanometres, all compartments are very similar. This appears to be independent of the respective cell cycle phase.

An overview of all results obtained in time-resolved measurements in cells subjected to stress treatments is given in Fig. 9.2. Different stress treatments generally influence overall crowding/ATP:ADP levels as well as their ratios between interphase compartments. The direction of changes, i.e. increase or

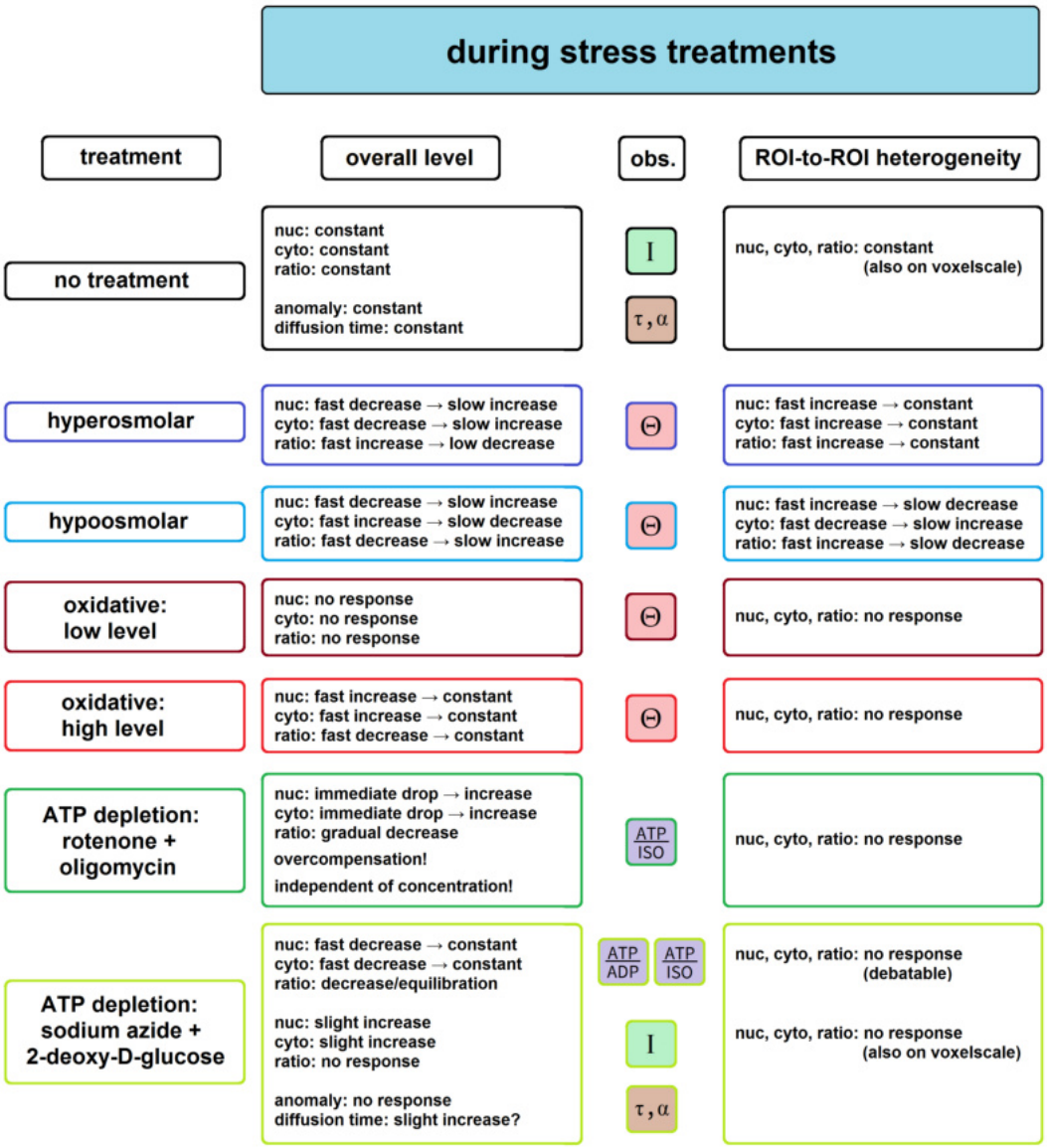

Figure 9.2: Overview: changes of overall levels and heterogeneities of various observables on multiple lengthscales in interphase cells subjected to stress treatments.

decrease of crowding/ATP:ADP levels, depends on the particular kind of stress treatment: available volume fractions decrease in response to hyperosmolar stress treatment, but increase in response to high levels of oxidative stress. They neither change in response to moderate levels of oxidative stress nor during ATP depletion. ATP:ADP as well as ATP:isosbestic point levels rapidly decrease and do not recover after exposure to sodium azide and 2-deoxy-D-glucose. During exposure to rotenone and oligomycin, ATP:isosbestic point levels decrease rapidly, too. In contrast to treatment with sodium azide and 2-deoxy-D-glucose, however, they recover quickly, their final levels exceeding initial levels considerably in most cases.
In all examples described in the preceding paragraph, both compartments respond in the same way, albeit often to a different degree. A notable exception to this generalization is exposure to hypoosmolar stress: here, available volume fractions increase in the cytoplasm, while they simultaneously decrease in the nucleoplasm. This can be explained by immediate decondensation of chromatin in the nucleus after influx of water.
ROI-to-ROI heterogeneities, on the other hand, appear to be rarely influenced at all by stress treatments. Significant changes in heterogeneity levels can only be observed in cells subjected to osmolar stress. In both compartments, ROI-to-ROI heterogeneities evolve in the direction opposite to the corresponding available volume fraction's. Neither oxidative stress nor ATP depletion impact crowding heterogeneities on the lengthscales investigated. Similarly, ROI-to-ROI heterogeneity levels of ATP:isosbestic point ratios appear not to change during partial ATP depletion by rotenone and oligomycin. They might, however, evolve in response to total ATP depletion by sodium azide and 2-deoxy-D-glucose.

While working on this thesis it became more and more apparent that all observables showed a substantial variation throughout the cell ensemble. No matter which measurement technique was applied, ensemble heterogeneities of overall available volume fractions were found to be in the range of 10 % to 20 %. Ensemble heterogeneities of compartment-wise ROI-to-ROI heterogeneities and their cell-wise ratios reached 50 % or even exceeded that value. Based on the experimental data described in chapters 5 to 8 we can only speculate about the origin of such pronounced ensemble heterogeneities. It would be most interesting to thoroughly investigate whether they are merely caused by sampling cells in morphologically indistinguishable, but nevertheless

different cell cycle phases or whether they represent an actual characteristic of the cell ensemble. This could be achieved by synchronizing cells prior to measurements, or by introducing additional markers that allow determining the exact cell cycle stage. Additional insight into crowding and crowding heterogeneities could be gained by monitoring a single cell throughout a complete cell cycle. However, this is quite a challenge. A somewhat easier-to-implement approach could be monitoring one cell's progression from late interphase into mitosis. This would provide further information about the relation between interphase and metaphase overall crowding ratios and might even allow to estimate absolute crowding levels in the compartments. Of course, ensemble heterogeneity might also be influenced by varying transfection and expression levels of EGFP. Repeating measurements in stably transfected cell lines could limit or even eliminate this influence on results.

In this thesis all experiments were performed on only one strain of one particular cell type. In further projects it should be tested whether the results obtained here hold true for other cell types as well. It could be especially interesting to repeat the experiments discussed above in human cell lines that were not derived from cancer cells. As cancer cells behave quite differently from non-cancerous cells[232] [233] important new insights could be gained from comparing crowding and heterogeneity levels in both cell types. But also investigating non-human cell lines might lead to a new understanding of intracellular organization. In particular, it might be informative to perform experiments on prokaryotic cells. Prokaryotic cells lack membrane-enclosed organelles. So they could be expected to be less heterogeneous than eukaryotic cytoplasm. On the other hand, clearly these cells require some form of - membraneless - compartmentalization in order to function efficiently. It would be interesting to analyse whether the compartmentalization based on localized transcription of proteins described by Montero-Llopis et al.[13] is visible in imaging data.

Of course in this thesis only a limited selection of stress treatments could be performed. These treatments were often applied in only one concentration. Based on these experiments, it might prove insightful to investigate dependence of cellular responses on concentrations of applied chemicals. As could be demonstrated in the case of oxidative stress, cellular responses can differ substantially at different concentrations of stressors.

Another approach would be to alternate between stress treatment and standard imaging medium during measurements. In this thesis, only the transition from standard medium to medium containing one particular kind of stressor

was monitored. However, cells subjected to osmotic pressure are known to counterbalance this pressure after an initial phase of water influx or efflux, respectively[163] [170]. Indeed after an initial, fast change in crowding levels and heterogeneities, these observables could be observed to gradually return to their initial levels. So it might prove interesting to investigate whether, after prolonged exposure to osmotic pressure, isoosmolar medium could provoke a similar initial reaction as hypo-/hyperosmolar medium. But also cellular responses to oscillations between exposure to apoptosis-inducing medium and exposure to standard medium could reveal new insights into intracellular organization. Experiments in cells exposed to alternating conditions could easily be implemented with the help of a microfluidics unit. This technique is currently being established in our group.
Regarding the newest developments in TCSPC construction, it might even be possible to perform spatially resolved lifetime-measurements at measurement times short enough to make them applicable to stress treatments: according to Alvarez et al.[234], a newly developed TCSPC unit allows to perform video-rate confocal FLIM measurements.
Finally, it is, of course, always possible to subject cells to various other kinds of treatment, to perform multiple treatments consecutively or even at the same time, or to perform the same treatments while using yet another kind of fluorescence marker.

The characterization of crowding levels, ratios, ATP:ADP ratios and their respective heterogeneities on multiple lengthscales in physiological conditions and during stress treatments might form a basis for describing intracellular architecture more accurately. This might be especially important in simulations of intracellular transport - directed motion as well as diffusion. But analyses of experimental techniques based on tracer motion, e.g. FRAP, might also profit from the insights gained in this thesis. In addition, as macromolecular crowding has a profound impact on many cellular process, especially reaction rates, it is important to be able to at least estimate to what extent local crowding levels can differ from each other.
Finally we can conclude that, especially when performing measurements in living organisms such as cells, scientists should always decide very carefully, which measurement loci should be chosen and, more important, which results can be averaged without loss of information and which results can't.

Part III

Characterizing a FRET-Based Crowding Sensor

Chapter 10

Opening and Closing Characteristics of fCrH2

In part II, the FRET-based crowding sensor fCrH2 was used in a number of measurements. This chapter briefly discusses insights into the opening and closing mechanism of this intramolecularly labelled sensor gained by means of FCS.

10.1 Motivation

In chapters 6 and 7, crowding on the nanoscale was characterized via the FRET-based crowding sensor fCrH2 introduced by Boersma et al.[104] and modified by Sukenik et al.[105]. fCrH2 is an intramolecularly labelled and genetically encodable biomolecule which uses AcGFP1 and mCherry, located at the N and C terminus of the protein, respectively, as a FRET pair. According to the description of the sensor given by Boersma et al.[104], the link between donor and acceptor consists of a conformationally flexible domain similar to flexible polymers like e.g. polyethylene glycol. When free volume decreases, this flexible domain assumes a more condensed conformation, thereby decreasing the distance between N and C terminus, which in turn increases FRET efficiency. The flexible domain features α-helical peptides to increase changes in distance between donor and acceptor and, thus, increase the sensor's sensibility to volume modulation.
The sensor was tested extensively by Boersma et al.[104] and Sukenik et al.[105] and was found to reflect indeed only the local excluded volume fraction. In particular, the effect of direct chemical interactions between sensor and surrounding cell protoplasm as well as self-association and aggregation of the

sensor on fluorescence readout was found to be negligible. The conformational change is reported to be reversible, continuous and to respond linearly to volume modulation.
Up to now a more precise insight into the mechanism of conformational changes has not been found. They happen fast enough to be feasible as a means of monitoring volume changes due to a varying osmolarity of the cell culture medium. But the exact time scale of opening and closing of the sensor is not known. Moreover, it is not known whether conformational changes of the flexible domain happen only due to stimulation by the surrounding crowders or whether fCrH2 has a tendency to display a stochastic opening and closing behaviour.
This chapter focuses on the analysis of the opening-closing dynamics of fCrH2 by means of FCS measurements. Bonnet et al.[119] and Wallace et al.[120] [121] established FCS as a method of investigating the opening and closing of DNA hairpin-loops equipped with a fluorophore and a quencher at their opposing ends. Their method was modified to accommodate the requirements of fCrH2. By way of extracting the time scale of opening and closing the nature of the conformational change itself can be deduced.

10.2 Experimental Procedure and Data Analysis

10.2.1 Original Experimental Procedure

Bonnet et al.[119] and Wallace et al.[120] [121] use a combination of FRET and FCS to investigate the conformational fluctuations of ssDNA hairpin loops (Fig. 10.1a) in a time-resolved manner. They employ two different types of DNA strands which they call "beacon" and "control". Both types of strands share the same DNA sequence with a fluorescent molecule attached to one end. The "beacon" type of DNA is additionally tagged with a quencher at the opposite end. Upon closing the beacon strand, fluorophore and quencher are close enough for FRET to occur. So the fluorophore remains dark after excitation. When opening the strand again, fluorescence is emitted again. As the "control" strand lacks a quencher, its fluorescence is independent of its conformation. Thus, in solution the "control" strand only displays diffusive behaviour, whereas the "beacon" strand features both diffusion and blinking due to opening-closing dynamics.

Assuming that photophysics, centre of mass diffusion and opening-closing dynamics are statistically independent processes, the autocorrelation function of blinking diffusing strands consists of three multiplicative factors, each describing one of the three processes. Consequently diffusing "control" strands only feature the diffusional and photophysical parts. So, after normalizing both curves to the same number of fluorescent particles in the confocal volume (Fig. 10.1b), the part of the autocorrelation curve describing the opening-closing kinetics can be extracted by calculating the ratio of "beacon" and "control" strands (Fig. 10.1c). As conformational fluctuations represent a Poisson process, their characteristic timescale τ_{fluc} can be obtained by fitting the ratiometric curve with the expression

$$G_{fluc}(\tau) = 1 + \frac{1-p}{p} \cdot e^{-\frac{\tau}{\tau_{fluc}}} \tag{10.1}$$

with p describing the fraction of open strands.

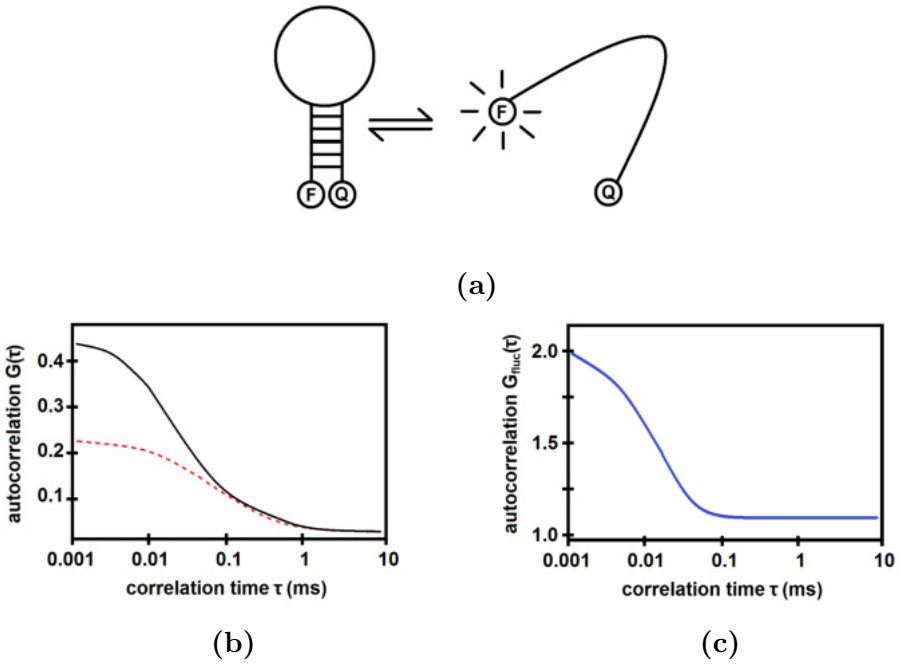

Figure 10.1: Original experimental procedure. (a) "Beacon" DNA hairpin with fluorophore (F) and quencher (Q) at opposing ends. In closed condition (left) fluorophore and quencher are close enough for FRET to occur, so there is no fluorescence emission. In open condition (right) no FRET occurs, therefore fluorescence is emitted. The "control" DNA strand differs from the "beacon" strand only in lacking the quencher. (b) "Control" (red, dashed) and "beacon" (black, solid) autocorrelation functions $G(\tau)$. (c) Ratio $G_{fluc}(\tau)$ of "beacon" and "control" autocorrelation functions. Only the part reflecting opening-closing dynamics remains. Figures inspired by[119].

10.2.2 Modified Experimental Procedure to Accommodate fCrH2

Bonnet et al.[119] were able to use two different kinds of DNA strands, "beacon" and "control", that differ only in the presence or absence of an additional quencher and thus the presence or absence of blinking. Unfortunately, a similar control strand for fCrH2 could not be obtained. Therefore the original experimental procedure was modified to accommodate a sensor consisting of a single, intramolecularly labelled molecule:
While illuminating the sample with wavelengths appropriate to excite the donor, both donor and acceptor fluorescence can be recorded. Both autocorrelation curves display blinking due to opening and closing of the sensor followed by FRET, as well as photophysical processes and centre of mass diffusion. If the acceptor is excited directly, however, opening and closing of the protein does not lead to blinking, as FRET only works in one direction. So the autocorrelation curves obtained in the acceptor channel upon direct acceptor illumination only display photophysical processes and centre of mass diffusion. Therefore FCS traces obtained in the acceptor channel during acceptor illumination can be utilized to extract opening-closing dynamics from FCS traces obtained in the donor channel during donor illumination (see Fig. 10.2a).
The DNA hairpin loops investigated in previous works can be manufactured in vitro and added to any desired surrounding fluid. This is not possible for fCrH2. The genetically encoded sensor cannot be built de novo in a test tube but must be expressed by living cells. Sukenik et al.[105] proposed a method of recombinantly expressing and purifying the sensor for in vitro studies. Lacking appropriate equipment this method could not be adopted. Therefore all measurements were done in lysates of HeLa cells previously transfected with DNA encoding fCrH2. So additional influences on the diffusion of tracer particles from the complex multiscale protoplasmic architecture were avoided. Lysis was performed with mammalian protein extraction reagent M-PER (see chapter 4 for detailed protocol), a proprietary detergent in 25 mM bicine buffer. According to the manufacturer's specification it does not denature proteins, so fCrH2 can be expected to be still fully functional after lysis.
Although the same protocol was followed for production of all lysates, the exact composition of the lysate cannot be controlled. Due to prolonged cell culture after plating and transfection, the total number of cells in the sample before lysis varied considerably. Additionally, intracellular compositions might differ between samples, due to variation in cell sizes, cell cycle phase of individual

cells etc. Cell culture medium and buffer from washing cells prior to application of M-PER cannot be removed completely. Finally, it cannot be controlled how thoroughly cells are actually lysed: there might still be some bigger aggregates and membrane fragments in the sample. Regarding fCrH2 itself, due to statistic fluctuations in transfection efficiency the number of fluorophores in the sample diverges. So each individually prepared cell lysate features its unique viscosity as well as sensor concentration. Thus, only measurements acquired in the same lysate preparation can be compared faithfully as they share all qualities and can be expected to display the same characteristics in both FRET and control measurements with the exception of blinking.
It must be kept in mind, however, that due to the different illumination wavelengths the confocal volumes in FRET and control measurement are of different size: the confocal volume is given by[235]

$$V_{conf} = \left(\frac{\pi}{2}\right)^{3/2} \omega_0^2 z_0 = \left(\frac{\pi}{2}\right)^{3/2} S\omega_0^3. \tag{10.2}$$

In this expression, ω_0 describes the radius in x, y-direction and z_0 the half-length in z-direction of the confocal volume, i.e. the distances from the volume's centre where intensity has decreased to $\frac{1}{e^2}$ of its maximum value. The dimensionless shape factor S describes the eccentricity of the confocal volume and depends on setup properties. The $\frac{1}{e^2}$-radius is connected to the $\frac{1}{2}$-radius $FWHM$ via $\omega_0 = \frac{FWHM}{\sqrt{2\ln 2}}$. Of course the full width at half maximum $FWHM$ linearly depends on the geometric mean of excitation and emission wavelengths[236]. So, ultimately, the confocal volume is proportional to the cube of this effective wavelength:

$$V_{conf} \propto \lambda_{eff}^3. \tag{10.3}$$

In order to accurately compare the diffusional part of the two curves, one must carefully normalize the control autocorrelation curve to match the FRET autocorrelation curve. This was achieved as follows:
The diffusion time τ_d that can be extracted from autocorrelation curves obtained by FCS measurements denotes the typical time a diffusing particle stays inside the confocal volume. So it depends on the confocal volume's size, namely on its radius in x-y-direction ω_0:

$$\tau_d = \frac{\omega_0^2}{4D_P}, \tag{10.4}$$

with the particles' diffusion coefficient D_P depending on size and shape of the diffusing particles, properties of the surrounding medium as well as temperature. As shown above the confocal volume's radius in turn linearly depends on the effective wavelength λ_{eff}. As all other instrument settings were held constant, only excitation wavelength and the recorded range of wavelengths differ between FRET and control measurements. Of course, emission covers a whole range of wavelengths. As the samples were too dilute to perform a spectral analysis of the emission range, emission maxima were used to determine effective wavelengths. Consequently the ratio of pinhole radii can only be estimated as

$$\frac{\omega_A}{\omega_D} = \frac{\lambda_A}{\lambda_D} \approx \frac{601\,\mathrm{nm}}{499\,\mathrm{nm}} \tag{10.5}$$

which renders an anticipated ratio of diffusion times of

$$\frac{\tau_A}{\tau_D} = \left(\frac{\omega_A}{\omega_D}\right)^2 = \left(\frac{\lambda_A}{\lambda_D}\right)^2 \approx \left(\frac{601\,\mathrm{nm}}{499\,\mathrm{nm}}\right)^2 \approx 1.45 =: \frac{1}{f_\tau}. \tag{10.6}$$

In both cases the same kind of tracer molecule moves through the same medium, i.e. the difference in diffusion times is caused solely by the varying size of the observation volume. In view of this fact the time axis of the control measurement can be rescaled by a factor of f_τ, so that τ_A equals τ_D. Simultaneously the size of the confocal volume has an effect on the expected particle number picked up by FCS measurements. As demonstrated above, the confocal volume depends on the cube of the effective wavelength. So the ratio of observation volumes can be estimated as

$$\frac{V_A}{V_D} = \left(\frac{\lambda_A}{\lambda_D}\right)^3 \approx \left(\frac{601\,\mathrm{nm}}{499\,\mathrm{nm}}\right)^3 \approx 1.75. \tag{10.7}$$

Assuming the number of donor and acceptor molecules emitting fluorescence photons in a given infinitesimal subvolume to be the same for both types of excitation, this would already account for a 1.75-fold higher number of fluorescent particles to be registered in the FCS measurements performed with 594 nm-illumination. The difference in recorded fluorescent particles in FRET and control measurements is, however, anticipated to be even more prominent. Presumably there will be at least a small fraction of sensor molecules in the closed conformational state at all times. FRET happens on a timescale of few nanoseconds, i.e. well out of the range of timescales accessible by means of FCS. That is why donor molecules in closed sensors appear dark for the detection method. This results in the fact that, during donor illumination,

the number of fluorescent particles in the confocal volume can be smaller than the actual number of fluorophores. Thus the rescaling factor for the $G(\tau)$-axis intercept, i.e. for the inverse particle number, is expected to be

$$f_{G(\tau)} \geq 1.75. \tag{10.8}$$

As both rescaling factors were deduced from estimates the exact rescaling factors had to be found heuristically. In order to accomplish this, both correlation time and correlation axis of the control measurement were repeatedly rescaled to realize the best possible overlap of diffusive parts of the autocorrelation curves.

Despite long fluorescence acquisition times (up to 300 s per measurement locus), autocorrelation curves showed high levels of noise. In order to minimize falsification of the "autocorrelation of blinking" by taking ratios of noisy data, all autocorrelation curves obtained in one sample under the same excitation wavelengths were averaged to generate smoother autocorrelation curves. However, this was found to be insufficient. So the rescaled and averaged autocorrelation curve of the control measurements was additionally fitted with a function describing centre-of-mass diffusion (see Eq. 3.13 and Fig. 10.2c). The averaged FRET autocorrelation curve was divided by this fitcurve to extract the "autocorrelation of blinking" (Fig. 10.2e).

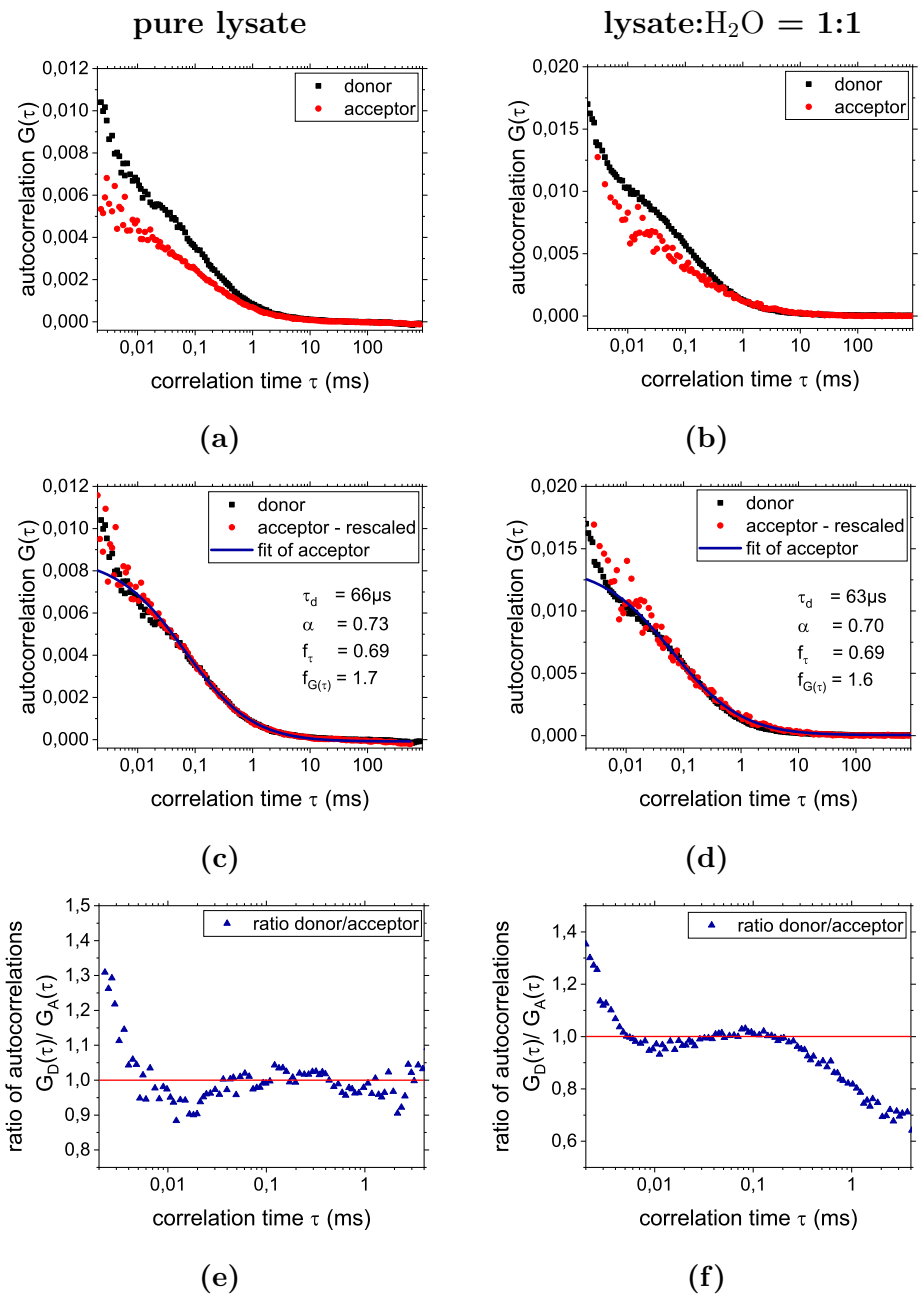

Figure 10.2: Modified experimental procedure. (a) Averaged donor and acceptor autocorrelation function in pure lysate. (b) Averaged donor and acceptor autocorrelation function in the same lysate diluted with water at a ratio of 1:1. (c) Averaged donor ACF autocorrelation function and twice rescaled averaged acceptor autocorrelation function with fit for diffusive motion in pure lysate. (d) Averaged donor ACF autocorrelation function and twice rescaled averaged acceptor autocorrelation function with fit for diffusive motion in lysate diluted with water. (e) Averaged donor autocorrelation function divided by fit to averaged acceptor autocorrelation function in pure lysate. (f) Averaged donor autocorrelation function divided by fit to averaged acceptor autocorrelation function in lysate diluted with water.

10.3 Results and Discussion

The anticipated "autocorrelation of blinking" part of the autocorrelation curve obtained in the donor channel upon donor illumination vanishes after carefully normalizing the original autocorrelation functions and taking their ratio (see Fig. 10.2e): all values in the ratiometric curve are very close to unity and do not display the typical shape that would be expected from an autocorrelation function - independent of the physical process it represents. While this might be due to insufficient statistics, there is a number of other possible - and presumably more probable - explanations why the "autocorrelation of blinking" cannot be extracted with the previously described method:
In fact, the assumption that open and closed fCrH2 molecules have the same diffusional properties might be wrong. After all, diffusion constants depend on the Stokes radii of diffusing molecules, so a change in the molecules' conformation might have some influence on the diffusion constant, which in turn might introduce an error into the evaluation method in the course of fitting the diffusional part of the autocorrelation. However, lysates are nowhere nearly as crowded as living cells. Thus steric hindrance of the tracer particle is much less pronounced. So a possible disparity in the diffusion coefficients of open and closed molecules is most probably negligible.
To avoid introducing yet another set of variables in the evaluation process, only the diffusional part of the acceptor autocorrelation was fitted. The photophysical part was neglected. This might introduce an error into the evaluation procedure itself. However, it might also be wrong to assume that photophysics is the same for both donor and acceptor. So even including photophysics in acceptor fitting need not necessarily improve results.
Another aspect that has to be taken into consideration is the process of preparing the lysate: to this end mammalian protein extraction reagent M-PER was used, which, according to the manufacturer's specifications, doesn't harm proteins in the lysing process. Indeed both EGFP and mCherry still emit fluorescence in the lysate. But it cannot easily be analysed whether the link between both molecules is still intact. It is possible that both fluorophores diffuse independently of each other. As they are similar in size they would still have similar diffusion times even after separation. As lysates cannot easily be characterized with respect to their diffusion properties, measured diffusion constants cannot be compared to literature values. Since lysate densities cannot be controlled with the equipment available, preparing lysates with single fluorophores cannot serve as a control either. Maybe double-illumination with

both 488 nm and 594 nm at the same time and checking the cross-correlation of both emission channels could clarify whether the manufacturer's specifications actually hold true.
The characteristic timescale of the opening-closing process could be in the same range as diffusion times of fCrH2 in HeLa lysate. So the dynamics could be completely masked by diffusional dynamics and be lost in the double rescaling process.
Finally, it must be taken into account that lysates are far less crowded than cells. This is due to the lysing agent as well as to remnants of culture medium and buffer which cannot be removed completely prior to lysis. While the exact fraction of non-cellular substances in the lysate is unknown, comparing diffusion times obtained in lysates and cells can give an impression of the difference between lysates and native cells. Unfortunately, as fCrH2 is generally expressed at a very high level, FCS experiments cannot be performed on this sensor in HeLa cells. So diffusion times of fCrH2 in HeLa lysate were compared to data of EGFP in mitotic HeLa cells[82]. These data were obtained by using the same setup as well as the same sample holders which were also used in this thesis. Still, taking into account the considerable difference in molecule size, diffusion times of fCrH2 in HeLa cells are expected to be higher than those of EGFP. In mitotic HeLa cells, the diffusion time of EGFP was found to be in the range of 170 µs to 320 µs. In contrast, diffusion times of fCrH2 in pure HeLa lysate were found to be in the range of 50 µs to 70 µs. Inserting the Einstein-Smoluchowski relation $D_P = \frac{k_B T}{6\pi\eta r_S}$ into Eq. 10.4, we find

$$\eta \propto \tau_d. \tag{10.9}$$

So the lysates prepared in this project can be estimated to be about four times less viscous than native cells. This implies the fact that crowding levels are significantly lower in lysates than in cells. Low crowding levels in turn make it quite possible that only a very limited number of fCrH2 molecules is in closed state in the first place. Consequently only very little FRET would occur.
This is supported by a simple dilution experiment (Fig. 10.2b, 10.2d and 10.2f): after obtaining a number of FCS traces in pure lysate, the sample is diluted approximately 1:1 with MilliQ water. Subsequently a new set of FCS traces is obtained. While the number of fluorophores in the confocal volume is reduced to approximately one half of the original particle concentration (see Fig. 10.2a and 10.2b), the ratio between donor and acceptor hardly changes (see Fig. 10.2e and 10.2f). Moreover, also diffusion times in diluted lysate are similar to those

obtained in pure lysate (30 µs to 60 µs). If dilution with a considerable amount of water virtually has no effect on opening-closing dynamics and only slightly changes the lysates' viscosities, the inevitable conclusion would be that in the pure lysate as it is crowding levels are so low that FRET events are quite rare.

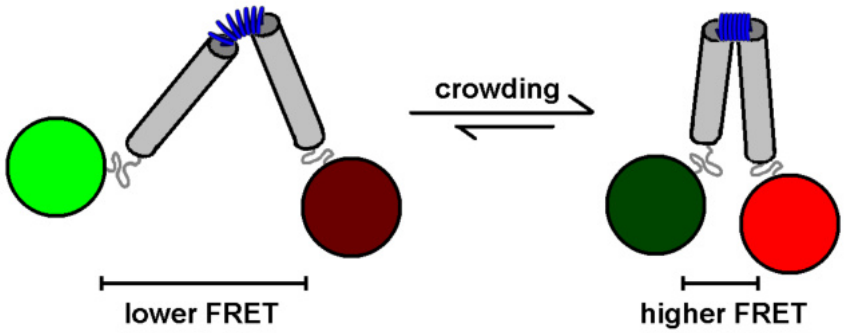

Figure 10.3: The linker in fCrH2 behaves like a spring. At low crowding levels (left) the spring assumes a relaxed conformation. Donor and acceptor are at a considerable distance, so only little or no FRET occurs. At high crowding levels (right) the molecule is "pushed" together by its surroundings, so the spring assumes a closed conformation. Donor and acceptor are close enough to obtain high FRET efficiencies.

This can be understood in terms of molecule structure: the link between donor and acceptor in the fCrH2 molecule might, in fact, not be a conformationally flexible domain that randomly opens and closes of its own accord. It could rather be similar to a spring requiring active pressing on its ends to change its conformation (see Fig. 10.3). In this case, the closed state would only be adopted if the molecule is "pushed" together by its surroundings. This is supported by a fact that can be seen in Fig. 10.2c and Fig. 10.2d: after correcting for the influence of differently sized confocal volumes the registered particles in both measurements were found to be virtually equal. Exciting the donor and registering acceptor fluorescence didn't work either as the acceptor fluorescence signal was too low. This again supports the theory that most molecules are in the open state. Unfortunately, while dilution e.g. with MilliQ water after lysis works quite well, artificial crowding of the lysate could not be done: only very limited amounts of lysate could be produced at the same time with the available resources. Moreover, due to rapid ageing effects lysates could not be stored. Maybe repeating the experiments in cells could work as there are higher crowding levels. However, the considerably more complex multi-scale architecture inside living cells would certainly have an impact on the signal-to-noise ratio in autocorrelation curves. What is more, fCrH2 transfection levels in cells tend to be far too high to successfully perform FCS measurements.

To sum it up, unless there is some inherent flaw to the measurement process that cannot be tested or couldn't be identified, the most probable explanation for the lack of an "autocorrelation of blinking" of fCrH2 is the fact that the molecule behaves like a spring that requires active "pushing" by an environment significantly more crowded than a cell lysate for FRET to occur. The time-scale of opening and closing dynamics would consequently mirror the time-scale of changes in crowding levels of the surrounding environment.

Chapter 11

Conclusion

This thesis primarily focused on describing intracellular crowding levels and crowding heterogeneities on multiple lengthscales. In HeLa interphase cells, available volume fractions in the nucleoplasm exceed those in the cytoplasm by about 20 %. The cytoplasm is not only more crowded than the nucleoplasm, but also features a ROI-to-ROI heterogeneity level of the available volume fraction nearly twice as high. On smaller lengthscales, i.e. on the lengthscale of several hundred nanometres, as well as on the 5 nm-scale, both compartments are very similar.
After nuclear envelope breakdown, former nucleoplasm and cytoplasm do mix, but only to some degree. The spindle periphery retains its higher crowding level only in part: available volume fractions are about 10 % higher in the spindle area than in the spindle periphery. This result justifies viewing spindle and spindle periphery as individual compartments, although they lack a separating membrane. Crowding heterogeneities, however, are similar in both compartments. This is independent of the lengthscale it is investigated at. Moreover, below lengthscales of a few hundred nanometres metaphase compartments display virtually the same heterogeneity levels as interphase compartments.

Overall crowding levels are influenced by osmolar stress and high levels of oxidative stress, but neither by low levels of oxidative stress nor by ATP depletion. ATP:ADP and ATP:isosbestic point levels are affected by total as well as by partial ATP depletion.
ROI-to-ROI heterogeneities of the respective observables were found to only change significantly during exposure to osmolar stress. A slight change of the ROI-to-ROI heterogeneity of ATP:ADP levels might occur during total ATP depletion.

In addition to describing intracellular crowding states, energy levels and their respective heterogeneities, the opening-closing-characteristics of one of the sensors employed in this thesis were analysed. Donor and acceptor of the FRET-based crowding sensor fCrH2 were found to be connected by a spring-like link that requires being actively pressed together by its surroundings in order to change its conformation from open to closed state. So the sensor, indeed, solely reflects the crowding state of its immediate surroundings.

Based on the results found in this thesis, the most pressing question left to be answered is the reason for the astonishingly high ensemble heterogeneities in all measurements. This problem could be analysed by repeating the experiments in synchronized cell cultures at different, well-defined cell cycle stages. Very interesting, but experimentally really challenging, would be monitoring individual cells throughout a complete cell cycle. Repeating the experiments described in this thesis in another cell line, especially a non-cancerous one, could provide new insights into the topic.
With respect to stress treatments, it should be attempted to repeatedly alternate between standard conditions and exposure to stressors. New developments in TCSPC detectors might open the possibility to perform lifetime-based experiments during exposure to stress treatments.

The results described in this thesis could potentially be utilized in simulations of intracellular transport. Thus especially fields such as nanomedicine or bioinformatics might benefit from various results established in this thesis. In addition, analyses of experimental techniques based on tracer motion might profit from the results. Insights into the heterogeneity levels of cellular fluids might even be used as a basis to develop new types of biomimetic fluids.
Last but not least, this thesis confirms recent findings on the existence of a considerable spatial heterogeneity within living cells. It is quite likely that this spatial heterogeneity of crowding states and energy levels contributes to a functional compartmentalization in cells that is independent of physical barriers such as membranes. It might thus contribute fundamentally to intracellular organization in species lacking membrane-enclosed organelles, i.e. prokaryotes and archaea. However, it remains to be tested whether those organisms do feature a similar spatial heterogeneity as the eukaryotic HeLa cells investigated in this thesis.

Moreover, even though cultured cells are expected to be genetically identical, cell ensembles feature a rather high ensemble heterogeneity of all observables. This is in line with previous studies showing that isogenic cell populations in nearly identical growth conditions can exhibit pronounced differences in phenotypic expression [237] [238]. Thus intra- and intercellular heterogeneities might, in the long run, even contribute to large-scale processes such as evolution.
So considering all facts, especially in biological samples the common practice to focus on averaged values appears rather questionable.

Part IV

Appendices

Appendix A

Statistics

Fluorophore Solutions

Solutions of Alexa488 in MilliQ water at different concentrations. All measurements in this table were performed at a PMT bias voltage of 900 V.

lengthscale	ensemble mean	standard deviation	standard error	ensemble heterogeneity	ensemble size
ROI-to-ROI	0.0178	0.0059	0.0009	0.3301	39 images
voxelscale	0.0229	0.0110	0.0006	0.4810	299 ROIs

FRAP

Half times of recovery in individual cells

$\tau_{1/2,\mathrm{nuc}}$ (s)	$\tau_{1/2,\mathrm{cyto}}$ (s)	$\frac{\tau_{1/2,\mathrm{nuc}}-\tau_{1/2,\mathrm{cyto}}}{\tau_{1/2,\mathrm{nuc}}}$ (‰)
73.4625	73.4548	0.1057
77.6872	77.7197	0.4179
59.3008	59.3083	0.1267
49.1100	49.1531	0.8771
38.9823	38.9838	0.0384
50.9420	50.9153	0.5225
65.4263	65.4134	0.1977
34.3822	34.3822	0.0002
36.5778	36.6009	0.6309
25.4087	25.4389	1.1885
67.6392	67.6951	0.8255
42.5482	42.5722	0.5621
76.6187	76.6159	0.0369
51.1403	51.1481	0.1518
4.4195	4.4181	0.3105
31.5754	31.5566	0.5951
41.5078	41.4789	0.6984
46.9538	46.9379	0.3387
59.1841	59.2061	0.3718
96.8490	96.8494	0.0049
33.9067	33.9063	0.0100

Averaged Half Times of Recovery/Loss

	$\tau_{1/2,\mathrm{nuc}}$ (s)	$\tau_{1/2,\mathrm{cyto}}$ (s)	$\frac{\tau_{1/2,\mathrm{nuc}}-\tau_{1/2,\mathrm{cyto}}}{\tau_{1/2,\mathrm{nuc}}}$ (‰)
average	50.6487	50.6550	0.3815
standard deviation	21.0923	21.0948	0.3356

EGFP

	lengthscale	compartment	ensemble mean	standard deviation	standard error	ensemble heterogeneity	ensemble size
interphase	overall	ratio	1.2048	0.1487	0.0167	0.1234	79 cells
	ROI-to-ROI	Nuc	0.0576	0.0289	0.0033	0.5022	79 cells
		Cyto	0.1274	0.0534	0.0060	0.4194	79 cells
		ratio	0.4935	0.2552	0.0287	0.5171	79 cells
	voxelscale	Nuc	0.0627	0.0429	0.0014	0.6839	893 ROIs
		Cyto	0.0742	0.0488	0.0015	0.6570	1009 ROIs
		$\delta_{nuc}/\delta_{cyto}$	0.8669	0.1070	0.0120	0.1234	79 cells
metaphase	overall	ratio	1.1083	0.0615	0.0057	0.0555	116 cells
	ROI-to-ROI	Spin	0.0528	0.0243	0.0023	0.4592	116 cells
		↳ Pole*	0.9923	0.0590	0.0039	0.0035	232 ROIs
		↳ Center*	1.0149	0.0502	0.0033	0.0025	232 ROIs
		↳ Border*	0.9964	0.0527	0.0024	0.0028	464 ROIs
		Per	0.0601	0.0252	0.0023	0.4193	116 cells
		ratio	0.9951	0.5479	0.0509	0.5506	116 cells
	voxelscale	Spin	0.0788	0.0579	0.0031	0.7349	351 ROIs
		↳ Pole	0.0740	0.0580	0.0061	0.0454	91 ROIs
		↳ Center	0.0801	0.0573	0.0062	0.0410	86 ROIs
		↳ Border	0.0807	0.0584	0.0044	0.0422	174 ROIs
		Per	0.0825	0.0644	0.0027	0.7806	560 ROIs
		$\delta_{spin}/\delta_{per}$	0.9151	0.1127	0.0105	0.1231	116 cells
nocodazole	overall	ratio	1.3088	0.1218	0.0367	0.0931	11 cells
	ROI-to-ROI	Nuc	0.0351	0.0066	0.0020	0.1880	11 cells
		Cyto	0.0814	0.0236	0.0071	0.2906	11 cells
		ratio	0.4566	0.1334	0.0402	0.2921	11 cells
	voxelscale	Nuc	0.0736	0.0331	0.0027	0.4495	145 ROIs
		Cyto	0.0804	0.0438	0.0032	0.5450	193 ROIs
		$\delta_{nuc}/\delta_{cyto}$	0.8657	0.0451	0.0136	0.0521	11 cells

* ROIs per cell normalized on mean intensity of cell prior to calculation of ensemble statistics per position.

Thresholds Obtained via Standard Errors of ROIs

sample	ensemble mean	standard deviation	standard error	ensemble heterogeneity	ensemble size
Nuc	0.0118	0.0065	0.0002	0.5492	1580 ROIs
Cyto	0.0117	0.0058	0.0001	0.4979	1580 ROIs
Spin	0.0106	0.0044	0.0001	0.4175	928 ROIs
Per	0.0084	0.0038	0.0001	0.4555	1392 ROIs
Nuc + Noc	0.0076	0.0013	0.0001	0.1740	220 ROIs
Cyto + Noc	0.0071	0.0013	0.0001	0.1898	220 ROIs
Alexa488	0.0091	0.0043	0.0001	0.4694	831 ROIs

FRET

	lengthscale	compartment	ensemble mean	standard deviation	standard error	ensemble heterogeneity	ensemble size
interphase	overall	ratio	1.0536	0.0347	0.0030	0.0329	138 cells
	ROI-to-ROI	Nuc	0.0105	0.0051	0.0004	0.4825	138 cells
		Cyto	0.0122	0.0059	0.0005	0.4841	138 cells
		ratio	1.0566	0.7326	0.0624	0.6934	138 cells
metaphase	overall	ratio	1.0012	0.0044	0.0008	0.0044	32 cells
	ROI-to-ROI	Spin	0.0047	0.0020	0.0004	0.4275	32 cells
		↳ Pole*	0.6246	0.0208	0.0026	0.0334	64 ROIs
		↳ Center*	0.6246	0.0205	0.0026	0.0328	64 ROIs
		↳ Border*	0.6245	0.0207	0.0018	0.0332	128 ROIs
		Per	0.0054	0.0046	0.0008	0.8558	32 cells
		ratio	1.1855	0.7571	0.1338	0.6639	32 cells
lysate	ROI-to-ROI	-	0.0027	0.0004	0.0002	0.1517	7 lysates

FLIM

	lengthscale	compartment	ensemble mean	standard deviation	standard error	ensemble heterogeneity	ensemble size
interphase	overall	ratio	0.9618	0.1721	0.0161	0.1789	114 cells
	ROI-to-ROI	Nuc	0.5843	0.2994	0.0280	0.5124	114 cells
		Cyto	0.3683	0.2127	0.0199	0.5775	114 cells
		ratio	1.7172	0.7401	0.0693	0.4310	114 cells
metaphase	overall	ratio	1.0241	0.1782	0.0310	0.1740	33 cells
	ROI-to-ROI	Spin	0.3443	0.2276	0.0396	0.6610	33 cells
		↳ Pole*	0.4491	0.1869	0.0230	0.0778	66 ROIs
		↳ Center*	0.4193	0.1512	0.0186	0.0545	66 ROIs
		↳ Border*	0.4178	0.1584	0.0138	0.0600	132 ROIs
		Per	0.3356	0.1814	0.0316	0.5406	33 cells
		ratio	1.0098	0.2537	0.0442	0.2512	33 cells

FLPM

short measurement time per locus

	lengthscale	compartment	ensemble mean	standard deviation	standard error	ensemble heterogeneity	ensemble size
interphase	overall	ratio	1.0081	0.0571	0.0089	0.0567	41 cells
	ROI-to-ROI	Nuc	0.1236	0.0361	0.0056	0.2923	41 cells
		Cyto	0.1181	0.0445	0.0069	0.3765	41 cells
		ratio	1.2765	0.8493	0.1326	0.6653	41 cells
metaphase	overall	ratio	1.0113	0.0608	0.0143	0.0601	18 cells
	ROI-to-ROI	Spin	0.1349	0.0279	0.0066	0.2072	18 cells
		Per	0.1272	0.0387	0.0091	0.3047	18 cells
		ratio	1.1654	0.4474	0.1055	0.3839	18 cells

long measurement time per locus

	lengthscale	compartment	ensemble mean	standard deviation	standard error	ensemble heterogeneity	ensemble size
interphase	overall	ratio	1.0707	0.0648	0.0138	0.0605	22 cells
	ROI-to-ROI	Nuc	0.0903	0.0356	0.0076	0.3942	22 cells
		Cyto	0.0801	0.0325	0.0069	0.4063	22 cells
		ratio	1.2919	0.7167	0.1528	0.5547	22 cells
metaphase	overall	ratio	1.0055	0.0891	0.0149	0.0886	36 cells
	ROI-to-ROI	Spin	0.1155	0.0371	0.0062	0.3215	36 cells
		Per	0.1238	0.0574	0.0096	0.4637	36 cells
		ratio	1.0523	0.4277	0.0713	0.4065	36 cells

Spindle Spatially Resolved

short time many loci - 18 cells:

position	ensemble mean parallel	standard deviation parallel	standard error parallel	ensemble heterogeneity parallel	ensemble mean perpendicular	standard deviation perpendicular	standard error perpendicular	ensemble heterogeneity perpendicular
pos1	0.6661	0.0599	0.0141	0.0054	0.6391	0.0611	0.0144	0.0058
pos2	0.6251	0.0915	0.0216	0.0134	0.6731	0.0726	0.0171	0.0078
pos3	0.6363	0.1141	0.0269	0.0204	0.6105	0.1047	0.0247	0.0180
pos4	0.6819	0.0781	0.0184	0.0089	0.6171	0.1045	0.0246	0.0177
pos5	0.6470	0.0825	0.0194	0.0105	0.6084	0.1229	0.0290	0.0248
pos6	0.6334	0.0945	0.0223	0.0141	0.6852	0.0623	0.0147	0.0057
pos7	0.6791	0.0665	0.0157	0.0065	0.6568	0.0664	0.0157	0.0067
pos8	0.6417	0.0887	0.0209	0.0123	0.5812	0.1049	0.0247	0.0189
pos9	0.6619	0.0547	0.0129	0.0045	0.6219	0.0952	0.0224	0.0146
pos10	0.6204	0.0844	0.0199	0.0045	0.6786	0.0492	0.0116	0.0036

long time few loci - 36 cells:

position	ensemble mean parallel	standard deviation parallel	standard error parallel	ensemble heterogeneity parallel	ensemble mean perpendicular	standard deviation perpendicular	standard error perpendicular	ensemble heterogeneity perpendicular
pos1	0.6055	0.0744	0.0124	0.0091	0.5637	0.0820	0.0137	0.0119
pos2	0.5916	0.0642	0.0107	0.0070	0.5602	0.0874	0.0146	0.0136
pos3	0.5901	0.0785	0.0131	0.0104	0.5808	0.0853	0.0142	0.0125
pos4	0.5950	0.0736	0.0123	0.0091	0.5852	0.0877	0.0146	0.0132
pos5	0.5744	0.0698	0.0116	0.0085	0.5721	0.0783	0.0130	0.0107
pos6	0.5766	0.0894	0.0149	0.0139	0.6148	0.0821	0.0137	0.0110

Perceval HR: physiological interphase cells

	lengthscale	compartment	ensemble mean	standard deviation	standard error	ensemble heterogeneity	ensemble size
ATP:ADP	overall	nuc	7.0139	0.7315	0.1560	0.1043	22 cells
		cyto	6.4445	0.6415	0.1368	0.0995	22 cells
		ratio	1.0886	0.0416	0.0089	0.0382	22 cells
	ROI-to-ROI	nuc	0.0269	0.0090	0.0019	0.3346	22 cells
		cyto	0.0243	0.0135	0.0029	0.5556	22 cells
		ratio	1.3279	0.6654	0.1419	0.5011	22 cells
ATP:ISO	overall	nuc	2.5656	0.2072	0.0282	0.0808	54 cells
		cyto	2.4986	0.1396	0.0190	0.0559	54 cells
		ratio	1.0262	0.0444	0.0060	0.0433	54 cells
	ROI-to-ROI	nuc	0.0243	0.0256	0.0035	1.0535	54 cells
		cyto	0.0239	0.0332	0.0045	1.3891	54 cells
		ratio	1.3275	0.8316	0.1132	0.6264	54 cells
	ROI-to-ROI	nuc	0.0199	0.0096	0.0013	0.4837	54 cells
	without	cyto	0.0177	0.0098	0.0013	0.5525	54 cells
	outliers	ratio	1.2497	0.5079	0.0691	0.4064	54 cells

Stress Treatments

treatment	sensor	ROIs/comp.	cells
no treatment	EGFP	20	1 (2x)
no treatment	EGFP (FCS)	1	1
hyperosmolar	fCrH2	10	11
hypoosmolar	fCrH2	10	15
oxidative (low)	fCrH2	10	3
oxidative (high)	fCrH2	10	3
rotenone/oligomycin, C1	Perceval HR	10	8
rotenone/oligomycin, C2	Perceval HR	10	8
rotenone/oligomycin, C3	Perceval HR	10	8
rotenone/oligomycin, C4	Perceval HR	10	8
sodium azide/2-deoxy-D-glucose	Perceval HR	10	22
sodium azide/2-deoxy-D-glucose	EGFP	10	19
sodium azide/2-deoxy-D-glucose	EGFP (FCS)	1	32

Appendix B

Chemicals, Equipment and Manufacturers

All cell measurements were performed in the Göteborg Strain of human cervical cancer cells (HeLa).

Chemicals

Cell Culture Media

name in text	**full name**	**manufaturer**
DMEM	Dulbecco's Modified Eagle Medium	Gibco (Life Technologies)
DPBS	Dulbecco's Phosphate Buffered Saline	Gibco (Life Technologies)
FCS	Fetal Calf Serum	Gibco (Life Technologies)
glucose-free medium	Dulbecco's Modified Eagle Medium [-] D-glucose	Gibco (Life Technologies)
glutamine	L-glutamine	Gibco (Life Technologies)
HEPES	HEPES Buffer Solution	Gibco (Life Technologies)
MEM	Minimum Essential Medium	Gibco (Life Technologies)
OptiMEM	OPTI-MEM Reduced Serum Medium	Gibco (Life Technologies)
penicillin	PenStrep Penicillin-Streptomycin	Gibco (Life Technologies)
streptomycin	PenStrep Penicillin-Streptomycin	Gibco (Life Technologies)
trypsin	0.25 % Trypsin-EDTA	Gibco (Life Technologies)

Transfection Reagents, DNA and Fluorophores

name in text	full name	manufaturer
Alexa488	Alexa488 on dextrane 10kDa	unknown
EGFP	enhanced green fluorescent protein, inserted in pCS2-based plasmid	O. Stemmann, University of Bayreuth
fCrH2	GFP/mCherry sensor fCrH2 inserted in pDream2.1 vector	M. Gruebele, University of Illinois
Fugene6	Fugene6 Transfection Reagent	Promega
Peqfect	peqFECT DNA Transfection Reagent	PEQLAB
Perceval HR	GW1-Perceval HR (Plasmid #49082)	Addgene
Polyplus jetPrime	jetPrime Transfection Reagent	PolyPlus

Chemicals Used in Stress Treatments and Lysis

name in text	full name	manufaturer
2-deoxy-D-glucose	2-Deoxy-D-glucose	Sigma-Aldrich
DMSO	Dimethyl Sulfoxide for cell culture	Applichem
M-PER	M-PER Mammalian Protein Extraction Reagent	Thermo Scientific
nocodazole	Nocodazole	Sigma Aldrich
oligomycin	Oligomycin	Calbiochem
rotenone	Rotenone	EMD Millipore Corp.
sodium azide	Sodium Azide	Sigma-Aldrich
sodium chloride	Natriumchlorid zur Analyse	Bernd Kraft GmbH

Microscope

chromaslide	Autofluorescent Plastic Slide (green)	Chroma
Microscope	Leica TCS SP5	Leica Microsystems
objective	63x/1.2 N.A. water immersion	Leica Microsystems
TCSPC unit	PicoHarp 300 TCSPC Module	PicoQuant
temperature box	temperature box	custom-made

Other Equipment

name	**full name**	**manufacturer**
cell culture flasks	Corning Flasks with 0.2 µm vent caps	Sigma Aldrich
centrifuges	Biofuge primo R centrifuge Fresco 17 Centrifuge	Heraeus Heraeus
culture dishes	6 Well Cell Culture Plate	Greiner bio-one Cellstar
glass pipets	glass pipets	Greiner bio-one Cellstar
incubator	HERAcell 150i CO_2 incubator	Thermo Scientific
microscopy chambers	ibiTreat μ-Slide: 2-well, 4-well, 8-well	Ibidi
MilliQ machine	MilliQ machine	Millipore Corp.
pipet boy	Easypet pipetboy	Eppendorf
pipets	pipetman pipets	Gilson
pipet tips	Tipone Safeguard	Starlab PEQLAB
refrigerator (at 4 °C/−20 °C)	Premium NoFrost	Liebherr
scales	Atilon d=0.01 g Atilon d=0.1 mg	Acculab Acculab
sterile bench	HERAsafe KS hood	Thermo Scientific
vortexer	vortexer	neoLab VWR

Bibliography

[1] J. Keizer, *Statistical Thermodynamics of Nonequilibrium Processes*. New York: Springer, 1987.

[2] F. Höfling and T. Franosch, "Anomalous transport in the crowded world of biological cells," *Reports on Progress in Physics*, vol. 76, p. 046602, 2013.

[3] L. Vlahos, H. Isliker, Y. Kominis, and K. Hizanidis, "Normal and Anomalous Diffusion: A Tutorial." arXiv:0805.0419v1 [nlin.CD]; https://arxiv.org/abs/0805.0419v1, 2008.

[4] G. Chalancon, C. N. J. Ravarani, S. Balaji, A. Martinez-Arias, L. Aravind, R. Jothi, and M. M. Babu, "Interplay between gene expression noise and regulatory network architecture," *Trends in Genetics*, vol. 28, no. 5, pp. 221–232, 2012.

[5] M. Kærn, T. C. Elston, W. J. Blake, and J. J. Collins, "Stochasticity in gene expression: from theories to phenotypes," *Nature Reviews*, vol. 6, pp. 451–464, 2005.

[6] D. Fraser and M. Kærn, "A chance at survival: gene expression noise and phenotypic diversification strategies," *Molecular Microbiology*, vol. 71, no. 6, pp. 1333–1340, 2009.

[7] L. Tsimring, "Noise in biology," *Reports on Progress in Physics*, vol. 77, p. 026601, 2014.

[8] Y. Ishihama, T. Schmidt, J. Rappsilber, M. Mann, F. U. Hartl, M. J. Kerner, and D. Frishman, "Protein abundance profiling of the Escherichia coli cytosol," *BMC Genomics*, vol. 9, no. 102, 2008.

[9] P. D. Schloss, R. A. Girard, T. Martin, J. Edwards, and J. C. Thrash, "Status of the Archaeal and Bacterial Census: an Update," *mBio*, vol. 7, no. 3, pp. e00201–16, 2016.

[10] K. J. Locey and J. T. Lennon, "Scaling laws predict global microbial diversity," *Proceedings of the National Academy of Sciences USA*, vol. 113, no. 21, pp. 5970–5975, 2016.

[11] C. Mora, D. P. Tittensor, S. Adl, A. G. B. Simpson, and B. Worm, "How Many Species Are There on Earth and in the Ocean," *PLOS Biology*, vol. 9, no. 8, p. e1001127, 2011.

[12] W. B. Whitman, D. C. Coleman, and W. J. Wiebe, "Prokaryotes: The unseen majority," *Proceedings of the National Academy of Sciences USA*, vol. 95, pp. 6578–6583, 1998.

[13] P. M. Llopis, A. F. Jackson, O. Sliusarenko, I. Surovtsev, J. Heinritz, T. Emonet, and C. Jacobs-Wagner, "Spatial organization of the flow of genetic information in bacteria," *Nature*, vol. 466, pp. 77–82, 2010.

[14] A. Jhaveri and V. Torchilin, "Intracellular delivery of nanocarrieres and Targeting to subcellular organelles," *Expert Opinion on Drug Delivery*, vol. 13, no. 1, pp. 49–70, 2016.

[15] A. Dinca, W.-M. Chien, and M. T. Chin, "Intracellular Delivery of Proteins with Cell-Penetrating Peptides for Therpeutic Uses in Human Disease," *International Journal of Molecular Sciences*, vol. 17, no. 263, pp. 1–13, 2016.

[16] A. R. Maity and D. Stepensky, "Limited Efficiency of Drug Delivery to Specific Intracellular Organelles Using Seubcellularly "Targeted" Drug Delivery Systems," *Molecular Pharmaceutics*, vol. 13, pp. 1–7, 2016.

[17] M. J. Schleiden, "Beiträge zur Phytogenesis," *Archiv für Anatomie, Physiologie und wissenschaftliche Medicin*, pp. 137–176, 1838.

[18] T. Schwann, *Mikroskopische Untersuchungen über die Uebereinstimmung in der Struktur und dem Wachsthum der Thiere und Pflanzen*. Berlin: Sander, 1st ed., 1839.

[19] C. R. Woese and G. E. Fox, "Phylogenetic structure of the prokaryotic domain: The primary kingdoms," *Proceedings of the National Academy of Sciences USA*, vol. 74, no. 11, pp. 5088–5090, 1977.

[20] C. R. Woese, O. Kandler, and M. L. Wheelis, "Towards a natural system of organisms: Proposal for the domains Archaea, Bacteria and Eucarya," *Proceedings of the National Academy of Sciences USA*, vol. 87, no. 12, pp. 4576–4579, 1990.

[21] L. Margulis and M. J. Chapman, *Kingdoms and Domains. An Illustrated Guide to the Phyla of Life on Earth*. Amsterdam: Academic Press, 4th ed., 2009.

[22] B. Alberts *et al.*, *Molecular Biology of the Cell, Reference Edition*. Garland Science, Taylor & Francis Group, 5th ed., 2008.

[23] B. P. Kelley, R. Sharan, R. M. Karp, T. Sittler, D. E. Root, B. R. Stockwell, and T. Ideker, "Conserved pathways within bacteria and yeast as revealed by global protein network alignment," *Proceedings of the National Academy of Sciences*, vol. 100, no. 20, pp. 11394–11399, 2003.

[24] J. Peregrín-Alvarez, C. Sanford, and J. Parkinson, "The conservation and evolutionary modularity of metabolism," *Genome Biology*, vol. 10, no. 6, pp. R63.1–R63.17, 2009.

[25] J. C. Xavier, K. R. Patil, and I. Rocha, "Metabolic models and gene essentiality data reveal essential and conserved metabolism in prokaryotes," *PLOS Computational Biology*, pp. 1–23, 2018.

[26] E. Callaway, "Deal done over HeLa cell line. Family of Henrietta Lacks agrees to release of genomic data," *Nature*, vol. 500, pp. 132–133, 2013.

[27] R. Skloot, *The Immortal Life of Henrietta Lacks*. Crown, 2010.

[28] J. W. Posakony, J. M. England, and G. Attardi, "Mitochondrial growth and division during the cell cycle in HeLa cells," *Journal of Cell Biology*, vol. 74, pp. 468–491, 1977.

[29] A. T. Hahn, J. T. Jones, and T. Meyer, "Quantitative analysis of cell cycle phase durations and PC12 differentiation using fluorescent biosensors," *Cell Cycle*, vol. 8, no. 7, pp. 1044–1052, 2009.

[30] "Bionumbers." http://book.bionumbers.org/how-long-do-the-different-stages-of-the-cell-cycle-take/, 2019. Downloaded on 29.05.2019.

[31] R. Berezney and D. S. Coffey, "Identification of a nuclear protein matrix," *Biochemical and Biophysical Research Communications*, vol. 60, no. 4, pp. 1410–1417, 1974.

[32] T. Pederson, "Half a Century of 'The Nuclear Matrix'," *Molecular Biology of the Cell*, vol. 11, pp. 799–805, 2000.

[33] K. Luby-Phelps, "Cytoarchitecture and Physical Properties of Cytoplasm: Volume, Viscosity, Diffusion, Intracellular Surface Area," *International Review of Cytology*, vol. 192, 2000.

[34] C. P. D. Souza and S. A. Osmani, "Double duty for nuclear proteins - the price of more open forms of mitosis," *Trends in Genetics*, vol. 25, no. 12, pp. 545–554, 2009.

[35] E. J. Lawrence, E. Boucher, and C. A. Mandato, "Mitochondria-cytoskeleton associations in mammalian cytokinesis," *Cell Division*, vol. 11, no. 3, 2016.

[36] N. Schweizer, N. Pawar, M. Weiss, and H. Maiato, "An organelle-exclusion envelope assists mitosis and underlies distinct molecular crowding in the spindle region," *Journal of Cell Biology*, vol. 210, no. 5, pp. 695–704, 2015.

[37] G. Shaw, "Ki67-Tubulin-2.jpg." https://en.wikipedia.org/wiki/File:Ki67-Tubulin-2.jpg, 2017. Downloaded on 22.01.2020. Published unter Creative Commons Attribution-Share Alike 4.0 International Licence (https://creativecommons.org/licenses/by-sa/4.0/deed.en). Figure was cropped.

[38] R. van Heesbeen, "MetaphaseIF.jpg." https://commons.wikimedia.org/wiki/File:MetaphaseIF.jpg, 2008. Downloaded on 22.01.2020. Image is in the Public Domain.

[39] F. R. Blattner, G. P. III, C. A. Bloch, N. T. Perna, V. Burland, M. Riley, J. Collado-Vides, J. D. Glasner, C. K. Rode, G. F. Mayhew, J. Gregor, N. W. Davis, H. A. Kirkpatrick, M. A. Goeden, D. J. Rose, B. Mau, and Y. Shao, "The Complete Genome Sequence of Escherichia coli K-12," *Science*, vol. 277, no. 5331, pp. 1453–1462, 1997.

[40] M.-J. Han and S. Y. Lee, "The Escherichia coli Proteome: Past, Present, and Future Prospects," *Microbiology and Molecular Biology Reviews*, vol. 70, no. 2, pp. 362–439, 2006.

[41] A. P. Minton, "Influence of excluded volume upon macromolecular structure and associations in 'crowded' media," *Current Opinion in Biotechnology*, vol. 8, pp. 65–69, 1997.

[42] A. P. Minton, "Confinement as a determinant of macromolecular structure and reactivity," *Biophysical Journal*, vol. 63, no. 4, p. 1090, 1992.

[43] F. Lanni, A. S. Waggoner, and D. L. Taylor, "Structural Organization of Interphase 3T3 Fibroblasts Studied by Total Internal Reflection Fluorescence Microscopy," *Journal of Cell Biology*, vol. 100, pp. 1091–1102, 1985.

[44] R. J. Ellis, "Macromolecular crowding: an important but neglected aspect of the intracellular environment," *Current Opinion in Structural Biology*, vol. 11, pp. 114–119, 2001.

[45] A. P. Minton and J. Wilf, "Effect of Macromolecular Crowding upon the Structure and Function of an Enzyme: Glyceraldehyde-3-phosphate Dehydrogenase," *Biochemistry*, vol. 20, no. 17, pp. 4821–4826, 1981.

[46] S. B. Zimmerman and A. P. Minton, "Macromolecular Crowding: Biochemical, Biophysical, and Physiological Consequences," *Annual Review of Biophysics and Biomolecular Structure*, vol. 22, pp. 27–65, 1993.

[47] J. D. van der Waals, "The equation of state for gases and liquids." Nobel Lecture, 1910.

[48] M. Weiss, M. Elsner, F. Kartberg, and T. Nilsson, "Anomalous Subdiffusion Is a Measure for Cytoplasmic Crowding in Living Cells," *Biophysical Journal*, vol. 87, no. 5, pp. 3518–3524, 2004.

[49] A. P. Minton, "The Influence of Macromolecular Crowding and Macromolecular Confinement on Biochemical Reactions in Physiological Media," *Journal of Biological Chemistry*, vol. 276, no. 14, pp. 10577–10580, 2001.

[50] H.-X. Zhou, G. Rivas, and A. P. Minton, "Macromolecular Crowding and Confinement: Biochemical, Biophysical, and Potential Physiological Consequences," *Annual Review of Biophysics*, vol. 37, pp. 375–397, 2008.

[51] B. van den Berg, R. Wain, C. M. Dobson, and R. J. Ellis, "Macromolecular crowding perturbs protein refolding kinetics: implications for folding inside the cell," *EMBO Journal*, vol. 19, no. 15, pp. 3870–3875, 2000.

[52] R. Swaminathan, S. Bicknese, N. Periasamy, and A. S. Verkman, "Cytoplasmic Viscosity Near the Cell Plasma Membrane: Translational Diffusion of a Small Fluorescent Solute Measured by Total Internal Reflection-Fluorescence Photobleaching Recovery," *Biophysical Journal*, vol. 71, pp. 1140–1151, 1996.

[53] J. A. Dix and A. S. Verkman, "Crowding Effects on Diffusion in Solutions and Cells," *Annual Review of Biophysics*, vol. 37, pp. 247–263, 2008.

[54] A. P. Minton, "How can biochemical reactions within cells differ from those in test tubes?," *Journal of Cell Science*, vol. 119, no. 14, pp. 2863–2869, 2006.

[55] M. T. Record, E. S. Courtenay, S. Cayley, and H. J. Guttman, "Biophysical compensation mechanisms buffering E. coli protein-nucleic acid interactions agains changing environments," *Trends in Biochemical Sciences*, vol. 23, pp. 190–194, 1998.

[56] S. B. Zimmerman and S. O. Trach, "Estimation of Macromolecule Concentrations and Excluded Volume Effects for the Cytoplasm of Escherichia coli," *Journal of Molecular Biology*, vol. 222, pp. 599–620, 1991.

[57] A. B. Fulton, "How Crowded Is the Cytoplasm?," *Cell*, vol. 30, pp. 345–347, 1982.

[58] G. Guigas and M. Weiss, "Sampling the Cell with Anomalous Diffusion - The Discovery of Slowness," *Biophysical Journal*, vol. 94, pp. 90–94, 2008.

[59] G. Guigas, C. Kalla, and M. Weiss, "The degree of macromolecular crowding in the cytoplasm and nucleoplasm of mammalian cells is conserved," *FEBS Letters*, vol. 581, pp. 5094–5098, 2007.

[60] M. G. S. Norris and N. Malys, "What is the true enzyme kinetics in the biological system? An investigation of macromolecular crowding effect upon enzyme kinetics of glucose-6-phosphate dehydrogenase," *Biochemical and Biophasical Research Communications*, vol. 405, pp. 388–392, 2011.

[61] K. L. Yap, J. Kim, K. Truong, M. Sherman, T. Yuan, and M. Ikura, "Calmodulin Target Database," *Journal of Structural and Functional Genomics*, vol. 1, pp. 8–14, 2000.

[62] M. Ganji, M. Docter, S. F. J. L. Grice, and E. A. Abbondanzieri, "DNA binding proteins explore multiple local configurations during docking via rapid rebinding," *Nucleic Acids Research*, vol. 44, no. 17, pp. 8376–8384, 2016.

[63] N. Tokuriki, M. Kinjo, S. Negi, M. Hoshino, Y. Goto, I. Urabe, and T. Yomo, "Protein folding by the effects of macromolecular crowding," *Protein Science*, vol. 13, pp. 125–133, 2004.

[64] O. Stiehl and M. Weiss, "Heterogeneity of crowded cellular fluids on the meso- and nanoscale," *Soft Matter*, vol. 12, pp. 9413–9416, 2016.

[65] J. V. Small, G. Isenberg, and J. E. Celis, "Polarity of actin at the leading edge of cultured cells," *Nature*, vol. 272, no. 13, pp. 638–639, 1978.

[66] D. W. Provance, A. McDowall, M. Marko, and K. Luby-Phelps, "Cytoarchitecture of size-excluding compartments in living cells," *Journal of Cell Science*, vol. 106, pp. 565–578, 1993.

[67] C. V. Taylor, "The Contractile Vacuole in Euplotes: An example of the sol-gel-reversibility of cytoplasm," *The Journal of experimental Zoology*, vol. 37, no. 3, pp. 259–289, 1923.

[68] J. W. Wojcieszyn, R. A. Schlegel, E.-S. Wu, and K. A. Jaboson, "Diffusion of injected macromolecules within the cytoplasm of living cells," *Proceedings of the National Academy of Sciences USA*, vol. 78, no. 7, pp. 4407–4410, 1981.

[69] T. E. Kreis, B. Geiger, and J. Schlessinger, "Mobility of Microinjected Rhodamine Actin within Living Chicken Gizzard Cells Determined by Fluorescence Photobleaching Recovary," *Cell*, vol. 29, pp. 835–845, 1982.

[70] Y.-L. Wang, F. Lanni, P. L. McNeil, B. R. Ware, and D. L. Taylor, "Mobility of cytoplasmic and membrane-associated actin in living cells," *Proceedings of the National Academy of Sciences USA*, vol. 79, pp. 4660–4664, 1982.

[71] K. Jacobson and J. Wojcieszyn, "The translational mobility of substances within the cytoplasmic matrix," *Proceedings of the National Academy of Sciences USA*, vol. 81, pp. 6747–6751, 1984.

[72] E. D. Salmon, W. M. Saxton, R. J. Leslie, M. L. Karow, and J. R. McIntosh, "Diffusion Coefficient of Fluorescein-labeled Tubulin in the Cytoplasm of Embryonic Cells of a Sea Urchin: Video Image Analysis of Fluorescence Redistribution after Photobleaching," *Journal of Cell Biology*, vol. 99, pp. 2157–2164, 1984.

[73] K. Luby-Phelps, D. L. Taylor, and F. Lanni, "Probing the Structure of Cytoplasm," *Journal of Cell Biology*, vol. 102, pp. 2015–2022, 1986.

[74] P. H. Viollier, M. Thanbichler, P. T. McGrath, L. West, M. Meewan, H. H. McAdams, and L. Shapiro, "Rapid and sequential movement of individual chromosomal loci to specific subcellular locations during bacterial DNA replication," *Proceedings of the National Academy of Sciences USA*, vol. 101, no. 25, pp. 9257–9262, 2004.

[75] T. J. Lampo, S. Stylianidou, M. P. Backlund, P. A. Wiggins, and A. J. Spakowitz, "Cytoplasmic RNA-Protein Particles Exhibit Non-Gaussian Subdiffusive Behavior," *Biophysical Journal*, vol. 112, pp. 532–542, 2017.

[76] E. R. Weeks, J. C. Crocker, A. C. Levitt, A. Schofield, and D. A. Weitz, "Three-Dimensional Direct Imaging of Structural Relaxation Near the Colloidal Glass Transition," *Science*, vol. 287, no. 5453, pp. 627–631, 2000.

[77] W. K. Kegel and A. van Blaaderen, "Direct Observation of Dynamical Heterogeneities in Colloidal Hard-Sphere Suspensions," *Science*, vol. 287, no. 5451, pp. 290–293, 2000.

[78] B. R. Parry, I. V. Surovtsev, M. T. Cabeen, C. S. O'Hern, E. R. Dufresne, and C. Jacobs-Wagner, "The Bacterial Cytoplasm Has Glass-like Properties and Is Fluidized by Metabolic Activity," *Cell*, vol. 156, pp. 183–194, 2014.

[79] B. Fabry, G. N. Maksym, J. P. Butler, M. Glogauer, D. Navajas, and J. J. Fredberg, "Scaling the Microrheology of Living Cells," *Physical Review Letters*, vol. 87, no. 14, pp. 148102–1 – 148102–4, 2001.

[80] P. Witzel, M. Götz, Y. Lanoiselée, T. Franosch, D. S. Grebenkov, and D. Heinrich, "Heterogeneities Shape Passive Intracellular Transport," *Biophysical Journal*, vol. 117, no. 2, pp. 203–213, 2019.

[81] P. Struntz and M. Weiss, "Multiplexed measurement of protein diffusion in Caenorhabditis elegans embryos with SPIM-FCS," *Journal of Physics D: Applied Physics*, vol. 49, no. 044002, 2016.

[82] N. Pawar, C. Donth, and M. Weiss, "Anisotropic Diffusion of Macromolecules in the Contiguous Nucleocytoplasmic Fluids during Eukaryotic Cell Division," *Current Biology*, vol. 24, pp. 1905–1908, 2014.

[83] P. Massignan, C. Manzo, J. Torreno-Pina, M. F. Garcia-Parajo, M. Lewenstein, and G. J. L. Jr., "Nonergodic Subdiffusion from Brownian Motion in an Inhomogeneous Medium," *Physical Review Letters*, vol. 112, p. 150603, 2014.

[84] B. Wang, J. Kuo, S. C. Bae, and S. Granick, "When Brownian diffusion is not Gaussian," *Nature Materials*, vol. 11, pp. 481–485, 2012.

[85] B. Wang, J. Guan, S. M. Anthony, S. C. Bae, K. S. Schweizer, and S. Granick, "Confining Potential when a Biopolymer Filament Reptates," *Physical Review Letters*, vol. 104, no. 11, p. 118301, 2010.

[86] T. Kühn, T. O. Ihalainen, J. Hyväluoma, N. Dross, S. F. Willman, J. Langowski, M. Vihinen-Ranta, and J. Timonen, "Protein Diffuion in Mammalian Cell Cytoplasm," *PLOS One*, vol. 6, no. 8, p. e22962, 2011.

[87] K. Luby-Phelps and D. L. Taylor, "Subcellular Compartmentalization by Local Differentiation of Cytoplasmic Structure," *Cell Motility and the Cytoskeleton*, vol. 10, pp. 28–37, 1988.

[88] L. W. Janson, K. Ragsdale, and K. Luby-Phelps, "Mechanism and Size Cutoff for Steric Exclusion from Actin-Rich Cytoplasmic Domains," *Biophysical Journal*, vol. 71, pp. 1228–1234, 1996.

[89] G. van den Bogaart, N. Hermans, V. Krasnikov, and B. Poolman, "Protein mobility and diffusive barriers in Escherichia coli: consequences of osmotic stress," *Molecular Microbiology*, vol. 64, no. 3, pp. 858–871, 2007.

[90] H. Freund and A. Berg, eds., *Geschichte der Mikroskopie. Leben und Werk grosser Forscher*, vol. I. Biologie. Frankfurt am Main: Umschau Verlag, 1963.

[91] A. Köhler, "Mikrophotographische Untersuchungen mit ultraviolettem Licht," *Zeitschrift für wissenschaftliche Mikroskopie und für mikroskopische Technik*, vol. 21, no. 2,3, pp. 129–165, 273–304, 1904.

[92] H. Freund and A. Berg, eds., *Geschichte der Mikroskopie. Leben und Werk grosser Forscher*, vol. III. Angewandte Naturwissenschaften und Technik. Frankfurt am Main: Umschau Verlag, 1966.

[93] Leica Microsystems, "Milestones in Incident Light Fluorescence Microscopy." https://www.leica-microsystems.com/science-lab/milestones-in-incident-light-fluorescence-microscopy/, 2017. Downloaded on 05.09.2019.

[94] J. R. Lakowicz, *Principles of Fluorescence Spectroscopy*. New York: Springer Science, 3rd ed., 2006.

[95] M. Planck, "Über das Gesetz der Energieverteilung im Normalspectrum," *Annalen der Physik*, vol. 309, pp. 553–563, 1901.

[96] M. Kasha, "Characterization of Electronic Transitions in Complex Molecules," *Discussions of the Faraday Society*, pp. 14–19, 1950.

[97] M. Y. Berezin and S. Achilefu, "Fluorescence Lifetime Measurements and Biological Imaging," *Chemical Reviews*, vol. 110, pp. 2641–2684, 2010.

[98] G. G. Stokes, "On the Change of Refrangibility of Light," *Philosophical Transactions of the Royal Society*, vol. 142, pp. 463–562, 1852.

[99] H. C. Ishikawa-Ankerhold, R. Ankerhold, and G. P. C. Drummen, "Advanced Fluorescence Microscopy Techniques - FRAP, FLIP, FLAP, FRET and FLIM," *Molecules*, vol. 17, pp. 4047–4132, 2012.

[100] J. C. Stockert and A. Blasquez-Castro, *Fluorescence Microscopy in Life Sciences*, ch. Dyes and Fluorochromes, pp. 61–95. Bentham Science Publishers, 2017.

[101] T. Förster, "Energiewanderung und Fluoreszenz," *Naturwissenschaften*, vol. 33, no. 6, pp. 166–175, 1946.

[102] T. Förster, "Zwischenmolekulare Energiewanderung und Fluoreszenz," *Annalen der Physik*, vol. 6, no. 2, pp. 55–75, 1948.

[103] A. D. Hoppe, *Imaging Cellular and Molecular Biological Functions*, ch. Quantitative FRET Microscopy of Live Cells, pp. 157–181. Berlin: Springer, 2007.

[104] A. J. Boersma, I. S. Zuhorn, and B. Poolman, "A sensor for quantification of macromolecular crowding in living cells," *Nature Methods*, vol. 12, no. 3, pp. 227–229, 2015.

[105] S. Sukenik, P. Ren, and M. Gruebele, "Weak protein-protein interactions in live cells are quantified by cell-volume modulation," *Proceedings of the National Academy of Sciences USA*, vol. 114, no. 26, pp. 6776–6731, 2017.

[106] E. Abbe, "Beiträge zur Theorie des Mikroskops und der mikroskopischen Wahrnehmung," *Archiv für Mikroskopische Anatomie*, vol. 9, pp. 413–418, 1873.

[107] U. Kubitschek, ed., *Fluorescence Microscopy. From Principles to Biological Applications*. Weinheim: Wiley-Blackwell, 2013.

[108] D. Axelrod, D. E. Koppel, J. Schlessinger, E. Elson, and W. W. Webb, "Mobility Measurement By Analysis of Fluorescence Photobleaching Recovery Kinetics," *Biophysical Journal*, vol. 16, no. 9, pp. 1055–1069, 1976.

[109] D. E. Koppel, D. Axelrod, J. Schlessinger, E. L. Elson, and W. W. Webb, "Dynamics of fluorescence marker concentration as a probe of mobility," *Biophysical Journal*, vol. 16, pp. 1315–1329, 1976.

[110] D. Axelrod, "Lateral motion of membrane proteins and biological function," *Journal of Membrane Biology*, vol. 75, pp. 1–10, 1983.

[111] M. Elsner, H. Hashimoto, J. C. Simpson, D. Cassel, T. Nilsson, and M. Weiss, "Spatiotemporal dynamics of the COPI vesicle machinery," *EMBO reports*, vol. 4, no. 10, pp. 1000–1005, 2003.

[112] M. E. van Royen, A. Zotter, S. M. Ibrahim, B. Geverts, and A. B. Houtsmuller, "Nuclear proteins: finding and binding target sites in chromatin," *Chromosome Research*, vol. 19, pp. 83–98, 2011.

[113] M. Kapustina, E. Vitriol, T. C. Elston, L. M. Loew, and K. Jacobson, "Modeling Capping Protein FRAP and CALI Experiments Reveals In Vivo Regulation of Actin Dynamics," *Cytoskeleton*, vol. 67, pp. 519–534, 2010.

[114] A. Tagawa, A. Mezzacasa, A. Hayer, A. Longatti, L. Pelkmans, and A. Helenius, "ASsembly and trafficking of caveolar domains in the cell," *Journal of Cell Biology*, vol. 170, no. 5, pp. 769–779, 2005.

[115] J. Ellenberg, E. D. Siggia, J. E. Moreira, C. L. Smith, J. F. Presley, H. J. Worman, and J. Lippincott-Schwartz, "Nuclear membrane dynamics and reassembly in living cells: targeting of an inner nuclear membrane protein in interphase and mitosis," *Journal of Cell Biology*, vol. 138, no. 6, pp. 1193–1206, 1997.

[116] N. B. Cole, C. L. Smith, N. Sciaky, M. Terasaki, M. Edidin, and J. Lippincott-Schwartz, "Diffusional mobility of Golgi proteins in membranes of living cells," *Science*, vol. 273, no. 5276, pp. 797–801, 1996.

[117] E. L. Elson and D. Magde, "Fluorescence Correlation Spectroscopy. I. Conceptual Basis and Theory," *Biopolymers*, vol. 13, pp. 1–27, 1974.

[118] D. Magde, E. L. Elson, and W. W. Webb, "Fluorescence Correlation Spectroscopy. II. An Experimental Realization," *Biopolymers*, vol. 13, pp. 29–61, 1974.

[119] G. Bonnet, O. Krichevsky, and A. Lichaber, "Kinetics of conformational fluctuations in DNA hairpin-loops," *Proceedings of the National Academy of Sciences USA*, vol. 95, pp. 8602–8606, 1998.

[120] M. I. Wallace, L. Ying, S. Balasubramanian, and D. Klenerman, "Non-Arrhenius kinetics for the loop closure of a DNA hairpin," *Proceedings of the National Academy of Sciences*, vol. 98, no. 10, pp. 5584–5589, 2001.

[121] M. I. Wallace, L. Ying, S. Balasubramanian, and D. Klenerman, "FRET Fluctuation Spectroscopy: Exploring the Conformational Dynamics of a DNA Hairpin Loop," *Journal of Physical Chemistry B*, vol. 104, no. 48, p. 11551, 2000.

[122] J. R. Lakowicz, H. Szmacinski, K. Nowaczyk, K. W. Berndt, and M. Johnson, "Fluorescence Lifetime Imaging," *Analytical Biochemistry*, vol. 202, pp. 316–330, 1992.

[123] E. B. V. Munster and T. W. G. Jr., "phiFLIM: A new method to avoid aliasing in frequency-domain fluorescence lifetime imaging microscopy," *Journal of Microscopy*, vol. 213, no. 1, pp. 29–38, 2004.

[124] B. D. Venetta, "Microscope phase fluorometer for determining the fluorescence lifetimes of fluorochromes," *Review of Scientific Instruments*, vol. 30, no. 6, pp. 450–457, 1959.

[125] T. Oida, Y. Sako, and A. Kusumi, "Fluorescence lifetime imaging microscopy (flimscopy). Methodology development and application to studies of endosome fusion in single cells," *Biophysical Journal*, vol. 64, pp. 676–685, 1993.

[126] A. D. Veres, *Analyse intrazellulärer Fluide mittels orts- und zeitaufgelöster Fluoreszenzspektroskopie*. PhD thesis, Universität Bayreuth, 2018.

[127] O. Stiehl, *On the crowding state of cellular and biomimetic fluids*. PhD thesis, Universität Bayreuth, 2016.

[128] D. R. J. Verboogen, N. G. Mancha, M. ter Beest, and G. van den Bogaart, "Fluorescence Lifetime Imaging Microscopy reveals rerouting of SNARE trafficking driving dendritic cell activation," *eLIFE*, vol. 6, p. e23525, 2017.

[129] T. J. Barnard, X. Yu, N. Noinaj, and J. Taraska, "Crystal Structure of Green Fluorescent Protein." http://www.rcsb.org/structure/4KW4, 2014. Image from the RCSB PDB (rcsb.org) of PDB ID 4KW4. Downloaded on 16.01.2020.

[130] ThermoFisher Scientific, "Fluorescence Spectra Viewer." https://www.thermofisher.com/de/de/home/life-science/cell-analysis/labeling-chemistry/fluorescence-spectra viewer.html.

[131] X. Shu, N. C. Shaner, C. A. Yarbrough, R. Y. Tsien, and S. J. Remington, "Novel Chromophores and Buried Charges Control Color in mFruits." http://www.rcsb.org/structure/2H5Q, 2006. Image from the RCSB PDB (rcsb.org) of PDB ID 2H5Q. Downloaded on 16.01.2020.

[132] A. M. Valencia, C. K. Collings, H. T. Dao, R. S. Pierre, Y. C. Cheng, J. Huang, Z. Y. Sun, H. S. Seo, N. Mashtalir, D. E. Comstock, O. Bolonduro, N. E. Vangos, Z. C. Yeoh, M. K. Dornon, C. Hermawan, L. Barrett, S. Dhe-Paganon, C. J. Woolf, T. W. Muir, and C. Kadoch, "Recurrent SMARCB1 Mutations Reveal a Nucleosome Acidic Patch Interaction Site That Potentiates mSWI/SNF Complex Chromatin Remodeling." http://www.rcsb.org/structure/6UCH, 2019. Image from the RCSB PDB (rcsb.org) of PDB ID 6UCH. Downloaded on 16.01.2020.

[133] M. Tantama, J. R. Martínez-François, R. Mongeon, and G. Yellen, "Imaging energy status in live cells with a fluorescent biosensor of the intracellular ATP-to-ADP ratio," *Nature Communications*, vol. 4, p. 2550, 2013.

[134] O. Yildiz, C. Kalthoff, S. Raunser, and W. Kuehlbrandt, "Structure of GlnK1 with bound effectors indicates regulatory mechanism for ammonia uptake." https://www.rcsb.org/structure/2j9c, 2007. Image from the RCSB PDB (rcsb.org) of PDB ID 2J9C. Downloaded on 16.01.2020.

[135] R. Y. Tsien, "The Green Fluorescent Protein," *Annual Review of Biochemistry*, vol. 67, pp. 509–544, 1998.

[136] R. Swaminathan, C. P. Hoang, and A. S. Verkman, "Photobleaching Recovery and Anisotropy Decay of Green Fluorescent Protein GFP-S65T in Solution and Cells: Cytoplasmic Viscosity Probed by Green Fluorescent Protein Translational and Rotational Diffusion," *Biophysical Journal*, vol. 72, pp. 1900–1907, 1997.

[137] A. S. Verkman, "Solute and macromolecule diffusion in cellular aqueous compartments," *Trends in Biochemical Sciences*, vol. 27, no. 1, pp. 27–33, 2002.

[138] O. Liarzi and B. L. Epel, "Development of a quantitative tool for measuring changes in the coefficient of conductivity of plasmodesmata induced by developmental, biotic, and abiotic signals," *Protoplasma*, vol. 225, pp. 67–76, 2006.

[139] M. Shamir, Y. Bar-On, R. Phillips, and R. Milo, "SnapShot: Timescales in Cell Biology," *Cell*, vol. 164, pp. 1302–1303, 2016.

[140] X. Wei, V. G. Henke, C. Strübing, E. B. Brown, and D. E. Clapham, "Real-Time Imaging of Nuclear Permeation by EGFP in Single Intact Cells," *Biophysical Journal*, vol. 84, no. 2, pp. 1317–1327, 2003.

[141] G. H. Patterson, S. M. Knobel, W. D. Sharif, S. R. Kain, and D. W. Piston, "Use of the Green Fluorescent Protein and Its Mutants in Quantitative Fluorescence Microscopy," *Biophysical Journal*, vol. 73, pp. 2782–2790, 1997.

[142] O. Seksek, J. Biwersi, and A. S. Verkman, "Translational Diffusion of Macromolecule-sized Solutes in Cytoplasm and Nucleus," *Journal of Cell Biology*, vol. 138, no. 1, pp. 131–142, 1997.

[143] M. Wachsmuth, W. Waldeck, and J. Langowski, "Anomalous Diffusion of Fluorescent Probes Inside Living Cell Nuclei Investigated by Spatially-resolved Fluorescence Correlation Spectroscopy," *Journal of Moleculare Biology*, vol. 298, pp. 677–689, 2000.

[144] H. Yokoe and T. Meyer, "Spatial dynamics of GFP-tagged proteins investigated by local fluorescence enhancement," *Nature Biotechnology*, vol. 14, pp. 1252–1256, 1996.

[145] P. L. Paine, L. C. Moore, and S. B. Horowitz, "Nuclear envelope permeability," *Nature*, vol. 254, pp. 109–114, 1975.

[146] D. Mohr, S. Frey, T. Fischer, T. Güttler, and D. Görlich, "Characterisation of the passive permeability barrier of nuclear pore complexes," *EMBO Journal*, vol. 28, no. 17, pp. 2541–2553, 2009.

[147] K. Ribbeck and D. Görlich, "Kinetic Analysis of translocation through nuclear pore complexes," *EMBO Journal*, vol. 20, no. 6, pp. 1320–1330, 2001.

[148] B. L. Timney, B. Raveh, R. Mironska, J. M. Trivedi, S. J. Kim, D. Russel, S. R. Wente, A. Sali, and M. P. Rout, "Simple rules for passive diffusion through the nuclear pore complex," *Journal of Cell Biology*, vol. 215, no. 1, pp. 57–76, 2016.

[149] K. Svoboda, D. W. Tank, and W. Denk, "Direct MEasurement of Coupling Between Dendritic Spines and Shafts," *Science*, vol. 272, no. 5262, pp. 716–719, 1996.

[150] A. Majewska, E. Brown, J. Ross, and R. Yuste, "Mechanisms of Calcium Decay Kinetics in Hippocampal Spines: Role of Spine Calcium Pumps and Calcum Diffusion through the Spine Neck in Biochemical Compartmentalization," *Journal of Neuroscience*, vol. 20, no. 5, pp. 1722–1734, 2000.

[151] T. Nguyen, N. Pappireddi, and M. Wühr, "Proteomics of nucleocytoplasmic partitioning," *Current Opinion in Chemical Biology*, vol. 48, pp. 55–63, 2019.

[152] D. Mazia, *Formation and Fate of Cell Organelles*, vol. 6, ch. Fibrillar Structure in the Mitotic Apparatus, pp. 39–54. New York, London: Academic Press, 1967.

[153] J. Pickett-Heaps, T. Spurck, and D. Tippit, "Chromosome Motion and the Spindle Matrix," *Journal of Cell Biology*, vol. 99, no. 1, pp. 137s–143s, 1984.

[154] N. Paweletz, "Membranes in the mitotic apparatus," *Cell Biology International Reports*, vol. 5, no. 4, pp. 323–336, 1981.

[155] Z. Liu and Y. Zheng, "A requirement for epsin in mitotic membrane and spindle organization," *Journal of Cell Biology*, vol. 186, no. 4, pp. 473–480, 2009.

[156] N. Schweizer, M. Weiss, and H. Maiato, "The dynamic spindle matrix," *Current Opinion in Cell Biology*, vol. 28, pp. 1–7, 2014.

[157] H. Hayashi, K. Kimura, and A. Kimura, "Localized accumulation of tubulin during semi-open mitosis in the Caenorhabditis elegans embryo," *Molecular Biology of the Cell*, vol. 23, pp. 1688–1699, 2012.

[158] J. K. Armstrong, R. B. Wenby, H. J. Meiselman, and T. C. Fisher, "The Hydrodynamic Radii of Macromolecules and Their Effect on Red Blood Cell Aggregation," *Biophysical Journal*, vol. 87, pp. 4259–4270, 2004.

[159] M. Wühr, T. Güttler, L. Peshkin, G. C. McAllister, M. Sonnett, L. Ishihara, A. C. Groen, M. Presler, B. K. Erickson, T. J. Mitchison, M. W. Kirschner, and S. P. Gygi, "The Nuclear Proteome of a Vertebrate," *Current Biology*, vol. 25, pp. 2663–2671, 2015.

[160] R. J. Vasquez, B. Howell, A.-M. C. Yvon, P. Wadsworth, and L. Cassimeris, "Nanomolar Concentrations of Nocodazole Alter Microtubule Dynamic Instability In Vivo and In Vitro," *Molecular Biology of the Cell*, vol. 8, pp. 973–985, 1997.

[161] A. Woehler, J. Wlodarczyk, and E. Neher, "Signal/Noise Analysis of FRET-Based Sensors," *Biophysical Journal*, vol. 99, p. 2344, 2010.

[162] R. Neher and E. Neher, "imizing imaging parameters for the separation of multiple labels in a fluorescence image," *Journal of Microscopy*, vol. 213, no. 1, pp. 46–62, 2004.

[163] M. B. Burg, "Response of renal inner medullary epithelial cells to osmotic stress," *Comparative Biochemistry and Physiology Part A*, vol. 133, pp. 661–666, 2002.

[164] C. Brocker, D. C. Thompson, and V. Vasiliou, "The role of hyperosmotic stress in inflammation and disease," *Biomolecular Concepts*, vol. 3, no. 4, pp. 345–364, 2012.

[165] E. K. Hoffmann, I. H. Lambert, and S. F. Pedersen, "Physiology of Cell Volume Regulation in Vertebrates," *Physiological Reviews*, vol. 89, pp. 193–277, 2009.

[166] E. Zlotek-Zlotkiewicz, S. Monnier, G. Cappello, M. L. Berre, and M. Piel, "Optical volume and mass measurements show that mammalian cells swell during mitosis," *Journal of Cell Biology*, vol. 211, no. 4, pp. 765–774, 2015.

[167] V. C. Hecht, L. B. Sullivan, R. J. Kimmerling, D.-H. Kim, A. M. Hosios, M. A. Stockslager, M. M. Stevens, J. H. Kang, D. Wirtz, M. G. V. Heiden, and S. R. Manalis, "Biophysical changes reduce energetic demand in growthfactor-deprived lymphocytes," *Journal of Cell Biology*, vol. 212, no. 4, pp. 439–447, 2016.

[168] J. Heo, F. Meng, and S. Z. Hua, "Contribution of aquaporins to cellular water transportobserved by a microfluidic cell volume sensor," *Analytical Chemistry*, vol. 80, no. 18, pp. 6974–6980, 2008.

[169] S. Son, J. H. Kang, S. Oh, M. W. Kirschner, T. J. Mitchison, and S. Manalis, "Resonant microchannel volume and mass measurements show thatsuspended cells swell during mitosis," *Journal of Cell Biology*, vol. 211, no. 4, pp. 757–763, 2015.

[170] Y. Ben-Ari, Y. Brody, N. Kinor, A. Mor, T. Tsukamoto, D. L. Spector, R. H. Singer, and Y. Shav-Tal, "The life of an mRNA in space and time," *Journal of Cell Science*, vol. 123, pp. 1761–1774, 2010.

[171] J. D. Finan, K. J. Chalut, A. Wax, and F. Guilak, "Nonlinear Osmotic Properties of the Cell Nucleus," *Annals of Biomedical Engineering*, vol. 37, no. 3, pp. 477–491, 2009.

[172] E. S. Oswald, P. hsiu G. Chao, J. C. Bulinski, G. A. Ateshian, and C. T. Hung, "Chondrocyte Nuclear Response to Osmotic Loading," *Proceedings of the 28th IEEE EMBS Annual International Conference*, vol. 1, pp. 3659–3661, 2006.

[173] H. J. Worman, J. Yuan, G. Blobel, and S. D. Georgatos, "A lamin B receptor in the nuclear envelope," *Proceedings of the National Academy of Sciences USA*, vol. 85, pp. 8531–8534, 1988.

[174] T. Cremer, A. Kurz, R. Zirbel, S. Dietzel, B. Rinke, E. Schröck, M. Speicher, U. Mathieu, A. Jauch, P. Emmerich, H. Scherthan, T. Ried, C. Cremer, and P. Lichter, "Role of chromosome territories in the functional compartmentalization of the cell nucleus," *Cold Spring Harbor Sympysia on Quantitative Biology*, vol. 58, pp. 777–792, 1993.

[175] H. Albiez, M. Cremer, C. Tiberi, L. Vecchio, L. Schermelleh, S. Dittrich, K. Küpper, B. Joffe, T. Thormeyer, J. von Hase, S. Yang, K. Rohr, H. Leonhardt, I. Solovei, C. Cremer, S. Fakan, and T. Cremer, "Chromatin domains and the interchromatin compartment form structureally defined and functionally interacting nuclear networks," *Chromosome Research*, vol. 14, pp. 707–733, 2006.

[176] L. Schermlleh, P. M. Carlton, S. Haase, L. Shao, L. Winoto, P. Kner, B. Burke, M. C. Cardoso, D. A. Agard, M. G. L. Gustafsson, H. Leonhardt, and J. W. Sedat, "Subdiffraction Multicolor Imaging of the Nuclear Periphery with 3D Structured Illumination Microscopy," *Science*, vol. 320, no. 5881, pp. 1332–1336, 2008.

[177] T. Cremer and C. Cremer, "Chromosome Territories, Nuclear Architecture and Gene Regulation in Mammalian Cells," *Nature Reviews Genetics*, vol. 2, pp. 292–301, 2001.

[178] R. Hancock, "A role for macromolecular crowding effects in the assembly and function of compartments in the nucleus," *Journal of Structural Biology*, vol. 146, no. 3, pp. 281–290, 2004.

[179] R. Hancock, "Internal organisation of the nucleus: assembly of compartments by macromolecular crowding and the nuclear matrix model," *Biology of the Cell*, vol. 96, pp. 595–601, 2004.

[180] J. D. Finan and F. Guilak, "The effects of osmotic stress on the structure and function of the cell nucleus," *Journal of Cell Biochemistry*, vol. 109, no. 3, pp. 460–467, 2010.

[181] H. J. Helbock, K. B. Beckman, M. K. Shigenaga, P. B. Walter, A. A. Woodall, H. C. Yeo, and B. N. Ames, "DNA oxidation matters: the HPLC-electrochemical detection assay of 8-oxo-deoxyguanosine and 8-oxo-guanine," *Proceedings of the National Academy of Sciences U.S.A.*, vol. 95, no. 1, pp. 288–293, 1998.

[182] F. Q. Schafer and G. R. Buettner, "Redox environment of the cell as viewed through the redox state of the glutathione disulfide/glutathione couple," *Free Radical Biology & Medicine*, vol. 30, no. 11, pp. 1191–1212, 2001.

[183] O. Hwang, "Role of Oxidative Stress in Parkinson's Disease," *Experimental Neurobiology*, vol. 22, no. 1, pp. 11–17, 2013.

[184] M. Valko, D. Leibfritz, J. Moncol, M. T. Cronin, M. Mazur, and J. Telser, "Free radicals and antioxidants in normal physiological functions and human disease," *International Journal of Biochemistry & Cell Biology*, vol. 39, no. 1, pp. 44–84, 2007.

[185] F. Bonomini, S. Tengattini, A. Fabiano, R. Bianchi, and R. Rezzani, "Atherosclerosis and oxidative stress," *Histology and Histopathology*, vol. 23, no. 3, pp. 381–390, 2008.

[186] N. Singh, A. K. Dhalla, C. Seneviratne, and P. K. Singal, "Oxidative stress and heart failure," *Molecular and Cellular Biochemistry*, vol. 147, no. 1-2, pp. 77–81, 1995.

[187] C. Wright, S. Milne, and H. Leeson, "Sperm DNA damage caused by oxidative stress: modifiable clinical, lifestyle and nutritional factors in male infertility," *Reproductive BioMedicine Online*, vol. 28, no. 6, pp. 684–703, 2014.

[188] J. Guz, D. Gackowski, M. Foksinski, R. R. ans Ewelina Zarakowska, A. Siomek, A. Szpila, M. Kotzbach, R. Kotzbach, and R. Olinski, "Comparison of oxidative stress/DNA damage in semen and blood of fertile and infertile men," *PLOS One*, vol. 8, no. 7, 2013.

[189] B. Halliwell, "Oxidative stress and cancer: have we moved forward?," *Biochemical Journal*, vol. 401, pp. 1–11, 2007.

[190] O. Handa, Y. Naito, and T. Yoshikawa, "Redox biology and gastric carcinogenesis: the role of Helicobacter pylori," *Redox Report*, vol. 16, no. 1, pp. 1–7, 2011.

[191] M. D. Evans and M. S. Cooke, "Factors contributing to the outcome of oxidative damage to nucleic acids," *BioEssays*, vol. 26, no. 5, pp. 533–542, 2004.

[192] S. V. Lennon, S. J. Martin, and T. G. Cotter, "Dose-dependent induction of aposis in human tumour cell lines by widely diverging stimuli," *Cell Proliferation*, vol. 22, no. 2, pp. 203–214, 1991.

[193] J. L. Lelli, L. L. Becks, M. I. Dabrowska, and D. B. Hinshaw, "ATP converts necrosis to aposis in oxidant-injured endothelial cells," *Free Radical Biology & Medicine*, vol. 25, no. 6, pp. 694–702, 1998.

[194] Y. Lee and E. Shacter, "Oxidative stress inhibits aposis in human lymphoma cells," *The Journal of Biological Chemistry*, vol. 274, no. 28, pp. 19792–19798, 1999.

[195] J. K. Sinha, S. Ghosh, U. Swain, N. V. Giridharan, and M. Raghunath, "Increased macromolecular damage due to oxidative stress in the neocortex and hippocampus of WNIN/Ob, a novel rat model of premature aging," *Neuroscience*, vol. 269, pp. 256–264, 2014.

[196] S. Pinto, V. N. Sato, E. A. De-Souza, R. C. Ferraz, H. Camara, A. P. F. Pinca, D. R. Mazzotti, M. T. Lovci, G. Tonon, C. M. Lopes-Ramos, R. B. Parmigiani, M. Wurtele, K. B. Massirer, and M. A. Mori, "Enoxacin extends lifespan of C. elegans by inhibiting miR-34-5p and promoting mitohormesis," *Redox Biology*, vol. 18, pp. 84–92, 2018.

[197] D. Gems and L. Partridge, "Stress-response hormesis and aging: "that which does not kill us makes us stronger"," *Cell Metabolism*, vol. 7, no. 3, pp. 200–2003, 2008.

[198] A. W. Segal, "How neutrophils kill microbes," *Annual Review of Immunology*, vol. 23, pp. 197–223, 2005.

[199] C. Nathan and M. U. Shiloh, "Reactive oxygen and nitrogen intermediates in the relationship between mammalian hosts and microbial pathogens," *Proceedings of the National Academy of Sciences U.S.A.*, vol. 97, no. 16, pp. 8841–8848, 2000.

[200] J. Gross and D. Bhattacharya, "Uniting sex and eukaryote origins in an emerging oxygenic world," *Biology Direct*, vol. 5, no. 53, 2010.

[201] H. Bernstein and C. Bernstein, *Biocommunication of Archaea*, ch. Sexual communication in archaea, the precursor to meiosis, pp. 103–117. Cham: Springer International Publishing, 2017.

[202] E. Hörandl and D. Speijer, "How oxygen gave rise to eukaryotic sex," *Proceedings of the Royal Society B*, vol. 285, no. 20172706, 2018.

[203] J. R. Knowles, "Enzyme-catalyzed phosphoryl transfer reactions," *Annual Review of Biochemistry*, vol. 49, pp. 877–919, 1980.

[204] R. H. G. Wright, A. Lioutas, F. L. Dily, D. Soronellas, A. Pohl, J. Bonet, A. S. Nacht, S. Samino, J. Font-Mateu, G. P. Vicent, M. Wierer, M. A. Trabado, C. Schelhorn, C. Carolis, M. J. Macias, O. Yanes, B. Oliva, and M. Beato, "ADP-ribose-derived nuclear ATP synthesis by NUDIX5 is required for chromatin remodeling," *Science*, vol. 352, no. 6290, pp. 1221–1225, 2016.

[205] S. Törnroth-Horsefield and R. Neutze, "Opening and closing the metabolite gate," *Proceedings of the National Academy of Sciences U.S.A.*, vol. 105, no. 50, p. 19565–19566, 2008.

[206] R. L. Veech, J. W. R. Lawson, N. W. Cornell, and H. A. Krebs, "Cytosolic Phosphorylation Potential," *The Journal of Biologicyl Chemistry*, vol. 254, no. 14, pp. 6538–6547, 1979.

[207] T. W. Traut, "Physiological concentrations of purines and pyrimidines," *Molecular and Cellular Biochemistry*, vol. 140, pp. 1–22, 1994.

[208] M. D. Meglasson, J. Nelson, D. Nelson, and M. Erecinska, "Bioenergetic Response of Pancreatic Islets to Stimulation by Fuel Molecules," *Metabolism*, vol. 38, no. 12, pp. 1188–1195, 38.

[209] S. Mörikofer-Zwez and P. Walter, "Binding of ATP to rat liver cytosolic proteins and its influence on the raio of free ATP/free ADP," *Biochemical Journal*, vol. 259, pp. 117–124, 1989.

[210] B. Gerdle, M. F. Forsgren, A. Bengtsson, O. D. Leinhard, B. Sören, A. Karlsson, V. Brandejsky, E. Lund, and P. Lundberg, "Decreased muscle concentrations of ATP and PCR in the quadriceps muscle of fibromyalgia patient - A 31P-MRS study," *European Journal of Pain*, vol. 17, pp. 1205–1215, 2013.

[211] G. Morris and M. Maes, "Mitochondrial dysfunctions in Myalgic Encephalomyelitis / chronic fatigue syndrome explained by activated immuno-inflammatory, oxidative and nitrosative stress pathways," *Metabolic Brain Disease*, vol. 29, pp. 19–36, 2014.

[212] N. Lengert and B. Drossel, "In silico analysis of exercise intolerance in myalgic encephalomyelitis/chronic fatigue syndrome," *Biophysical Chemistry*, vol. 202, pp. 21–31, 2015.

[213] S. Myhill, N. E. Booth, and J. McLaren-Howard, "Chronic fatigue syndrome and mitochondrial dysfunction," *International Journal of Clinical and Experimental Medicine*, vol. 2, pp. 1–16, 2009.

[214] F. Schütt, S. Aretz, G. U. Auffarth, and J. Kopitz, "Moderately Reduced ATP Levels Promote Oxidative Stress and Debilitate Autophagic and Phagocytic Capacitites in Human RPE Cells," *Investigative Ophthalmology & Visual Science*, vol. 53, no. 9, pp. 5354–5361, 2012.

[215] H. Imamura, K. P. H. Nhat, H. Togawa, K. Saito, R. Iino, Y. Kato-Yamada, T. Nagai, and H. Noji, "Visualization of ATP levels inside single living cells with fluorescence resonance energy transfer-based genetically encoded indicators," *Proceedings of the National Academy of Sciences*, vol. 106, no. 37, pp. 15651–15656, 2009.

[216] W. J. Hayes and E. R. Laws, eds., *Handbook of Pesticide Toxicology*, vol. 2. San Diego, New York, Boston, London, Sydney, Tokyo, Toronto: Academic Press, Inc., 1st ed., 1991.

[217] S. L. M. nad P. Andy Li, "Neuroprotective role of mitochondrial uncoupling protein 2 in cerebral stroke," *Journal of Cerebral Blood Flow and Metabolism*, vol. 29, pp. 1069–1078, 2009.

[218] S. Heinz, A. Freyberger, B. Lawrenz, L. Schladt, G. Schmuck, and H. Ellinger-Ziegelbauer, "Mechanistic Investigations of the Mitochondrial Complex I Inhibitor Rotenone in the Context of Pharmacological and Safety Evaluation," *Scientific Reports*, vol. 7, no. 45465, 2017.

[219] Y. Kagawa and E. Racker, "Partial resolution of the enzymes catalyzing oxidative phosphorylation. VIII. Properties of a factor conferring oligomycin sensitivity on mitochondrial adenosine triphosphatase," *The Journal of Biological Chemistry*, vol. 241, no. 10, pp. 2461–2466, 1966.

[220] H.-W. Heldt and B. Piechulla, *Pflanzenbiochemie*. Berlin Heidelberg: Springer, 5th ed., 2015. p. 118.

[221] M. Jastroch, A. S. Divakaruni, S. Mookerjee, J. R. Treberg, and M. D. Brand, "Mitochondrial proton and electron leaks," *Essays in Biochemistry*, vol. 47, no. 1, pp. 53–67, 2010.

[222] S. R. Benedict, "A reagent for the detection of reducing sugars," *Journal of Biologicyl Chemistry*, vol. 5, pp. 485–487, 1909.

[223] Sigma-Aldrich, "Benedict's reagent." https://www.sigmaaldrich.com/catalog/product/sial/11945?lang=de&region=DE, 2019. Downloaded on 31.10.2019.

[224] J. R. Garrett, X. Wu, S. Jin, and K. Ye, "pH-Insensitive Glucose Indicators," *Biotechnology Progress*, vol. 24, no. 5, pp. 1085–1089, 2008.

[225] M. C. Bennett, G. W. Mlady, Y.-H. Kwon, and G. M. Rose, "Chronic In Vivo Sodium Azide Infusion Induces Selective and Stable Inhibition of Cytochrome c Oxidase," *Journal of Neurochemistry*, vol. 66, pp. 2606–2611, 1996.

[226] Sigma-Aldrich, "2-Deoxy-D-glucose." https://www.sigmaaldrich.com/catalog/product/sigma/d8375?lang=de&region=DE, 2019. Downloaded on 26.09.2019.

[227] H. Xi, M. Kurtoglu, and T. J. Lampidis, "The Wonders of 2-Deoxy-D-Glucose," *IUBMB Life*, vol. 66, no. 2, pp. 110–121, 2014.

[228] A. N. Wick, D. R. Drury, H. I. Nakada, and J. B. Wolfe, "Localization of the primary metabolic block produced by 2-deoxyglucose," *Journal of Biological Chemistry*, vol. 224, no. 2, pp. 963–969, 1957.

[229] S. Nagata, "Apoptotic DNA Fragmentation," *Experimental Cell Research*, vol. 256, pp. 12–18, 2000.

[230] M. G. Bottone, G. Santin, F. Aredia, G. Bernocchi, C. Pellicciari, and A. I. Scovassi, "Morphological Features of Organelles during Apoptosis: An Overview," *Cells*, vol. 2, pp. 294–305, 2013.

[231] G. Guigas, C. Kalla, and M. Weiss, "Probing the Nanoscale Viscoelasticity of Intracellular Fluids in Living Cells," *Biophysical Journal*, vol. 93, no. 1, pp. 316–323, 2007.

[232] M. Shackleton, "Normal stem cells and cancer stem cells: similar and different," *Seminars in Cancer Biology*, vol. 20, pp. 85–92, 201.

[233] L. Zhang, W. Zhou, V. E. Velculescu, S. E. Kern, R. H. Hruban, S. R. Hamilton, B. Vogelstein, and K. W. Kinzler, "Gene Expression Profiles in Normal and Cancer Cells," *Science*, vol. 276, no. 5316, pp. 1268–1272, 1997.

[234] L. A. J. Alvarez, B. Widzgowski, G. Ossato, B. van den Broek, K. Jalink, L. Kuschel, M. J. Roberti, and F. Hecht, "SP8 FALCON: a novel concept in fluorescence lifetime imaging enabling video-rate confocal FLIM," *Nature Methods (Advertising Feature/Application Note)*, 2019.

[235] V. Buschmann, B. Krämer, F. Koberling, R. Macdonald, and S. Rüttinger, "Quantitative FCS: Determination of the Confocal Volume by FCS and Bead Scanning with the MicroTime 200," application note, PicoQuant GmbH, 2009.

[236] B. Amos, G. McConnell, and T. Wilson, *Handbook of Comprehensive Biophysics*, ch. Confocal microscopy. Elsevier, 2011.

[237] P. Kourilsky, "Lysogenization by Bacteriophage Lambda. I. Multiple Infection and the Lysogenic Response," *Molecular and General Genetics*, vol. 122, pp. 183–195, 1973.

[238] A. Arkin, J. Ross, and H. H. McAdams, "Stochastic Kinetic Analysis of Developmental Pathway Bifurcation in Phage λ-Infected Escherichia coli Cells," *Genetics*, vol. 149, pp. 1633–1648, 1998.

List of Cited Figures

Including Notes on Copyright

All other images were made by the author of this thesis.

List of Figures

Including Acquisition Settings and External Sources

List of Tables

List of Publications

Publications Directly Connected to This Thesis

Article

- C. Donth, M. Weiss: A quantitative assessment of the spatial crowding heterogeneity in cellular fluids; Physical Review E 99(052415):1-6, 2019 (Editor's Suggestion)

Conference Posters (as Presenting Author)

- C. Donth, M. Weiss: Assessing the Spatial Heterogeneity of Crowding via Imaging and FRET; QBI Göttingen 2018
- C. Donth, M. Weiss: Assessing the Spatial Heterogeneity of Crowding in Living Cells; DPG Frühjahrstagung Berlin 2018
- C. Donth, M. Weiss: Assessing the Spatial Heterogeneity of Crowding in Living Cells; Profilfeldtagung Molekulare Biowissenschaften Lichtenfels 2018

Other Publications

Articles

- N. Pawar, C. Donth, M. Weiss: Anisotropic Diffusion of Macromolecules in the Contiguous Nucleocytoplasmic Fluid during Eukaryotic Cell Division; Current Biology 24(16):1905-1908, 2014
- D. Remmler, T. Schwaar, M. Pickhardt, C. Donth, E. Mandelkow, M.G. Weller, H.G. Börner: On the way to precision formulation additives: 2D-screening to select solubilizers with tailored host and release capabilities; Journal of Controlled Release 285:96-105, 2018

Conference Posters (as Presenting Author)

- N. Pawar, C. Donth, M. Weiss: Subcellular Organization of Eukaryotes during Mitosis; DPG Frühjahrstagung Regensburg 2016
- O. Stiehl, C. Donth, M. Weiss: Probing the Heterogeneity of Cellular Fluids; DPG Frühjahrstagung Regensburg 2016

Acknowledgements

First of all I would like to thank Prof. Dr. Matthias Weiss for allowing me to do the projects discussed in this thesis, thus providing me with the opportunity to earn a doctoral degree in his group.

I would certainly have failed in providing the measurement statistics needed in order to get meaningful results if it weren't for Dr. Gernot Guigas and, especially, Dr. Philipp Struntz. Thank you for helping me cope with a plethora of issues with our oh-so-sensitive microscope!
I want to thank our technical assistants, Pamela Anger, Christina Gräbner, Andrea Hanold, Alexandra Stadler and Kathrin Weidner-Hertrampf for their advice and guidance in all lab issues.
Usually computer technicians don't get noticed as long as everything works as it's supposed to. So I want to thank Ralf Pihan for indeed not having to call him to aid very often.
Thank you to Dr. Andreas Veres for providing me with WORKBENCH - this program really can do anything if you only know how to use it!
Thank you to Christopher Greve and Dr. Olivia Stiehl for providing me with the code I could base my lifetime analyses on.
Thank you to Dr. Dario Remmler at Humboldt University for letting me contribute to his interesting study on peptide-polymer conjugates.
A special thank you goes to all my proofreaders: Rebecca Benelli, Konstantin Speckner, Wolfgang Groß and Anneliese Donth for reading and editing this thesis, thus eliminating all grammar issues and enhancing its general readability and comprehensibility.
I would like to thank our secretaries, Margot Lenich and Jennifer Hennessy, as well as the dean's secretary, Susanne Süss, for helping me to fulfil all formal requirements.

Working is much more fun if you're surrounded by great colleagues. Therefore I want to thank all the current and former members of the Weiss and Kress groups.
Especially I want to thank Dr. Andreas Veres for being such a great office neighbour during the first three years of my thesis - I started missing the philosophical discussions we used to have the first day you were gone...
I want to thank Dr. Csilla-Maria Ferencz for stimulating discussions concerning various scientific topics, but also for companionship while waiting desperately for the cafeteria to finally open, for spontaneously meeting in Berlin, and for teaching me my very first (and only) Hungarian sentences!
A huge thank you goes to Konstantin Speckner for joining me on countless afternoon walks around the campus, for 'conspiratorial' discussions and for generally being a great office companion.
I want to thank Rebecca Benelli for our early-morning swimming sessions, and for numerous helpings of mousse au chocolat, brownies, cakes, ... I'm sure the others will by grateful if you keep 'practising' a little longer ;-)
I want to extend my gratitude to all my current and former office 'cohabitants'. Your deadpan humour as well as your unlimited supplies of chocolate and sweets helped me to cope with numerous throwbacks and the every-day madness of my work.

A very huge thank you goes to Wolfgang for patiently listening to my numerous complaints, for keeping me sane through all parts of this work and for being there whenever I needed you.
Another huge thank you goes to my family: Mostly you couldn't help me with my actual work, but you always made me feel welcome and let me feel your unconditional support. It was only recently that I realized this attitude doesn't come naturally in all families.
Especially I want to thank Dr. Lisa Rapp. Basically your idea of organizing an exhibition stopped me from abandoning my thesis in the first place...
A very special thank you goes to my friend Nader Rezazadeh. Knowing your story repeatedly helped me to put things into perspective.
Last, but not least, I want to express my gratitude towards a host of friends: Lisa, Fabian, Vera, Franzi, Lisa, Marlene, Emrah, Bengü, Lena, Olli Pirata & all members of Grupo Cativeiro, Thea, Andrea and many others I have left unnamed but to whom I am deeply grateful for helping me in more ways than I can recall and for simply being there.

Eidesstattliche Versicherung

Hiermit versichere ich an Eides statt, dass ich die vorliegende Arbeit selbstständig verfasst und keine anderen als die von mir angegebenen Quellen und Hilfsmittel verwendet habe.

Weiterhin erkläre ich, dass ich die Hilfe von gewerblichen Promotionsberatern bzw. -vermittlern oder ähnlichen Dienstleistern weder bisher in Anspruch genommen habe, noch künftig in Anspruch nehmen werde.

Zusätzlich erkläre ich hiermit, dass ich keinerlei frühere Promotionsversuche unternommen habe.

Bayreuth, den 28. Februar 2020

Claudia Maria Donth